There is nothing permanent, except change

Acknowledgments

Studying at Ghent University was as so: I started to learn about the Earth and ended up understanding the World. In many ways, it was actually not what I expected it to be; however, it was the place where I met wonderful people and the place that made me the person I am now. I was able to develop some useful skills and became more conscious about who I am.

I would like to thank two amazing people: Prof. Dr. Jean-Pierre Henriet and his wife Prof. Dr. Christine Iserentant. They helped me through the darkest period I knew in my life.

For my thesis research, which was a remarkable and interesting experience, I would like to thank Prof. Dr. Peter Van den Haute from the research unit of Mineralogy and Petrology (Ghent University) for the use of the polishing lab; Prof. Dr. Patric Jacobs from the research unit of Sedimentary Geology and Engineering Geology (Ghent university) for the use of the sedimentology lab; Prof. Dr. Veerle Cnudde from the research unit of Sedimentary Geology and Engineering Geology (Ghent University) for the use of the petrographic microscope; Dr. Jan Van den Bulcke from the Laboratory of Wood Technology (Faculty of Bio-engineering, Department of Forest and Water management, Ghent University) for the use of the tree-ring microscope; Prof. Dr. Laszlo Vincze and Dr. Geert Silversmit from the X-ray Microspectroscopy and Imaging Group (Ghent University) for the μ-XRF measurements.

Furthermore, I certainly would like to thank Prof. Dr. Marc De Batist (Renard Centre of Marine Geology, Ghent University) for giving me the chance to work on this project, providing the materials, and proofreading my thesis. I also want to express my appreciation for Drs. Maarten Van Daele (Renard Centre of Marine Geology, Ghent University) for advising me throughout this research, helping me to develop my research skills, introducing me to the impregnation techniques and for proofreading everything I wrote. Furthermore: Dr. Katrien Heirman for providing additional data and information on the study area; Drs. Jasper Moernaut for helping with proofreading. Finally, my reading commission: Dr. Elie Verleyen (Protistology and Aquatic Ecology, Ghent University) and Dr. Sébastien Bertrand (Renard Centre of Marine Geology, Ghent University). I also would like to thank Dr. Sébastien Bertrand for the interesting conversation and personal comments on my study area, as well as for providing me extra and exclusive information.

I also do not want to forget to thank my sister Maya Verlaak and my boyfriend Robert Blatt for providing me interesting background information and insight into spectral analysis. Furthermore, Robert Blatt for helping me with proofreading, but also for supporting me in every way. My parents, who supported me through my dreams.

TABLE OF CONTENTS

1. Introduction

Natural archives of past climates and environments, such as laminated sediments, are necessary to improve our understanding of climate changes during the Holocene period and further back in time. They can also be useful in estimating the degree of human impact on past environments. Sedimentary records that archive data about natural and anthropogenic climate change can extend our knowledge about trends, variabilities, events and the forcing factors behind climate change. With this information it is possible to develop and verify climate modeling. In the research focusing on the human impact on climate one needs time-scales relevant to society, this is a temporal resolution of less than 30 years. Varved lake sediments are one of the few types of geological records that can provide this high resolution (Zolitschka, 2007).

Using the principle of cause and effect on these natural archives, researchers were also able to establish the leads and lags in climate signals between both the two hemispheres and between the southern mid-latitudes and Antarctica. They proposed different processes and tested new models to understand the mechanisms behind global climate change and the flexibility of these changes (Sugden *et al*., 2005). However, there are many competing hypotheses about these mechanisms. Some of these are based on synchrony between the two hemispheres, others on asynchrony. The followers of the synchrony hypothesis focus on the synchrony of the Ice Ages between the two hemispheres. This idea was established from the broad similarity that was observed between ice core records in Greenland and Antarctica and ocean cores on time-scales longer than a millennium. On a millennial and sub-millennial time-scale, researchers also observed an apparent synchrony of glacier fluctuations in the European Alps, South America and New Zealand. The synchrony hypothesis assumes that global climate is forced by orbital insolation changes in the northern hemisphere and the interaction with the growth and decay of mid-latitude ice sheets. Additionally, it indicates that global climate changes through atmospheric mechanisms. The competing hypothesis argues that millennial-scale asynchrony was observed in some ice core records, ocean cores and vegetation and peat archives (Sugden *et al*., 2005). Sugden *et al*. (2005) refer to the studies of Blunier *et al*. (1997,1998) and Blunier and Brook (2001), which argue that the southern hemisphere leads the northern hemisphere or vice versa (White and Steig, 1998 in Sugden *et al*., 2005). Asynchrony is thought to be the reflection of the ocean bi-polar seesaw. The suggestion that this bipolar seesaw is driven from the north is explained by the fact that a cooling in the north suppresses the North Atlantic thermohaline circulation and leads to a warming in the southern ocean. In the same way a warming in the north will lead to a cooling in the southern ocean (Crowley, 1992; Broecker, 1998 and Clark *et al*., 2002 in Sugden *et al*., 2005). However, it is also thought that the bi-polar seesaw could be driven from the south, through mechanisms of wind stress affecting mixing and production of Antarctic waters (e.g. Toggweiler and

Samuels, 1995 in Sugden *et al*., 2005) or by changes in sea ice extent (Knorr and Lohmann, 2003 in Sugden *et al*., 2005 and Bianchi *et al*., 2004).

In this thesis research we will discuss a sedimentary record from Laguna Parrillar, Southern Patagonia, Chile. Southern Patagonia is particularly important in climate research because it can offer terrestrial climate records in the dominantly oceanic domain of the southern hemisphere (Sugden *et al*., 2005). Lake sediments from Laguna Parrillar can be used to determine the relative position, strength and cyclicity of global atmospheric circulation systems (e.g. Westerlies) that affect the whole southern hemisphere (Heirman *et al*., 2009). Because the area of Patagonia spans the southern westerlies, it holds the promise of linking climatic processes in mid-latitudes with those of the Antarctic domain and the location also allows for the ability to test the competing hypotheses about the mechanisms of climate change (Sugden *et al*., 2005).

The two main approaches to analyzing the sedimentary record from Laguna Parrillar are a microscope analysis technique (using a tree-ring measuring microscope) and an image analysis technique (using a script file developed at Tufts University (USA, Massachusetts, Medford)). Besides these techniques, also a color analysis and µ-XRF analysis has also been performed. With the color analysis, a spectral analysis was performed to detect cyclicities. The µ-XRF analysis helped establish a model to understand the genesis of the laminations. Zolitschka (2007) emphasizes the importance in first developing a model on the processes that formed the different lamina, prior to counting and measuring varve thickness. To do so, we also examined the thin sections under a petrographic microscope. Zolitschka (2007) further explains that this varve model will characterize specific features in varve composition, which are later used to determine boundaries between successive varves and to identify laminas of no chronological meaning (e.g. turbidites). We will then count and measure the thickness of the different lamina, as well as on the thin sections with the tree-ring measuring microscope, as on the collected digital images through the script files of Tufts University.

The aim of this study is to obtain high resolution palaeoclimatological and palaeoenvironmental information on the Late Pleistocene sedimentary record from Laguna Parrillar and to reveal possible cyclical events in the laminated sediment core. We want to conclude whether the lamina successions are varves, and so seasonally formed glacial varves, or represent another type of cyclical event. We will make a comparative study of the advantages and disadvantages of the use of microscope analysis techniques and the use of image analysis techniques.

In what follows, we will summarize some previous research and the Geology of the study area. We will discuss the Materials and Methods on the field and in the lab. We will provide the results from the observations on the petrographic microscope, the results of the microscope analysis, computer

analysis, the color analysis, the spectral analysis and the µ-XRF analysis. We will discuss advantages and disadvantages of the methods used, show relationships between the parameters and sediment properties and present some hypotheses.

2. The study area

The present study was conducted on sedimentary records from Laguna Parrillar (latitude: -53,41182 °S; longitude: -71,28645°W), located on the Brunswick Península in Chile, in the region of Patagonia, the southernmost part of South America (see Fig.1).

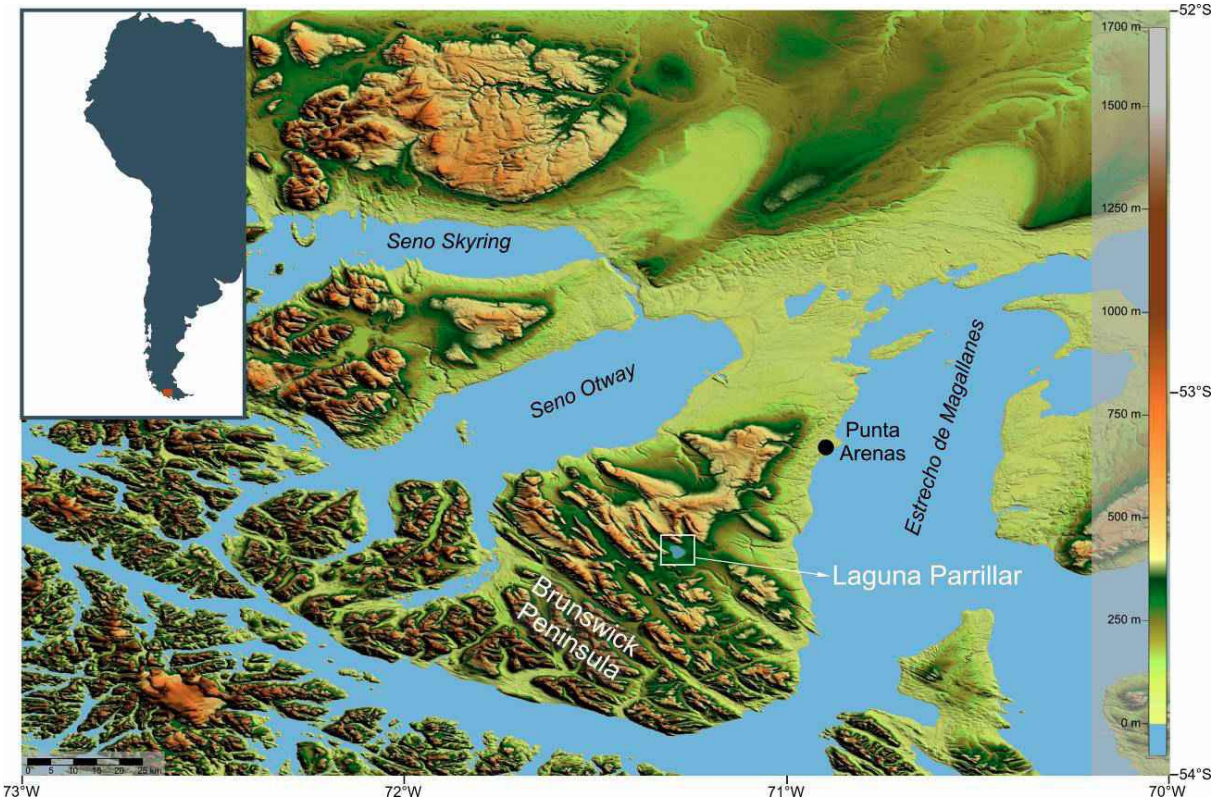

Fig. 1: SRTM (Shuttle Radar Topography Mission) image of the Brunswick Península in Chile and location of Laguna Parrillar; Source: expedition report Heirman *et al*., 2009

2.1 Geology

The Strait of Magellan and Bahìa Inùtil area is located at the junction of the Scotia, South American and Antarctic plates (Diraison *et al*., 1997 in Bentley *et al*., 2005) (see Fig.2). The Magellan fault cuts through the southwestern limits of the area, crossing the Magellan Strait near Puerto del Hambre, the northern part of Isla Dawson, and extending into Tierra del Fuego (Bentley *et al*., 2005). The Magellanes Fault System is a left-lateral transcurrent plate margin that separates the South American plate from the Scotia plate (see Fig.2). This fault system was formed in response to the opening of

Drake's Passage, found between South America and Antarctica at 30-35 Ma (Mazzarini and D'Orazio, 2003). The Scotia Plate supports the Cordillera Darwin and is partly composed of granites and metamorphic rocks (Bentley *et al*., 2005).

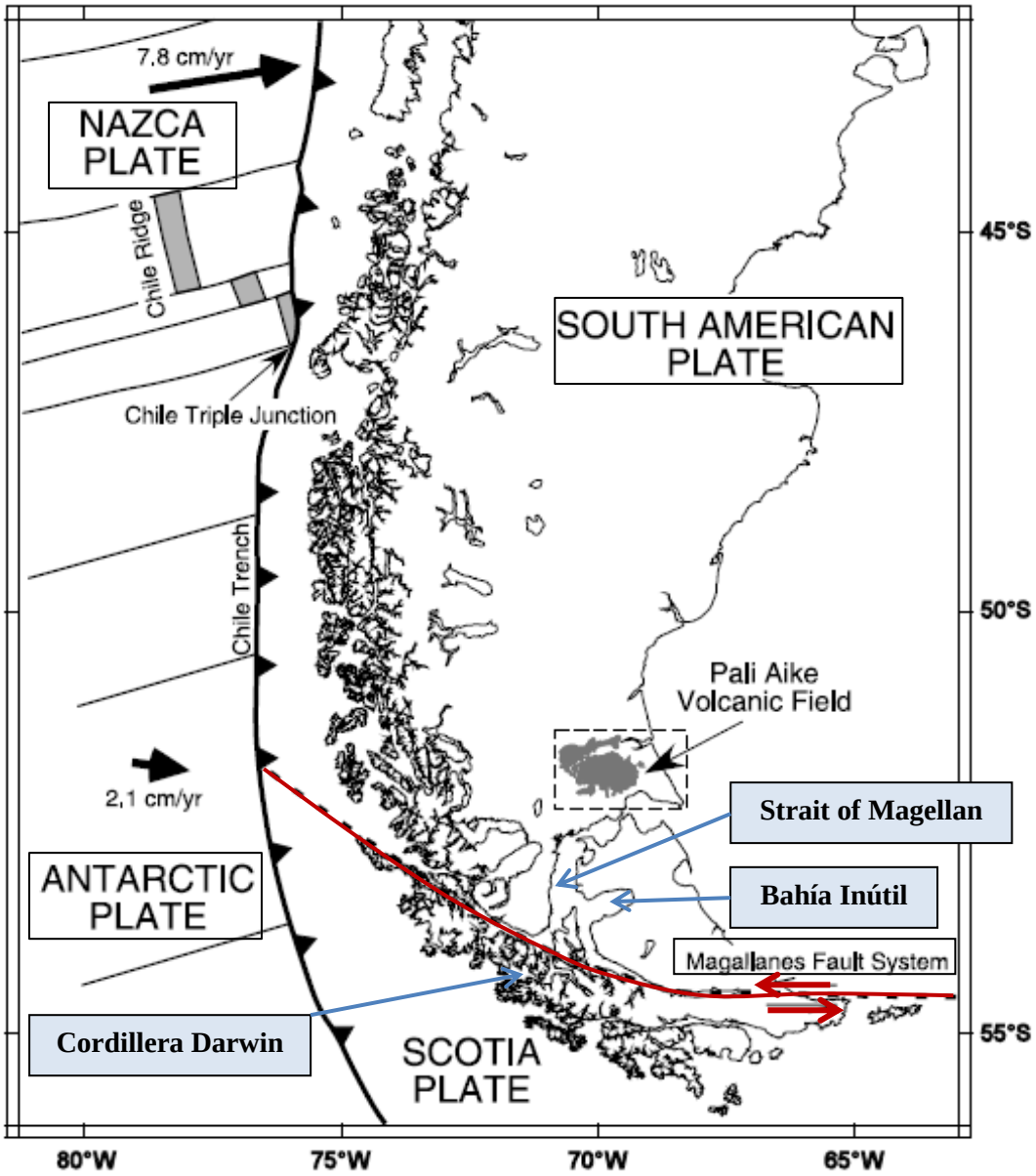

Fig. 2: Schematic geodynamic setting of southern South America and the adjacent Pacific Ocean. The sketch shows the fracture zones of the oceanic Nazca and Antarctic plates (thin lines), the trace of the Chile Trench (heavy line with triangles on the overriding plate), the trace of the transcurrent margin between the Scotia and South American plates (dashed line), and the Chile spreading ridge (grey stripes). The two large black arrows are the convergence vectors of the Nazca and Antarctic plates with respect to South America according to the NUVEL-1A model of DeMets *et al* (1994) (Mazzarini and D'Orazio, 2003).

The Andes form an arc between the north-south oriented Patagonian Cordillera and the east-west oriented Darwin Cordillera that bind the Magellan Basin on its western and southern sides (see Fig.3).

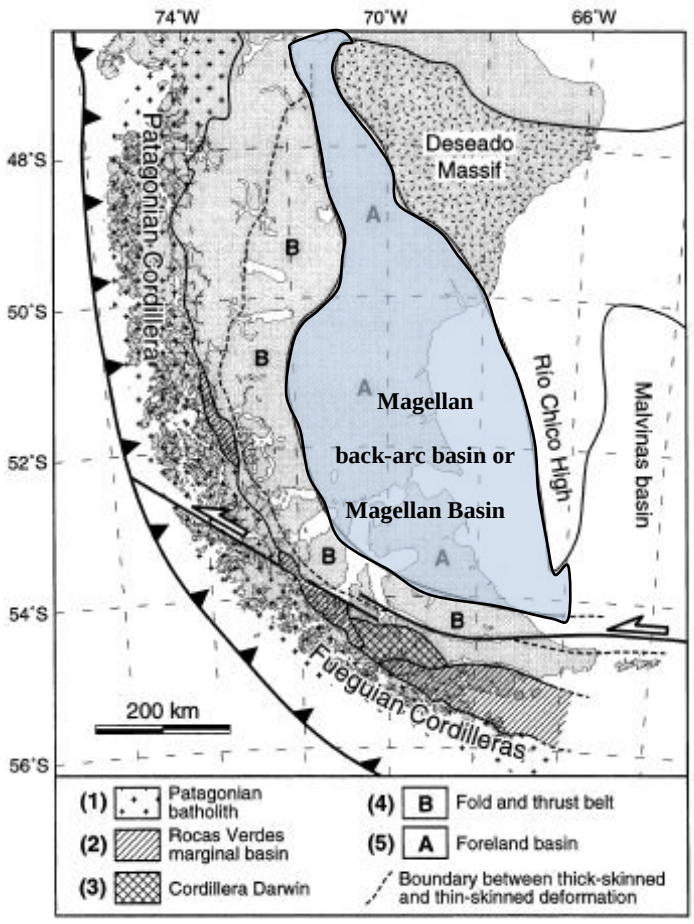

Fig. 3: Map of the southern tip of South America, showing five tectonic provinces (adapted and extrapolated northwards from Klepeis, 1994) and main Cordillera (Patagonian in NW, Fueguian in SE) (Diraison *et al.*, 2000).

Both the arc and the basin were formed from complex tectonics at the southwestern margin of Gondwana since the Late Triassic. The basin went through three main stages. First there was a stage of regional extension from Triassic to Early Cretaceous, which formed a NNW trending rift system leading to the opening of the Magellan back-arc basin. This was contemporary with the early opening of the Southern Atlantic Ocean. Secondly, closure of the back-arc basin during the Late Cretaceous coincided with changes in plate tectonics. The closure of the basin was associated with the uplift of the Cordillera and thermal subsidence of the Magellan Basin. Thirdly, during the Cenozoic, the Magellan Foreland Basin was formed, and deformation propagated cratonwards through a fold-and-thrust belt (Diraison *et al*., 1996). The Magellan Foreland Basin includes the Atlantic segment and a section of the central segment of the Magellan Strait (Bartole *et* al., 2008). The sedimentary infill of the basin has a local thickness of as much as 8 km. Around the Magellan Straits, the Cenozoic sediments have a degree of symmetry in their distribution (see Fig.4). The structural pattern in the southern Andes and Magellan Basin is consistent with the complex tectonic context of southern South America. Deformation is due to the relative motions between the Nazca, Antarctic, Scotia and South American plates. The deformations include shortening in directions subperpendicular to the mountain belts and strike-slip movements. Along the southern Patagonian Andes, a right-lateral strike-slip component existed, and along the Cordillera Darwin, a left-lateral strike-slip component could be found. In the space between them, stretching along the arc has resulted in the formation of rift valleys (Diraison *et al*., 1996).

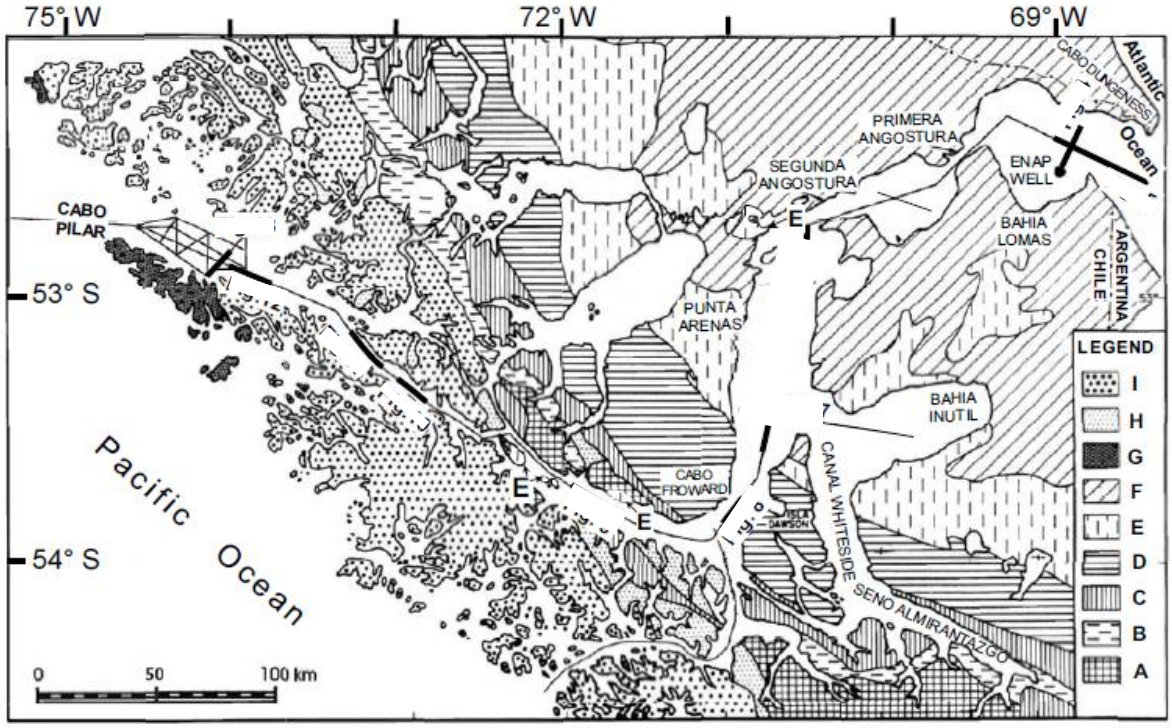

Fig. 4: Geology of the Magellan Strait area (modified from Bambati *et al*., 1991 and from S.N.G.M., 2003). Symbols: A) Undifferentiated Paleozoic rocks; B) Silica rich volcanic and volcaniclastic Jurassic to Early Cretaceous rocks; C) and D) Early and Late Cretaceous sedimentary rocks, respectively; E) Cenozoic marine paralic and continental rocks; F) Quaternary fluvioglacial sediments; G) Undifferentiated Late Paleozoic-Early Mesozoic sedimentary and volcanic rocks; H) Late Jurassic-Early Cretaceous effusive and intrusive rocks; I) Patagonian Batholith (Bartole *et al*., 2008).

The Magellan Foreland Basin is an asymmetric depression, and its depocentre axis is located near the sub-Andean fold and thrust belt (Bartole *et al*., 2008). The stratigraphy of the basin consists of a pre-Mesozoic schistose and gneissic basement overlain by a more than 7000 m thick Early Cretaceous to Pliocene sedimentary fill that consists of a sequence of marine clastic sedimentary rocks (Olea and Davies, 1977 and Cañón and Ernst, 1974 in Bartole *et al*., 2008). Corresponding to the three main phases of the basin development, the sedimentary infilling of the basin can be divided into three major packages (Biddle *et al*., 1986 in Bartole *et al*., 2008). The lowermost package is a syn-rift Triassic to upper Jurassic package, the second is a late to post-rift sedimentary section of upper Jurassic to upper Cretaceous age, and the third is a foreland basin, eastward-thinning package of uppermost Cretaceous to Cenozoic age (Bartole *et al*., 2008). A final regression in the Miocene transformed the foreland basin into a shallow-water area (Olea and Davis, 1977 in Bartole *et al*., 2008). During the Neogene and Quaternary, several glacial expansions moulded the Patagonia and Tierra del Fuego region, leaving a widespread distribution of glacigenic landforms (Bartole *et al*., 2008; Rabassa *et al*., 2000). Bentley *et al*. (2005) mapped and correlated four main glacial stages (B to E) within the last glaciation and deglaciation deposits, and McCulloch *et al*. (2005a) resolved the chronological problems within this previous research. They conclude, as discussed above, that the Last Glacial Maximum is

represented by Stage B, culminating around 25200 - 23100 cal. years BP. Three minor glacial advances followed Stage B: during Stage C (21700 - 20300 cal. years BP), during Stage D (17500 cal. years BP), and one during Stage E (15507 – 11773 cal. years BP).

2.2 Geography

Fig. 5: The region of Patagonia (16°S – 56°S) and the Andean Cordillera; Source: https://globalhistorycullen.wikispaces.com/file/view/3887-004-73462CE0.gif/74509089/3887-004-73462CE0.gif

Patagonia, occupying the eastern and western side of the southern Andean cordillera (41°S to 56°S), spans several climatic zones (see Fig.5). Northern Patagonia is characterized by deserts, the south by ice fields (see Fig.5) that represent the largest extent of ice in the Southern Hemisphere outside Antarctica. The Chilean southern Andes (27°S - 56°S) follow a north-south trend, until 50°S where the Andes curve eastwards into the island of Tierra del Fuego. South of 38°S, the mean elevation of 4000 m lowers to 2000 m (Rabassa and Clapperton, 1990 in McCulloch *et al*, 2005a). Small glaciers rest on the Andean peaks between 42°S and 46°S, and from 46°S to 52°S the peaks are covered by the North Patagonian and South Patagonian ice fields (see Fig.6). The Magellan region, south of 51°S, includes the southern extent of the South Patagonian ice field that end where the Andes drop below 500 m in altitude (see Fig.5). The elevation rises again at the Cordillera Darwin (2438 m), an area that supports a number of small ice fields (see Fig.6). To the north and east of the Cordillera Darwin and to the Atlantic coast, the Tierra del Fuego area is low lying (0-200 m) (see Fig.5). The Peninsula Brunswick, with its highest point at 1269 m, is located west of the Strait of Magellan. The peninsula forms part of the South American mainland. In between the Tierra del Fuego, Peninsula Brunswick and the Cordillera Darwin, lies Isla Dawson (McCulloch *et al*, 2005a) (see Fig.7).

Fig. 6: The Northern and Southern Patagonian Ice Fields and the ice fields of Cordillera Darwin; Source: http://maps.grida.no/go/graphic/south_america_southern_ice_fields

There are two major marine waterways. Firstly, there is the central stretch of the Strait of Magellan between the mainland of Chile and the island Tierra del Fuego. Secondly, the Bahía Inútil embayment can be found, which is a northeast-southwest oriented branch of the Magellan Strait (Bentley *et al*., 2005) (see Fig.7). The Magellan Strait has a length of approximately 560 km, running from the Atlantic to the Pacific Ocean. Three segments can be recognized, each with a distinct orientation. The eastern Atlantic segment shows a ENE-WSW orientation and is nearly 140 km long from the Atlantic opening to the Segunda Angostura (see Fig.7). The central segment extends 140 km in a north-south direction down to Paso del Hambre. South of this location, the Magellan Strait bends to the northwest towards the Pacific Ocean, forming the western Pacific segment. This segment stretches almost parallel to the Andean Cordillera, for nearly 280 km, and as far as the Pacific entrance at Cabo Pilar (Bartole *et al*., 2008) (see Fig.7).

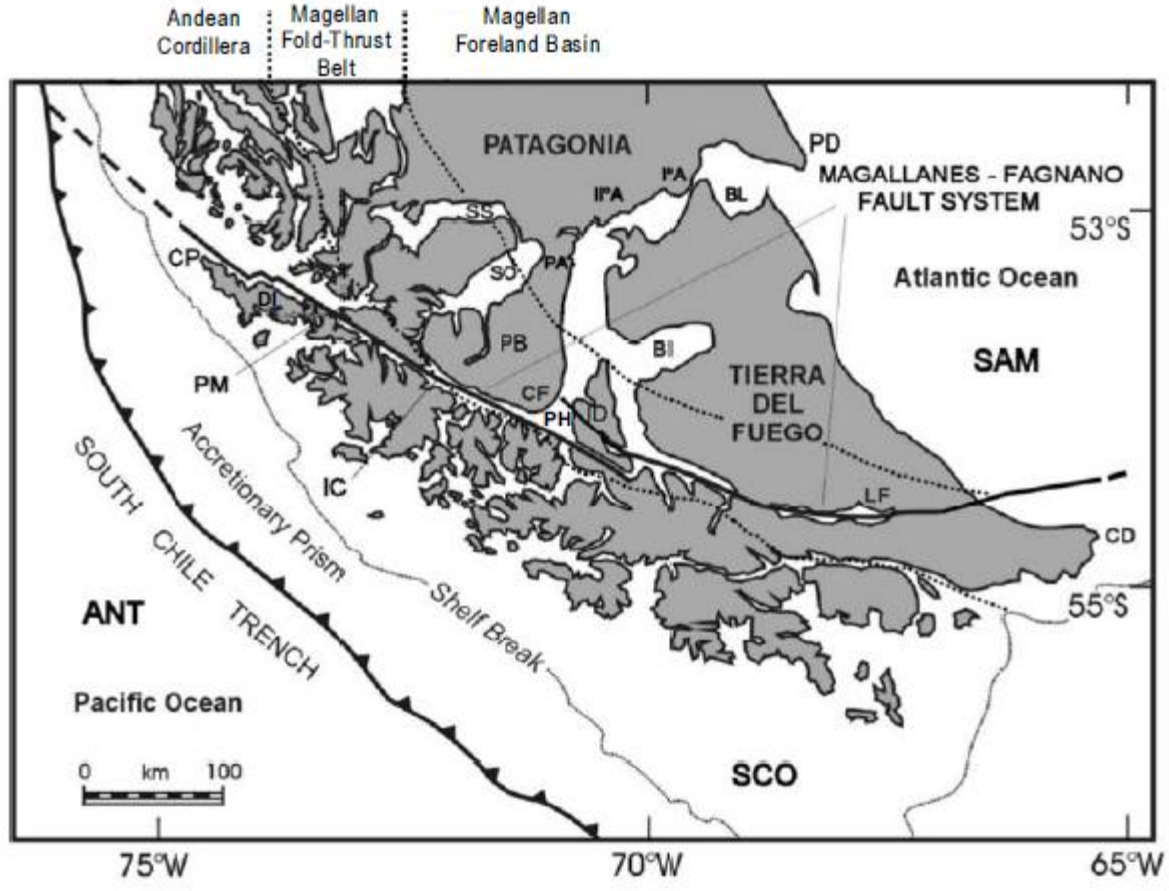

Fig. 7: Plate boundaries and morphotectonic provinces at the southern tip of South America. ANT: Antarctic plate; SAM: South American plate; SCO: Scotia plate. Geographic names referenced in this figure: I°A, II°A: Primera and Segunda Angostura; BI: Bahía Inútil; BL: Bahía Lomas; CF: Cabo Froward; CP: Cabo Pilar; DI: Isla Desolación; IC: Isla Carlos III; ID: Isla Dawson; LF: Lago Fagnano; PA: Punta Arenas; PB: Peninsula Brunswick; PD: Punta Dungeness; PH: Paso del Hambre; PM: Paso del Mar (Bartole *et al*., 2008).

Precipitation decreases from west to east, from 5000 mm to 300 mm (McCulloch and Davies, 2001). South of 38°S, the convergence of the south Pacific subtropical high and the polar front produces low

pressure areas and storms throughout the year. Therefore, the region experiences precipitation all year, with a point of maximum precipitation at 50°S (Romero, 1985 in McCulloch *et al*, 2005a). This is the zone of the westerly storm tracks, transporting moisture from the Pacific Ocean. Most of it falls along the coast and on the western flanks of the Andean Cordillera, creating a rain shadow on the eastern flanks of the mountain range (McCulloch and Davies., 2001; McCulloch *et al*, 2005a). During the southern hemisphere's winter (June-August) the Antarctic sea ice advances; during the summer (November-January) it retreats. This seasonal cycle of advance and retreat in sea ice coincides with the seasonal shift in the distribution of the Westerlies. During winter, the expansion of the sea ice forces the polar front to move 5° of latitude equatorwards and gives the Chilean Lake District (extending from 39°15'S to 43°20'S) its winter precipitation (McCulloch *et al*, 2005a).

There is a north-south decrease in mean annual temperature, from 12°C at 38°S to 6°C at 53°S (in the vicinity of Punta Arenas). The climatic zonations, as well as the topographical zonations discussed above, are reflected in the vegetation cover of southern Patagonia (McCulloch and Davies, 2001; McCulloch *et al*., 2005a).

2.2.1 South Patagonian vegetation cover

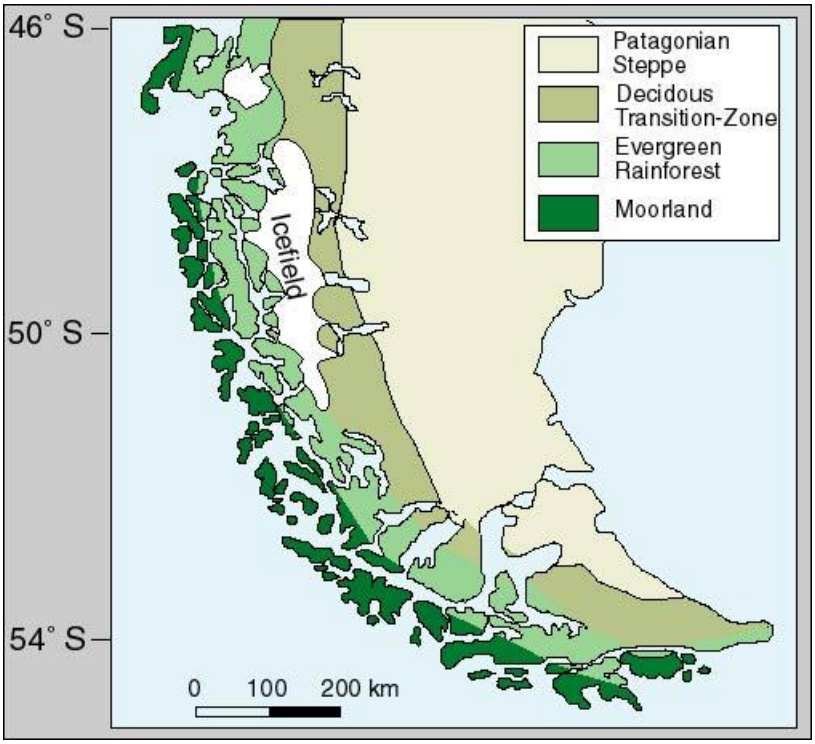

Fig. 8: The vegetation pattern in southernmost South America; Source:http://www.sfu.ca/~jkoch/older_stuff/fieldtrips/Patagonia/pataveget/pataveget.htm

Mesophytic species are found in the north, and cold tundra and alpine flora are found in the high Andes. Vegetation becomes more verdant with the latitudinal increase in precipitation (McCulloch *et al*., 2005a). Four ecotones (see Fig.8) lie in a north-south orientation, their boundaries determined by the west-east precipitation gradient. Until south of 50°S, the boundaries follow the same curve

eastwards as the Andes. The extreme west (Pacific coastal archipelago) and south of the Andes are occupied by the Magellanic moorland. Precipitation in this area, ranges from 2000 to 5000 mm a year. Where both the precipitation is between 800 and 4000 mm a year, and where boreal conditions exist, evergreen forests (rainforest) dominate. Along the eastern flanks of the Andean cordillera, deciduous forests are present, where precipitation is between 400 and 800 mm a year. Where precipitation drops below 400 mm a year, steppe vegetation can be found (McCulloch *et al*., 2005a). This type of vegetation occupies eastern Patagonia in the eastern and southeastern margins of Chile, most of Argentine Patagonia and in Tierra del Fuego (Moore, 1983 in McCulloch and Davies, 2001; McCulloch *et al*., 2005a). During the Last Glaciation, the rainforest ecotones moved more northwards and the steppe/tundra ecotone expanded in southern Patagonia (Villagran, 1988 in McCulloch *et al*., 2005a).

3. Materials and methods

3.1 On the field

The survey at Laguna Parrillar (Reserva Forestal Laguna Parrillar, Región de Magallanes y la Antarctica chilena) took place from 30 March to 2 April 2009. To record the position of all the samples taken, a GARMIN hand held GPS system was used.

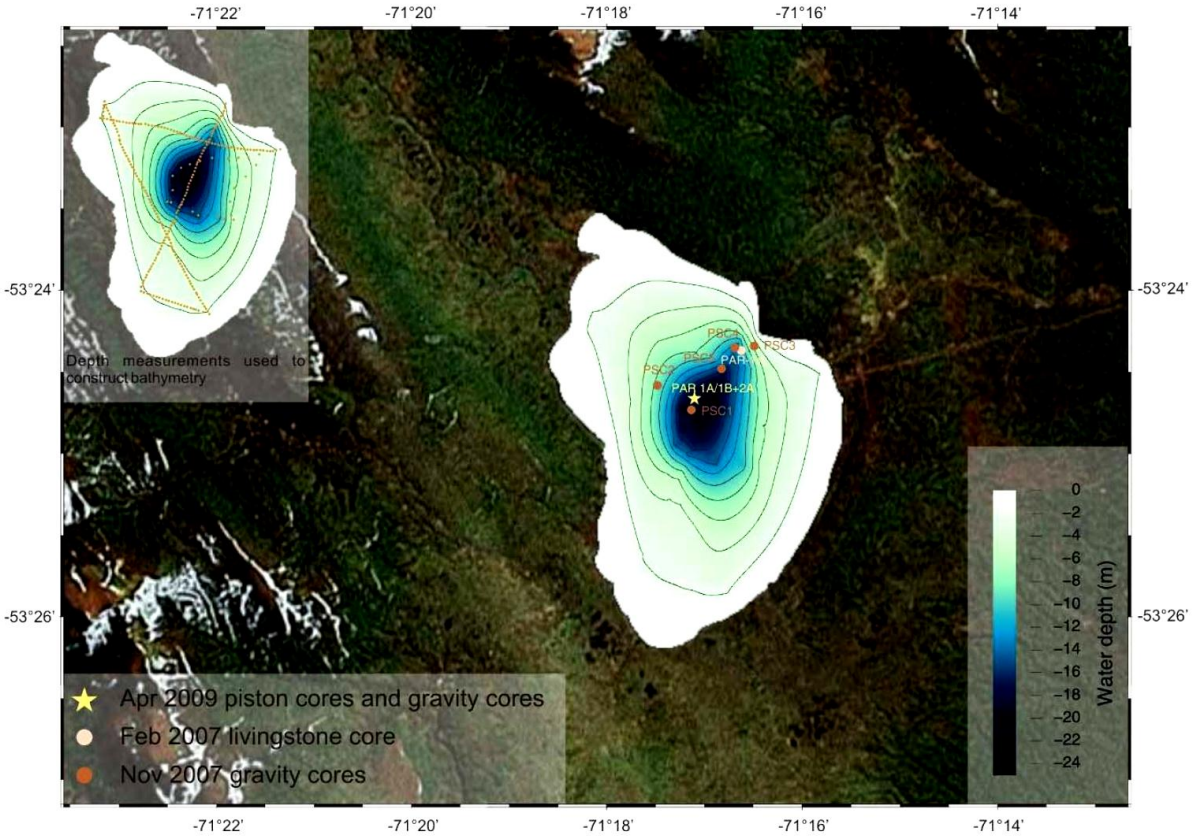

Fig. 9: Bathymetric map of Laguna Parrillar (based on the depth soundings of the field campaigns in 2007) with the location of all the cores taken during the field campaigns in 2007 and in 2009

Fig. 10: The platform used on Laguna Parrillar

A Parametric Echosounding System, SES 96 from INNOMAR, was used to obtain information about the geometry of the sedimentary infill of the lake and to determine the best spot to take the sediment cores (see Fig.9). The echosounding system was mounted on the same platform that was later used for the coring. To determine the sound velocity of the lake water, a CTD measurement was performed. Echosounding was limited to the central and deepest part of the lake, because there was no penetration in shallower waters. To take a long sediment core a UWITEC piston core system and platform was used (see Fig.10). The platform was kept in position during coring by four anchors, one at each corner. During the field survey, three piston cores and three gravity cores were collected. In this study, we will

discuss a part of the PAR 1A piston core that has a total length of 5 m, with a sediment depth of 0 to 5 m, and a diameter of 60 mm. The PAR 1A core was taken on 1 April 2009, at a latitude of -53,41182°S and longitude of -71,28645°W (Heirman *et al.*, 2009).

3.2 In the lab

3.2.1 Sampling

Sampling of the cores consists of sub-sampling, followed by a freezing process using liquid nitrogen, after which the sub-samples were transferred into a freeze-drying chamber. We used the methods of Boës *et al*. (2005) with little modifications. Prior to sub-sampling, the cylindrical cores were sampled with a plastic, 1 m long and 4 cm wide, U-channel, of which the bottom was covered with aluminum foil. The aluminum foil makes it easier to later remove the thin brick stone shaped sub-samples and avoid major deformation of the sediment. The U-channel was pushed carefully by hand into the sediment, and then removed slowly by inclining the cylindrical core to make sure no sediment was left behind.

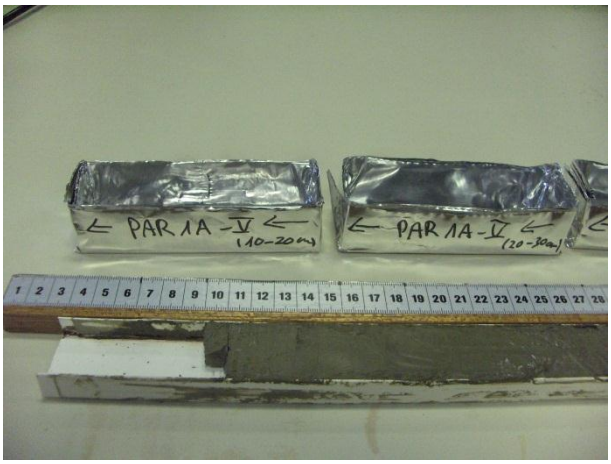

Fig. 11: Aluminum boxes and U-channel with sediment ready for sub-sampling

The sub-samples taken were approximately 11 cm long and were transferred into aluminum boxes (see Fig.11). These aluminum boxes were then placed in a large plastic box with liquid nitrogen, which boils at -196°C in atmospheric pressure conditions of 1 atm. The liquid nitrogen is used for freezing the samples (see Fig.12). These lyophilization (freezing and freeze-drying) methods where previously proposed by Bouma (1969), Pike and Kemp (1996) and Francus (1998).

During the freezing process with liquid nitrogen, interstitial liquid water is removed by sublimation. This fosters a quick drop in temperature, which will enable the growth of small cubic ice crystals instead of larger hexagonal crystals (Francus, 1998). A disadvantage of this technique is that the shock of quick freezing causes a micro structure of freezing-cracks (Boës *et al*., 2005).

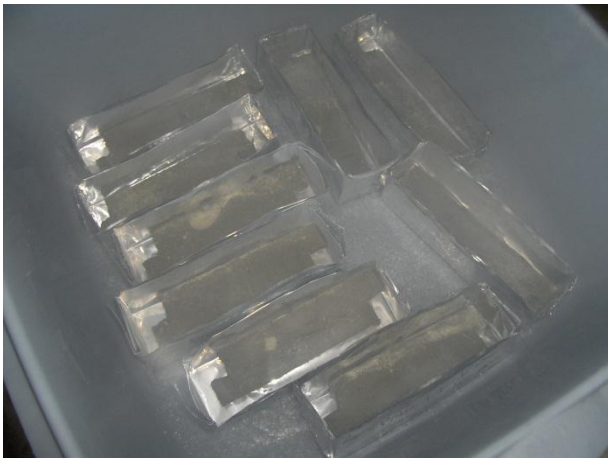

Immediately after this freezing process, the samples were transferred into a freeze-drying chamber under vacuum, in which the temperature is lowered till -40°C. In the freeze-drying chamber, the ice will sublimate and water vapor is collected in a condenser (Boës *et al*., 2005 and Crevello *et al*., 1981). After two days in the freeze-drying chamber, the samples are dry and ready for the impregnation treatment.

Fig. 12: Freezing of the samples in liquid nitrogen

3.2.2 Impregnation

Impregnation of the samples with a resin will reveal laminations that are not visible on the fresh core, and will therefore reduce underestimation of the number of laminations. Coarser grained sediments, with respect to finer grained sediments, and more porous compared with less porous sediments, react in a different way on the resin. Therefore, the laminations become more visible. We followed the impregnation method used by Boës *et al*. (2005).

The impregnation procedure is carried out in an exsiccator under controlled pressure conditions (see Fig.13, Fig.14). The vacuum level during impregnation is 500 mbar (half of the atmospheric pressure). A lower pressure will facilitate the impregnation, but one should be careful not to lower pressure too much when working on very fine grained/low porosity sediments, as this can cause damage to the sediment texture (Boës *et al*., 2005).

Fig. 13: Exsiccator connected to the vacuum pump

The impregnation mixture consists of 130 ml TRA resin, 50 ml acetone, 8 droplets MEKP (methylethyketon peroxide), 0.4 droplets cobalt(II)2-ethylhexanoate 65 wt% (catalysator). This is a modified recipe, modified after Boës *et al*. (2005).

The saturation of the sediment with the resin mixture is by capillarity. The acetone is added to lower the viscosity of the resin in order to accelerate the resin flux into the sediment pores (Lamoureux,

Fig. 14: Aluminum boxes with sediment samples ready for impregnation

1994). The acetone-resin mixture is added carefully in separate steps to avoid the formation of air bubbles. We start with adding a thin layer of the acetone-resin mixture on the bottom and after 5 minutes, another thin layer is added. Ten minutes later 1/4 of the aluminum boxes are filled with the resin, and, after a total of 30 minutes, the mixture is added up to nearly the edge of the sediment. One and two hours after starting the impregnation, more of the mixture is added up to the edge of the sediment. After a total of 4 hours, the boxes are filled until the mixture just covers the sediment; 15 minutes later, the rest of the box is filled with the resin. After each of these steps the samples are brought under lower pressure conditions of 500 mbar to remove possible air bubbles and to fasten the impregnation of the resin into the sediment pores. After completion of all these steps, the samples are left to air-dry for three days until the resin has become hard. Then, the samples are placed in an oven at 40-50 °C for two days so that they are completely dry. However, this is also done to compensate for energy loss and to accelerate the polymerization rate, since during polymerization, the temperature increases and the polymerization rate decreases. After this procedure, the impregnated sediment blocks can be conserved for a long duration, and thin sections can be prepared.

3.2.3 Preparing the thin sections

The procedure for making thin sections from the impregnated blocks starts with removing a layer off the top part of the blocks. This is to ensure that the top surface of the block is horizontally in comparison with the bottom surface of the block, where a slice of sediment with equal thickness will have to be cut off in order to prepare the thin section. The polishing machine works with a rotating disc covered with diamond powder and can precisely remove very thin, micrometer-thick layers from the surface of the blocks. A constant flow of cooling oil from the polishing disc is maintained on the surface of the block. One should pay special attention at this point, as a warming up of the block, caused by the polishing procedure, can cause the surface of the block to start expanding and curving, so one should pay attention for this. After polishing has concluded, it can be the case that the thickness of the sediment is still a little uneven. This can be corrected by polishing the surface manually with some polishing oil. After this, the sample is cleaned very well with ethanol. A glue-like substance is then prepared on the base of 20 ml of TRA resin (the same resin used for the impregnation of the samples), 14 droplets of MEKP, 7 droplets of cobalt(II)2-ethylhexanoate 1% and 15 droplets of Dynasylan. This mixture is spread out over the polished bottom surface of the block; a glass plate is

pressed on top of it, and the whole is placed under a heavy weight for a night until it is dry. However, after 30-45 minutes, the glue that dripped from the sides is first cleaned up. The thin section can be made on the following day. The main part of the block, the section attached to the glass plate, will be cut off so that only a slice of approximately 1 mm remains. This thin slice is then polished further with the polishing machine until a thin section of 30 µm is obtained. The thin section is cleaned once more, and a covering glass plate is attached on top of it, with another glue-like substance; However, this time it is created without the Dynasylan. When the glue is dry, the thin section can be cleaned and is now ready for use.

3.3 Methods

3.3.1 Petrographic microscope observations

To describe the sample PAR1A-III (50-60) in detail, an Olympus BH-2 optical microscope was used. The grain size, type of grain, the shape of the grains (roundness), the sorting of the grains, and possible fining upwards or coarsening upwards trends, were described for each lamina. For an overall view on the thin section, a magnification of 10 X 4 was used. Measurements on the grain size were performed at a magnification of 10 X 10. To be able to relate and compare these observations with the high-resolution image scan taken from the surface of the sample, a scale-bar was drawn on the thin section and transferred onto the high-resolution image scan of sample PAR1A-III (50-60).

For these petrographic microscope observations, the sample PAR1A-III (50-60) was chosen, as it is characterized by a variety of different types of laminae, recognized on the scanned image. By describing these different laminae in detail, one is able to create a representation of the laminae in the rest of the core.

3.3.2 Measuring lamina thickness, and counting laminations

In what follows, we will discuss the two main methods that were used to analyze the samples. The first method uses a microscopic analysis with a tree-ring measuring microscope, using the thin sections. The other method involves image analysis with a script file developed at Tufts University and the program StratiSignal. For this method, the high-resolution image scans, obtained from the impregnated sample blocks, are used.

3.3.2.1 Microscope analysis technique with thin sections

The microscope analysis was performed with a tree-ring measuring Olympus SZX12 microscope connected to a computer running the program TSAPWIN. The program collects and displays what was measured on the microscope. For these measurements the thin sections were used. The measurements consist of measuring the thickness of the observed lamina by placing the vertical part of the crosshair on the boundaries between laminae and clicking with the computer mouse to transfer the measurement to the computer. The thin sections were measured from top to bottom using the following tree ring settings: "from bark to pith" and "from left to right". The option "early wood/late wood" was chosen to indicate that the first boundary selected, would be the bottom of the first coarse grained/ light colored layer and that the last boundary would be the top of the last coarse grained/ light colored layer or bottom of the last fine grained/dark colored layer.

The TSAPWIN program saves the collected data in Heidelberg files, which were transferred into Excel files with the program PAST32. The data for each sample consists of a column displaying only the thicknesses of the coarse grained/ light colored layers, a column displaying only the thicknesses of the fine grained/dark colored layer, and one displaying the couplet thickness, the sum of the thickness of the coarse grained/light colored layer and the fine grained/dark colored layer.

3.3.2.2 Computer analysis technique with sample image scans

To perform an image analysis on the samples, we used a script file developed at Tufts University (USA, Massachusetts, Medford), that runs in UTHSCSA (University of Texas Health Sciences Center at San Antonio). The developed script file, Varve300.itm, takes advantage of the image analysis utilities of UTHSCSA (Wilcox *et al.*, 1996).

Digital images were collected from the polished sides of the impregnated sample blocks with a CanoScan4400F table scanner at high-resolution, with an output size of 2592 x 1944 pixels and an output resolution of 1000 dpi, the images were produced in BMP-format. The samples were scanned in two overlapping parts together with a scale bar placed along the side of the sample roughly perpendicular to the bedding. As the program is designed to rotate the images in a correct position for calibration, the samples need to be scanned in landscape view with the bottom side of the samples to the left. We also renamed the sample images, as the program only loads images with a name limited to six alphanumeric characters. Before loading these images into the program, they were resampled to a resolution of 800 x 600 pixels, using CorolPhotoPaintX3. This allowed them to be opened completely in the measurement's program window without slide bars. After saving the collected images in the appropriate folder, they can be loaded into the varve analysis program and calibrated using the scale

bar. Following image calibration, the measurement of varve thickness (or lamina thickness) can be started. Completed images are saved together with a data table (Wilcox *et al.*, 1996).

3.3.3 Color analysis

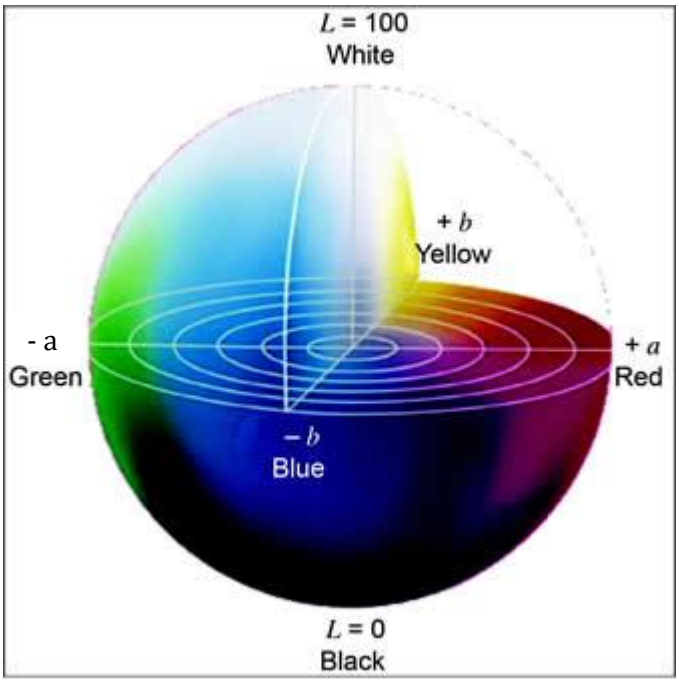

Fig. 15: Three-dimensional representation of the L*a*b* color space

The color analysis was performed on the complete record (PAR1A-III, PAR1A-IV and PAR1A-V), as well as on the part of sample PAR1A-III(50-60) on which also a µ-XRF analysis was performed (see further). To perform a color analysis in the program StratiSignal, high-resolution images (2592 x 1944 pixels) were used. The three-dimensional L* a* b* model was chosen as a color space model (see Fig.15). This model defines the color of an object using the three coordinates L, a and b, in which L stands for lightness, ranging from 100 (complete lightness) to 0 (complete darkness). The a-coordinate changes from red (a>0) to green (a<0), and the b-coordinate changes from yellow (b>0) to blue (b<0). For every image, three color analysis graphs were created (100% L, 100% a, and 100% b).

3.3.4 µ-XRF analysis

Also a micro XRF analysis was performed on the sample PAR1A-III (50-60). The XRF spectra were recorded at Ghent University with an EDAX EAGLE-III microprobe (see Fig.16), equipped with a Rh X-ray tube and a glass polycapillary for X-ray focusing.

The spectra were recorded in a vacuum with a LN2 cooled Si(Li) energy dispersive detector. The source voltage was 40 kV, the source current 180 µA, the beam size 100 µm, and the shaping time was 17 µs. The mapping was performed with 11 s/ pixel, and 50 µm step in X and Y direction . The dimensions were 50 µm X 50 µm, and the collection time was 72 h 10 min.

Fig. 16: An EDAXEAGLE-III microprobe

A 2D map of 20 mm by 2 mm on the core piece was recorded. Unfortunately, the sample started moving halfway the map after each return to the start of a new line, this because the sample block was curved. Therefore, only 20 lines can be considered as the useful part of the map.

3.3.5 Spectral analysis

On the color analysis dataset, we performed a spectral analysis by the use of "XLSTAT time". This Excel tool is able to transform a time series into its coordinates in the space of frequencies and to analyze its characteristics in this space. XLSTAT displays a table with the values for the frequency, period, the cosine coefficients of the Fourier transform, the sine coefficients of the Fourier transform, the phase of the spectrum, the values of the periodogram, and the spectral density (estimate of spectral density). Additionally, it also displays a periodogram and a spectral density chart on both the frequency and period scales. The spectral density corresponds to the transform of a continuous time series. The program first obtains the discrete Fourier coordinates, the cosine and sine transforms, and then the periodogram. By the use of a smoothing function, a spectral density estimate (or discrete spectral average estimator) can be obtained, which is a better estimator of the spectrum. From the spectral density charts, seasonal components can be identified. XLSTAT offers five different kernel weightings: Bartlett, Parzen, Quadratic spectral, truncated and Tukey-Hanning.

The Bartlett kernel is one of the first spectral methods, developed by Bartlett in 1964. Not many research uses the truncated or quadratic methods; however, a study that compared the Parzen method

with the Hanning method (Tadros and Shaltout, 2003) was found. They concluded that the Hanning method is more favorable to identify more frequencies, which may help in the identification of different cycles. Fagel *et al*. (2008) studied climate oscillations on lacustrine sediments from southern Chile. They applied spectral analysis on the total varve thickness to identify potential periodicities in the signal. However, they use spectral methods that are not offered by XLSTAT. Consequently, we chose the Hanning method from the five methods offered by XLSTAT, on the base of the study by Tadros and Shaltout (2003). We will use the Bartlett method to compare to our results from the Hanning method.

3.4 The age data

The age data used in this study was obtained from a ^{14}C dating on tephra layers in the core. Only a few tephra layers were sampled for ^{14}C dating. The calibration curve used was IntCal09.14C, and an age-depth model was constructed (see Fig.17), weighted by the calibrated probabilities. Calendar age point estimates were calculated for depths based on the weighted average of all the age-depth curves. The calendar-scale used was cal. BP at a resolution of 1 year. Ages were calculated for every 0.1 cm depth, from 0.5 (minimum depth) to 694.6 (maximum depth) cm (pers. comm. Heirman K.).

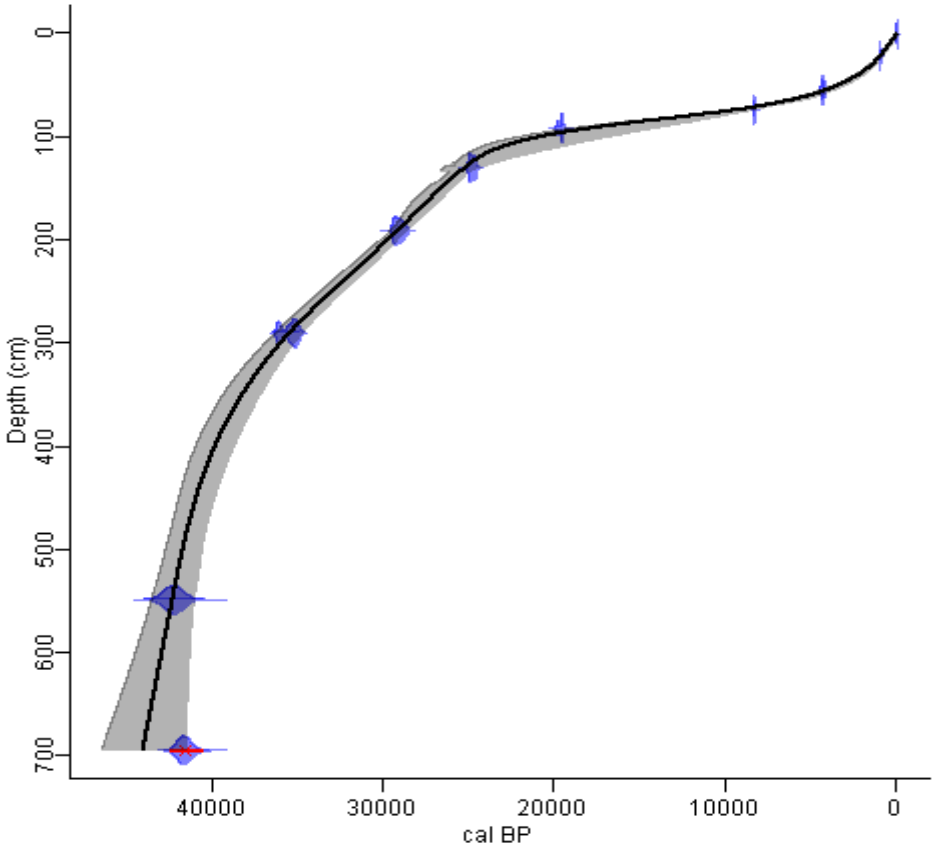

Fig. 17: Age-depth model; source: K. Heirman

4. Previous Research

4.1 History of the study of varved lake sediments

Varves were initially considered deposits typically related to glacial melt-water entering a proglacial lake. The term ‘varve’ is the Swedish word for ‘cyclic layer’. The Swedish Geological Survey used it for the first time in 1862 to describe rhythmically deposited clays in a proglacial environment. In 1912, Gerard De Geer defined the term ‘varve’ as a deposit representing one complete annual cycle and consisting of a coarse-grained pale summer layer and a fine-grained dark winter layer. De Geer used the chronological information stored in varved clays, deposited near the margin of the retreating Scandinavian ice sheet, to determine the time elapsed since the end of the Pleistocene (Zolitschka, 2007).

De Geer was convinced that solar forcing controls meltwater discharge and, in turn, varve thickness variations. When De Geer failed to prove his hypothesis, because his long-distance correlation was found to be unreliable, it discredited the use of varve chronologies for a long time. This was intensified by the discovery of a new, and apparently very precise dating method in 1949, i.e. radiocarbon dating (Zolitschka, 2007).

From the 1970s, varved lake sediments became of interest again. There was a need for high-resolution information in order to support the debate about human impact on environment. The popularity of the varved records also rose because of the discovery of new coring techniques and more sophisticated analytical tools. Since the 1980s, the term ‘varve’ was extended to all annually laminated sediments on continents as well as in the oceans. Additionally, it has become increasingly obvious that radiocarbon dating does not provide calendar year chronologies but needs to be calibrated. For calibration, it is common to use dendrochronology. This works well for the Holocene period, but for the Late Glacial period or earlier, trees become rare or absent. Annually laminated sediments can be successfully used for calibration of the radiocarbon dates (Zolitschka, 2007).

4.2 Formation and preservation of varved lake sediments

The formation of varved lake sediments depends on the overall climatic conditions. Seasonal variability of temperature and precipitation is the main controlling factor. The seasonal climatic variation is responsible for the succession of different life forms in the lake waters and also for the physical and chemical processes in the lake and its catchment. Seasonal climatic variation controls biological productivity, precipitation of authigenic minerals in the lake and the transport of allochthonous, minerogenic and organic particles from the catchment area to the lake (Zolitschka, 2007).

Lake sediments are usually a mixture of sediments of different origin, in which three end-members can be discerned: 1) clastic sediments, 2) biogenic sediments, and 3) evaporitic sediments. Clastic sediments are minerogenic components transported from the catchment area or by atmospheric deposition to the lake. Biogenic sediments consist of organic matter, generated by biological productivity, which sink to the lake bottom. Chemical precipitation of minerals produces evaporitic sediments. Different varve types are related to these depositional processes. We hence discern three main types of varves: 1) clastic varved sediments, 2) organic varved sediments, and 3) evaporitic varved sediments (see Fig.18 A,B,C). The clastic varved sediments occur in a colder climate, since clastic sediments predominate in a cold climate. Intensive physical erosion produces high amounts of minerogenic detritus, which is transported into the lake. The sediment transport is related to the annual freeze-thaw cycle and amount of runoff (melt-water and/or precipitation). Such lakes are poor in nutrients, which inhibits high organic productivity and the formation of organic varved sediments. Organic varved sediments form under temperate humid climatic conditions. The catchment area is covered with vegetation, which reduces the availability and transport capability of clastic material. Chemical weathering dominates in these conditions, which releases nutrients from the bedrock. Therefore, the lakes are nutrient rich. Evaporitic varved lake sediments occur under arid or semiarid climatic conditions. These varves may be formed if the salinity and pH of the lake water increases through enhanced evaporation. This causes the saturation of specific salts, which precipitate out of the water column. Clear environmental constraints are necessary to produce these varve types, but mostly they are the result of a combination of processes (Zolitschka, 2007).

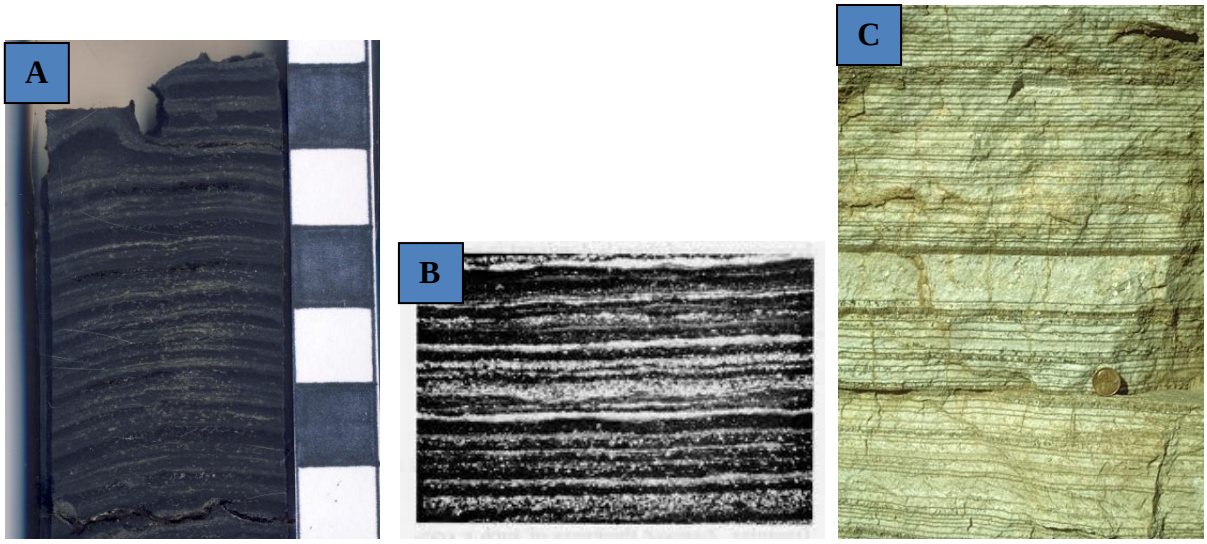

Fig. 18: A) top part of sample PAR1A-III(50-60), a clastic varved sediment: pale layers are coarser grained sediment, darker layers are finer grained sediment, scale-bar is a cm-scale; B) organic varves, composed of dark colored diatom laminae alternating with light-colored calcite laminae, source: http://search.datapages.com/data/doi/10.1306/212F767B-2B24-11D7-8648000102C1865D; C) Evaporitic varved sediments. Dark laminae are calcite plus organic matter, light laminae are gypsum, these are annual layers reflecting variations between summer (evaporitic) and winter (less evaporitic) conditions; source: http://geoinfo.nmt.edu/staff/scholle/graphics/permphotos/111.html

Long records with annual laminations only occur in lakes with a continuous sedimentation and with a pronounced seasonal climate forcing. However, equatorial lakes do not necessarily have a clear seasonal signal, and internal processes can prevent varve preservation. These internal processes are the burrowing activities of benthic organisms (bioturbation), resuspension of bottom sediments through wind- or density-driven lake water circulations and bottom currents that interrupt the continuous sedimentation. When a lake basin is deep with a small surface area and is geomorphologically protected, we can exclude the latter two internal processes. Morphological features, together with eutrophic conditions, can favor the formation of anoxic bottom waters, related to the decomposition of organic material near the sediment surface. This reduces or excludes the presence of bottom-dwelling organisms and so reduces bioturbation (Zolitschka, 2007).

4.3 El Niño Southern Oscillation (ENSO)

El Niño Southern Oscillation is a natural part of the global climate system. It occurs across the tropical and subtropical Pacific Ocean to the Indian Ocean as a consequence of interactions between ocean and atmosphere (see Fig.19). The importance of this phenomenon in the global climate system can be found in the fact that it is the next feature that explains a large amount of the climatic variability after the seasonal cycle and the Monsoon system (Allen, 2000).

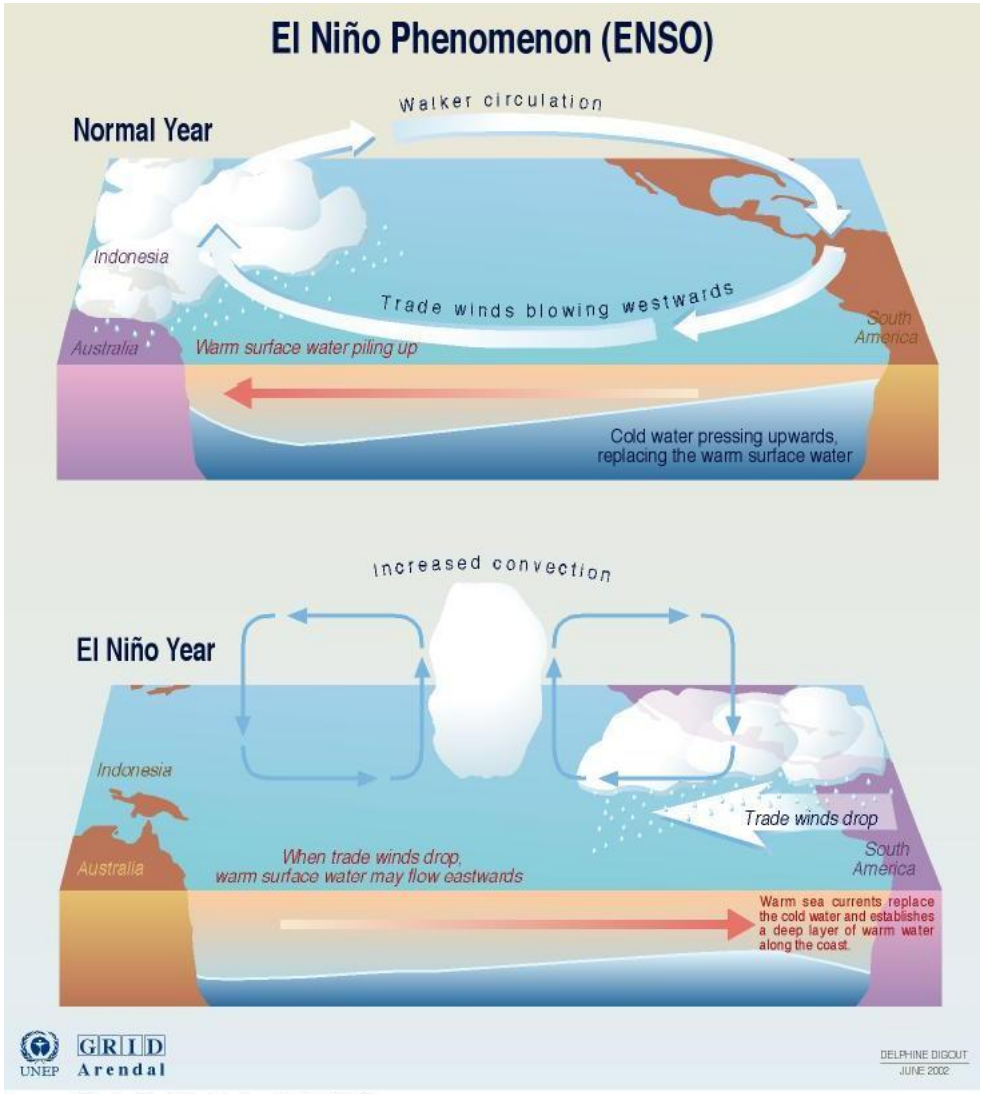

Fig. 19: The El Niño phenomenon. Source: http://maps.grida.no/go/graphic/el-ni-o-southern-oscillation-enso-phenomenon.

A lot of effort has been put into climate research to improve our understanding of the different types of natural variability in the global climate system. There is a growing interest in the interactions between the El Niño Southern Oscillation (ENSO) phenomenon and lower frequency decadal- to secular-scale (i.e. a long-term non-periodic variation) fluctuations in climate. To reach these study aims, new global, historical and instrumental data compilations are being analyzed, and more sophisticated objective analysis techniques are being used to resolve important physical links and modulations involving dominant climate signals (Allen, 2000). However, most of the research has its focus on the Holocene period, from 10 ka till present time. Some research goes further back in time: from 10 ka till 16 ka-20 ka. Going further and further back in time, causes more difficulties in drawing conclusions, because climate, oceanographic and atmospheric conditions could have been very different than they are today. Therefore, conclusions become more speculative and much more approximative of real conditions. Also, for this thesis research, which uses a sedimentary record with an age of 29000-40000 cal. years

BP, we will have to use the existing research and present time knowledge to understand which conditions could have existed 29000-40000 cal. years BP.

The ENSO climate pattern consists of two parts, the "El Niño" and the "Southern Oscillation". The El Niño is characterized by variations in sea surface temperature, while the Southern Oscillation is the atmospheric component of El Niño and is characterized by oscillations of mean sea level pressure. ENSO is an irregular/aperiodic phenomenon that reoccurs in a range of 2 to 7 year and alternates between to extremes: El Niño and La Niña events. The warm ENSO phase is called "El Niño", the cold phase is called "La Niña". Individual El Niño or La Niña events are never exactly the same and can vary in magnitude, spatial extent, onset, duration, cessation, etc. Spectral analyses of global historical sea surface temperature and mean sea level pressure anomalies reveal significant climate signals at 2-2.5, 2.5-7, 11-13, 15-20, 20-30, and 60-80 years and a long-term secular trend. The ENSO signal consists of quasi-biennial (2 to 2.5 years) and lower frequency (2.5 to 7 years) components. These components interact to produce important modulations of the ENSO phenomenon, but the longer duration characteristics and climate fluctuations are the result of decadal- to secular-scale influences. Long lasting El Niño and La Niña phases are explained as owing to the phasing of quasi-decadal (11-13 year) and interdecadal (15-20 year) ENSO-like signals with the higher frequency (2-2.5 year) and lower frequency (2.5-7 year) components (Allen, 2000).

During an El Niño event, warming of the tropical regions (Pacific and Indian Oceans) leads to the displacement of important rainfall systems, which causes massive redistributions of climatic regimes. Major variations in mass, energy and momentum, as a result of the redistribution of equatorial rainfall regimes, are communicated to the more temperate regions of the earth. This is because the tropical regions are connected through teleconnection patterns to the mid- and high latitudes in both hemispheres (Allen, 2000).

The possible relationships between the ENSO phenomenon and the other features of the global climate system on various time and space frames needs to be further unraveled. Features as the North Atlantic Oscillation, the Arctic Oscillation, the North Pacific Oscillation and the Antarctic Circumpolar Wave can be possibly coupled to ENSO. There is also growing evidence that the ENSO phenomenon is not spatially or temporally stable in the longer term and responds on a number of timescales. The ENSO phenomenon appears to be modulated by the natural decadal-scale to secular-scale variability of the climate system including possible anthropogenic influences. In turn, global climate is also modulated by the natural decadal-scale to secular-scale variability of the climate system (and anthropogenic influence) through the ENSO phenomenon (Allen, 2000).

To study the past ENSO record, a lot of different palaeoclimate indicators are available, each of which is sensitive to somewhat different aspects of climatic variations. The studies on the ENSO phenomenon in past times try to answer questions as, for example, how long ENSO has been operating in its present form. Most of the present evidence suggests that during glacial times, ENSO did not leave the same spatial or temporal expression in the palaeoclimate record as it does today. Research on the long-term history of the ENSO phenomenon becomes very important, especially in those time intervals when the climate boundary conditions (orbitally determined seasonal insolation, global ice cover, sea level, aerosols etc.) were different from those of today. Because of the excessive effects that the ENSO phenomenon has on societies, there are a lot of concerns about its future behavior. In unraveling the past aspects of ENSO, one needs to know if ENSO is an unstable oscillation between cold or warm tropical ocean states that can alternately become permanently "El Niño-like" or permanently "La Niña-like", or if it is an intermittent oscillation as it is now (i.e. How robust is ENSO in relation to changes in the boundary conditions?). Another important question to ask is how we can isolate the ENSO phenomenon, as expressed in the palaeoclimate-proxy record, from other climatic forcing parameters when boundary conditions are different than those of today. A final question can be how robust the ENSO climate teleconnections are when boundary conditions change (Markgraf and Diaz, 2000).

Both the high- and low-resolution changes in the ENSO phenomenon can be investigated in the palaeoclimate record. The high-resolution records, as for example tree-rings, varved sediments and ice cores, register manifestations that can be attributed to single ENSO events. High-resolution records for long time periods are rare and are not generated for all regions. Low-resolution records can also be used, but these need to be interpreted with more caution. It is important to use a multiproxy approach of a single record, which includes the analysis of different indicators that respond to different aspects of ENSO. This approach will reduce the possibility that some other, non-ENSO, environmental factors are responsible (Markgraf and Diaz, 2000). Markgraf and Diaz (2000) conclude in their synthesis about the past ENSO record, in which they discuss a time interval from 16 ka till present day, that it is very likely that during full Glacial and Late Glacial times, the expression of the ENSO variability may have been quite different from its expression in modern climate. At these time intervals, the surface boundary conditions were different than those of today and with greatly altered land/ocean distribution (especially in the western Pacific). The terrestrial palaeoclimate records show precipitation teleconnection patterns that are not comparable to the modern patterns, and high palaeoclimate variability might be due to other causes. There is some theoretical support for the absence of ENSO, at least in its present form, during cold tropical sea surface temperature intervals. Some evidence indicates that the large-scale circulation patterns associated with ENSO are quite robust in time, but some of these associations may weaken or even disappear at times (Markgraf and Diaz, 2000). Mann *et al*. (2000) analyzed global patterns of reconstructed surface temperatures for insights into the

behavior of the El Niño Southern Oscillation and the related climatic variability for the past three centuries. They examined how the global ENSO pattern changes over time and discovered that certain features of the pattern appear to be remarkably robust (at least for the multidecadal and longer time periods), while other features are more variable. They concluded a robust signature of ENSO from the observation of the classic "horseshoe" pattern: a warm eastern tropical Pacific and west coast of North America, and a cold central North Pacific. They also found some striking evidence of nonstationarity in ENSO teleconnection. The pattern of the period 1801 till 1850 is different from the pattern dominated by all other time periods ("horseshoe" pattern). Mann *et al*. (2000) believe that this pattern arises from a breakdown of interannual ENSO variability. This had impacts on the frequency of extremes and on global teleconnection patterns of ENSO during that period. They also found some support that this breakdown of ENSO variability may be associated with the impacts of external (including anthropogenic) forcings of climate (Mann *et al*., 2000). The question of the robustness of the ENSO teleconnections still remains a current topic of research (Markgraf and Diaz, 2000).

4.4 The Antarctic Oscillation (AAO)

The Antarctic Oscillation is the dominant pattern of non-seasonal variations in tropospheric circulation south of 20 °S (Thompson and Wallace, 2000). It is an oscillation-like pattern in the middle and high southern latitudes, in the pressure belt across Chile and Argentina (Carvalho *et al*., 2005). The Antarctic Oscillation is characterized by zonally symmetric or "annular" structures with pressure anomalies of one sign, centered in the Antarctic and anomalies of the opposite sign centered around 40-50 °S (see Fig.20). In the Northern Hemisphere, there is an analog of this annular mode, the Arctic Oscillation or AO (Thompson and Wallace, 2000). Thompson and Wallace (2000) showed that the structures of the Northern Hemisphere and Southern Hemisphere are similar. They are similar in the zonally averaged geopotential height and zonal wind fields, as well as in the mean meridional circulations. The Antarctic Oscillation and Arctic Oscillation are both observed throughout the year in the troposphere, but are amplified during the 'active seasons'. For the Northern Hemisphere, the active season is midwinter; for the Southern Hemisphere, it is late spring (Thompson and Wallace, 2000).
Thompson and Wallace (2000) also explain that during these 'active seasons' the annular modes modulate the strength of the Lagrangian mean circulation in the lower stratosphere, the total column ozone, the tropopause height over the mid- and high latitudes, and also the strength of the trade winds of their respective hemispheres.

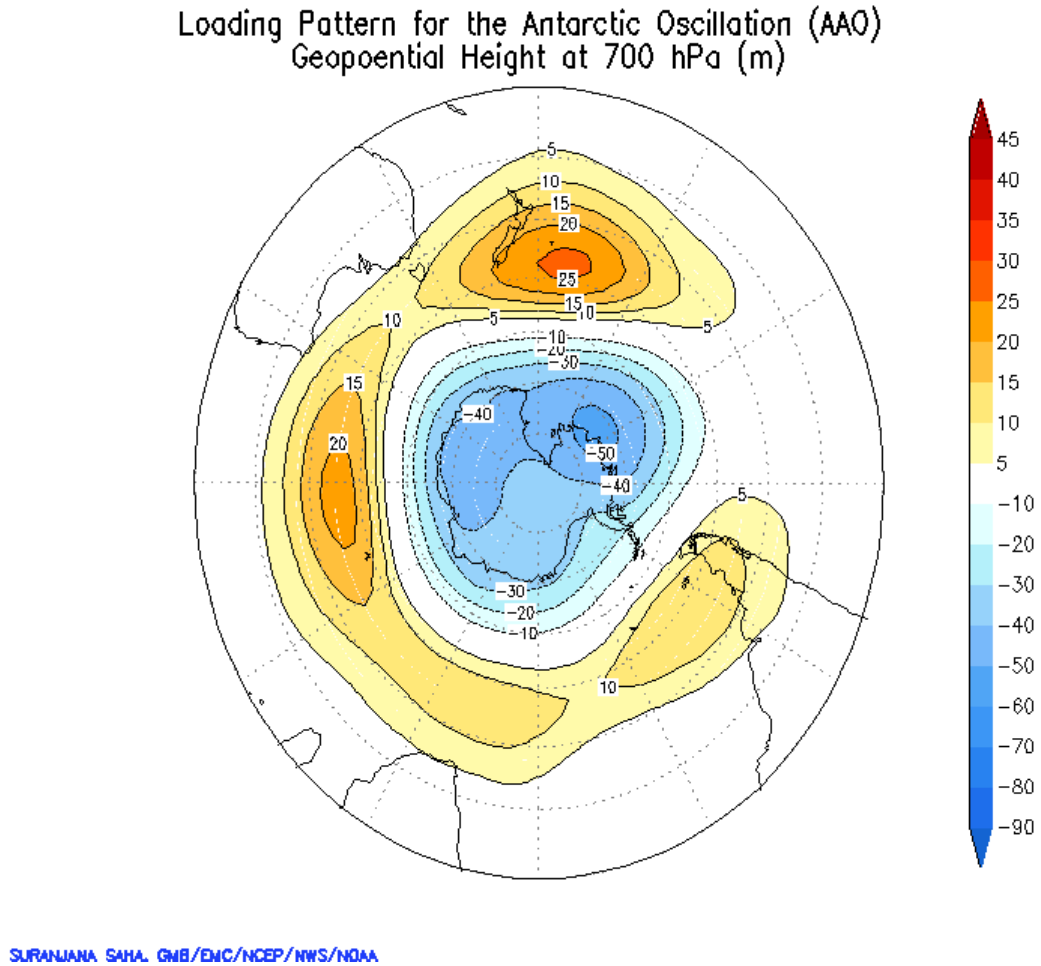

Fig. 20: The annular structure of the Antarctic Oscillation. Source: http://www.emc.ncep.noaa.gov/gmb/ssaha/indices/aao_load.gif

Silvestri and Vera (2003) examined the relationships between the Antarctic Oscillation and the precipitation in southeastern South America, for the period between 1979 and 1999. It is generally accepted that southeastern South America is one of the regions in the world most affected by ENSO, although not all of the precipitation variability can be explained by changes in sea surface temperature conditions in the equatorial Pacific. Other forcing factors may have an influence on the precipitation anomalies.

Silvestri and Vera (2003) showed that the Antarctic Oscillation influence is particularly strong during winter and late spring but of opposite sign. They also conclude that the Antarctic Oscillation variability is strongly related with precipitation changes, which can explain the fraction of precipitation variability that cannot be related to ENSO. The precipitation over southeastern South America during winter is associated with the passage of cyclonic baroclinic systems. The existence of a low-frequency anticyclonic (cyclonic) anomaly over that region during positive (negative) Antarctic Oscillation phases will reduce (enhance) the activity of the cyclonic synoptic systems, and will therefore cause a decrease (intensification) in precipitation over southeastern South America. The

Antarctic Oscillation related circulation anomaly pattern seems to affect moisture transport and convergence over extratropical South America. Moisture is transported from the Amazon region over the tropical South Atlantic and then westward into southeastern South America. During fall and spring, an anticyclonic (cyclonic) anomaly related with a positive (negative) Antarctic Oscillation phase will reduce (enhance) these northerly moisture fluxes (Silvestri and Vera, 2003).

Silvestri and Vera (2003) also discuss the influence of the Antarctic Oscillation on the ENSO signal. The correlation coefficient between the ENSO and Antarctic Oscillation indexes is not significant throughout the year over the considered period. However, during austral spring, a significant correlation exists, and the Antarctic Oscillation activity produces a strong modulation of the ENSO signal on southeastern South American precipitation (Silvestri and Vera, 2003). According to Thompson and Wallace (2000), they also conclude that spring is the most active season of the Southern Hemisphere lower stratosphere circulation. The Antarctic Oscillation fluctuations during spring are associated with cooling (warming) at the tropopause level at the polar (tropical regions). This out-of-phase relationship between tropical and polar temperatures is not evident in the other seasons (Thompson and Wallace, 2000).

Carvalho *et al*. (2005) focused their study on the variability of the Antarctic Oscillation during austral summer (December-January-February). The aim of their study was to investigate if there are distinct Antarctic Oscillation phases related to the variability of convection and circulation in the tropics caused by interannual variation phenomena, such as El Niño or La Niña. They also investigated if there are variations of circulation in the tropics and subtropics on intraseasonal time scales, which are related to distinct phases of the Antarctic Oscillation. Furthermore, they also examined if tropical anomalies, such as the Madden Julian Oscillation (see Fig.21), can play a role in modulating phases of the Antarctic Oscillation, and how the extratropical cyclone properties in the Southern Hemisphere respond to modifications in the circulation associated with distinct phases of the Antarctic Oscillation. Carvalho *et al*. (2005) focused their analysis on the austral summer period, because this is the wet monsoon season in tropical South America but also the period when the ENSO phases reach their mature stage. Additionally, during austral summer, the tropical/ subtropical intraseasonal anomalies that propagate eastward are quite active. These phenomena can modulate the circulation in the upper and lower troposphere. In contrast with the research of Carvalho *et al*. (2005), Thompson and Wallace (2000) concluded that the active season of the Southern Hemisphere annular mode is observed in November, instead of during austral summer according to the research of Carvalho *et al*. (2005).

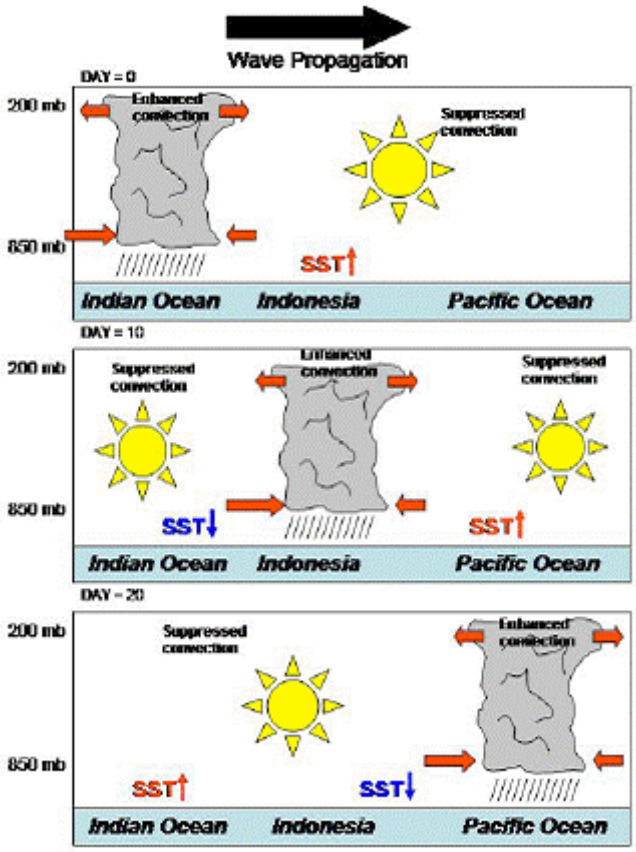

Fig. 21: The propagation of the Madden Julian Oscillation. Source: http://www.calclim.dri.edu/ccw200606.html

Carvalho *et al*. (2005) summarize that during the El Niño (La Niña) austral summer season, the weakening (strengthening) of the annular mode, and therefore the seesaw, along with an increase (decrease) of geopotential anomalies over Antarctica, is consistent with the dominant negative (positive) phases of the Antarctic Oscillation. They also conclude that the dominant signal of the daily Antarctic Oscillation during the austral summer season seems to be the response of the atmospheric circulation to the anomalous convective activity over the Pacific. Positive (negative) Antarctic Oscillation phases are favored by the enhancement (weakening) of convection over Indonesia and weakening (enhancement) over the central Pacific, and a westward (eastward) shifting of the South Pacific Convergence Zone and the consequent weakening (enhancement) of the Hadley circulation.

In regards to the relationships between the Antarctic Oscillation and intraseasonal activity, Carvalho *et al*. (2005) conclude that, despite latitudinal fluctuations, negative (positive) Antarctic Oscillation phases prevail during periods of increased (decreased) intraseasonal activity in the Southern Hemisphere, from the tropics to the extratropics. The positive (negative) Antarctic Oscillation phases are related to increased (decreased) intraseasonal activity in the Northern Hemisphere near 45°N (Carvalho *et al*., 2005).

Due to the known importance of the Madden Julian Oscillation in modulating the circulation in the tropics and subtropics, Carvalho *et al*. (2005) also investigated the possible links with the Antarctic Oscillation. They found that the negative phases of the Antarctic Oscillation are related to the eastward propagation of intraseasonal anomalies that are able to enhance convection over the central Pacific and the South Pacific Convergence Zone. The positive phases of the Antarctic Oscillation are favored when convection is suppressed (Carvalho *et al*., 2005). They also explain that the teleconnection patterns in the 200 hPa zonal wind daily anomalies show two zonally symmetric features at approximately 45°S and 60°S, related to the Southern Hemisphere subtropical and polar jets, respectively. During the negative Antarctic Oscillation phases, the subtropical feature is displaced equatorward, whereas the high-latitude feature is weaker, except for two regions around 180°W and 100°W. The positive Antarctic Oscillation phases are characterized by a poleward shift of the subtropical feature and an intensification of the high-latitude feature (Carvalho *et al*., 2005).

Finally, Carvalho *et al*. (2005) conclude that the importance of variations in the Antarctic Oscillation can be observed in the extratropical cyclone properties. Cyclones tend to form and move to lower latitudes during negative phases of the Antarctic Oscillation and also have higher central pressures compared to the positive Antarctic Oscillation phases. These relationships between the Antarctic Oscillation and baroclinic instability are consistent with the fact that the Antarctic Oscillation is an internal mode of the mid to high latitudes. In turn, the internal mode is affected by the variability in convection and circulation from the tropics to mid-latitudes and from intraseasonal to interannual time scales (Carvalho *et al*., 2005).

4.5 The Southern Hemisphere Westerlies

The Westerlies are the prevailing winds between 30° and 60° latitude and can be found beneath the Ferrel cell (see Fig.22). The Ferrel cell's existence depends upon the Hadley and Polar cells, which are a direct consequence of surface temperatures. The Hadley and Polar cells are closed loops, the Ferrel cell is not. Because the Ferrel cell lies in between the Hadley and Polar cells, and there is no strong heat source nor a strong cold sink to drive convection, the upper flow of the Ferrel cell is not well defined. However, the base of the cell, characterized by movement of air masses, is well defined. The location of the air masses is in part influenced by the location of the jet stream. The jet streams are narrow air currents and are found near the tropopause, the transition between the troposphere and stratosphere. Jet streams are west to east flowing winds with a meandering shape. The Northern Hemisphere, as well as the Southern Hemisphere, have a strong polar jet (7 - 12 km above sea level) and a weaker subtropical jet (10 - 16 km above sea level) (see Fig.22, Fig.23). The overall movement

of the surface air, at the base of the Ferrel cell, is from 30° to 60° latitude, from a high pressure zone to a low pressure zone. Because of the Coriolis effect, they curve towards the east, causing west to east streaming winds, the Westerlies. The Westerlies are driven by pole - equator temperature and pressure gradients. They are stronger in the Southern Hemisphere, where there is less land than in the Northern Hemisphere between 40°S and 60°S to cause the winds to slow down, than in the Northern Hemisphere. Additionally, the Westerlies are strongest during the winter season and when the pressure is lower over the poles. They are weakest during the summer season and when the pressure is higher over the poles (Shulmeister *et al*., 2004).

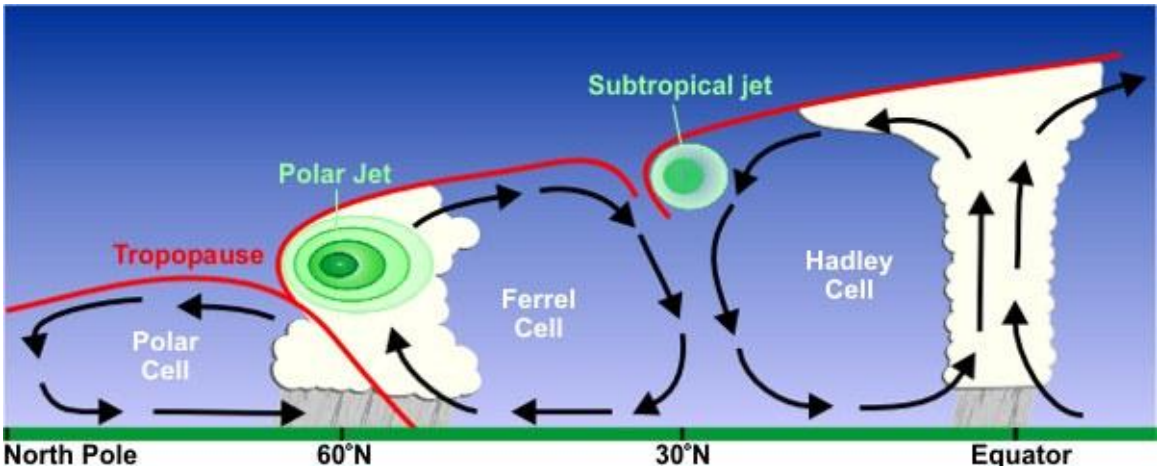

Fig. 22: the polar and subtropical jet stream (source: http://www.srh.noaa.gov/jetstream/global/jet.htm)

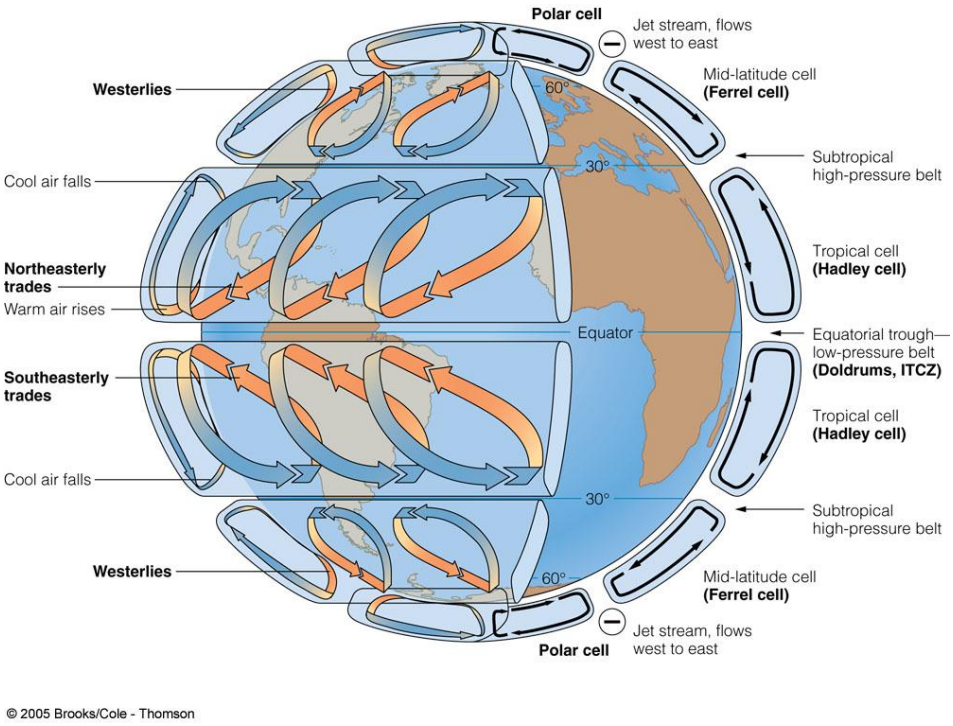

Fig. 23: atmospheric cells (source: http://science.kennesaw.edu/~jdirnber/oceanography/LecuturesOceanogr/LecCurrents/0813.jpg)

Much of the poleward transport of energy in the Southern Hemisphere circulation is achieved by short-lived eddies, which are synoptic-scale (i.e. a time scale of 1 to 10 days) baroclinic (i.e density depends both on the temperature and pressure) storms. The variability of the Westerlies on a time scale of 1 to 10 days is in the form of baroclinic waves. These are responsible for most of the meridional transport of heat and momentum during the whole year (Karoly *et al*., 1998 in Shulmeister *et al*., 2004). On a time scale of a month or longer, most of the variability is caused by the "High Latitude Mode" or the Antarctic Oscillation (for the Southern Hemisphere); however, it does not have a strongly preferred time scale. It varies randomly from a positive polarity (strengthened polar vortex or polar low pressure zone) to a negative polarity (weakened polar vortex). It stays in one polarity for several weeks, before flipping over to the opposite polarity in a few days. On a seasonal to inter-annual time scale, the High Latitude Mode remains the dominant pattern of variability, together with the Pacific – South American Mode, that appear to be forced by anomalous tropical heating (convection) associated with the El Niño Southern Oscillation (ENSO) cycle and with a shorter-term intra-seasonal variability. Also on decadal and longer time scales the High Latitude Mode is prominent. There is a trend towards increasing positive values (a stronger polar vortex) over the last several decades. This is thought to be related with the global temperature signal and/ or to decreases in the stratospheric ozone over both poles during the past two decades (Thompson and Wallace, 2000; Kushner *et al*., 2001; Thompson and Solomon, 2002 in Shulmeister *et al*., 2004). A warming (expanding) of the Hadley circulations in the tropics increases the strength of the zonal mean circulation, and this leads to a strengthening of the polar vortex, which in turn leads to isolation of the polar regions. On the other hand, a cooling (shrinking) of the Hadley circulations weakens the polar vortex (Shulmeister *et al*., 2004).

Researchers try to reconstruct past atmospheric circulations in order to link the variability in these circulations to the glacial/interglacial cycles. A primary proxy used for palaeo-wind studies is wind-blown sediment. There are distinct characteristics for wind-blown grains, but these are not always diagnostic. Provenance studies are necessary to determine the sediment source and, therefore, the direction of transport. Other proxies used for palaeo-wind studies depend on biological (e.g. higher wind speeds, causing upwelling, generates plankton blooms) or physical responses (e.g. annually laminated sediments) to the secondary effects of wind flows (Shulmeister *et al*., 2004).

The Southern Hemisphere Westerlies have three main types of response to climate change. The intensity of the circulation can change, the main latitudinal track of the circulation can change or the tracks of the surface frontal systems can change (Markgraf *et al*., 1992 in Shulmeister *et al*., 2004).

Wyrwoll *et al*. (2000) discuss in their research the claim of a poleward (southward) displacement of the Southern Hemisphere mid-latitude westerly circulation at the Last Glacial Maximum. The original

claim of this poleward displacement relied on a Late Quaternary palaeoenvironmental record from the western region of southern South America, investigated by Markgraf (1987). This was criticized by Heusser (1989), who concluded that the Southern Hemisphere westerlies were intensified and moved northwards instead of southwards. In later research, Markgraf *et al*. (1992) concluded that at the Last Glacial Maximum the Westerlies over South America were compressed at both their northern and southern margins and, therefore, restricted to the latitude band of 43-50°S. Clapperton (1993) added the suggestion that the existence of the ice cap over the Chilean/Argentinian Lake region at the Last Glacial Maximum required increased precipitation associated with a northward displacement of the Southern Hemisphere Westerlies (Wyrwoll *et al*., 2000).

Wyrwoll *et al*. (2000) used the UGAMP (Universities Global Atmospheric Modeling Programme) general circulation model to evaluate the Southern Hemisphere storm track activity at the Last Glacial Maximum. This model is based on the forecast model of the European Centre for Medium Range Weather Forecasting and is adapted for palaeoclimate modeling. They explain that possible changes in the position of the Southern Hemisphere Westerlies can be obtained through modeling of associated storm tracks. These storm tracks are regions with high day-to-day weather variabilities and are a reflection of the general baroclinic instability linked to mean westerly flow. Storm tracks are a surrogate for the associated hydrological conditions. As sea surface temperatures affect the hydrological cycle and the heat exchange between ocean and atmosphere, storm track reconstructions are influenced by the CLIMAP sea surface temperature estimates utilized.

From the results of the simulations Wyrwoll *et al*. (2000) suggested that at the Last Glacial Maximum a general poleward (southward) displacement of the zonal maximum of the Southern Hemisphere Westerlies occurred. This supports the original suggestions by Markgraf (1987) from the palaeoenvironmental evidence. However, Wyrwoll *et* al. (2000) also concluded that this is a generalization, and that the changes in the Westerly circulation do not follow a simple poleward displacement but that there are possibly significant regional differences. They further explain that the poleward displacement of the Westerlies at the Last Glacial Maximum are a strongly zonal response to the equatorward shift of the sea ice margin, enhancing the ‘cold-pole attractor’ effect provided by the Antarctic ice sheet. Additionally, there was a lower moisture content of the atmosphere at the Last Glacial Maximum, enhancing the effectiveness of a poleward movement of the Westerlies, because moisture has the effect of fixing the location of the Southern Hemisphere storm tracks.

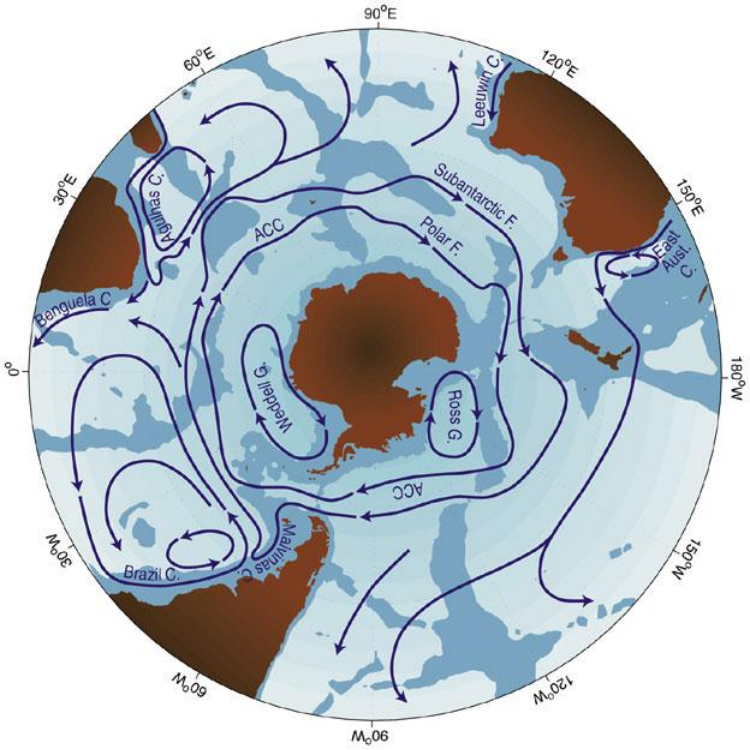

Fig. 24: the Antartcic Circumpolar Current (ACC), Subantarctic front and Polar front (source: http://www.science-in-salamanca.tas.csiro.au/themes/climate/currents.htm)

The Westerlies drive the West Wind Drift or Antarctic Circumpolar Current, which flows from west to east around Antarctica and is the dominant feature of the Southern Ocean (Shulmeister *et al*., 2004). The location of the Antarctic Circumpolar Current (see Fig.24), and its associated subtropical gyres, is strongly linked to the latitude of the maximum wind stress of the Southern Hemisphere Westerlies. The Antarctic Circumpolar Current plays an essential role in the thermohaline circulation and global climate. From a number of proxy records, one could infer a more northward location of the westerly winds by 5-6° latitude during glacial periods. More recent studies show that a global cooling of 3°C can cause an equatorward shift of 7° in latitude of the maximum wind stress of the Southern Hemisphere Westerlies and also a concurrent equatorward shift of the Antarctic Circumpolar Current, together with the subtropical gyres. Such a northward shift in the southern margins of the subtropical gyres and associated fronts has important oceanographic and climatic implications (Sijp and England, 2008).

The poleward, southern boundary of the subtropical gyres in the Southern Hemisphere is the Subantarctic front (see Fig.23), an important region for ventilation of the subtropical thermocline. It is also a region with thermostats, controlling the temperature of the system, and associated with the formation of mode water. The Antarctic Intermediate Water is formed south of the Subantarctic front (see Fig.24) in a weakly stratified region and north of the latitudes of upwelling of Circumpolar Deep Water into the Antarctic Circumpolar Current (England *et al*., 1993) (see Fig.25).

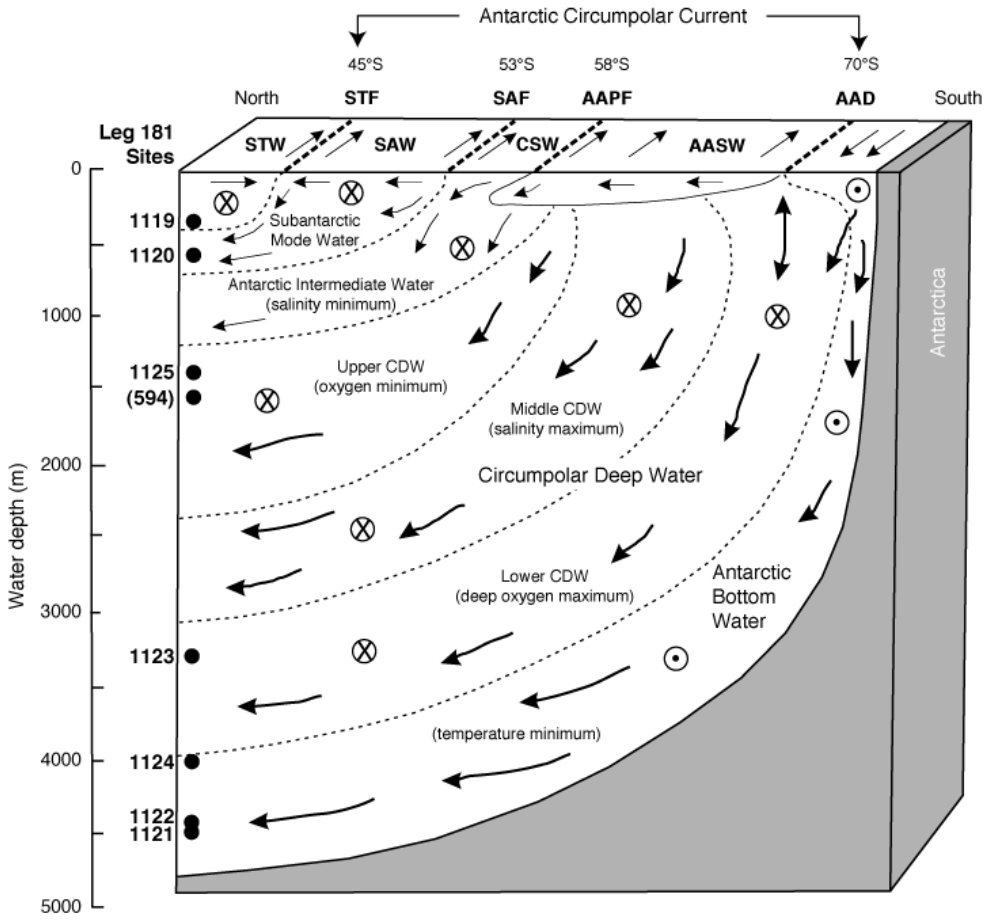

Fig. 25: Water masses, fronts and circulation patterns at the southwest pacific section of the Southern Ocean, STF=subtropical front, SAF=subantarctic front, AAPF=Antarctic Polar front, AAD=Antarctic Divergence, CDW=Circumpolar Deep Water, STW=Subtropical Water, SAW=Subantarctic Water, CSW=Circumpolar Surface Water, AASW=Antarctic Surface Water (source: http://www-odp.tamu.edu/publications/181_SR/synth/s_f5.htm)

A northward shift of the Southern Hemisphere Westerlies will cause a northward migration of the southern boundaries of the subtropical gyres and the associated regions where fronts, convection and mode water formation occur. Thus, such a wind shift leads to a shift in the latitudinal origin of water entering the ventilated thermocline from the surface. An equatorward migration moves the source regions into regions with a warmer surface air temperature. This causes a significant subsurface warming inside the ventilated thermocline of the Indian and Pacific Oceans. A northward wind shift can also have an impact on the formation processes of deep and bottom water at high latitudes. The upwelling of Circumpolar Deep Water into the Antarctic Circumpolar Current is believed to be driven by the divergence in zonal wind stress at Drake Passage (Sijp and England, 2008).

4.6 Dust deposition and past climate variability

4.6.1 The role of dust in climate change

The presence of mineral or soil dust aerosol in the atmosphere has already been documented a long time ago; however, only since the last two decades have researchers recognized that dust is an active component of the global climate system. Dust not only could have played an important role in past climate changes, it can also contribute to the climate changes in the future. However, our understanding of the role of dust in the global climate system is still rudimentary. A better understanding of the magnitude of the various effects of dust will depend on the development and application of global models of the dust cycle and its interaction with the other components of the Earth system (Harrison *et al*., 2001).

4.6.2 The modern dust cycle and its role in the climate system

The modern dust cycle (see Fig.26) observations show that the mineral dust aerosols are entrained into the atmosphere by aeolian deflation of surface material in areas with sparse vegetation. Today 30 % of the continental area is a potential source for dust. There are natural dust sources, but also artificial or anthropogenic sources. There is evidence that changes in land use can cause a substantial increase in the amount of dust in the atmosphere. Satellite data and meteorological observations indicate that there is a strong seasonal cycle in dust production and transport. The entrainment of dust into the atmosphere is affected by individual meteorological events (e.g. cold front, frontal systems etc.). The seasonal and interannual changes in atmospheric circulation patterns influence the frequency of dust-generating events. The dust fluxes to the atmosphere show a high temporal variability on timescales from days to decades (Harrison *et al*., 2001).

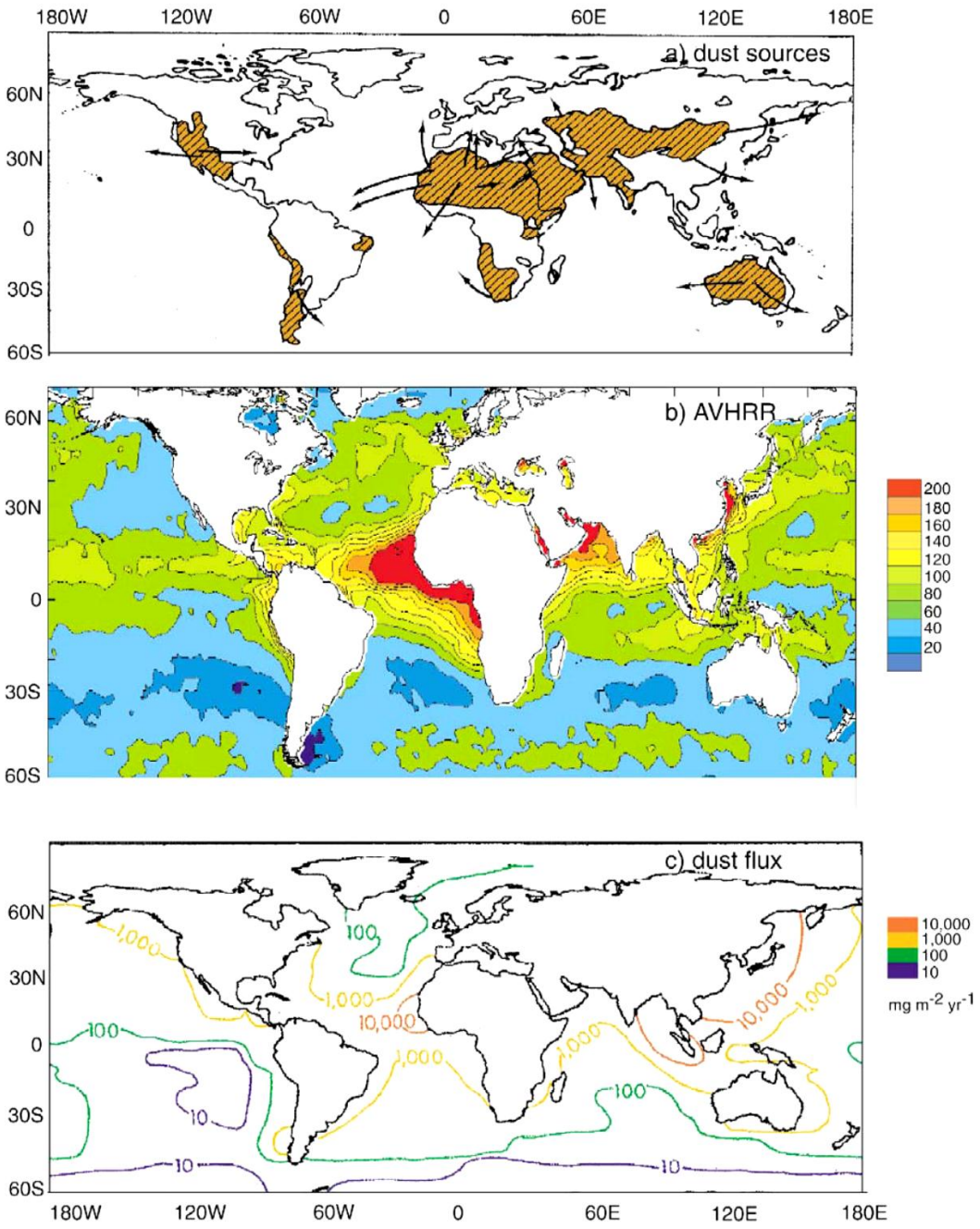

Fig. 26: (a) modern dust source regions and wind trajectories (After Livingstone and Warren, 1996), (b) zones of high atmospheric dust concentrations (from Husar *et al.*, 1997), (c) global fluxes (mg m^{-2} $year^{-1}$) of mineral aerosols to the ocean (after Duce *et al.*, 1991); source: Harrison *et al.*, 2001

In the climate system, dust plays a role in energy exchange, in atmospheric chemistry (e.g. dust has a neutralizing effect on rainwater acidity, affects the atmospheric nitrogen and sulphur cycles), and in biogeochemical cycles (dust as a source of nutrients in marine and terrestrial ecosystems) (Harrison *et al.*, 2001). Through the absorption and scattering of both the incoming solar radiation and outgoing terrestrial radiation, the mineral dust can modify the radiation budget (Liao and Seinfeld, 1998). Researchers first assumed that the net radiative effect of dust produced a cooling at the land surface and warming at the altitude of the dust layers. However, now it is known that dust may either cause a

warming or a cooling at the surface. The net radiative effect depends on the characteristics of the dust, its concentration, its vertical distribution in the atmospheric column, the particle size distribution, the mineralogy and external variables including albedo and temperature of the underlying surface. The characteristics of the dust particles will affect the balance between scattering and absorption of energy. An increase in dust concentration will increase the amount of absorbed energy (Harrison *et al*., 2001). Smaller particles are more effective in scattering energy than larger particles (Liao and Seinfeld, 1998), but also the shape of the particles (degree of sphericity) can have an influence on the effectiveness of scattering. Dust particles transported over large distances in the atmosphere have a size range from 0.1 to 20 µm, but close to the source regions the particle can have sizes up to 50 µm in diameter. Dust consists of a mixture of minerals, and the particles of dust can occur as individual mineral grains or as pure or mixed-mineral aggregates. The degree to which the dust occurs as aggregates will affect the size distribution and also the radiation budget, as aggregates are larger than a single grain dust particle (Harrison *et al*., 2001).

In general, for a surface with a low albedo (e.g. forest, ocean), dust will warm the upper atmosphere and cool the surface, whereas, when the surface has a high albedo (e.g. ice sheets, fresh snow, deserts), the converse is true. However, in case of the presence of a relatively thick dust layer, and when the atmosphere is well mixed and saturated, the dust layer may have no impact on the surface temperature (Harrison *et al*., 2001).

A further, indirect impact of dust in the atmosphere on the radiation budget is that the dust particles can act as cloud condensation nuclei (Twomey *et al*., 1984 in Harrison *et al*., 2001). Increasing the number of cloud condensation nuclei will lead to a decrease in the size of the cloud condensation nuclei, and this will increase cloud reflectivity (Shine and Forster, 1999 in Harrison *et al*., 2001). Lohmann and Feichter (1997) found that a decrease in the size of individual cloud condensation nuclei also reduces the chance of precipitation events and, therefore, increases the lifetime of clouds and decreases the wet deposition rates of the dust. However, the net impact of dust on clouds is still unclear (Lohmann and Feichter, 1997).

The entrainment of dust in the atmosphere will happen from the moment that the wind speed exceeds a certain critical threshold. The critical wind shear velocity will depend on grain size, shape and density, but also on the occurrence of aggregates, strength of the inter-particle forces and surface coherence. The roughness of the surface and the presence of a vegetation cover will decrease the energy of the surface winds and make it difficult to reach the critical threshold. Long distance transport of dust is possible when the meteorological conditions are favorable to carry the entrained dust into the higher levels of the troposphere (Harrison *et al*., 2001). There are two mechanisms to remove the dust from the atmosphere: dry deposition by gravitational settling and wet deposition by precipitation. Dry

deposition determines the deposition rates close to the source area of the dust, because the importance of dry deposition increases as the mean size of the particles increases. The deposition of far-travelled dust particles depends more on wet deposition through precipitation (Harrison *et al*., 2001; Tegen, 2003).

4.6.3 The dust cycle at the Last Glacial Maximum

For the patterns of dust deposition, researchers concluded that different records (e.g. ice caps, marine sediments, loess deposits) confirm that the Last Glacial Maximum was a period of higher atmospheric dust loadings than today, and they also show the existence of strong spatial pattern of dust enhancement. While most places in the world experienced an increased dust deposition at the Last Glacial Maximum, there were also some regions where the dust fluxes were less than today (Harrison *et al*., 2001) (see Fig.27). An example is a spectral analysis by Rea (1994) of marine records covering several glacial-interglacial cycles off northwestern South America, which shows that dust loadings were less during glacials than interglacials.

To reveal the dust provenance at the Last Glacial Maximum, mineralogical (clay-minerals) and isotopic (long-lived radiogenic isotopes: $^{87}Sr/\ ^{86}Sr$, $^{143}Nd/\ ^{144}Nd$ etc.) tracers are used. The dust samples are characterized using these tracers (presence/absence and relative abundance), and this is then compared with samples from the potential source areas (Basile *et al*., 1997). This method assumes that the mineralogy and radiogenic isotope composition of dust reflects the geographical location of its source area, and is not modified during transport (Harrison *et al*., 2001). As source area for the dust deposited in Greenland during the Last Glacial Maximum, Eastern Asia was suggested (Biscaye *et al*., 1997 in Harrison *et al*., 2001). Studies from the Last Glacial Maximum record on Antarctica suggest that the dust was derived from Patagonia (Basile *et al*., 1997).

Three factors can possibly explain why atmospheric dust loadings and dust deposition rates were higher during glacial periods compared to interglacial periods: increased wind speeds, the reduced intensity of the hydrological cycle, and the expansion of dust source areas (Harrison *et al*., 2001). Harrison *et al*. (2001) summarize the findings from earlier research. Simulations of glacial climates show an increase in the wind intensities both at the surface as higher in the atmosphere. A reduced intensity of the hydrological cycle allows the dust to remain longer in the atmosphere. The expansion of the dust source areas can be due to:

1) extensive fine-grained outwash deposition along the margins of the Northern Hemisphere ice sheets;
2) an increase of the land area by exposure of the continental shelves because of a lowered sea level;

3) reduced vegetation cover. There is abundant evidence that there was an increase in potential dust source areas at the Last Glacial Maximum and that the climate conditions were much more arid than today (Harrison *et al*., 2001).

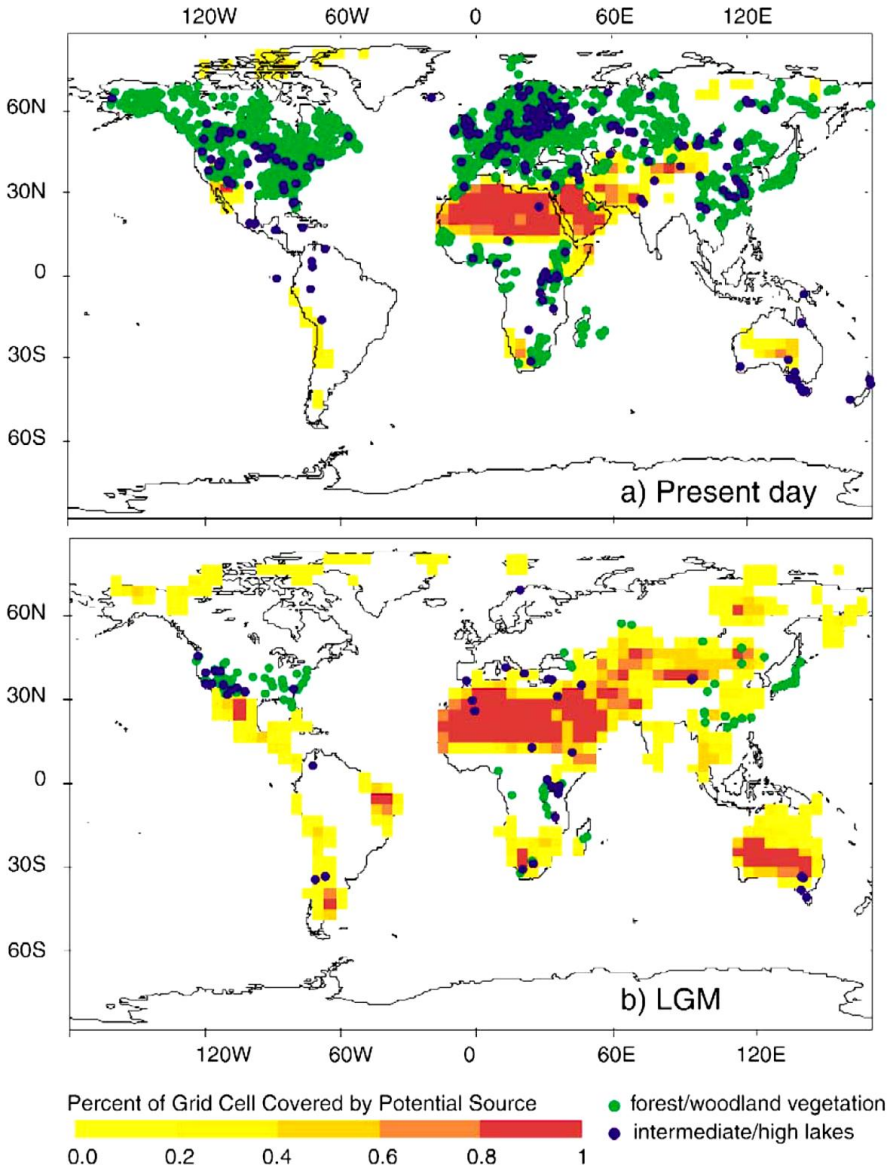

Fig. 27: Simulated potential dust source areas from the Mahowald *et al*. (1999) experiments, as a result of simulated changes in climate and vegetation changes. (a) at present day, (b) at the Last Glacial Maximum. Source: Harrison *et al*., 2001.

4.6.4 Links between Patagonian Ice Sheet fluctuations and Antarctic dust variability

Sugden *et al*. (2009) investigated the relationship between the Antarctic dust record from Dome C and the Patagonian glacial fluctuations for the past 80,000 years. They showed that the dust peaks observed in Antarctica coincide with periods in Patagonia when rivers of glacial melt water deposited sediment directly onto outwash plains. Outwash plains are an important source of windblown dust because, firstly, the sediment load delivered by the glacier consists of a high proportion of dust size particles. Secondly, there is a diurnal and seasonal variability of dust flow. Diurnally, the sediment is deposited over a wide area; it dries out and becomes available for removal in the following hours. Seasonally, higher loads of suspended sediment occur as summer melting flushes out of the bed of the glacier. Thirdly, during glacial periods a larger area of the continental shelf in Patagonia was exposed by lower sea levels; thus, rivers were longer than those of today (Sugden *et al*., 2009). Outwash plains, like those in Patagonia, have long been recognized as an important dust source (Sugden *et al*., 2009); furthermore, isotopic tracers suggest that South America is the dominant dust source for the dust fluxes in Antarctica (Grousset *et al*., 1992; Basile *et* al., 1997 and Gaiero *et al*., 2007 in Sugden *et al*., 2009).

The entrainment of dust depends on several factors, in which wind velocity plays an important role. Silt and finer particles become entrained at wind velocities of 4-8 $m.s^{-1}$; however, the Patogonian wind velocities are much higher, with monthly maximum wind velocities ranging from 15 to 25 $m.s^{-1}$ near Punta Arenas. It is likely that during glacial times the dust entrainment was enhanced by the overall increase of the vigour of atmospheric circulation (Sugden *et al*., 2009).

When the glacier front retreats into the subglacial basin behind the outwash plain, a proglacial lake forms between the new glacier front and the outwash plain, in which the sediments accumulate. Thereby, the sediment supply to the outwash plain is abruptly cut off, even while water discharge remains constant or increases. This reduction in sediment supply causes the river to incise its channel into the pre-existing outwash plain, forming terraces. The terraces are protected against wind erosion by a lag of surface stones and increasing vegetation cover. The effect of a withdrawing glacier front consists of a sudden reduction of both the quantity of sediment available for wind erosion and the size of the contributing outwash plain. The results of the research show that the dust peaks in Antarctica coincide with stages when Patagonian glaciers discharged directly onto outwash plains. The stages in which the glaciers ended in pro-glacial lakes produced no dust peaks (Sugden *et al*., 2009). Sugden *et al*. (2009); therefore, it is proposed that the variable sediment supply, resulting from Patagonian glacial fluctuations, may have acted as an on/off switch for Antarctic dust deposition. At the last glacial termination, the Patagonian glaciers retreated quickly into lakes. This may help to explain why

the decline in Antarctic dust, coinciding with this event, preceded the main phase of warming, sea level rise and reduction in Southern Hemisphere sea ice extent (Sugden *et al*., 2009).

Kaiser and Lamy (2010) investigated the glacial interval of the core from ODP site 1233, located 38 km off the Chilean coast, on the upper continental slope (see Fig.28). From their previous research, they showed that the concentration of Fe in the continental margin sediments at site 1233 is a faithful proxy for the bulk terrestrial input from the Andean hinterland. The strong similarities between the Fe and Ti records confirm this interpretation, as Ti reflects detrital input (e.g. Haberzettl *et al*., 2010).

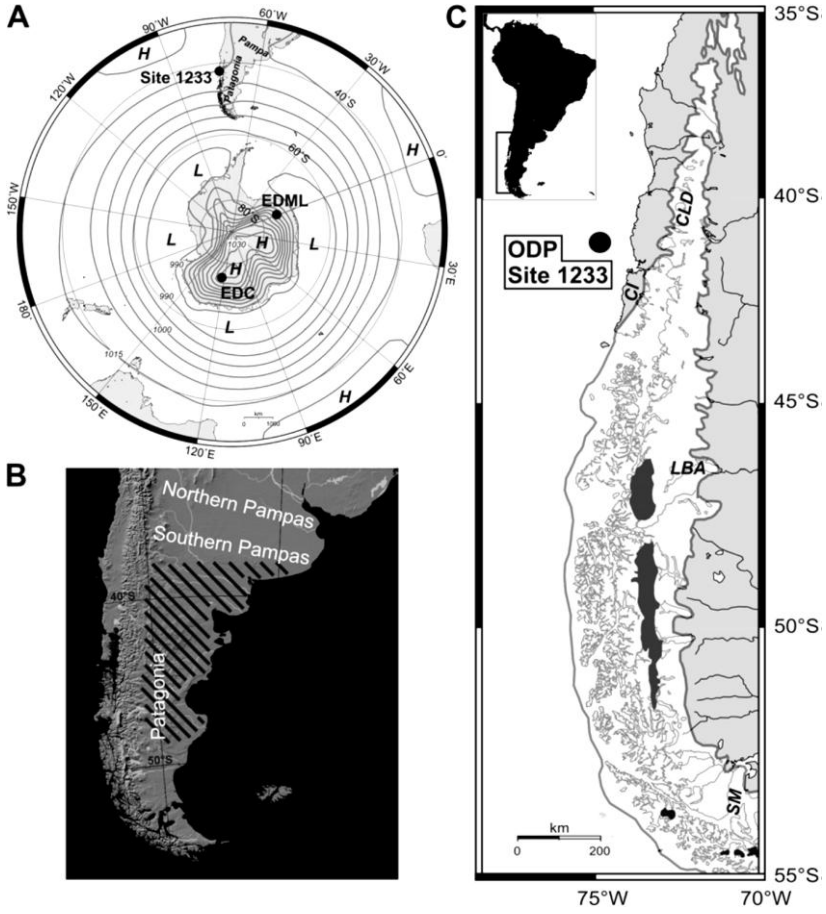

Fig. 28: (A) location of ODP Site 1233 and the EPICA Dome C (EDC), the high (H) and low (L) pressure cells are shown, as well as the pathways of the westerly and easterly (over Antarctica) winds (i.e. the parallel isobars), (B) present day active dust source area, (C) present day Northern and Southern Patagonian Ice Fields (dark grey), and the Patagonian Ice Sheet extension at the Last Glacial Maximum. Source: Kaiser and Lamy, 2010.

The Fe and Ti records from site 1233 record North Patagonian Ice Sheet advances (Fe and Ti maxima) and retreats (Fe and Ti minima) during the last glacial period (Kaiser and Lamy, 2010). During the last glacial period, the North Patagonian Ice Sheet (north of ~48°S) was located very proximal to site 1233, and changes in the melt-water sediment supply to the ocean caused changes in the terrigeneous input (Kaiser and Lamy, 2010). Kaiser and Lamy (2010) mention two main factors that can change the

amount of dust during the last glacial period as recorded in the Antarctic ice cores: firstly, changes in dust production and, secondly, variations in dust deflation and transport. They suggest that these two factors are closely related to the location of the Southern Hemisphere Westerlies in the southeast Pacific region. Other researchers (e.g. McCulloch *et al*., 2000) already suggested a northward extension of the Southern Hemisphere Westerlies during the last glacial period. Together with a mean temperature lowering of 6-7 °C, the northward extended Westerlies would increase humidity and, thus, growth of the Patagonian Ice Sheets. The advanced Patagonian Ice Sheets would increase the total erosion rate and thus enhance the supply of fluvio-glacial outwash material in eastern Patagonia (Kaiser and Lamy, 2010). As explained by Sugden *et* al. (2009), the enormous amounts of glacial flour would be deposited, forming immense outwash plains where the dust entrainment can take place. The higher ice surface altitude, linked to the growth of the Patagonian Ice Sheets, would increase the precipitation on the western side of the Andes by enhancing the orographic rise of moist Pacific air masses and favor foehn winds on the lee side of the Andes. The foehn winds would intensify aridity and increase dust mobilization in the Southern Pampas and Patagonia (Gaiero *et al*., 2007 in Kaiser and Lamy, 2010). This scenario is valid for the coldest periods of the last glacial period, MIS 4, late MIS 3 and MIS 2. During early to mid MIS 3, the Southern Hemisphere was relatively warmer, the extension of Antarctic sea ice was reduced and the Southern Hemisphere Westerlies were probably restricted further south than during the colder periods. During these warmer periods, the size and height of the Patagonian Ice Sheets were reduced; as a consequence, there was a decrease in the glacial activity of the Patagonian Ice Sheets and dust production. Additionally, the increased humidity, soil moisture and vegetation cover east of the Andes, in absence of the foehn winds, would decrease dust entrainment and transport (Kaiser and Lamy, 2010).

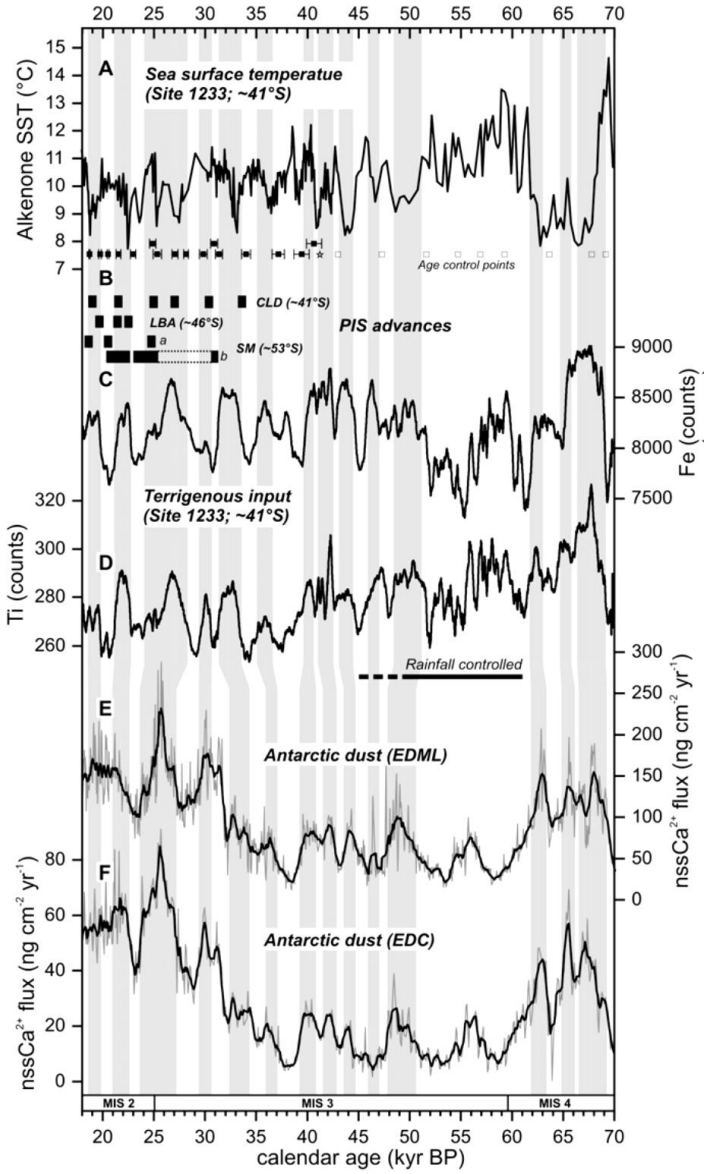

Fig. 29: the relationships between sea surface temperatures (A), Patagonian Ice Sheet activity (C-D) and Antarctic dust variability (E-F). Source: Kaiser and Lamy, 2010.

Besides the Southern Hemisphere Westerlies, sea level fluctuations also played a role in dust variability (Kaiser and Lamy, 2010). Kaiser and Lamy (2010) showed that the high dust fluxes during MIS 4, late MIS 3 and MIS 2 occurred during sea level low stands. The relative sea level was at -150 m during MIS 2 (corresponding to an eustatic sea level of about -105 m) and was close to or above -80 m (corresponding to an eustatic sea level of -60 m) during early MIS 3. A relative sea level change is a change relative to a fixed point in the sediment pile, whereas an eustatic sea level change refers to global changes in sea level relative to a fixed point, which is the center of the Earth. Furthermore, the Argentine shelf undergoes a morphological change: from 0 to -80 m the shelf has a steep slope, but it is rather flat from -80 m to -150 m (Wolff *et al*., 2006 in Kaiser and Lamy, 2010). This means that the largest increase of exposed shelf area occurred during late MIS 3 and MIS 2, when the sea level dropped between -80 m and -150 m (Kaiser and Lamy, 2010).

In the short term trends of dust variability, the sea surface temperature plays an important role. The North Patagonian Ice Sheet variability is shown to be very sensitive to offshore sea surface temperature changes. During MIS 4, late MIS 3 and MIS 2, a 0.5 to 0.7 ka delay has been shown between sea surface temperature warming and Fe decreases (ice sheet retreat phases). This was attributed to the ice dynamics (inertia of the North Patagonian Ice Sheet). However, no delay was observed between sea surface cooling and Fe increases (ice sheet growing phases) (Kaiser and Lamy, 2010) (see Fig.29).

4.7 Glacier fluctuations during the LGM and Late Glacial/Holocene transition

In this section, we will discuss studies of glacier fluctuations in the Central Strait of Magellan and Bahía Inútil region in southernmost South America. During the Last Glacial Maximum (LGM), the Patagonian ice fields in southern South America expanded from 35°S to 56°S. Patagonia is therefore an ideal location to study the southern hemisphere mid-latitude environmental changes during the waning of this ice field (McCulloch *et al*., 2005a). The study of glacial deposits in the Magellan region started since Darwin noted some of the glacial landforms during his expedition with the HMS Beagle in 1833 (Bentley *et al*., 2005). Nordenskjöld (1899) and Caldenius (1932) showed that the coastlines of the Magellan Strait and Bahía Inútil have a complex pattern of moraines and meltwater channels (Bentley *et al*., 2005). The distribution, morphology and weathering of the observed landforms suggest that the Strait was occupied by ice during several glacial cycles (e.g. Meglioli, 1992; Rabassa *et al*., 2000 in Bentley *et al*., 2005). These first studies were followed by many others.

Studies of the old glacial deposits, together with recent $^{40}Ar/^{39}Ar$ and K/Ar dating of basaltic lava flows, showed that the most extensive glacial advance may have occurred 1.1 Ma years ago (Singer *et al*., 2004 in Bentley *et al*., 2005). This indicates that these glacial landforms are probably amongst the oldest on Earth, not considering Antarctica. Also, the most recent deposits of the last glacial cycle in the Magellan region have been studied. Several of these studies provide maps (see Fig.30), some have tried to establish a chronology of glaciation using weathering characteristics, tephrochronology, radiocarbon dating (Bentley *et al*., 2005), or, more recently, exposure dating using cosmogenic isotopes (Kaplan *et al*., 2008)

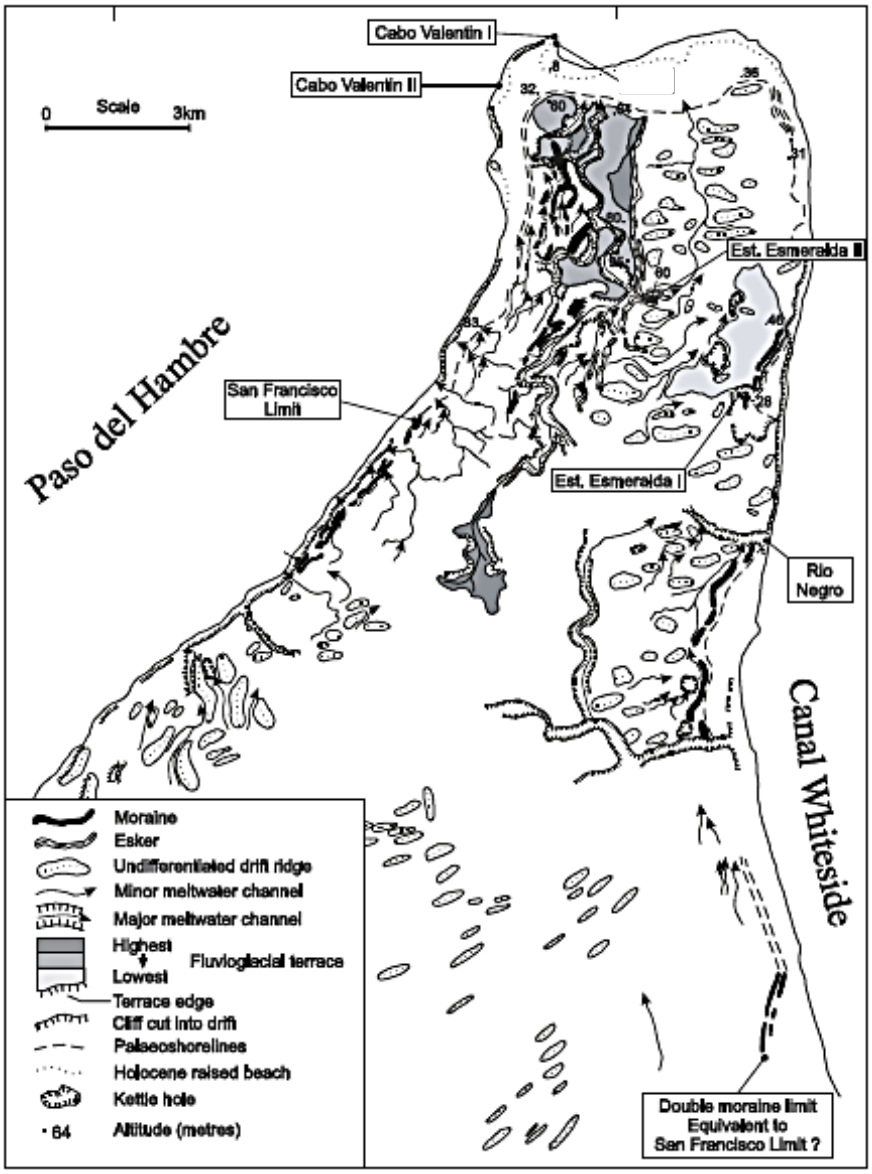

Fig. 30: Geomorphological map of the northern end of Isla Dawson, reproduced from McCulloch and Bentley (1998), source: Bentley *et al*., 2005.

Bentley *et al*. (2005) firstly indicated the importance of the finding that the deposits of the central Magellan Strait belong to the last glacial cycle, and that deglaciation left a complex geomorphological record. Secondly, studies have also shown that developing a chronology in the Magellan region is tricky because of the difficulties with radiocarbon dating in the area (aridity, lignite-contamination and composite landforms). Therefore, it is essential to have a clear geomorphological basis from which to interpret dates on glacier fluctuation. In order to do so, Bentley *et al*. (2005) remapped the geomorphology of the central Strait of Magellan and Bahía Inútil at a high resolution (see Fig.30).

To create a geomorphological map and to date the glacial deposits, Bentley *et al*. (2005) used: 1) weathering contrasts, 2) melt-water channels, 3) correlations between four main Stages, and 4) raised shorelines.

1) Clear contrasts in weathering in the Magellan region were attributed to different ages of the landforms. They distinguished four broad groups of landforms in the region on the basis of morphology, weathering, soil cover and color. The groups of landforms that are lying inside a clear weathering break are assigned to the last glaciations (Groups 3 and 4). Landforms outside this break are concluded to be older deposits and are, therefore, not further discussed in their study (Groups 1 and 2).
2) They suggest to use meltwater channels to delimit ice margins, because the channels are prominent features and as deep or deeper and more continuous than the associated moraines.
3) They mapped and correlated four main Stages (B to E) within the last glaciation and deglaciation deposits. They used the Stages for the glacial limits provided by Clapperton *et al*. (1995) and discovered that Stage A was actually lying within the Group 2 deposits, so part of the older glacial deposits. Stage B is the outermost, oldest limit, north of Punta Arenas. Stage E is the innermost, youngest group of moraines on Isla Dawson (see Fig.31).
4) Three groups of raised shorelines imply that proglacial ice-dammed lakes were present during deglaciation.

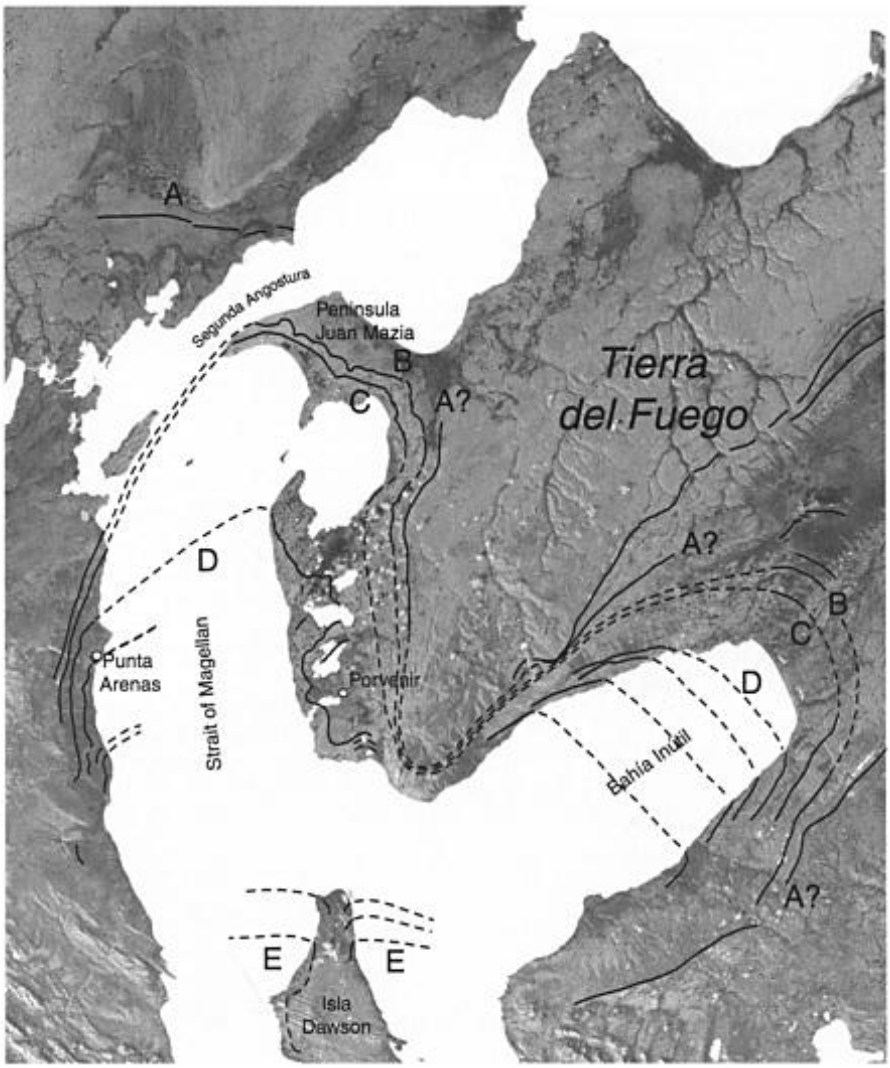

Fig. 31: The Stages of deglaciation in the Magellan Strait and Bahía Inútil. Stage A limits come from Clapperton *et al*. (1995) , all the other limits from Bentley *et al*. (2005), Source: Sugden *et al*., 2005.

McCulloch *et al*. (2005a) tried to resolve the chronological problems in previous work and provide a consistent chronology for the most up-to-date glacial geomorphological mapping of ice limits formed during the Last Glacial Maximum and during the Late Glacial/Holocene transition provided by Bentley *et al*. (2005a). McCulloch *et al*. (2005a) had to conclude that the precise age of the glacial Stage A remains unknown; however, it is certain that it is from before the last glaciation, older than 90000 years BP. The Magellan and Bahía Inútil glacier advanced at Stage B (25200 - 23100 cal. years BP), sometime before Stage C (21700 – 20300 cal. years BP) and sometime before Stage D (17500 cal. years BP). At the end of glacial Stage D, the Magellan glacier retreated into the fjords of the Cordillera Darwin (see Fig.32). This caused the ice-dam, damming the proglacial lake of glacial Stage D, to collapse and, therefore, drainage of the lake towards the Pacific Ocean became possible (McCulloch *et al*., 2005a). Evidence, coming from the raised shorelines observed above the post-Stage D peat layers, suggests that the Magellan glaciers readvanced (Stage E) into the southern Strait of

Magellan. They reformed the ice dam and created a large proglacial lake (15507 – 14348 cal. years BP) (McCulloch *et al*., 2005b). The final collapse of the ice dam and drainage of the lake happened at 12578 – 11773 cal. years BP, which is during the coldest phase of the Younger Dryas. This Late Glacial ice advance (Stage E) coincides with the Antarctic Cold Reversal recognized in the Vostok core. However, there is an anti-phase relationship between this glacial advance and the Bølling-Allerød warming shown in the Greenland ice cores (GISP). This suggests a clear anti-phase behavior between the two hemispheres during the Late Glacial/Holocene transition (McCulloch *et al*., 2005a) (see Fig.31, Fig.32).

McCulloch *et al*. (2005a) discovered that the overall pattern of glaciation is consistent with the timing of glacier advances in Lago Buenos Aires (46.5°S), which culminated between 23000 and 16000 years BP and also with the Chilean Lake District glacier advances (at 26100 – 25850 and 18052 – 17458 cal. years BP). For the overall pattern of the glacier advances, two important conclusions were made:

1) The timing suggests a northern hemisphere signal, because the most extensive glacier advances were in phase with the coldest interval of the Greenland isotopic ($\delta\ ^{18}O$) palaeotemperature record or GISP.
2) The chronological data from the Magellan region and from Lago Buenos Aires suggest that the earliest glacier advances during the Last Glacial maximum (25000 – 23000 cal. years BP) were the largest.

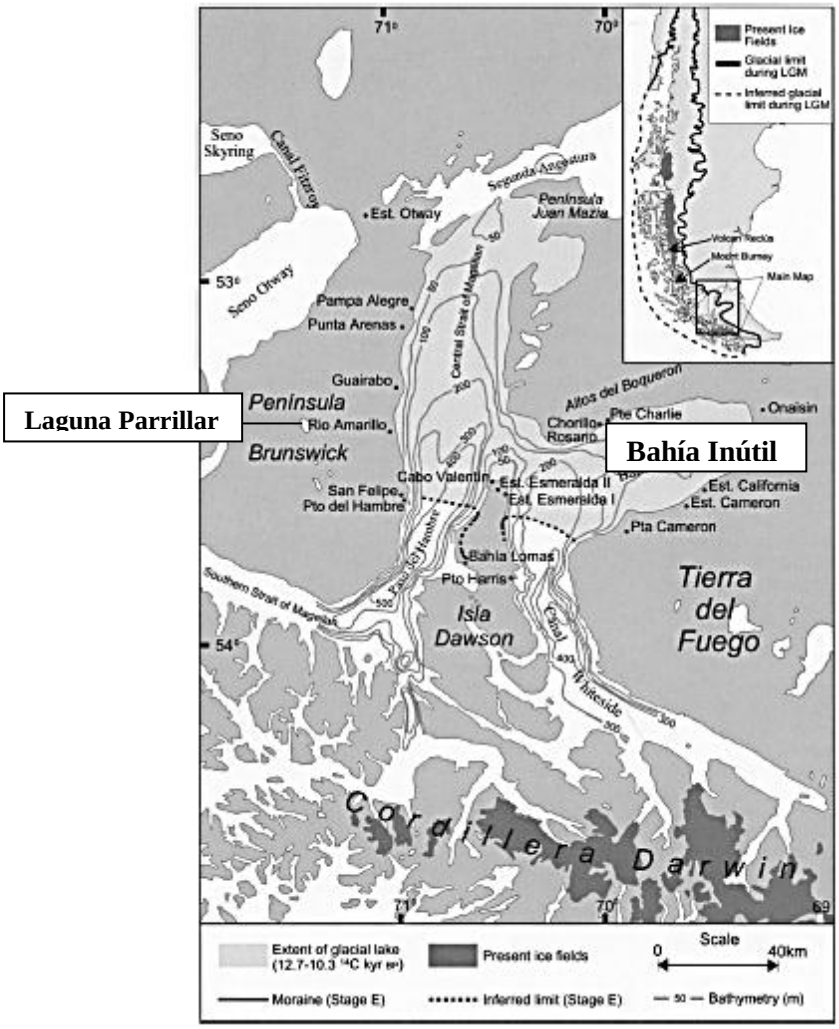

Fig. 32: Limits of the glacier advance of Stage E, and proglacial lake combining results from Clapperton *et al.* (1995), McCulloch and Bentley (1998), and McCulloch *et al.* (2005b), Source: McCulloch *et al.*, 2005b.

McCulloch *et al.* (2005b) further discuss evidence for a succession of ice-dammed lakes in the central Strait of Magellan (53°S) between 17000 and 12250 cal. years BP (see Fig.32). They examined litho-stratigraphical and morphological evidence, evaluated existing ^{14}C dates and presented new ^{14}C dates. They also placed the glacial lakes in a wider regional context of deglaciation in southernmost South America during the Late-Glacial/Holocene transition. During the period of glacial lake formation and associated glacier readvances, there was a simultaneous rapid and widespread glacier retreat of the Patagonian ice fields located further north. This suggests that the lakes were coeval with the Antarctic Cold Reversal and persisted the Late Glacial/Holocene transition. The observed asymmetrical latitudinal response in glacial behavior may suggest two possible mechanisms. It may be the reflection of the sensitivity of the glaciers in the Strait of Magellan to regional climatic changes. During the Late Glacial/Holocene transition, there were changes in the distribution of precipitation due to latitudinal shifts in the westerly storm tracks. Another possible mechanism may be that the observed asymmetry is the reflection of the overlapping spheres of northern hemisphere and Antarctic climatic influence in

the Magellan region. Superimposed on globally synchronous climatic changes, the Southern Ocean and associated land masses may also exhibit sub-millennial scale behavior, which is out of phase with that of the North Atlantic Ocean (McCulloch *et al*., 2005b).

4.8 Patagonian Ice Sheet fluctuations for the past 60000 years

Caniupán *et al*. (in press) studied the Patagonian Ice Sheet changes of southernmost Chile (53°S) over the past 60000 years. From their alkenone-based sea surface temperature record, they revealed a long-term warming trend over MIS 3 (60-25 ka), followed by a cooling towards the Last Glacial Maximum. These results differ from the sea surface temperature results from ODP Site 1233 (Kaiser and Lamy, 2010). Caniupán *et al*. (in press) argue that these differences reflect a regional cooling related to the proximal location of the Southern Patagonian Ice Sheet and related melt-water supply. They show this for at least the Last Glacial Maximum (23-19 ka). During late MIS 3 and MIS 2, they also detected a slight trend towards lighter (lower) planktonic $\delta\ ^{18}O$, which they consider to be a reflection of fresh water supply by the Patagonian Ice Sheet, and so a freshening of subsurface water masses, or possibly with a combination of other causes. They also performed an ice rafted debris study on their core and concluded that pulses of ice rafted debris coincide with ice sheet advances. The highest values of ice rafted debris were found during late MIS 3 and MIS 2. For the past 60000 years, the sea surface temperatures oscillated between a minimum of 4.4 °C (18.8 ka BP) and a maximum of 13 °C (9.6 ka BP). They observe an overall pattern of low temperatures (on average: 7 °C) from 60 ka BP to 19 ka BP. During early MIS 3, temperatures were up to ~9 °C, around 50 ka BP there was a temperature minimum of ~5 °C. Thereafter they observed a long-term warming trend of ~2 °C, persisting until 25 ka BP, followed by a cooling trend of ~3 °C, leading to the Last Glacial Maximum. At the Chilean margin between 30 and 41 °S, the sea surface temperatures were substantially reduced (for 5-7 °C compared to the early Holocene values) at the Last Glacial Maximum. Caniupán *et al*. (in press) argue that the expansion of the sea ice around Antarctica and the northward displacement of the southern westerly winds gave a 5-6 ° northward shift of the Antarctic Circumpolar Current, thereby causing the lower temperature values at the Chilean margin.

5. Results

5.1 Petrographic microscope observations

On the image scans of the sample PAR1A-III (50-60) (i.e. PAR1-11 and PAR1-12), the overall view revealed three different types of laminations: 1) laminae with a very dark appearance (low-lightness value), 2) laminae with an intermediate dark appearance (intermediate-lightness value), and 3) laminae with a pale appearance (high-lightness value). More detailed characteristics of these three types of laminae were determined by means of observations under the petrographic microscope: i.e. grain size, grain shape, sorting, etc. (see Table 1).

Table 1: The petrographic microscope observations

Sample: PAR1A-III (50-60) (thin section) and PAR1-11/ PAR1-12 (image)	Type of grain (sand, silt,clay; VC=very coarse C=coarse; F=fine; VF=very fine)	Grainsize (mm) (measured at magnification 10X10)	Shape grain (roundness) (WR=well rounded; R=rounded; SR=subrounded; SA=subangular; A=angular; VA=very angular	Sorting (VW=very well sorted; W=well sorted; M=moderately sorted; P=poorly sorted	Orientation? CU=Coarsening or FU=fining upwards?	Sharp or faint boundary (b= base, t=top boundary)?	Distance range (cm) in the sample (according to the scale)
Lamina 1 (top)	Silt-sand; VC	0.01 – 0.15 Fine silt to fine sand	A to SR	M	/	t: sharp b: sharp	[0 ; 0.5]
Lamina 2	Silt-sand; C	<0.01 – 0.1 Very fine silt to very fine sand	A to SR	P	/	t: sharp b: sharp	[0 ; 0.5] [0.5 ; 1]
Lamina 3	Silt; VF	<0.01 Very fine silt	/	VW	/	t: sharp b: sharp	[0.5 ; 1]
Lamina 4	Silt-sand; C	<0.01 – 0.1 Very fine silt to very fine sand	A to SR	P	CU	t: sharp b: faint	[0.5 ; 1]
Lamina 5	Silt; VF	<0.01 Very fine silt	/	VW	/	t: faint b: sharp	[1 ; 1.5]
Lamina 6	Silt-sand; C	0.01 – 0.1 Fine silt to very fine sand	A to SR	P	/	t: sharp b: faint	[1 ; 1.5]
Lamina 7	Silt; F	<0.01 – 0.02 Very fine silt to medium silt	A to SA	P	/	t: faint b: faint	[1 ; 1.5]

Lamina 8	Silt-sand; C	0.01 – 0.1 Fine silt to very fine sand	A to R	P	/	t: faint b: faint	[1 ; 1.5]
Lamina 9	Silt; VF	<0.01 Very fine silt	/	VW	/	t: faint b: faint	[1.5 ; 2]
Lamina 10	Silt-sand; VC	0.02 – 0.15 Fine silt to fine sand	A to SR	P	/	t: faint b: faint	[1.5 ; 2]
Lamina 11	Silt; VF	<0.01 Very fine silt	/	VW	/	t: faint b: faint	[1.5 ; 2]
Lamina 12	Silt; F	0.01 – 0.05 Fine silt to coarse silt	A to SR	P	/	t: faint b: faint	[2 ; 2.5]
Lamina 13	Silt; VF	<0.01 Very fine silt	/	VW	/	t: faint b: faint	[2 ; 2.5]
Lamina 14	Silt-sand; C	0.01 – 0.1 Fine silt to very fine sand	A to SR	P	/	t: faint b: faint	[2 ; 2.5]
Lamina 15	Silt; VF	<0.01 Very fine silt	/	VW	/	t: faint b: faint	[2 ; 2.5]
Lamina 16	Silt; F	0.02 – 0.05 Fine silt to coarse silt	A to SR	M	/	t: faint b: faint	[2 ; 2.5] (at base grain 0.5 mm diameter)
Lamina 17	Silt; F	<0.01 – 0.01 Very fine silt to fine silt	/	VW (but one big subangular grain)	FU	t: faint b: sharp	[2 ; 2.5]
Lamina 18	Silt; F	<0.01 – 0.01 Very fine silt to fine silt	/	M – VW	FU	t: sharp b: faint	[2.5 ; 3]
Lamina 19	Silt-sand; C	0.01 – 0.1 Fine silt to very fine sand	A to SR	P	/	t: faint b: faint	[2.5 ; 3]
Lamina 20	Silt; VF	<0.01 Very fine silt	/	VW	/	t: sharp b: faint	[2.5 ; 3]
Lamina 21	Silt; F	0.01 – 0.05 Fine silt to coarse silt	A to SR	P	/	t: sharp b: faint	[2.5 ; 3]
Lamina 22	Silt; VF	<0.01 Very fine silt	/	VW	/	t: sharp b: faint	[2.5 ; 3]
Lamina 23	Silt; F	0.01 – 0.03 Fine silt to medium silt	A to SR	P	/	t: sharp b: faint	[2.5 ; 3]

Lamina 24	Silt; VF	<0.01 Very fine silt	/	VW	/	t: sharp b: faint	[2.5 ; 3]
Lamina 25	Silt; F	0.01 – 0.05 Fine silt to coarse silt	A to SR	P	/	t: sharp b: faint	[2.5 ; 3]
Lamina 26	Silt; F	<0.01 – 0.05 Very fine silt to coarse silt	A to SR	M	/	t: sharp b: faint	[2.5 ; 3]
Lamina 27	Silt; VF	<0.01 Very fine silt	/	VW	/	t: sharp b: faint	[2.5 ; 3]
Lamina 28	Silt-sand; C	0.01 – 0.1 Fine silt to very fine sand	A to SR	M – P	/	t: sharp b: faint	[3 ; 3.5]
Lamina 29	Silt; F	<0.01 – 0.01 Very fine silt to fine silt	/	VW	/	t: sharp b: faint	[3 ; 3.5]
Lamina 30	Silt-sand; C	0.01 – 0.1 Fine silt to very fine sand	A to SR	M – P	/	t: faint b: sharp irregular	[3 ; 3.5]
Lamina 31	Silt; F	<0.01 – 0.01 Very fine silt to fine silt	/	VW	/	t: sharp b: sharp irregular	[3 ; 3.5]
Lamina 32	Silt; VF	<0.01 Very fine silt	/	VW	/	t: sharp irregular b: faint	[3 ; 3.5]
Lamina 33	Silt-sand; C	0.01 – 0.1 Fine silt to very fine sand	A to SR	M – P	/	t: sharp b: faint	[3 ; 3.5]
Lamina 34	Silt; VF	<0.01 Very fine silt	/	VW	/	t: sharp b: faint	[3 ; 3.5]
Lamina 35	Silt-sand; C	0.01 – 0.1 Fine silt to very fine sand	A to SR	M – P	/	t: faint b: sharp irregular	[3 ; 3.5]
Lamina 36	Silt; VF	<0.01 Very fine silt	/	VW	/	t: sharp irregular b: sharp irr.	[3.5 ; 4]
Lamina 37	Silt-sand; C	0.01 – 0.1 Fine silt to very fine sand	A to SR	P	/	t: sharp irregular b: sharp irr.	[3.5 ; 4]
Lamina 38	Silt; VF	<0.01 Very fine silt	/	VW	/	t: sharp irr. b: faint	[3.5 ; 4]
Lamina 39	Silt-sand; C	0.01 – 0.1 Fine silt to very fine sand	A to SR	P	/	t: faint b: faint	[4 ; 4.5]

Lamina 40	Silt; F	<0.01 – 0.01 Very fine silt to fine silt	/	VW	/	t: faint b: faint	[4 ; 4.5]
Lamina 41	Silt-sand; C	0.01 – 0.1 Fine silt to very fine sand	A to SR	P	/	t: faint b: faint	[4 ; 4.5]
Lamina 42	Silt; F	<0.01 – 0.04 Very fine silt to coarse silt	/	P	/	t: faint b: faint	[4 ; 4.5]
Lamina 43	Silt-sand; C	0.01 – 0.1 Fine silt to very fine sand	A to R	P	/	t: faint b: faint	[4 ; 4.5]
Lamina 44	Silt; F	<0.01 – 0.01 Very fine silt to fine silt	/	VW	/	t: faint b: sharp	[4 ; 4.5]
Lamina 45	Silt-sand; VC	0.01 – 0.15 Fine silt to fine sand	A to SR	P	FU	t: sharp b: faint	[4 ; 4.5]
Lamina 46	Silt; F	<0.01 – 0.01 Very fine silt to fine silt	/	VW	FU (second part)	t: faint b: faint	[4 ; 4.5]
Lamina 47	Silt; F	0.01 – 0.05 Fine silt to coarse silt	A to SR	P	FU (first part)	t: faint b: faint	[4 ; 4.5]
Lamina 48	Silt; F	<0.01 – 0.01 Very fine silt to fine silt	/	VW	FU (second part)	t: faint b: faint	[4.5 ; 5]
Lamina 49	Silt; F	0.01 – 0.05 Fine silt to coarse silt	A to SR	P	FU (first part)	t: faint b: sharp irr.	[4.5 ; 5]
Lamina 50	Silt; VF	<0.01 Very fine silt	/	VW	/	t: sharp irregular b: sharp irr.	[4.5 ; 5]
Lamina 51	Silt-sand; C	0.01 – 0.1 Fine silt to very fine sand	A to SR	P	CU	t: sharp irregular b: sharp irr.	[4.5 ; 5]
Lamina 52	Silt; VF	<0.01 Very fine silt	/	VW	/	t: sharp irr. b: sharp irr.	[5 ; 5.5]
Lamina 53	Silt-sand; C	0.01 - 0.1 Fine silt to very fine sand	A to R	M – P	/	t: sharp irr. b: faint	[5 ; 5.5]
Lamina 54	Silt; F	<0.01 – 0.01 Very fine silt to fine silt	/	VW	/	t: faint b: faint	[5 ; 5.5]
Lamina 55	Silt-sand; C	0.01 – 0.1 Fine silt to very fine sand	A to R	M – P	/	t: faint b: faint	[5 ; 5.5]

Lamina 56	Silt; F	<0.01 – 0.01 Very fine silt to fine silt	/	VW	/	t: faint b: faint	[5 ; 5.5]
Lamina 57	Silt-sand; C	0.01 – 0.1 Fine silt to very fine sand	A to R	M – P	/	t: faint b: faint	[5 ; 5.5]
Lamina 58	Silt; F	<0.01 – 0.01 Very fine silt to fine silt	/	VW	/	t: faint b: faint	[5 ; 5.5]
Lamina 59	Silt-sand; C	0.01 – 0.1 Fine silt to very fine sand	A to R	M – P	/	t: faint b: faint	[5 ; 5.5]
Lamina 60	Silt; F	<0.01 – 0.01 Very fine silt to fine silt	/	VW	/	t: faint b: faint	[5 ; 5.5]
Lamina 61	Silt-sand; C	0.01 – 0.1 Fine silt to very fine sand	A to R	M – P	/	t: faint b: faint	[5 ; 5.5]
Lamina 62	Silt; F	<0.01 – 0.01 Very fine silt to fine silt	/	VW	/	t: faint b: faint	[5 ; 5.5]
Lamina 63	Silt; F	0.01 – 0.05 Fine silt to coarse silt	A to SR	M – P	/	t: faint b: faint	[5 ; 5.5]
Lamina 64	Silt; F	<0.01 – 0.01 Very fine silt to fine silt	/	VW	/	t: faint b: faint	[5 ; 5.5]
Lamina 65	Silt-sand; C	0.01 – 0.1 Fine silt to very fine sand	A to SA	M – P	/	t: faint b: faint	[5 ; 5.5]
Lamina 66	Silt; F	<0.01 – 0.01 Very fine silt to fine silt	/	VW	/	t: faint b: sharp	[5 ; 5.5]
Lamina 67	Silt; VF	<0.01 Very fine silt	/	VW	/	t: sharp b: sharp	[5.5 ; 6]
Lamina 68	Silt-sand; C	0.01 – 0.1 Fine silt to very fine sand	A to SR	M	CU (second part)	t: sharp b: faint	[5.5 ; 6]
Lamina 69	Silt; F	<0.01 -0.01 Very fine silt to fine silt	/	VW	CU (first part)	t: faint b: sharp	[5.5 ; 6]
Lamina 70	Silt; VF	<0.01 Very fine silt	/	VW	/	t: sharp b: sharp	[5.5 ; 6]
Lamina 71	Silt-sand; VC	0.01 – 0.15 Fine silt to fine sand	A to R	VW	/	t: sharp b: sharp	[6 ; 6.5]

Lamina 72	Silt-sand; C	0.01– 0.1 Fine silt to very fine sand	A to R	P	/	t: sharp b: sharp irr.	[6 ; 6.5]
Lamina 73	Silt; VF	<0.01 Very fine silt	/	VW	/	t: sharp irr. b: faint	[6 ; 6.5]
Lamina 74	Silt-sand; C	0.01 -0.1 Fine silt to very fine sand	A to R	P	/	t: faint b: sharp	[6 ; 6.5]
Lamina 75	Silt; VF	<0.01 Very fine silt	/	VW	/	t: sharp b: faint	[6 ; 6.5]
Lamina 76	Silt-sand; VC	0.01 – 0.15 Fine silt to fine sand	A to R	M – P	/	t: faint b: faint	[6.5 ; 7]
Lamina 77	Silt; F	<0.01 – 0.05 Very fine silt to coarse silt	A to SA	M – P	/	t: faint b: faint	[6.5 ; 7]
Lamina 78	Silt-sand; C	0.01 – 0.1 Fine silt to very fine sand	A to SA	P	/	t: faint b: faint	[6.5 ; 7]
Lamina 79	Silt; F	<0.01 – 0.02 Very fine silt to medium silt	A to SA	M	/	t: faint b: faint	[6.5 ; 7]
Lamina 80	Silt-sand; C	0.01 – 0.1 Fine silt to very fine sand	A to SR	P	/	t: faint b: faint	[6.5 ; 7]
Lamina 81	Silt; F	<0.01 – 0.01 Very fine silt to fine silt	A to SA	M	/	t: faint b: faint	[6.5 ; 7]
Lamina 82	Silt-sand; C	0.01 – 0.1 Fine silt to very fine sand	A to R	P	/	t: faint b: faint	[6.5 ; 7]
Lamina 83	Silt; F	<0.01 – 0.02 Very fine silt to medium silt	A to SA	M	/	t: faint b: sharp	[7 ; 7.5]
Lamina 84	Silt; VF	<0.01 Very fine silt	/	VW	/	t: sharp b: faint	[7 ; 7.5]
Lamina 85	Silt; F	0.01 – 0.05 Fine silt to coarse silt	A to SA	P	/	t: faint b: sharp	[7 ; 7.5]
Lamina 86	Silt; VF	<0.01 Very fine silt	/	VW	/	t: sharp b: sharp	[7 ; 7.5]
Lamina 87	Silt-sand; VC	0.01 – 0.15 Fine silt to fine sand	A to SR	M	/	t: sharp b: sharp	[7 ; 7.5]

Lamina 88	Silt; F	<0.01 – 0.03 Very fine silt to medium silt	A to SA	P	/	t: sharp b: sharp	[7.5 ; 8]
Lamina 89	Silt-sand; C	0.01 – 0.1 Fine silt to very fine sand	A to SA	M	/	t: sharp b: sharp	[7.5 ; 8]
Lamina 90	Silt-sand; C	<0.01 – 0.1 Very fine silt to very fine sand	A to SR	P	/	t: sharp b: faint	[7.5 ; 8]
Lamina 91	Silt; F	0.01 – 0.04 Fine silt to coarse silt	A to SR	M – W	/	t: faint b: faint	[7.5 ; 8]
Lamina 92	Silt; F	<0.01 – 0.02 Very fine silt to medium silt	A	P	/	t: faint b: faint	[7.5 ; 8]
Lamina 93	Silt-sand; C	0.01 – 0.1 Fine silt to very fine sand	A to SR	M – P	/	t: faint b: sharp	[7.5 ; 8]
Lamina 94	Silt; F	<0.01 – 0.01 Very fine silt to fine silt	/	M	/	t: sharp b: faint	[7.5 ; 8]
Lamina 95	Silt-sand; C	0.01 – 0.1 Fine silt to very fine sand	A to SR	M – P	/	t: faint b: sharp irr.	[7.5 ; 8]
Lamina 96	Silt; VF	<0.01 Very fine silt	/	VW	/	t: sharp b: sharp	[8 ; 8.5]
Lamina 97	Silt-sand; VC	0.01 – 0.15 Fine silt to fine sand	A to SR	M	/	t: sharp b: faint	[8 ; 8.5]
Lamina 98	Silt-sand; C	<0.01 – 0.1 Very fine silt to very fine sand	A to SR	P	/	t: faint b: sharp	[8 ; 8.5]
Lamina 99	Silt; VF	<0.01 Very fine silt	/	VW	/	t: sharp b: sharp	[8 ; 8.5]
Lamina 100	Silt-sand; C	0.01 – 0.1 Fine silt to very fine sand	A to R	P	/	t: sharp b: sharp	[8 ; 8.5]
Lamina 101	Silt; VF	<0.01 Very fine silt	/	VW	/	t: sharp b: sharp	[8.5 ; 9]
Lamina 102	Silt-sand; C	0.01 – 0.1 Fine silt to very fine sand	A to R	M - P	/	t: sharp b: faint	[8.5 ; 9]

Lamina 103	Silt; F	<0.01 – 0.02 Very fine silt to medium silt	A to SA	P	/	t: faint b: faint	[8.5 ; 9]
Lamina 104	Silt-sand; C	0.01 – 0.1 Fine silt to very fine sand	A to R	M – P	/	t: faint b: sharp	[8.5 ; 9]
Lamina 105	Silt; VF	<0.01 Very fine silt	/	VW	/	t: sharp b: sharp	[8.5 ; 9]
Lamina 106	Silt-sand; C	0.01 – 0.1 Fine silt to very fine sand	A to R	P	/	t: sharp b: faint	[9 ; 9.5]
Lamina 107	Silt; F	<0.01 – 0.01 Very fine silt to fine silt	/	M	/	t: faint b: faint	[9 ; 9.5]
Lamina 108	Silt-sand; C	0.01 – 0.1 Fine silt to very fine sand	A to R	P	/	t: faint b: sharp	[9 ; 9.5]
Lamina 109	Silt; F	<0.01 – 0.01 Very fine silt to fine silt	/	M – VW	/	t: sharp b: faint	[9 ; 9.5]
Lamina 110	Silt; F	<0.01 – 0.05 Very fine silt to coarse silt	A to SA	M	CU	t: faint b: sharp	[9 ; 9.5]
Lamina 111	Silt; VF	<0.01 Very fine silt	/	VW	/	t: sharp b: sharp	[9 ; 9.5]
Lamina 112	Silt; F	0.01 – 0.05 Fine silt to coarse silt	A to SR	M	/	t: sharp b: faint	[9.5 ; 10]
Lamina 113	Silt; F	<0.01 – 0.01 Very fine silt to fine silt	/	W – VW	/	t: faint b: sharp	[9.5 ; 10]
Lamina 114	Silt-sand; VC	0.01 – 0.15 Fine silt to fine sand	A to R	M	/	t: sharp b: sharp	[10 ; 10.5]
Lamina 115	Silt; VF	<0.01 Very fine silt	/	VW	/	t: sharp b: sharp	[10 ; 10.5]
Lamina 116	Silt-sand; C	0.01 – 0.1 Fine silt to very fine sand	A to SA	M – P	/	t: sharp b: faint	[10 ; 10.5]
Lamina 117	Silt; VF	<0.01 Very fine silt	/	VW	/	t: faint b: faint	[10 ; 10.5]
Lamina 118	Silt-sand; C	0.01 – 0.1 Fine silt to very fine sand	A to SA	M – P	/	t: faint b: faint	[10 ; 10.5]

Lamina 119	Silt; F	<0.01 – 0.02 Very fine silt to medium silt	A to SA	P	/	t: faint b: faint	[10 ; 10.5]
Lamina 120	Silt-sand; C	0.01 – 0.1 Fine silt to very fine sand	A to SA	M – P	/	t: faint b: sharp	[10 ; 10.5]
Lamina 121	Silt; VF	<0.01 Very fine silt	/	VW	/	t: sharp b: faint	[10 ; 10.5]
Lamina 122	Silt; F	0.01 – 0.05 Fine silt to coarse silt	A to SA	M – W	CU	t: faint b: sharp	[10 ; 10.5]
Lamina 123	Silt; VF	<0.01 Very fine silt	/	VW	/	t: sharp b: sharp	[10.5 ; 11]
Lamina 124	Silt-sand; C	0.01 – 0.1 Fine silt to very fine sand	A to SR	M	/	t: sharp b: faint	[10.5 ; 11]
Lamina 125	Silt; F	<0.01 – 0.01 Very fine silt to fine silt	/	VW	/	t: faint b: faint	[10.5 ; 11]
Lamina 126	Silt-sand; C	0.01 – 0.1 Fine silt to very fine sand	A to SR	M	/	t: faint b: sharp	[10.5 ; 11]
Lamina 127	Silt; VF	<0.01 Very fine silt	/	VW	/	t: sharp	[10.5 ; 11]

The low-lightness laminae appear to consist of very well sorted, very fine silt (<0.01 mm), and some of moderately to very well sorted, very fine silt to fine silt ((<0.01)-0.01 mm). These laminations are the most fine grained of the sample.

The intermediate-lightness laminae consist of a more coarse grained silt. In the sample we observed for the intermediate-lightness laminae, a grain size range of 0.01-0.05 mm, from fine silt to coarse silt. These laminae are moderately to poorly sorted and have grains with shapes from sub-rounded at the top part of the sample to more sub-angular from the interval [6.5 ; 7] towards the base of the sample (see Table 1).

The high-lightness laminae are the coarsest grained laminations of the sample. These laminae are silt-sand layers consisting of a grain size ranging between 0.01 and 0.15 mm, from fine silt to fine sand. The coarsest grained silt-sand layers are poorly to moderately sorted. The less coarse grained silt-sand layers are poorly sorted or poorly to moderately sorted, and a few are moderately sorted. These

observations can be summarized as follows: the darker the appearance (or the lower the lightness) of the laminations, the smaller the grain size is and the better the sediment is sorted.

Also, some observations of grain size trends were made. Laminae 4, 51, 68 and 69 together, 110 and 122 show a coarsening upwards trend, whereas laminae 17, 18, 45, 46 and 47 together and laminae 48 and 49 together show a fining upwards trend (see Table 1). The characteristics of the boundaries between laminae were examined as well. The base and top boundary of the coarsening upwards laminae are faint and sharp or sharp and sharp, respectively. For the fining upwards laminae, the base and top boundary are sharp and sharp, faint and faint, sharp and faint, or faint and sharp, respectively (see Table 1).

5.2 Microscope analysis of the laminated sediment

The microscope analysis, performed on the complete record (PAR1A-III, PAR1A-IV and PAR1A-V), uncovered some interesting aspects of the laminations. The coarse grained silt-sand laminae combined with the fine grained laminae (low-lightness, very fine silt laminae and intermediate-lightness, coarse silt laminae) form a couplet. The total amount of couplets found is 1347 within a time span of 11879 years. The minimum thickness measured for the fine grained laminae is 0.001 cm; the maximum thickness measured is 1.349 cm. The minimum thickness measured for the coarse grained laminae is 0.002 cm; the maximum thickness is 0.681 cm. For the couplets, a minimum thickness of 0.015 cm and a maximum thickness of 1.534 cm was measured.

5.2.1 Correlations and relationships between the data

When plotting the thickness of all the fine grained laminae against the thickness of all the coarse grained laminae (Fig.33), a very bad correlation of $R^2 = 0.0269$ was found, and there is a data cluster within the region of thickness values below 0.4 cm. The thickness of all the coarse grained laminae varies between 0.002 and 0.7 cm, and the thickness of all the fine grained laminae varies between 0.001 and 0.6 cm (see Fig.33). There is one deviating data point. The fine grained laminae, as well as the coarse grained laminae, show a minimum thickness. The minimum thickness of all the fine grained laminae (red line in Fig.33) seems to move to higher values as the thickness of the coarse grained laminae rises. The same seems to be true for the minimum thickness of all the coarse grained laminae (yellow line in Fig.33).

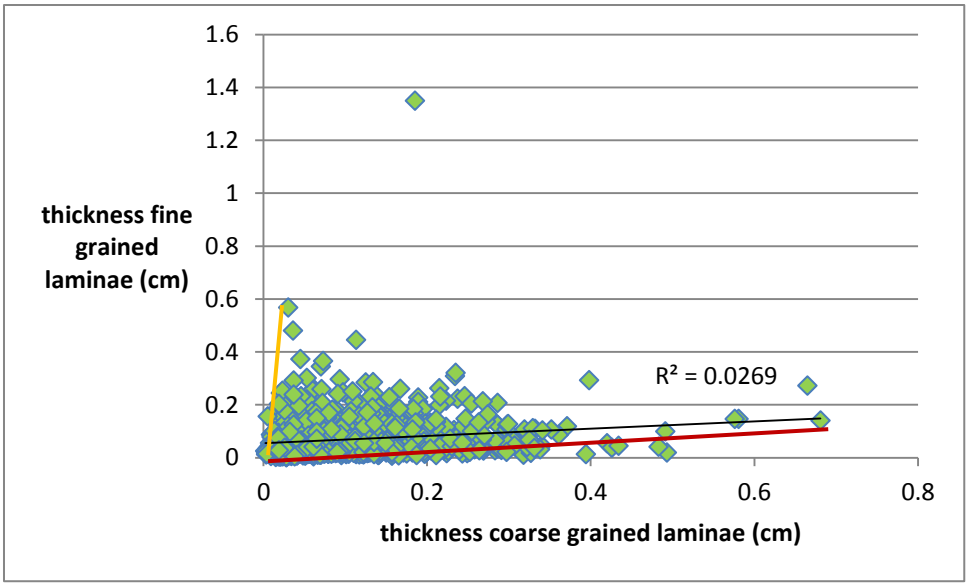

Fig. 33: correlation between all the fine grained laminae and all the coarse grained laminae

Plotting the thickness of the couplets (= thickness coarse grained lamina + thickness fine grained lamina) against the fine grained laminae, a weak, positive correlation of R^2 = 0.5104 (Fig.34) was obtained. Though, plotting the thickness of the couplets against the thickness of the coarse grained laminae gives a good, positive correlation of R^2 = 0.6519 (Fig.35).

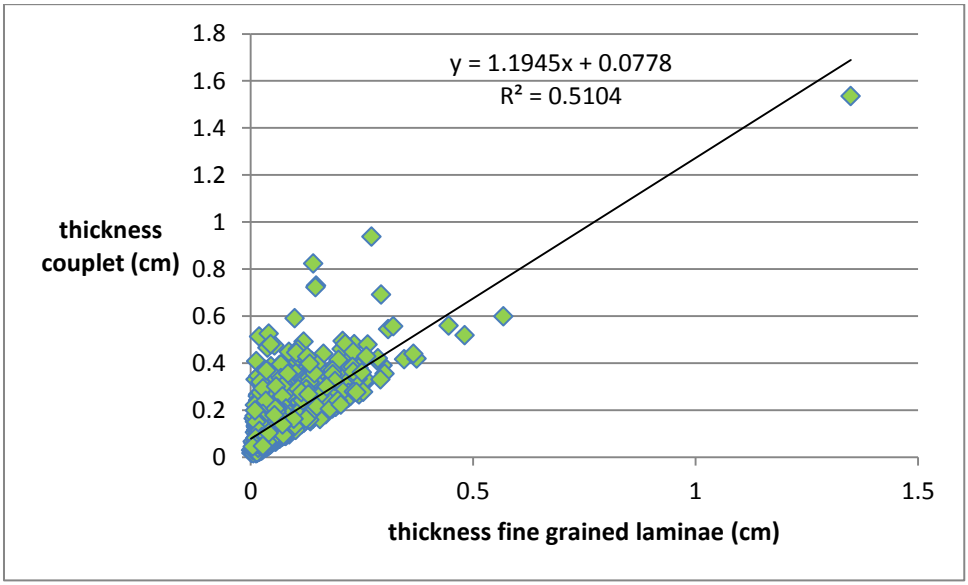

Fig. 34: correlation between all the couplets and all the fine grained laminae

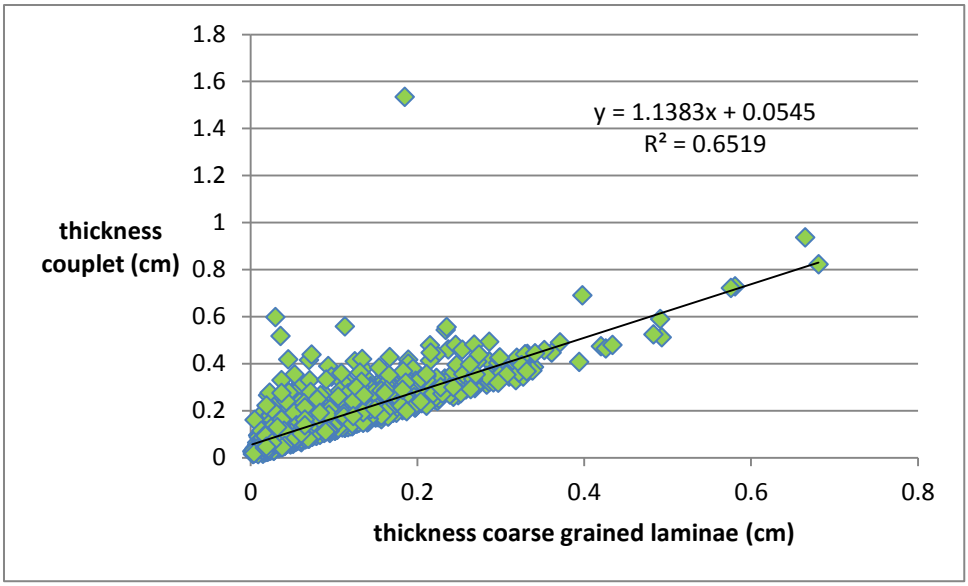

Fig. 35: correlation between all the couplets and all the coarse grained laminae

5.2.2 Variations through time

The thickness of all the couplets, all the fine grained laminae and all the coarse grained laminae were plotted against time. Here a graph is shown comparing the variations of the couplet thickness with the variations in thickness of all the fine grained laminae (Fig.37) and all the coarse grained laminae (Fig.36). Additionally, Fig.38 shows the relationship of the variations of thickness between all the coarse grained and all the fine grained laminae. For the thickness of all the fine grained laminae, thickness of all the coarse grained laminae, and the corresponding age data, moving averages, with a subset size of 4 data points, were calculated and plotted (Fig.39).

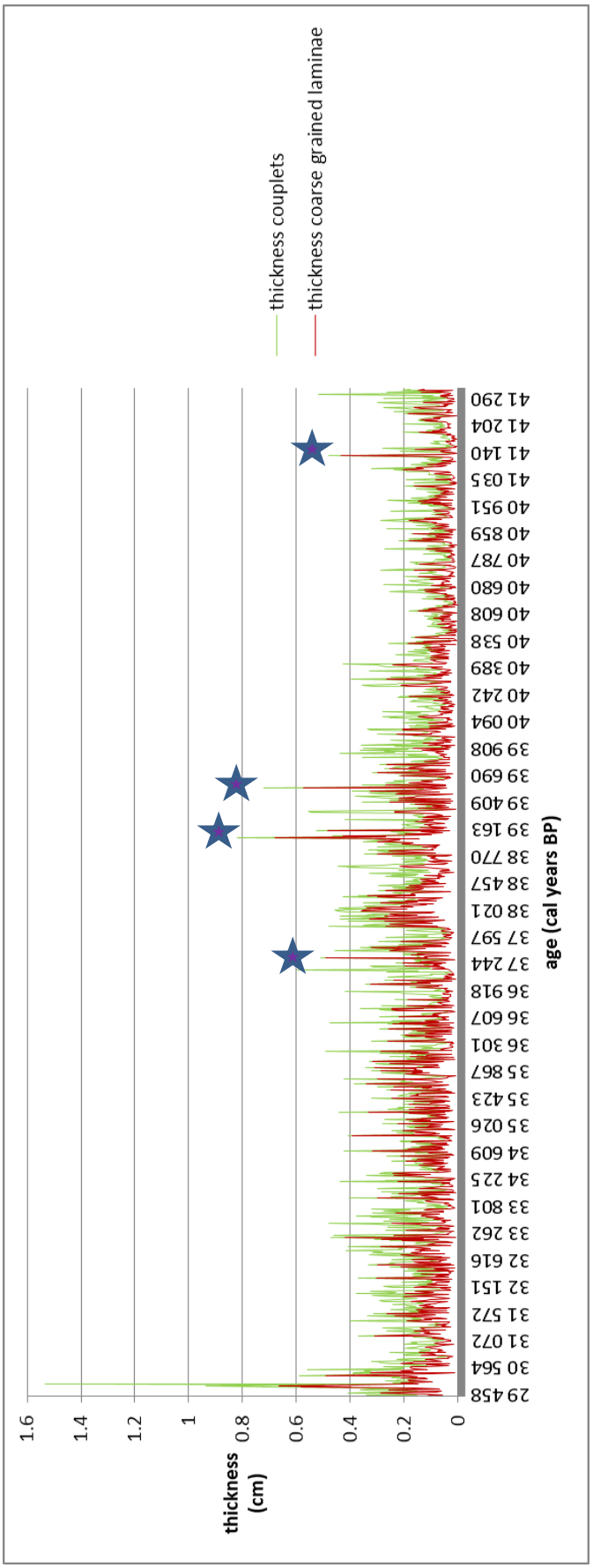

Fig. 36: all couplets and all coarse grained laminae, against a time axis

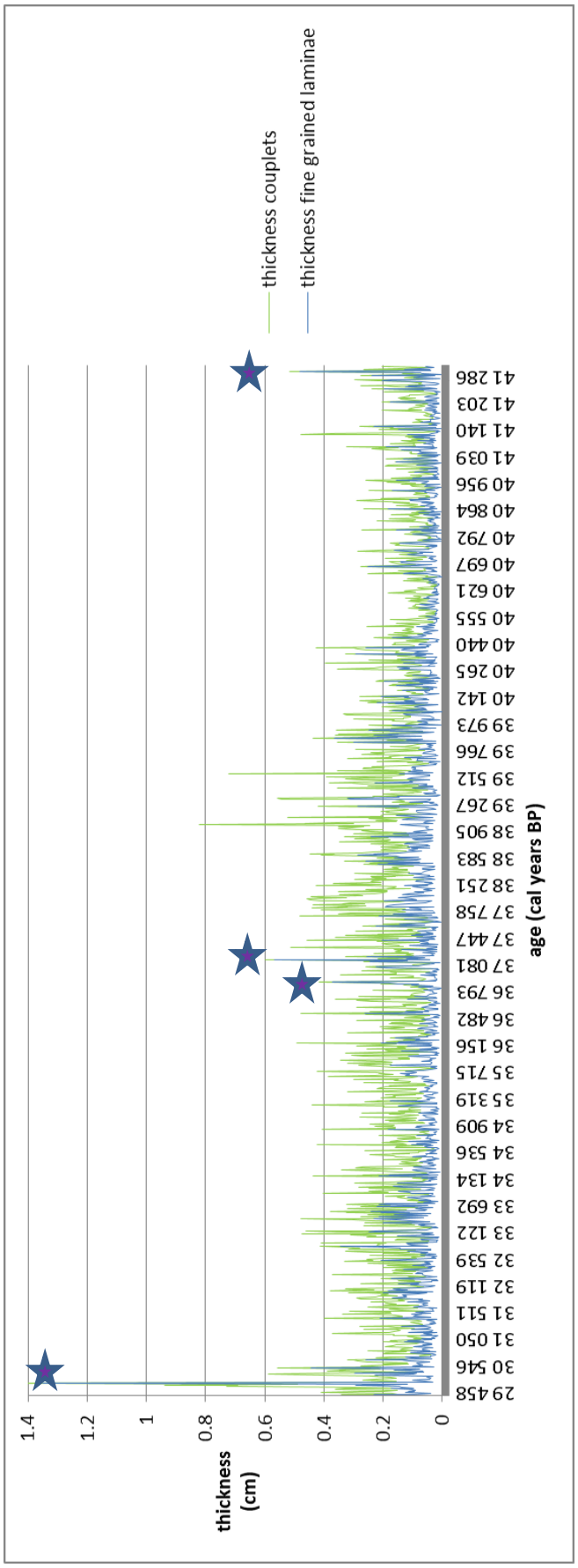

Fig. 37: : all couplets and all fine grained laminae, against a time axis

The Fig.36 demonstrates that the variations in the thickness of all the coarse grained laminae closely follows the variations of the couplet thickness. The couplet thickness and thickness of all the coarse grained laminae seem to be related. A similar observation was made earlier, when it was shown that the couplet thickness and the thickness of all the coarse grained laminae correlated well ($R^2 = 0.6519$). The variations in the thickness of all the fine grained laminae are not always following the couplet thickness variations (see Fig.37). For example, around the age of 35715 cal. years BP, 37758 cal. years BP, 38251 cal. years BP and 38905 cal. years BP the thickness peaks of the fine grained laminae are lower than the couplet thickness peaks.

Furthermore, some distinct peaks can be observed. Some of the peaks of the fine grained lamina thickness are as high as the peaks of the couplet thickness at that same place. This happens for example at an age of 30044 cal. years BP, 36918 cal. years BP, 37170 cal. years BP and 41316 cal. years BP (see purple stars in Fig.37). There are also peaks of the coarse grained lamina thickness that are as high as the couplet thickness peaks. This can be observed, for example, at an age of 37335 cal. years BP, 39053 cal. years BP, 39601 cal. years BP and at 41138 cal. years BP (see purple stars in Fig.36).

In Fig.38, the relationship between the variations of all the coarse grained laminae and all the fine grained laminae become clear. Sometimes the peaks largely differ in height. To better interpret these relationships, a graph, showing the calculated moving averages of the thickness of all the fine grained and all the coarse grained laminae, will be used (Fig.39). For the calculation of the moving averages a subset size of 4 data points was used. Two types of intervals can be roughly distinguished.

Interval I runs from 29548 to 34169 cal. years BP and is characterized by the fact that the coarse grained lamina and fine grained lamina thickness variations follow each other; this means that the peaks are more or less of the same height within this interval.

Interval II runs from 34169 to 40095 cal. years BP and is characterized by large peak height differences. Interval II shows a larger thickness for the coarse grained laminae and a smaller thickness for the fine grained laminae. However, within interval II, the opposite situation has been observed, in which the coarse grained lamina thickness shows lower peaks, and the fine grained lamina thickness shows higher peaks, has been observed too. This happens around 36303.28 cal. years BP, 36838.04 cal. years BP, 37083.50 cal. years BP, 37605.68 cal. years BP and 38587.23 cal. years BP.

Finally, Interval III, which looks more or less the same as interval I, runs from 40095 to 41331cal. years BP. Within Interval III, the peaks of the fine grained and coarse grained lamina thickness variations follow each other.

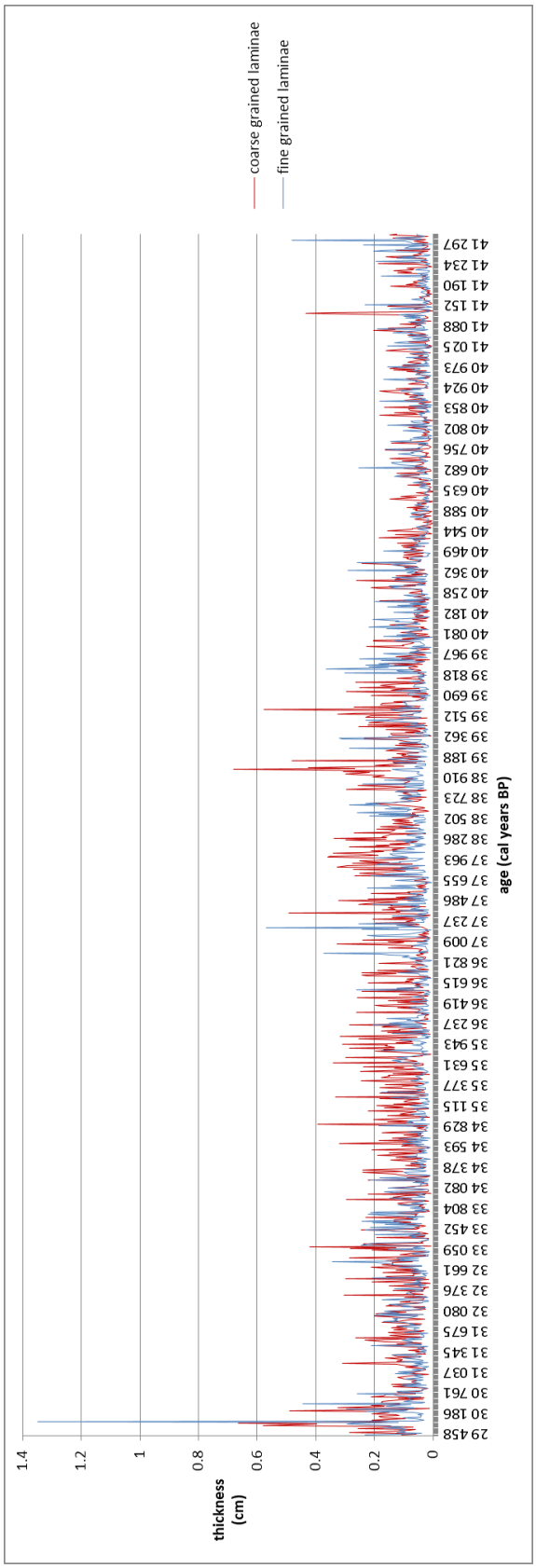

Fig. 38: all coarse grained and all fine grained laminae, against a time axis

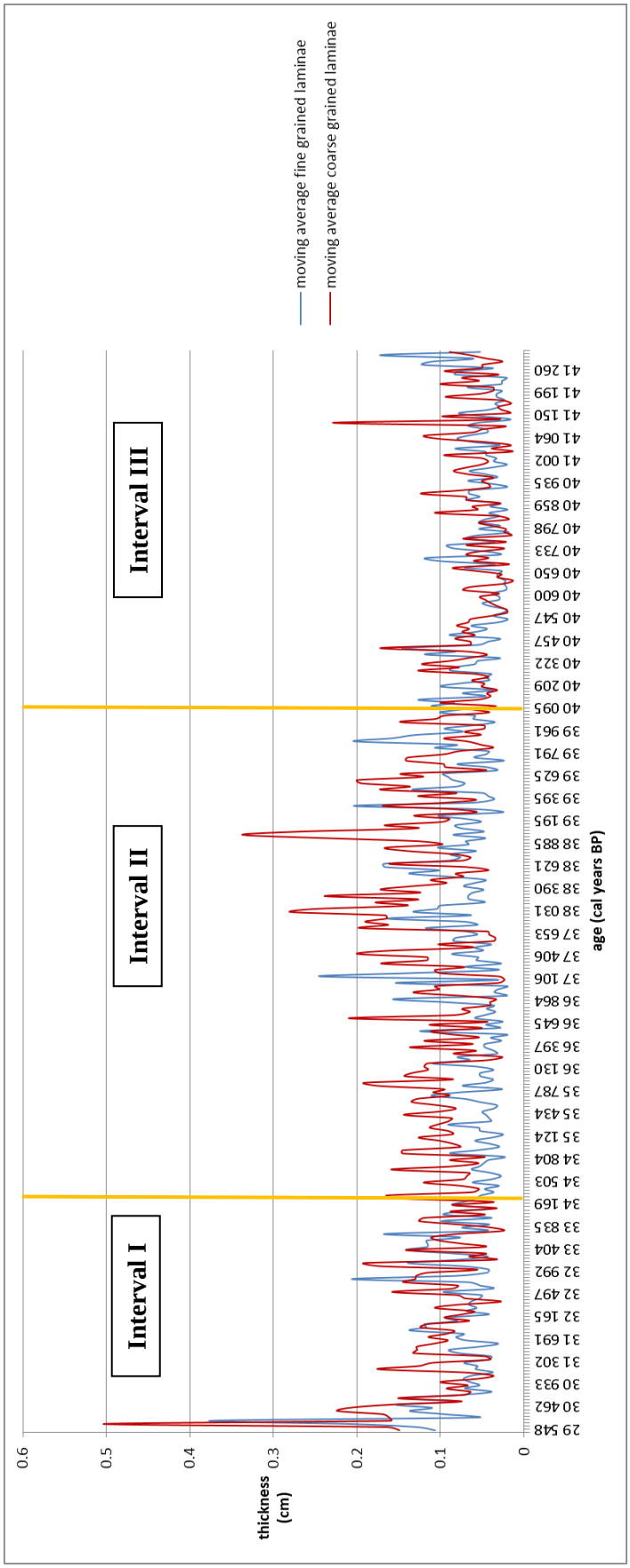

Fig. 39: moving average, with subset size of 4 data points, for all the fine grained and all the coarse grained laminae; plotted against a time axis

From the thickness dataset of all the fine grained laminae, both the thick laminae with a thickness between 0.2 and 0.7 cm and the thin laminae (thickness < 0.2 cm) (the names “thick laminae” and “thin laminae” will further only be used for referring to the thick and thin laminations of the fine grained part) were selected. Many more thin laminae than thick laminae were found. The thin ones are evenly spread over the whole record and show a sinusoidal course, of which the higher peaks reach thickness values between 0.1 and 0.2 cm. The thick laminae do not occur everywhere in the record but show more solitary events. At least six high peaks (above a thickness of 0.3 cm) can be recognized, which cluster in groups of two peaks (see Fig.40).

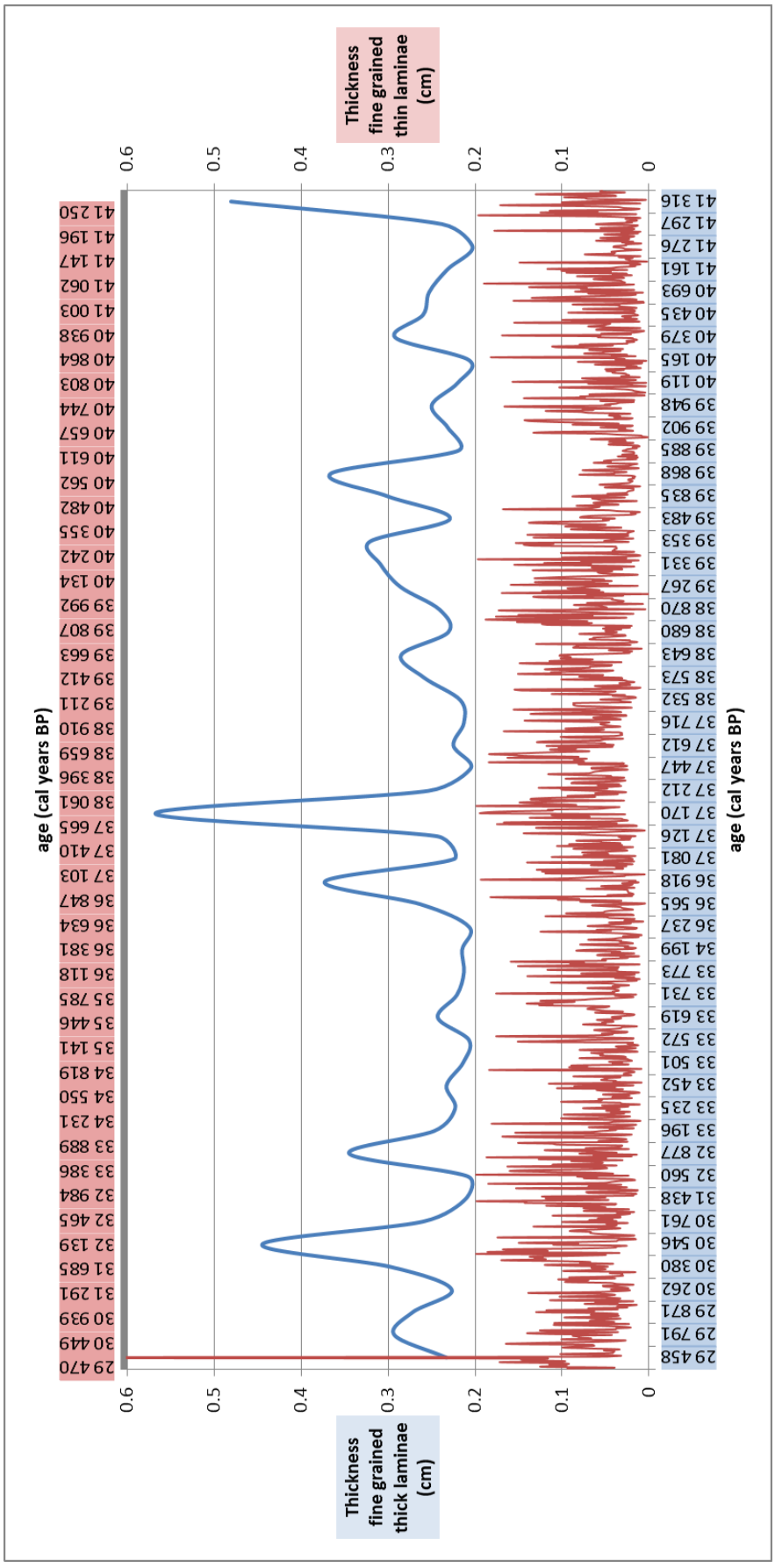

Fig. 40: The fine grained part of the whole record showing the thickness of the thick and thin laminae, within this fine grained part, separately

5.3 Image analysis of the laminated sediment

5.3.1 Computer analysis

The computer analysis data revealed some characteristics of the laminae. The computer measurements were performed from the bottom to the top of the core (PAR1A-III, PAR1A-IV and PAR1A-V), instead of from the top to the bottom as for the microscope measurements. The total amount of couplets obtained with the computer analysis is 1272, within a time span of 11906 years. The minimum thickness measured for the coarse grained laminae is 0.015 cm; the maximum thickness measured is 1.903 cm. The minimum thickness measured for the fine grained laminae is 0.008 cm; the maximum thickness measured is 0.44 cm. For the couplets, the minimum thickness is 0.034 cm; the maximum thickness is 2.076 cm.

5.3.1.1 Correlations and relationships between the data

The thickness of all the fine grained laminae and the thickness of all the coarse grained laminae show a very bad correlation (R^2= 0.0064). Furthermore, there is a data cluster within the region thickness below 0.3 cm. For one particular thickness of the coarse grained laminae, different thicknesses of fine grained laminae exist. The same is true for one particular thickness of the fine grained laminae. The red line drawn in Fig.41 at the base of the cluster of data points shows that all the fine grained laminae together have a minimum thickness. This minimum thickness moves to higher values when the thickness of the coarse grained laminae increases. Additionally, the yellow line drawn in Fig.41 shows that the minimum thickness of all the coarse grained laminae contains a constant value for different possible thicknesses of fine grained laminae.

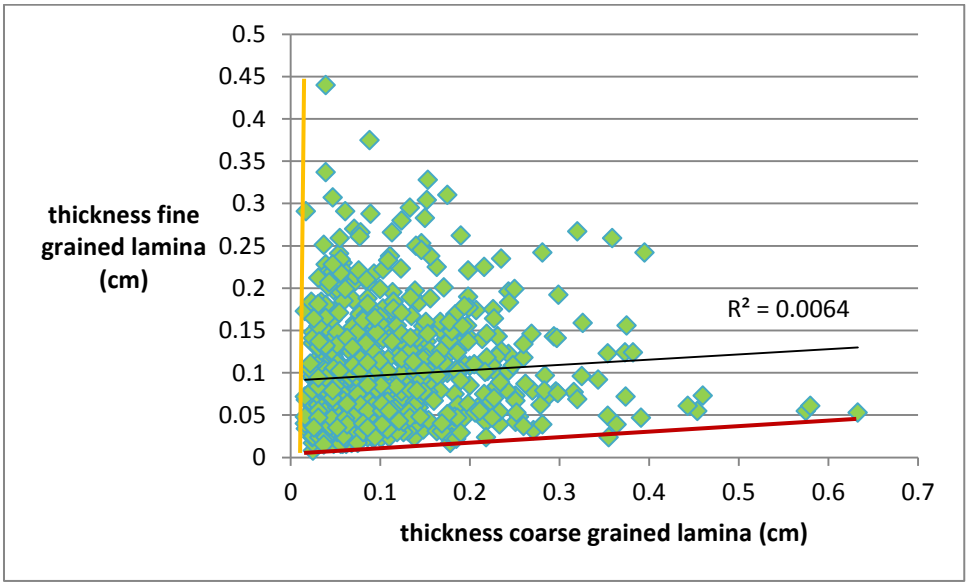

Fig. 41: Correlation between the thickness of all the fine and all the coarse grained lamina

A bad correlation (R^2= 0.3175) was found for the thickness of the couplets (thickness fine grained lamina + thickness coarse grained lamina) and the thickness of the fine grained laminae, but a good correlation of R^2= 0.7445 exists for the thickness of the couplets and the thickness of the coarse grained laminae (see Fig.42 and Fig.43).

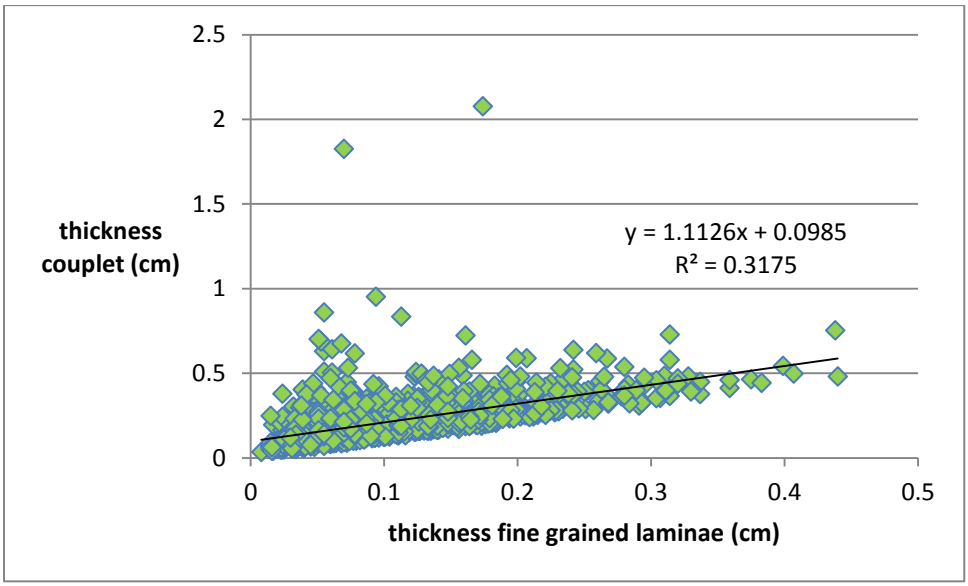

Fig. 42: Correlation between all the couplets and all the fine grained laminae

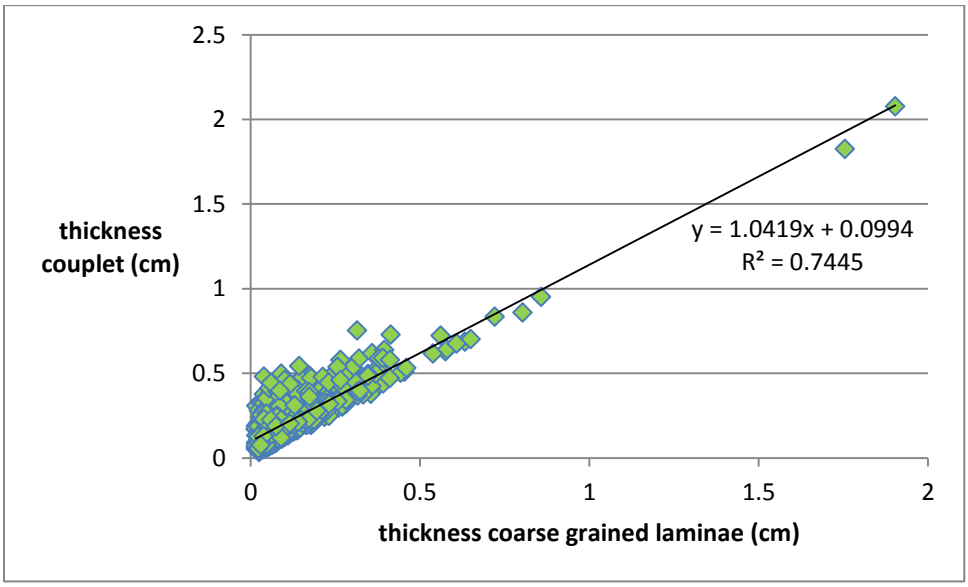

Fig. 43: Correlation between all the couplets and all the coarse grained laminae

In order to discuss the genesis and characteristics of the laminations, the laminae with the darkest appearance (further called: “low-lightness laminae”) were selected. These low-lightness laminae are the finest in grain size, determined from the results of the petrographic microscope observations. This selection was performed at sight, by using the digital images of the samples. There is a practical reason to perform the selection at sight. Using a color analysis requires that one should choose a certain lightness level below which the laminae appear to the human eye as having a very dark appearance. This can take some time to get results, whereas the human eye can select different grey values (or lightness-values) much faster. Also, laminae with a less dark appearance (further called: “intermediate-lightness laminae”) were selected. These are less fine grained than the low-lightness laminae, determined from the results of the microscope observations. These were then plotted against the thickness of their corresponding coarse grained laminae.

The results are shown in Fig.44, and Fig.45 is a zoom into the area of main difference within the graph of Fig.44. The low-lightness laminae have a higher minimum thickness than the intermediate-lightness laminae. However, both of the minimum thicknesses do not stay constant when the thickness of the coarse grained laminae rise. On the contrary, the coarse grained laminae show a constant minimum thickness. Not a single, good correlation was found between the thickness of the low-lightness laminae and the thickness of the intermediate-lightness laminae with the thickness of the coarse grained laminae. Furthermore, there were no correlations between the thickness of the low-lightness laminae and the thickness of the intermediate-lightness laminae with the couplet thickness.

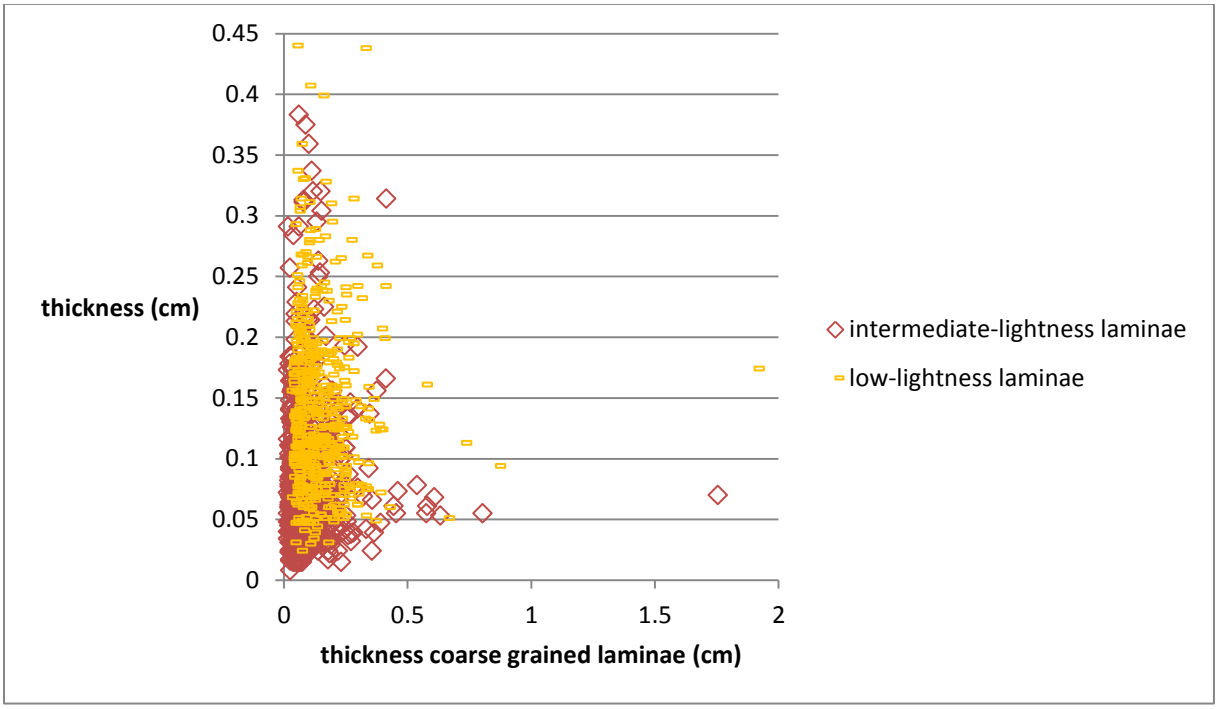

Fig. 44: comparison of the low-lightness and intermediate-lightness laminae, plotted against the thickness of their corresponding coarse grained laminae

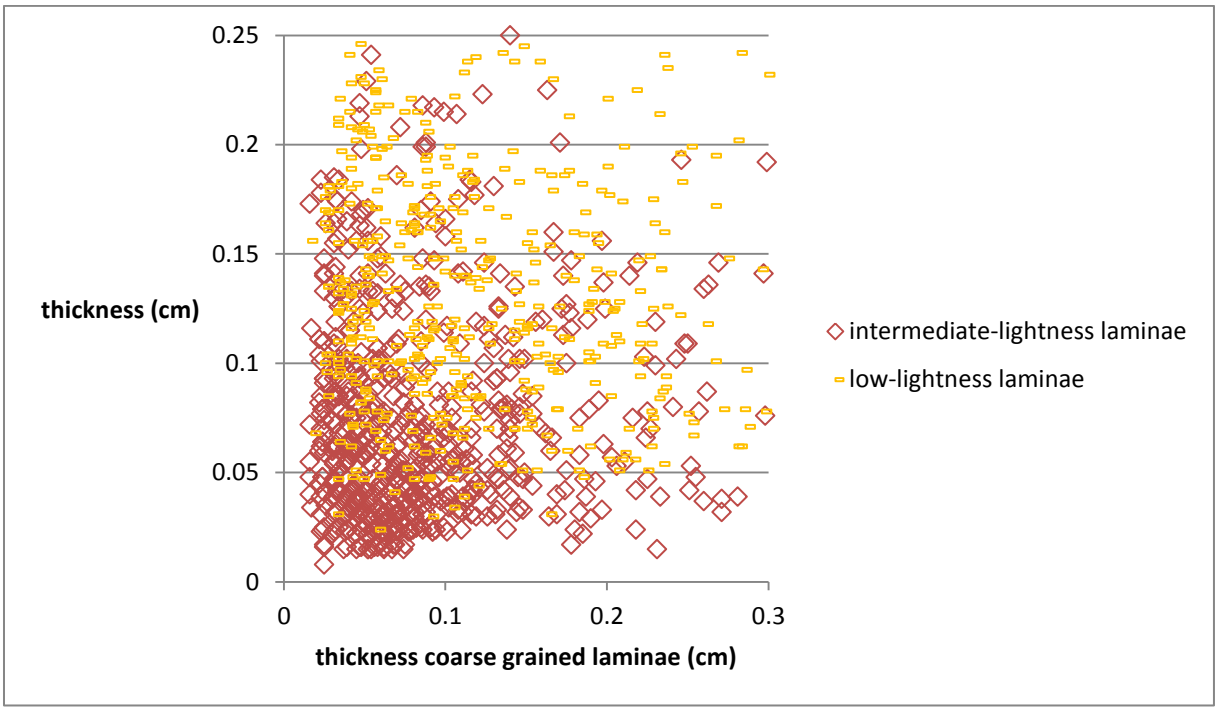

Fig. 45: Zoom of the graph in Fig.44

From the low-lightness laminae, the thickest laminations were selected, with a thickness between 0.2 and 0.5 cm. For each of these the corresponding coarse laminae were selected, as well as the couplet thickness. The sum of the thickness of all the intermediate-lightness laminae and all the coarse grained laminae, lying in between the low-lightness laminae, was calculated. However, only very poor correlations were found between the total thickness of the selected intermediate-lightness laminae and the total thickness of the selected coarse grained laminae with the low-lightness laminae (see Fig.46 for an example). The same weak correlations are obtained when we consider all the low-lightness laminae, instead of only the thickest.

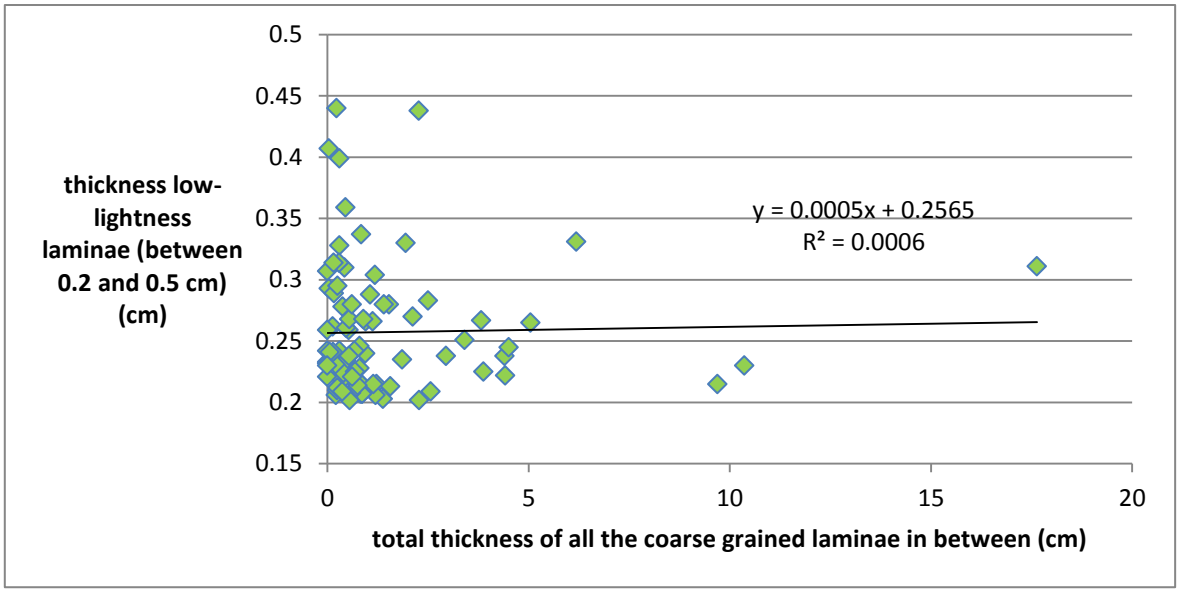

Fig. 46: the thickness of the thickest low-lightness laminae and the total thickness of the coarse grained laminae in between them

5.3.1.2 Variations through time

A moving average with a subset size of 4 for the couplet thickness, the thickness of all the fine grained laminae, and the thickness of all the coarse grained laminae, was calculated. The couplet thickness, the thickness of all the fine grained laminae, and the thickness of all the coarse grained laminae were then plotted against a time axis.

Comparing the variations in thickness of the couplets with the variations in thickness of all the fine grained laminae (see Fig.47), it becomes clear that they mostly differ in peak height. However, for example at 33669 cal. years BP, 34076 cal. years BP, and 36240 cal. years BP the peaks are almost as high. As mentioned above, the correlation of the thickness of all the fine grained laminae thickness and the couplet thickness was weak, with R^2= 0.3175. In Fig.48, the variations in thickness of all the coarse grained laminae and the variations in couplet thickness are compared, and they demonstrate that they follow each other more closely in peak height.

The couplet thickness variations reveal some very clear (high) peaks at 37429 cal. years BP (within interval C, see Fig.47, 48 and 49) and some at 31766 cal. years BP, 31267 cal. years BP, 30404 cal. years BP, and 29952 cal. years BP (within interval A; these peaks are made clear in Fig.47, Fig.48 and Fig.49 with purple stars). From young to old, the following intervals were found:

Interval A demonstrates some peaks of opposite direction when the couplet thickness variations are compared with the variations in thickness of all the fine grained laminae, or when the coarse grained

and fine grained laminae thickness variations are compared with each other. The couplet thickness variations and the thickness variations of the coarse grained laminae follow each other well in peak height.

Interval B shows that the peak heights of the fine grained laminae follow the couplet thickness peaks better than the peak heights of the coarse grained laminae, which becomes clear when comparing the fine grained and coarse grained laminae.

Within interval C, the coarse grained laminae peaks follow strongly the couplet peaks, whereas the fine grained laminae peaks are lower. Only around 37066 cal. years BP are both the coarse grained laminae peaks and the fine grained laminae peaks as high.

Interval D is expressed by a very strong connection in peak height between the fine grained laminae and the coarse grained laminae. Solely for the two distinct couplet peaks at 38368 and 38874 cal. years BP do the coarse grained laminae peaks come closer to the couplet peak height than do the fine grained laminae peaks.

Finally, interval E also exhibits good peak height similarities between the coarse grained and fine grained laminae. However, it is less good than in interval D, since at some places the fine grained laminae peaks are much lower than the couplet thickness peaks.

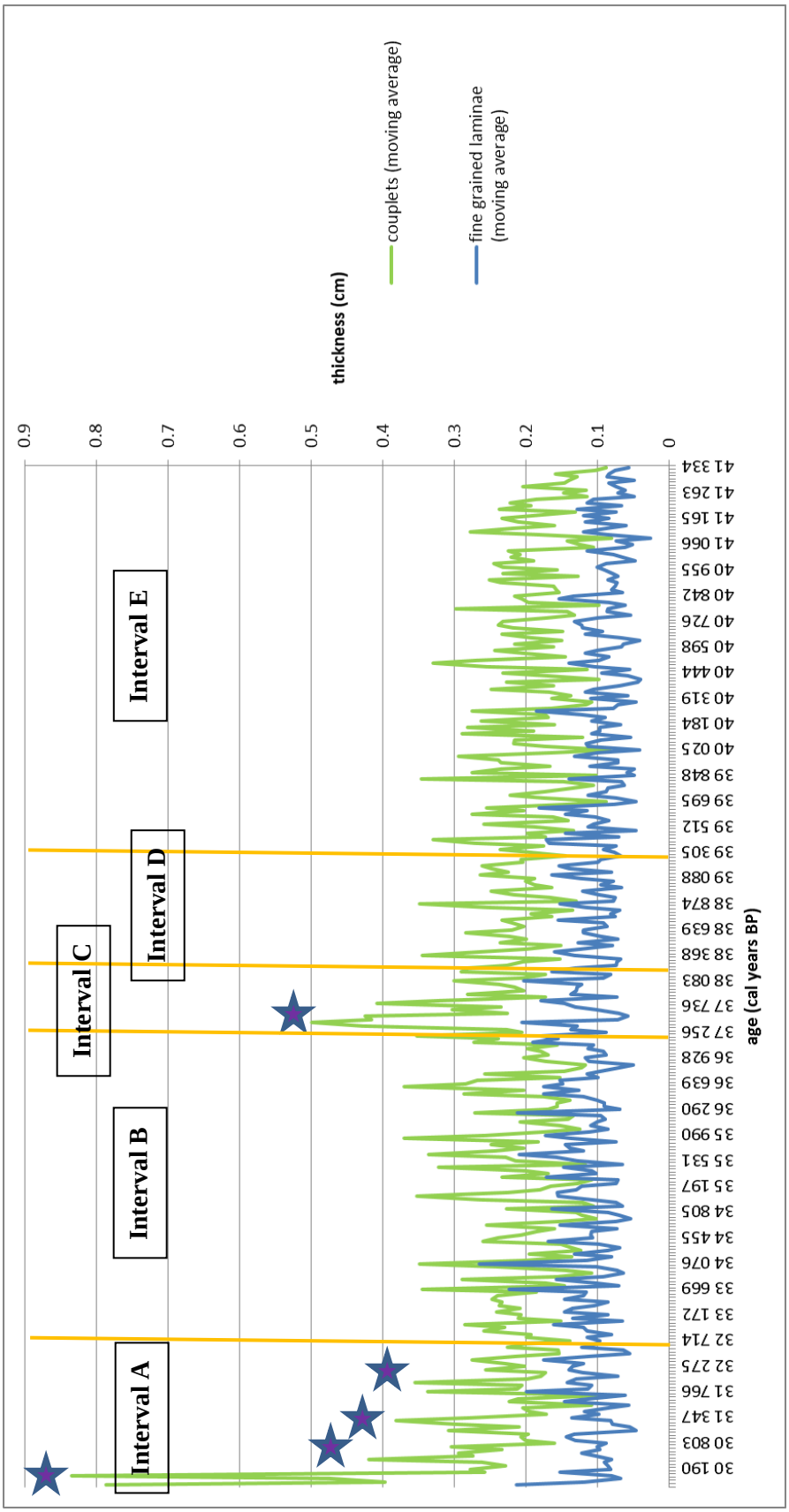

Fig. 47: couplet thickness and thickness of all the fine grained laminae (moving average with subset size 4)

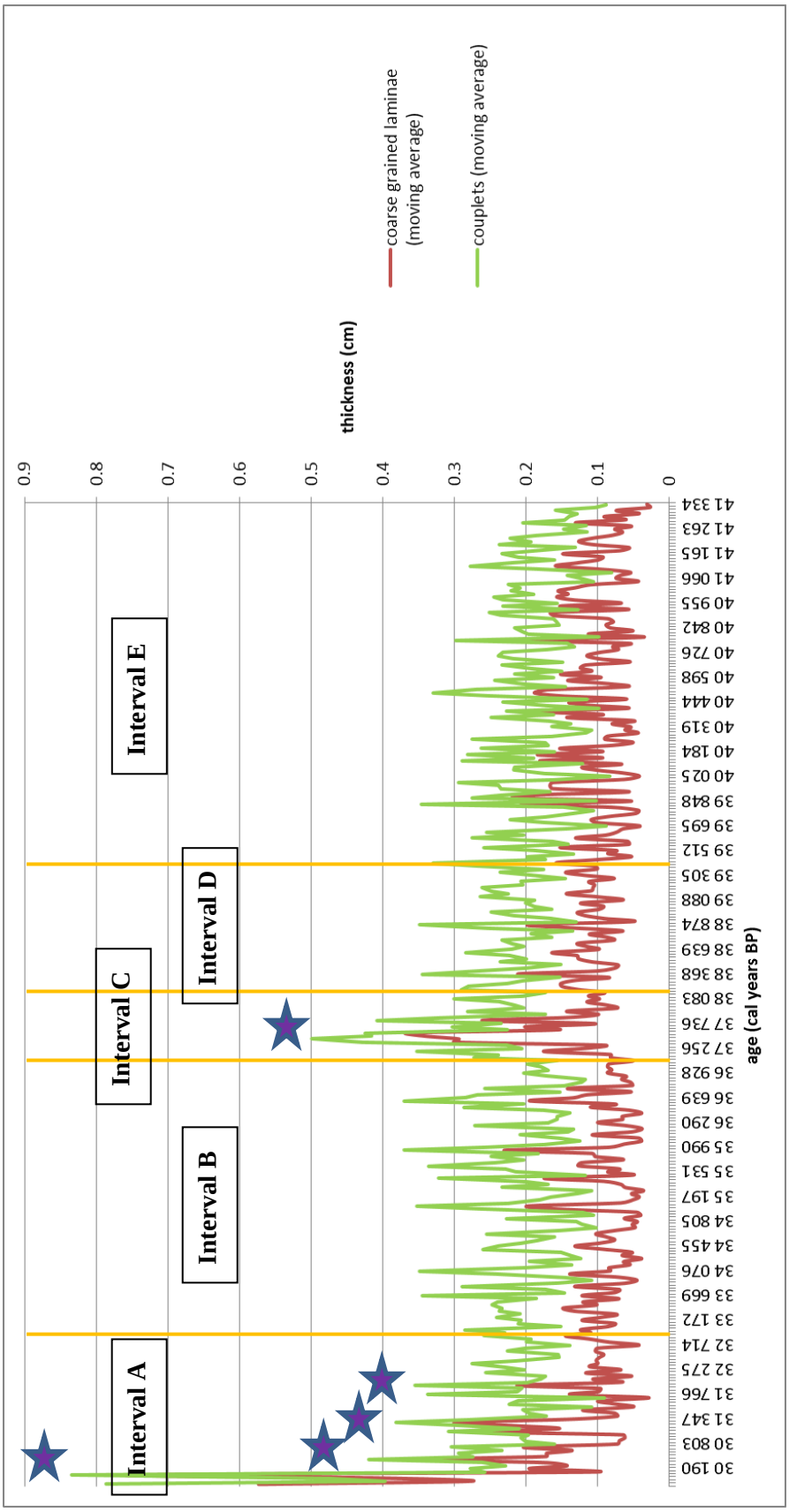

Fig. 48: couplet thickness and thickness of all the coarse grained laminae (moving average with subset size 4)

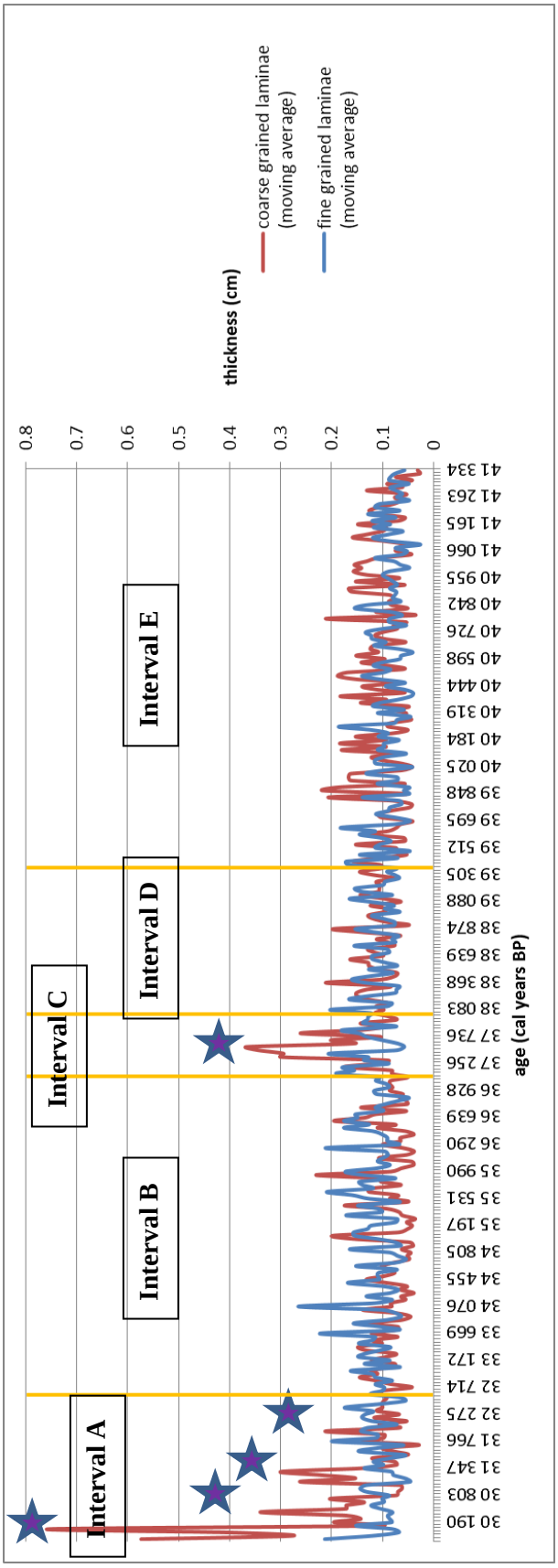

Fig. 49: : thickness of all the fine grained and all the coarse grained laminae (moving average with a subset size of 4)

For all the fine grained laminae, all the coarse grained laminae and the couplet thicknesses, as well as for the corresponding a ges, moving averages with a subset size of 10 and 7 were calculated. For the thickness of the intermediate-lightness laminae and the low-lightness laminae, as well as for their corresponding ages, moving averages with a subset size of 4 were calculated. All of these laminae are compared in Fig.50 and Fig.51, using the same division in intervals (A to E) as for Fig.47, Fig.48 and Fig.49.

At 37429 cal. years BP (i.e. the couplet peak within interval C), there is not only an increase in the importance of the thickness of the coarse grained laminations in the core, but also of the low-lightness laminae, which have a grain size fraction between <0.01 and 0.01 mm. Also, the couplet peaks within interval E in Fig.50 and Fig.51 show higher values for the coarse grained laminae thickness. The low-lightness laminae also show some higher peaks, but these are less pronounced than the one in interval C. The intermediate-lightness laminae do not show pronounced changes in thickness. They follow more or less the same pattern as the fine grained laminae thickness.

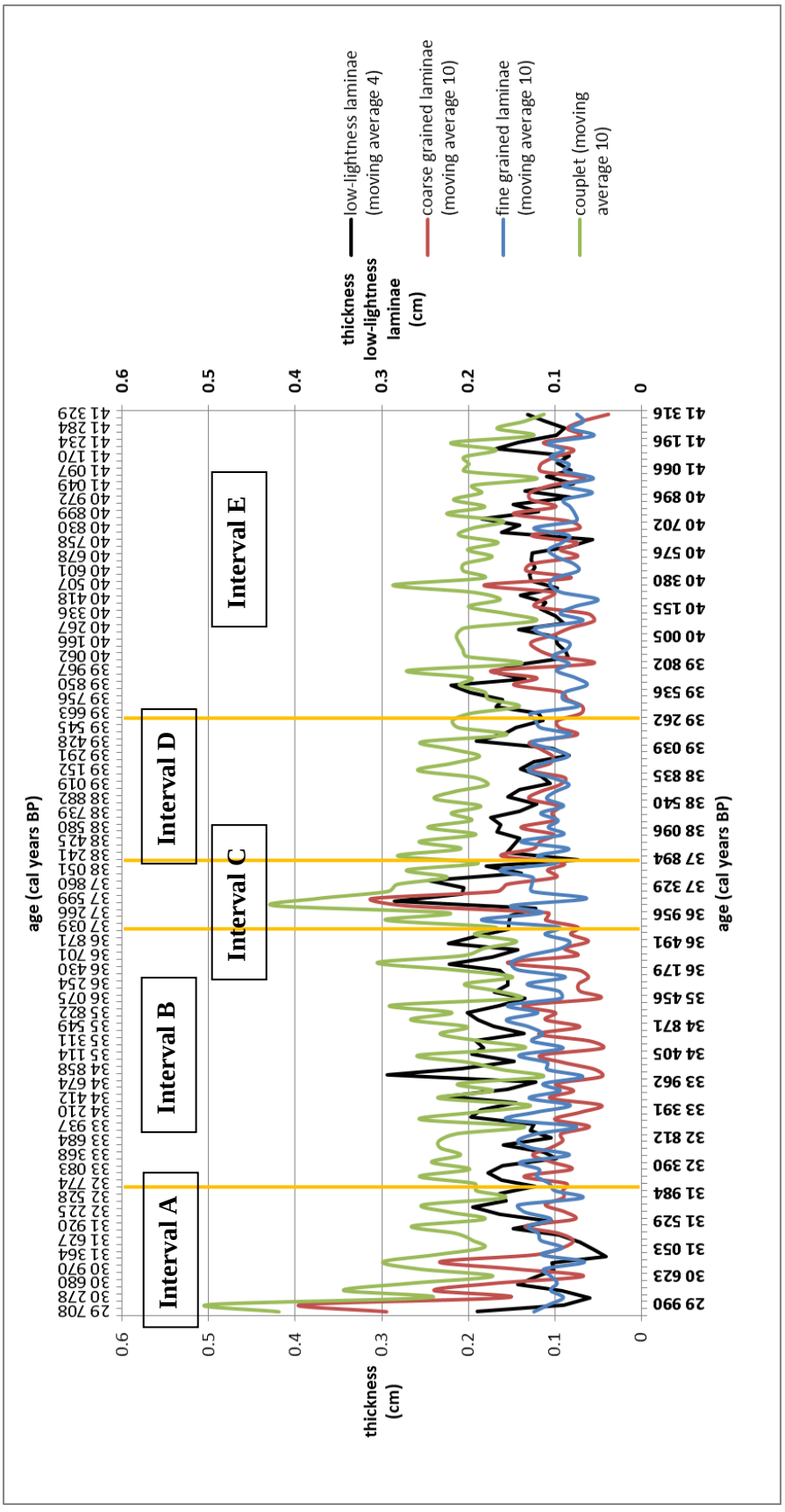

Fig. 50: comparison of all the low-lightness laminae with all the couplets, all fine grained and all coarse grained laminae against a time axis

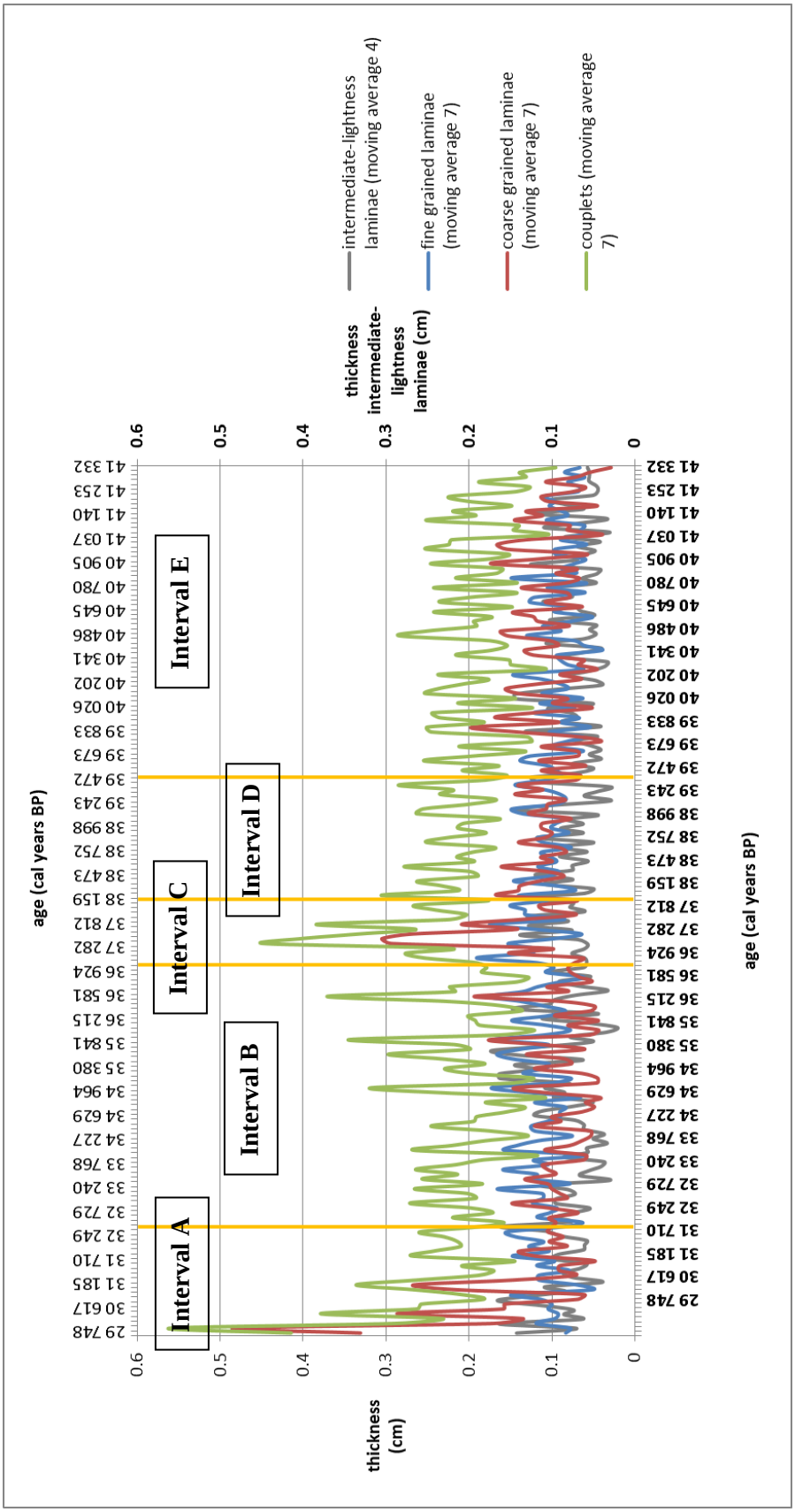

Fig. 51: comparison of all the intermediate-lightness laminae with all the couplets, all fine grained and all coarse grained laminae against a time axis

In Fig.52, the low-lightness laminae and the intermediate-lightness laminae are compared. The intermediate-lightness laminae fluctuate mostly within a thickness of 0.05 and 0.15 cm, only five peaks are higher than 0.15 cm. This occurs at: 30083, 30905, 33013, 35616 and 35995 cal. years BP. The low-lightness laminae fluctuate between a thickness of 0.05 and 0.3 cm, and show some very distinct high peaks, clustering in groups of two or three peaks. Peaks higher than 0.25 cm occur at 34083 and 37121 cal. years BP. Some other peaks are higher than 0.2 cm: at 33689, 36234, 36491, 37502 and 39608 cal. years BP.

Between 33000 and 40000 cal. years BP, the low-lightness laminae differ the most in thickness from the intermediate-lightness laminae. Within this interval, the low-lightness peaks reach a thickness above 0.2 cm or 0.15 cm, whereas the intermediate-lightness laminae fluctuate between a thickness of 0.05 and 0.15, with some events depicting a fluctuation between a thickness of 0.05 and 0.1 cm. The intermediate-lightness and low-lightness laminae differ the least within the interval from 29549 to 33000 cal. years BP and within the interval from 40000 to 41316 cal. years BP, where they fluctuate both between a thickness of 0.05-0.2 cm and 0.05-0.15 cm, respectively. However, from around 41000 cal. years BP, the low-lightness laminae, which start to peak above 0.15 cm, and the intermediate-lightness laminae seem to start differing from each other again.

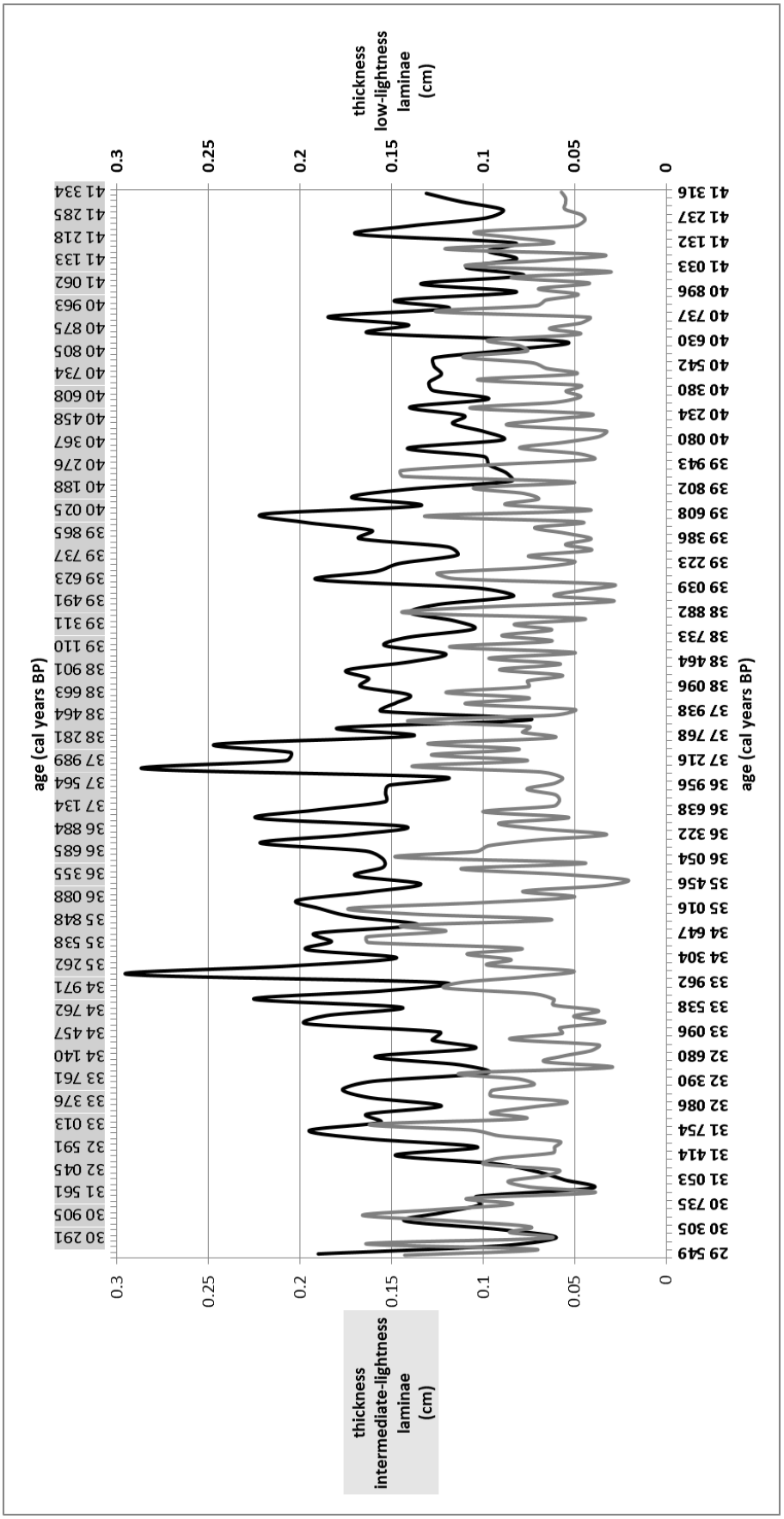

Fig. 52: the thickness variations of the low-lightness laminae and the intermediate-lightness laminae (moving average with subset size 4) against a time axis

5.3.2 Color analysis

5.3.2.1 Results from the Lab color space analysis of the record

Fig.53, 54 and 55 show the results of the color analysis performed on the cores PAR1A-III, PAR1A-IV and PAR1A-V, plotted against a time axis. The L-value peaks and the b-value peaks are of the same direction, whereas the a-value peaks have an opposite direction. We further analyzed the L, a and b color values. The L-value was split up in three components, the a-value and the b-value each in two components.

If the a-value is negative, then the color moves more towards the green side, when the a-value is positive, then the color moves more towards the magenta side of the a-axis of the 3D color space. Negative b-values correspond to a more blue color, positive b-values correspond to the more yellow side of the b-axis. For the L-value, a certain boundary had to be chosen within which a data point could be identified as having a high-lightness and others as having a lower lightness. Therefore, a boundary value of 28 was selected. Every L-value larger or equal to 28 will be evaluated as having a high-lightness, L-values smaller than 28 will be evaluated as having a lower-lightness. For the lower lightness part, an extra division was made between "low-lightness" and "intermediate-lightness". Every point in the dataset with a L-value larger or equal to 20, but lower than 28, was appointed to have an intermediate-lightness.

It was noticed that only a few points in the whole core (PAR1A-III, PAR1A-IV and PAR1A-V) had a green color combined with yellow. Additionally, these colors seemed to combine dominantly with a high-lightness, a few combined with the intermediate-lightness, and only one with a low-lightness (see Fig.57 and Fig.58). Most parts of the whole record showed a-values and b-values that were expressed in blue and magenta as colors, and these dominantly combined with a lower-lightness, being "intermediate" or "low" (see Fig.56).

In Fig.58, two high peaks for the yellow b-value can be observed. The green a-value shows peaks at the same or almost the same place, but of an opposite direction (as discussed in the beginning of this section). The yellow b-value shows a high peak at 31681 cal. years BP. The green a-value peaks at 32411 cal. years BP. Another high peak for the yellow b-value occurs at 40169 cal. years BP, corresponding with a lower (and opposite direction) peak for the green a-value. Whereas the opposite is true at 39468 cal. years BP, where the green a-value peak is higher (but still with an opposite direction) than the yellow b-value peak at that age. Several other, but smaller peaks, can be recognized for both the green a-value and yellow b-value. For the magenta a-values and blue b-values in Fig.56,

no recognizable features were found, except maybe between 38000 and 41000 cal. years BP, where the L, a and b-value peaks overlap each other.

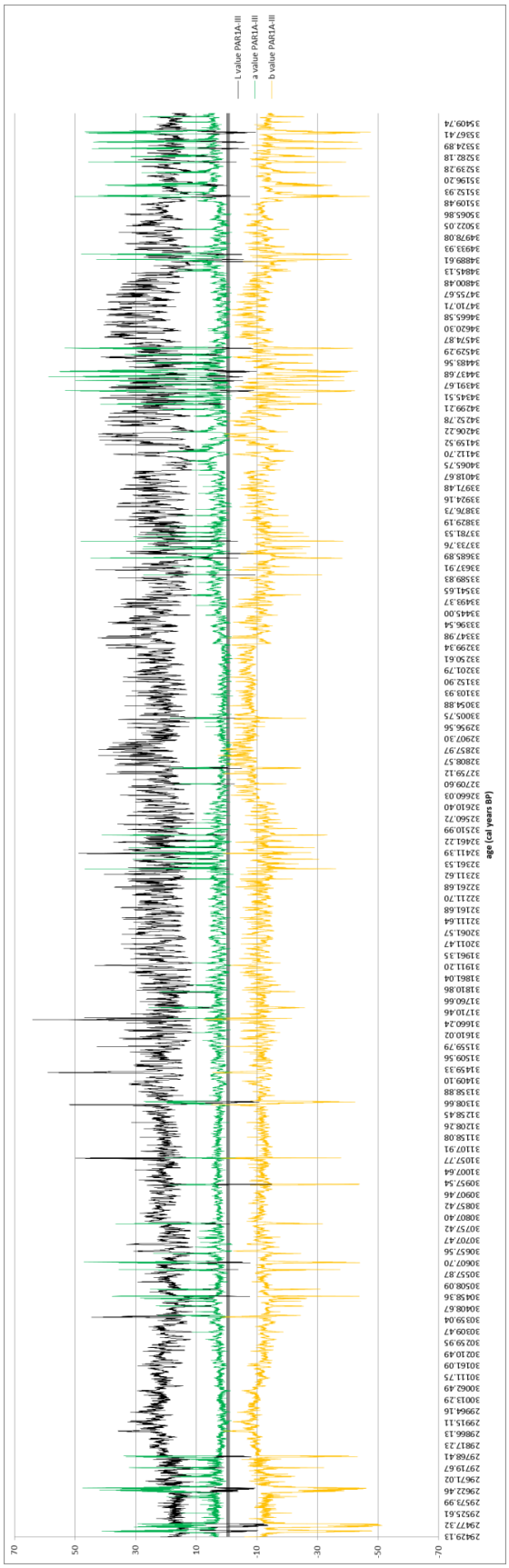

Fig. 53: Color analysis on PAR1A-III; L, a and b-values shown

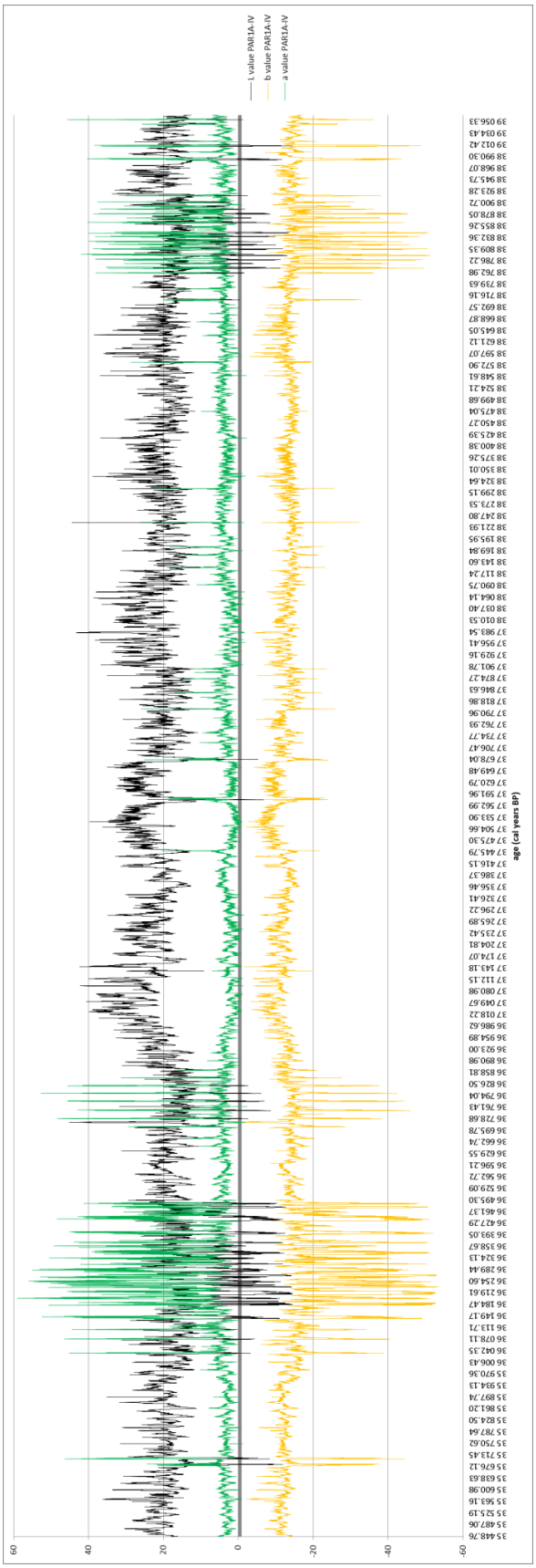

Fig. 54: Color analysis on PAR1A-IV; L, a, and b-values shown

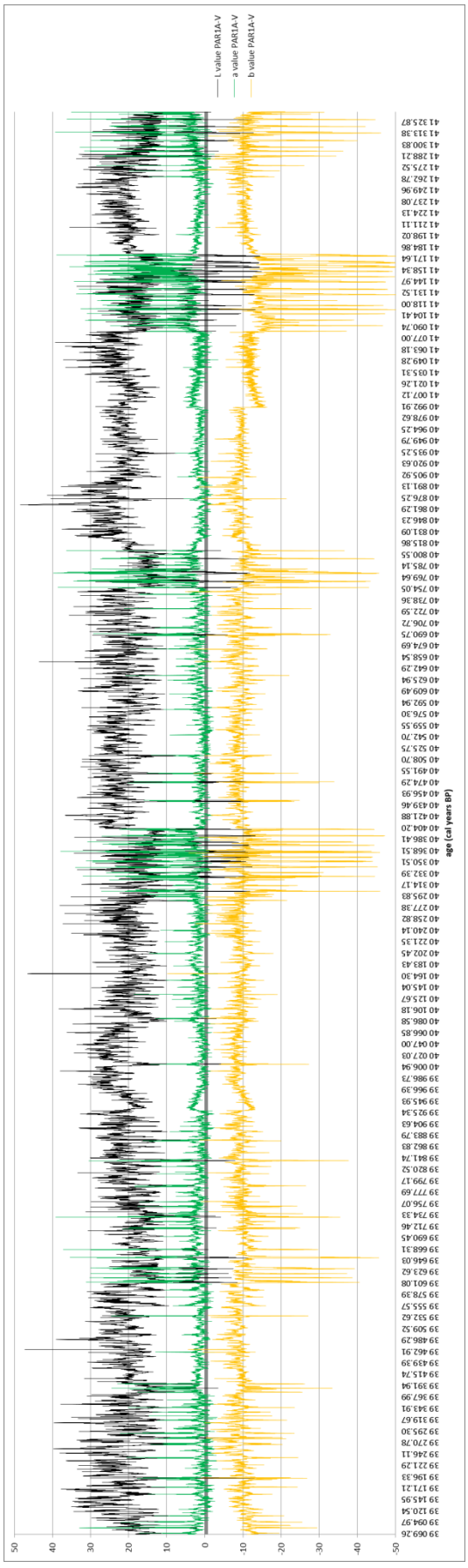

Fig. 55: Color analysis on PAR1A-V; L, a and b-values shown

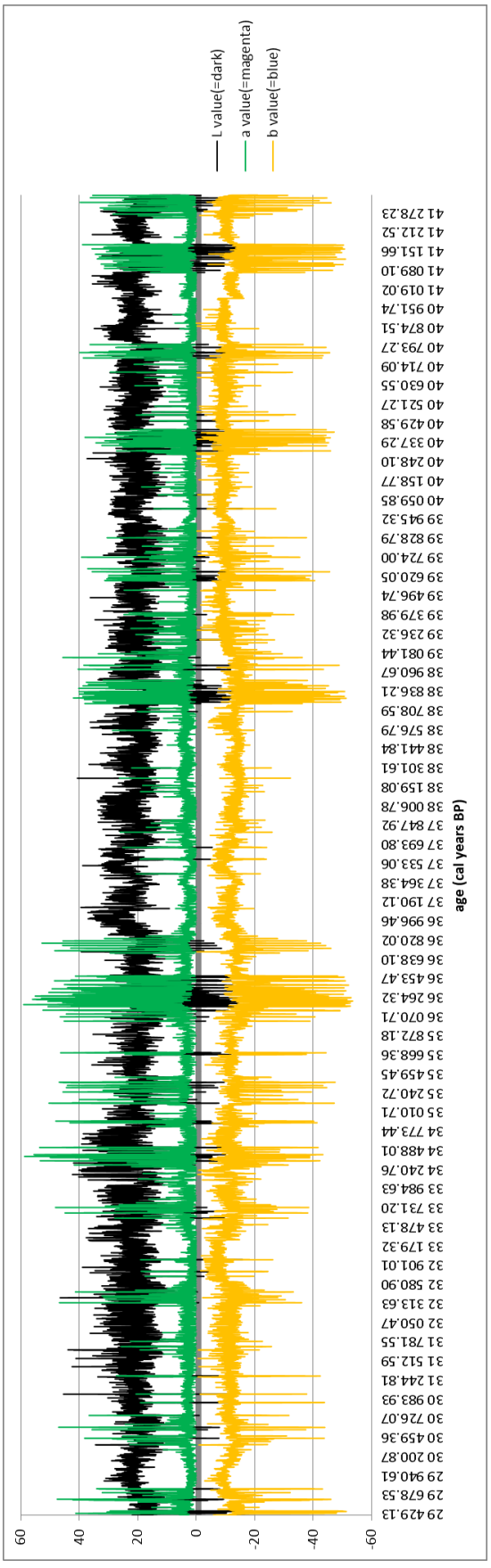

Fig. 56: PAR1A-III, PAR1A-IV and PAR1A-V with magenta and blue as selected a-values and b-values (L, a, and b-values shown)

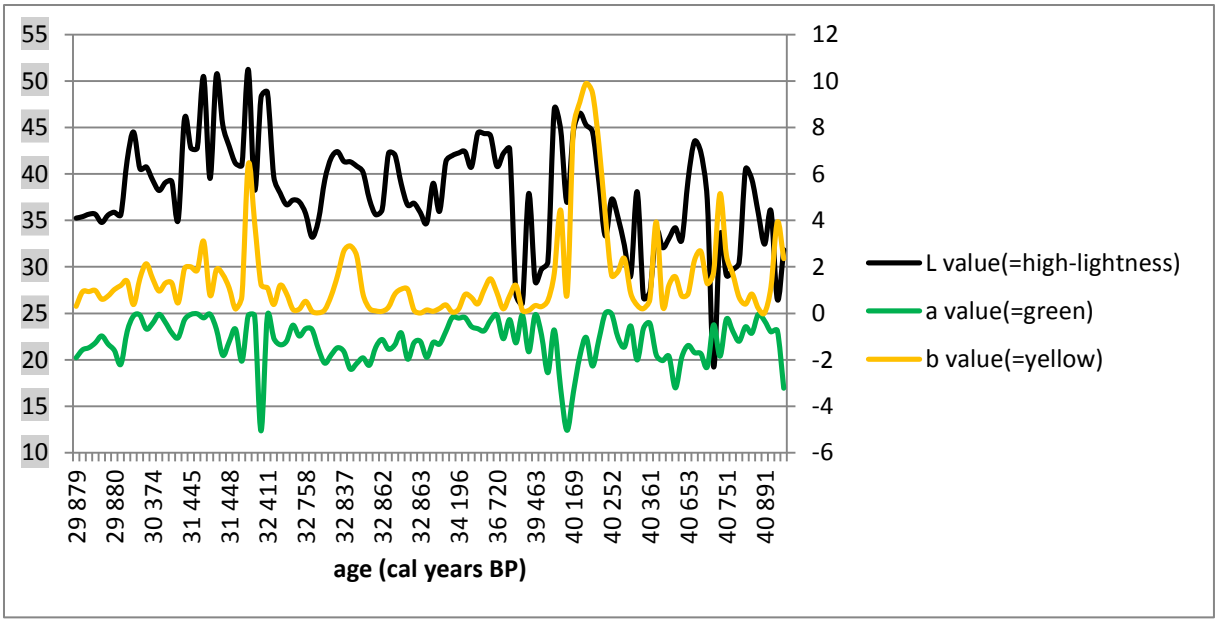

Fig. 57: PAR1A-III, PAR1A-IV and PAR1A-V with green and yellow as selected a-values and b-values (L, a and b shown)

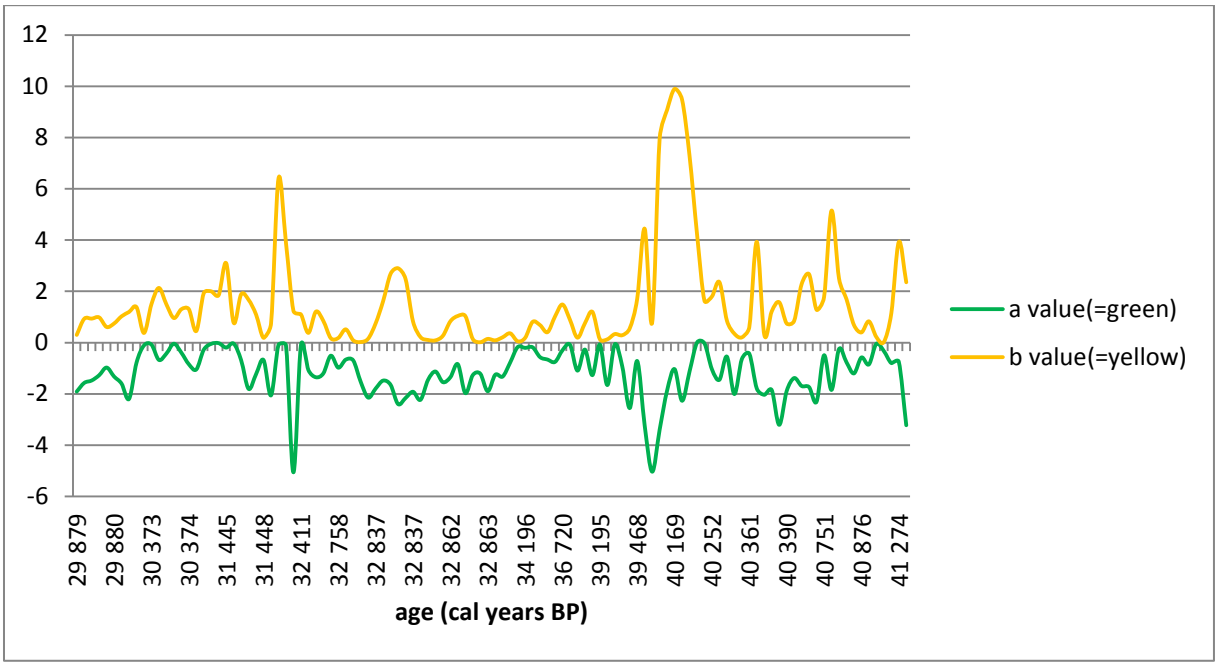

Fig. 58: PAR1A-III, PAR1A-IV and PAR1A-V with green and yellow as selected a-values and b-values (a and b shown)

5.3.2.2 Spectral analysis on the color analysis dataset

The spectral analysis was only performed on the color analysis dataset. A linear interpolation was carried out in between the data points for which we had age information. For the color analysis dataset, this resulted in gradual changes in the age from one data point to the next one. However, for the datasets from the microscope analysis and computer analysis, the age data did not vary gradually after the linear interpolation was performed, but in too large jumps. The program XLSTAT cannot perform a spectral analysis when this is the case.

5.3.2.3 Spectral analysis: results for the L-value

A frequency interval between 0.001 and 0.1 cycles/year was chosen, because, firstly, the largest relevant cycle that can be seen on the results from the color analysis (see section 5.3.2.1) is around 1000 years. Secondly, the amount of detail that is visible in the frequency graph gets lost if an interval that is too large is chosen (see Fig.59 and Fig.60). However, the cycles will be selected from the period graph (see Fig.61) showing a period interval between 0 and 1000 years. To have a better view on the smaller cycles, a period interval between 30 to 100 years (see Fig.62) and a period interval between 0 to 30 years (see Fig.63) were also displayed.

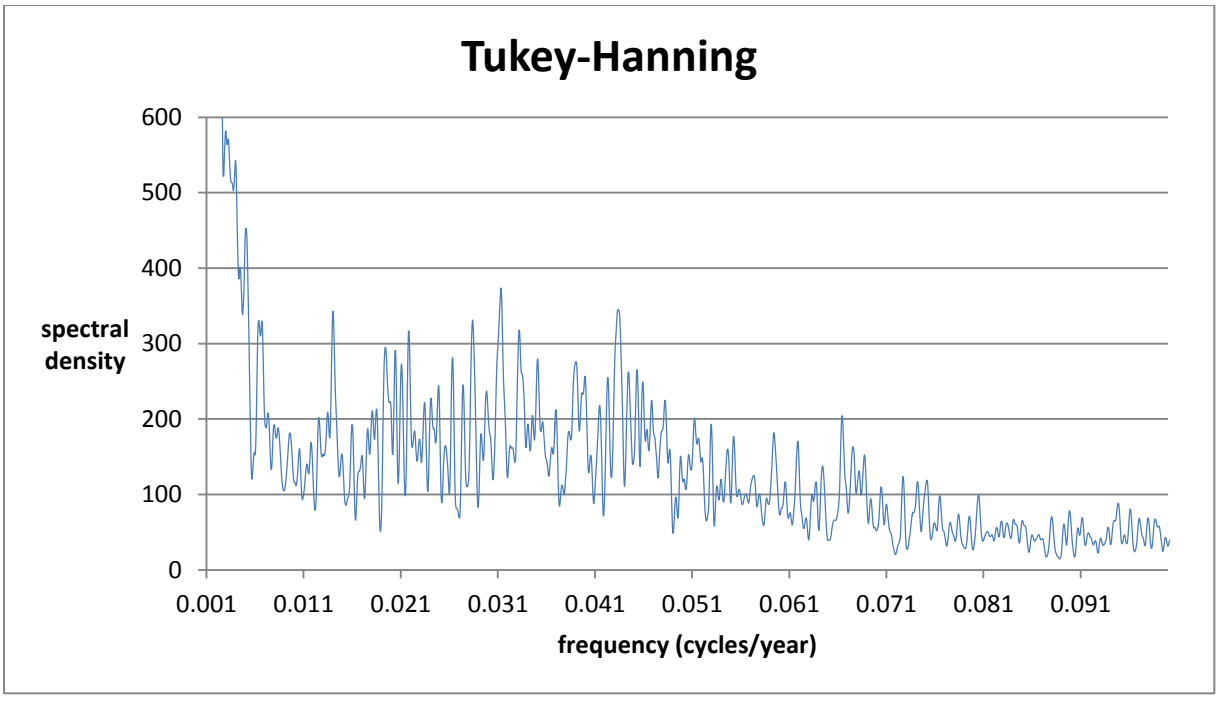

Fig. 59: Tukey-Hanning spectral analysis on the L-value: spectral density against frequency (interval 0.001-0.1 cycles/year)

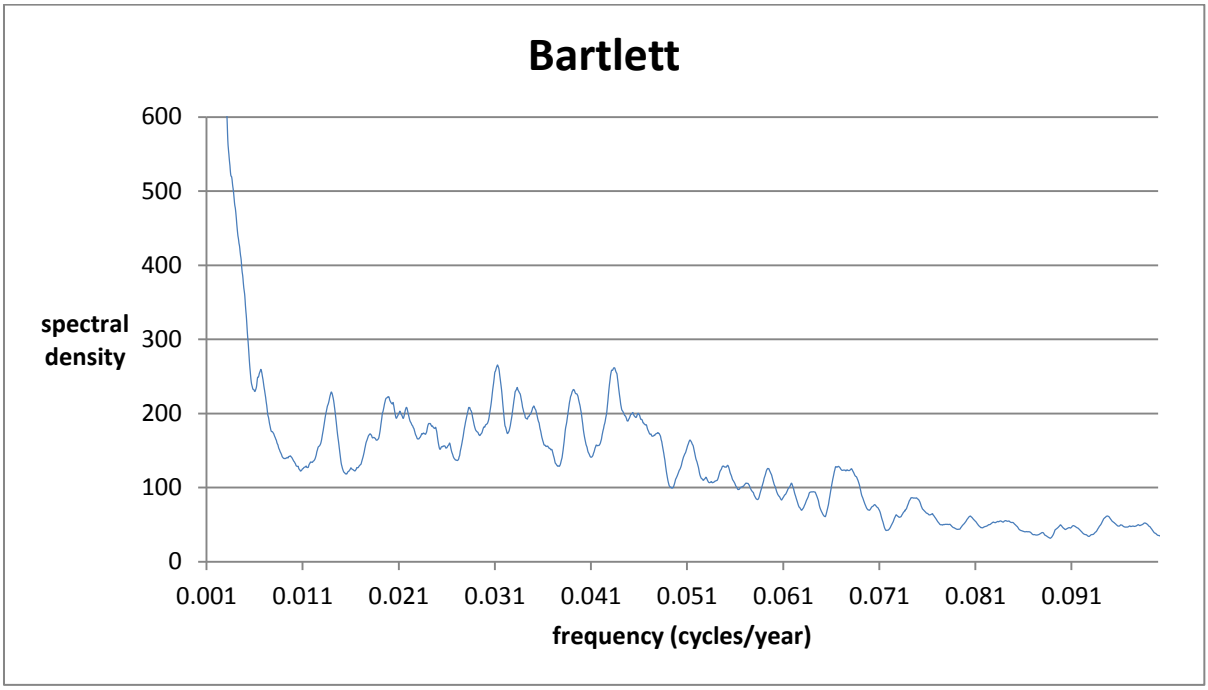

Fig. 60: Bartlett spectral analysis on the L-value: spectral density against frequency (interval 0.001-0.1 cycles/year)

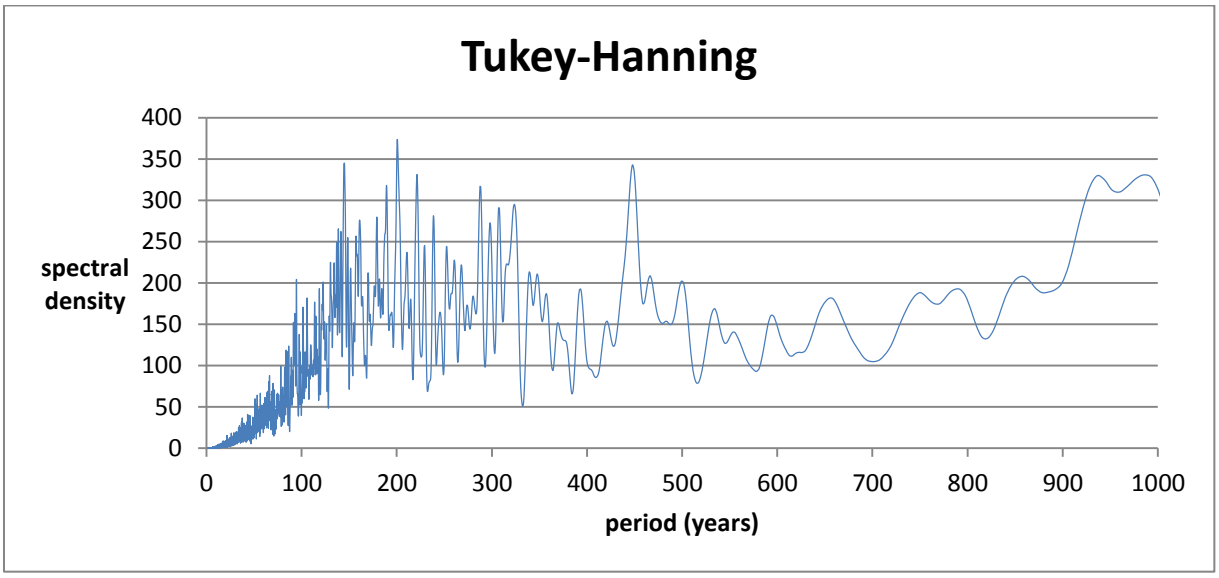

Fig. 61: Tukey-Hanning spectral analysis on the L-value: spectral density against period (interval (0-1000 years)

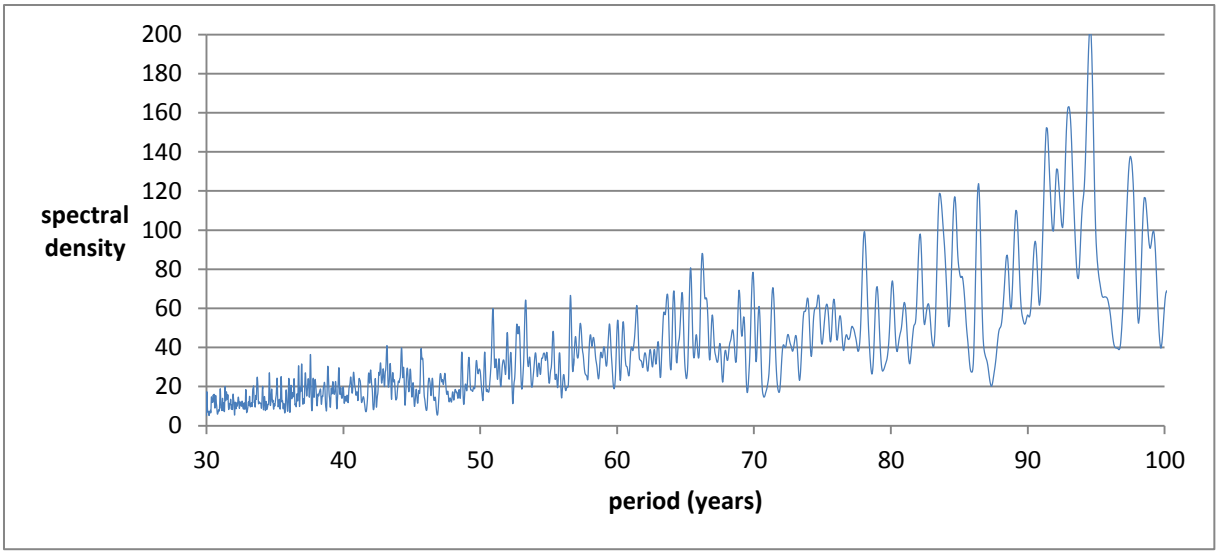

Fig. 62: Zoom of Fig.43, period between 30 and 100 years (Tukey-Hanning)

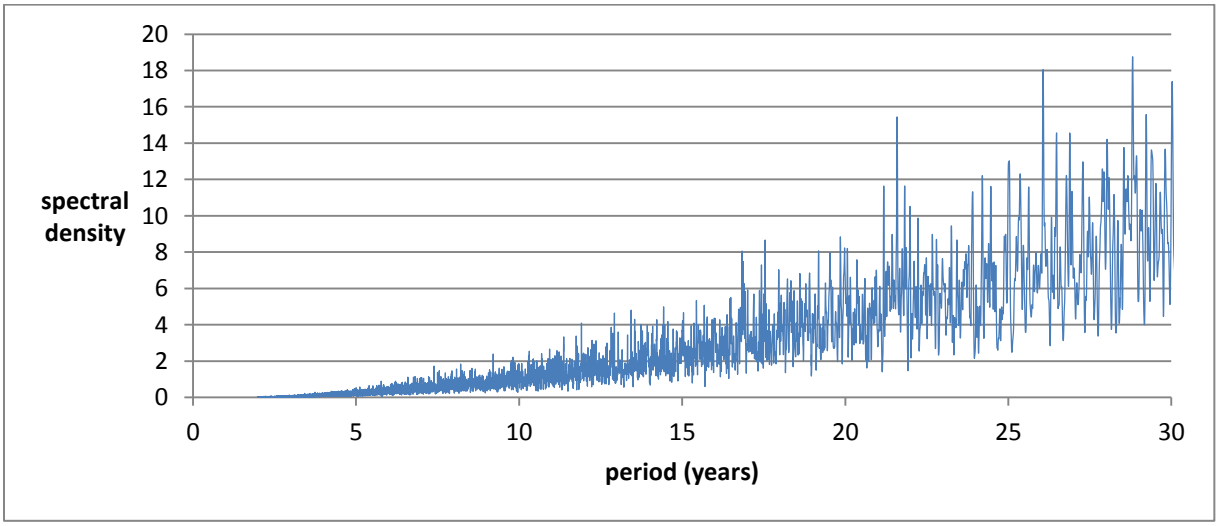

Fig. 63: Zoom of Fig.43, period between 0 and 30 years (Tukey-Hanning)

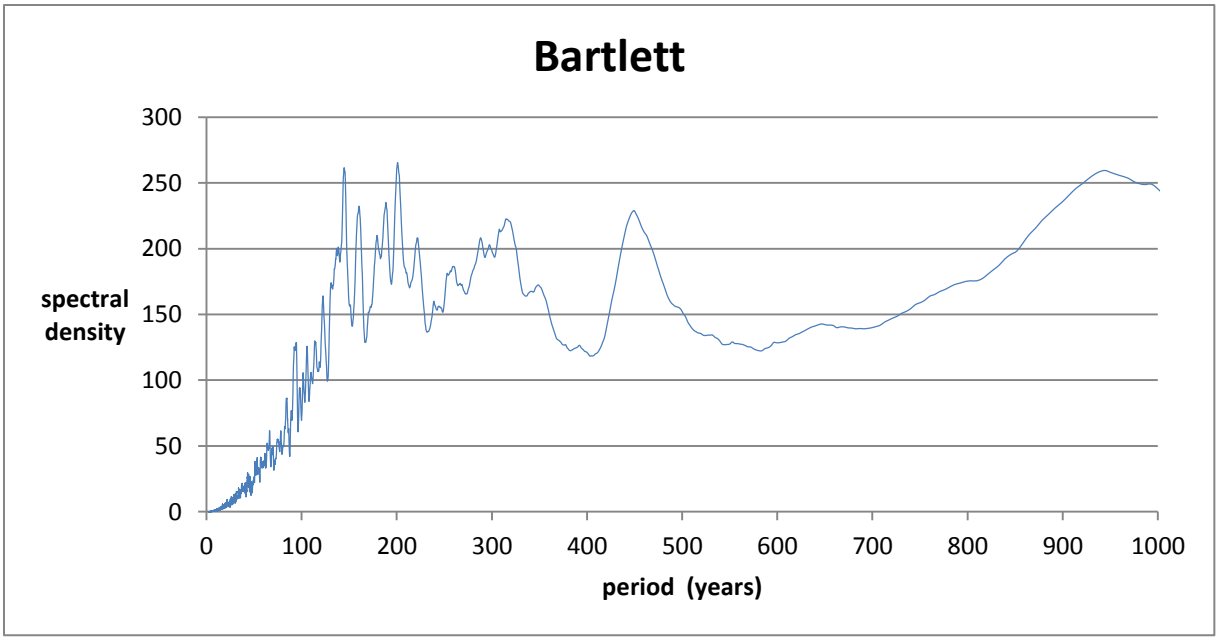

Fig. 64: Bartlett spectral analysis on the L-value: spectral density against period (interval 0-1000 years)

From Fig.61, with a period interval between 100 and 1000 years, some apparent important cycles could be selected above a spectral density of 150. Cycles of 145-146, 162, 187, 190, 202, 211, 222, 229, 239, 260, 267, 269, 288, 298, 308, 325, 348-349, 359, 393, 450, 468, 501, 537, 596, 658, 755, 792, 865, and 994 years were found.

For the interval between 30 and 100 years (Fig.62), from which cycles were selected above a spectral density of 20, the following cycles were obtained: 37-40, 40-50, 50-60, 60-70, 70-80, 80-90, and 90-100 years. The zoom into the interval between 0 and 30 years (Fig.63) yielded cycles of 17, 18, 20, 22, 24, 25, 27, and 28 years (above a spectral density of 2).

5.3.2.4 Spectral analysis: results for the a-value

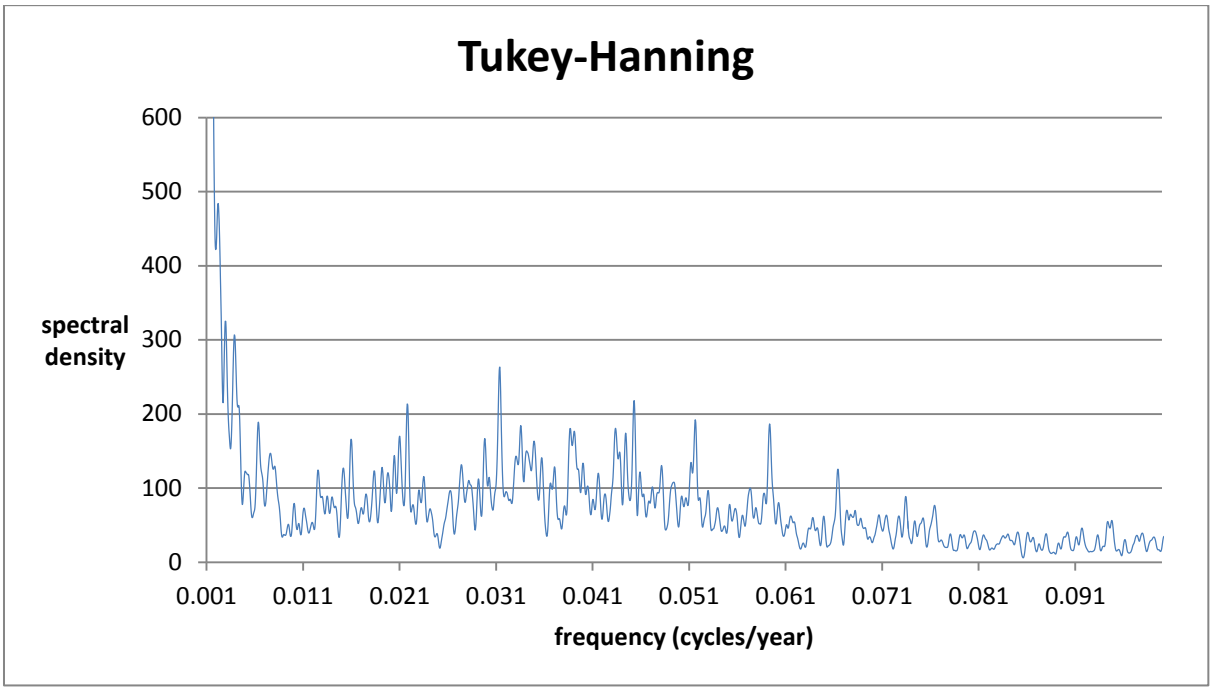

Fig. 65: Tukey-Hanning spectral analysis on the a-value: spectral density against frequency (interval 0.001-0.1 cycles/year)

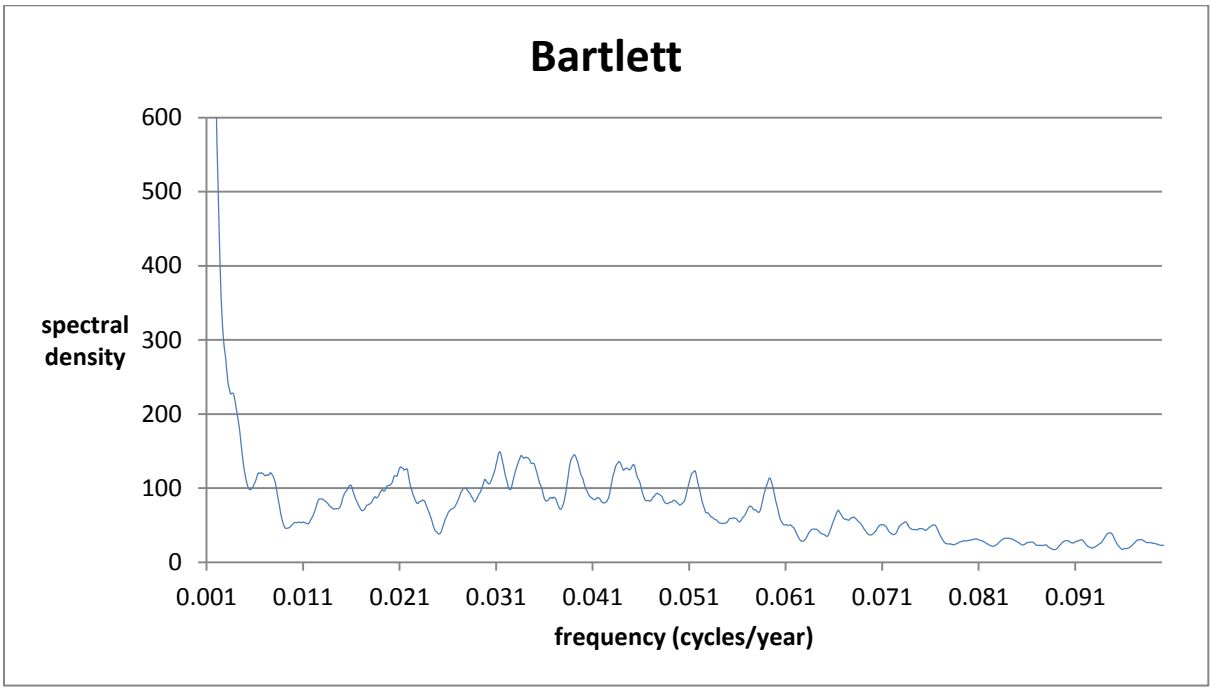

Fig. 66: Bartlett spectral analysis on the a-value: spectral density against frequency (interval 0.001-0.1 cycles/year)

For the period interval between 100 and 1000 years, the Tukey-Hanning spectral analysis on the a-value yielded several cycles. As many apparent important cycles above a spectral density of 100 were selected. The following cycles were extracted: 106, 122, 145, 163, 190-199, 201, 211, 230, 268, 289, 301, 308, 328, 343, 395, 417, 504, 787, 833, and 994 years (see Fig.67). For the period interval between 30 and 100 years, cycles above a spectral density of 20 were selected. The following cycles were obtained: 35, 41, 43, 52-54, 56-58, 60-70, 70-80, 80-90, and 90-100 years (see Fig.68). For the smallest cycles, selected above a spectral density of 2, cycles of 10, 13, 14, 17, 18-20, 21-23, and 26-29 years were found (see Fig.69).

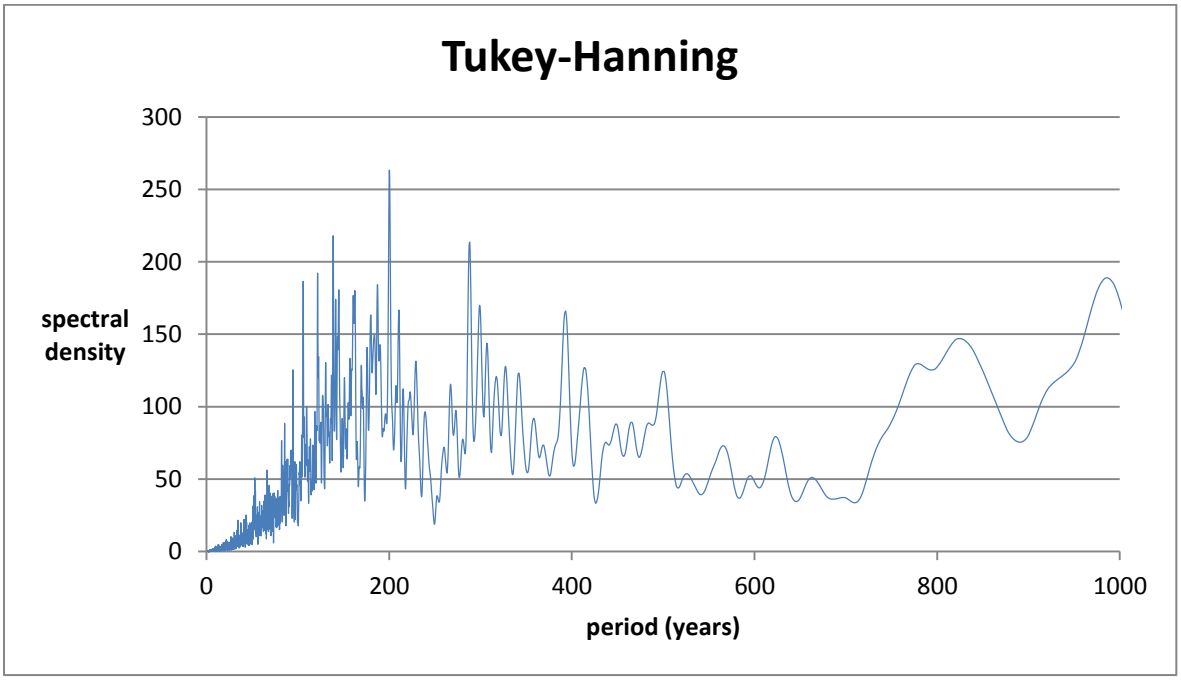

Fig. 67: Tukey-Hanning spectral analysis on the a-value: spectral density against period (interval 0-1000 years)

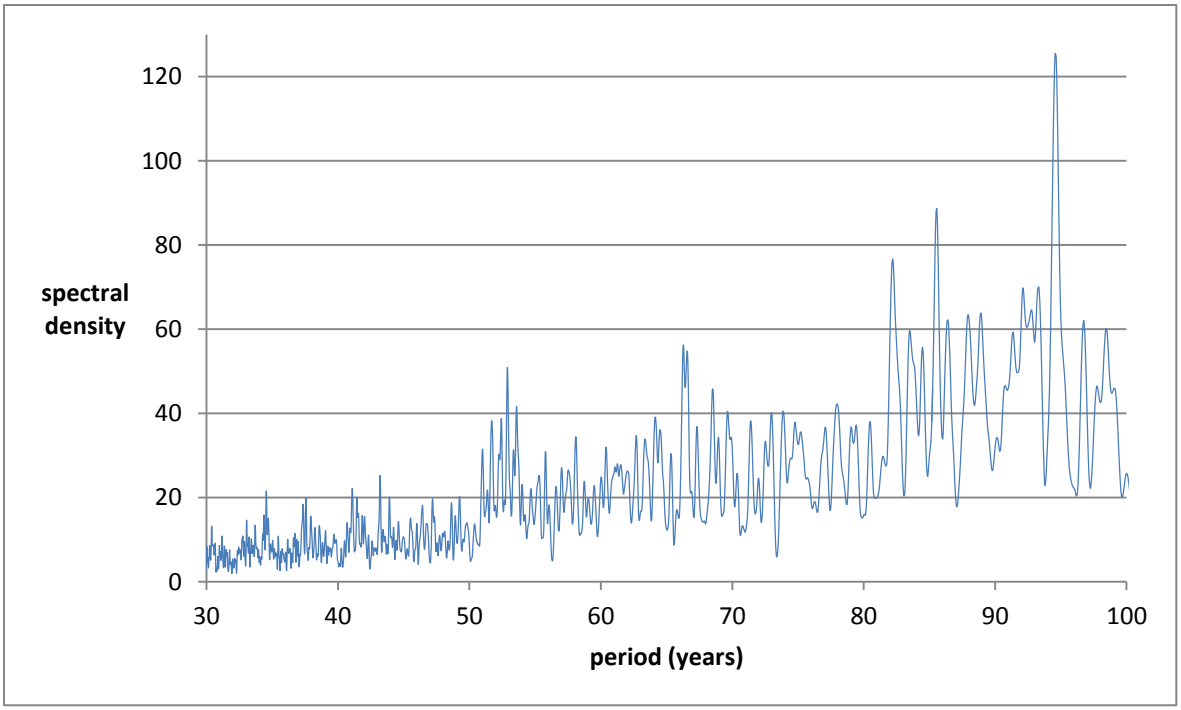

Fig. 68: Zoom of Fig.49, period interval between 30 and 100 years (Tukey-Hanning)

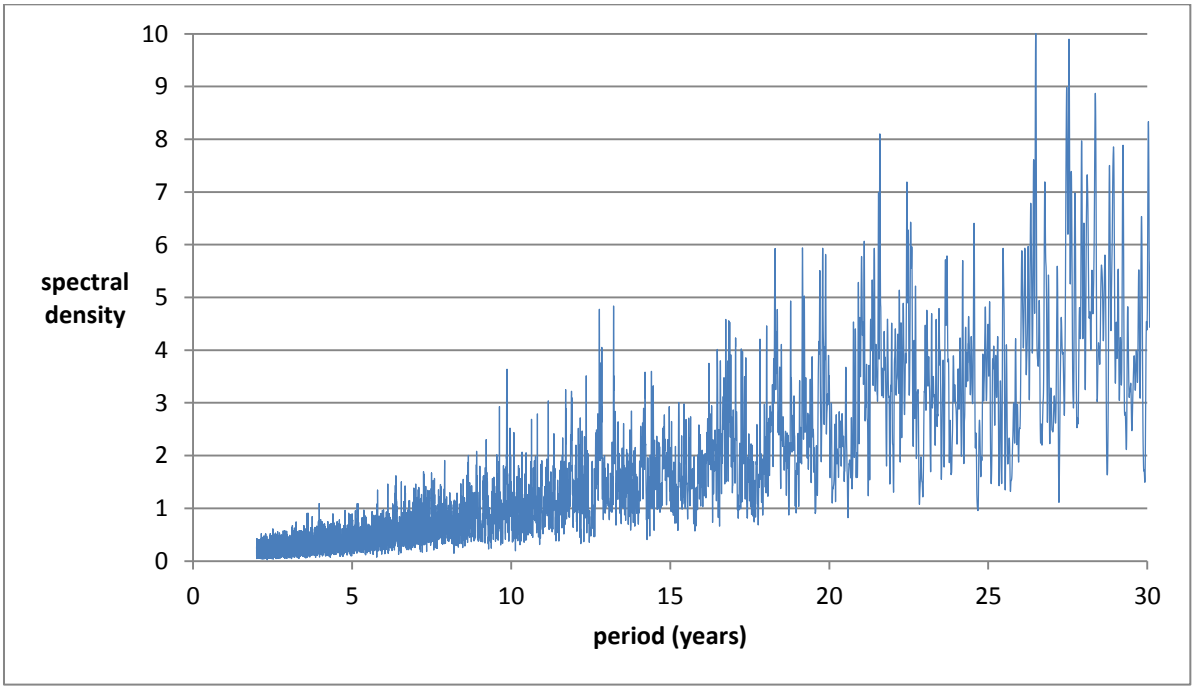

Fig. 69: Zoom of Fig.49, period interval between 0 and 30 years (Tukey-Hanning)

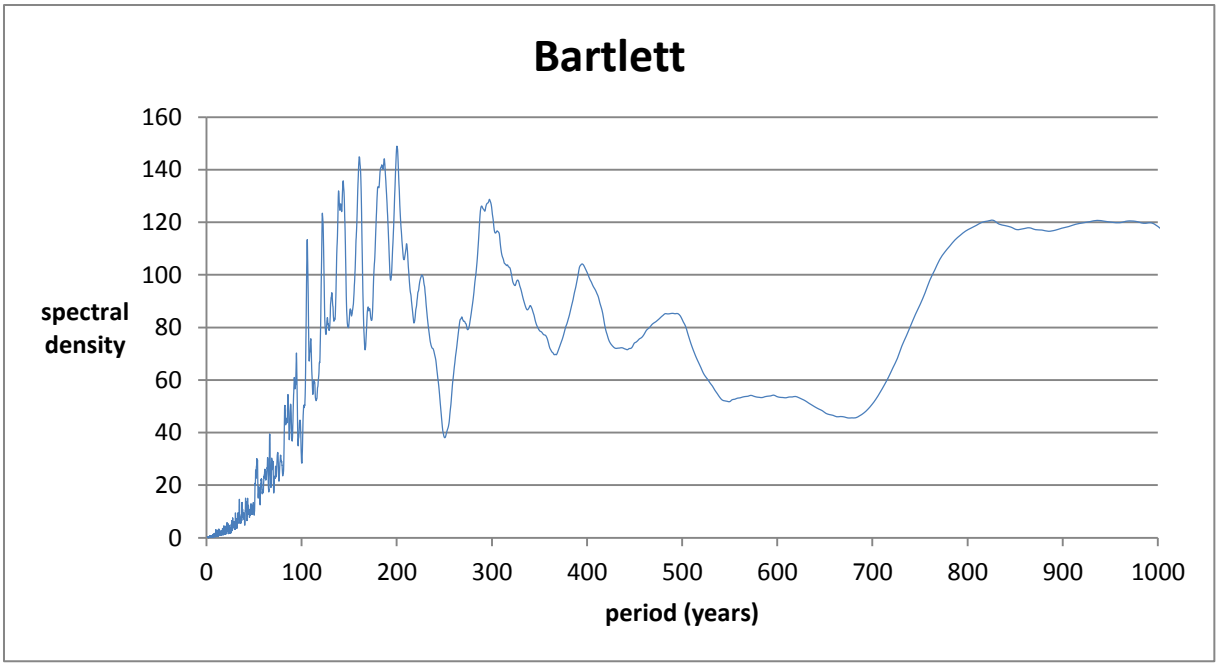

Fig. 70: Bartlett spectral analysis on the a-value: spectral density against period (interval 0-1000 years)

5.3.2.5 Spectral analysis: results for the b-value

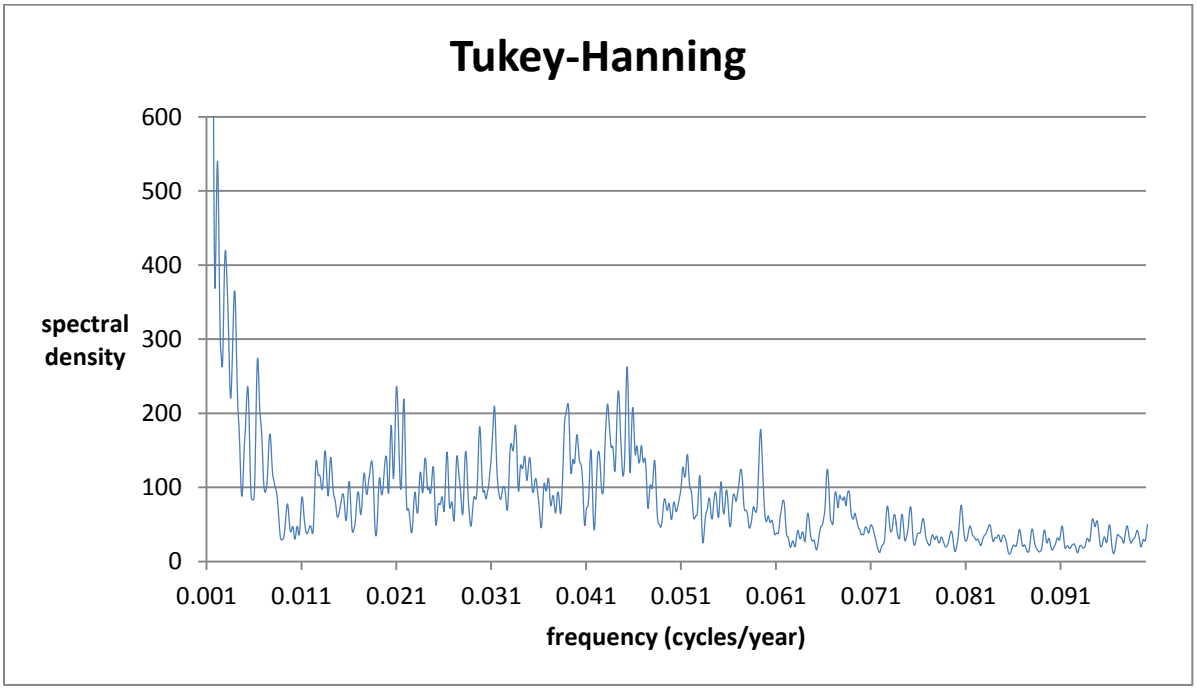

Fig. 71: Tukey-Hanning spectral analysis on the b-value: spectral density against frequency (interval 0.001-0.1 cycles/year)

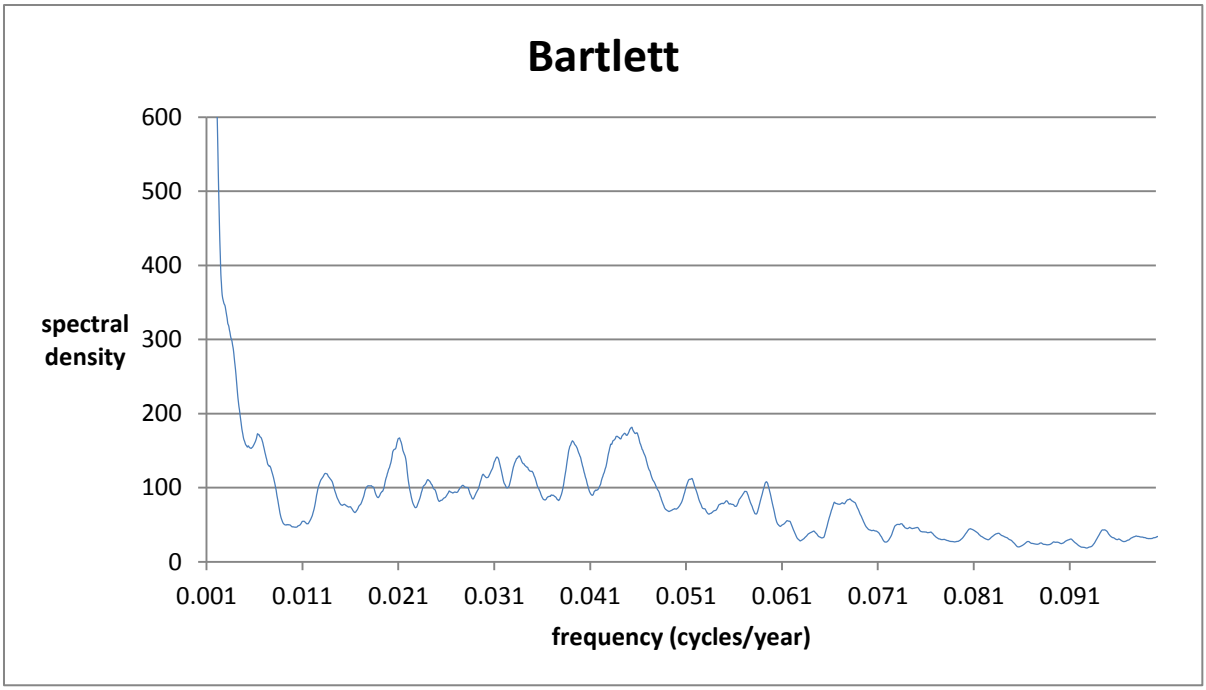

Fig. 72: Bartlett spectral analysis on the b-value: spectral density against frequency (interval 0.001-0.1 cycles/year)

Within the period interval of 100 to 1000 years, cycles above a spectral density of 100 (see Fig.73) were selected. Cycles of 106, 146, 162, 202, 211, 239, 267, 301, 309, 317-318, 344, 357, 448, 468, 504, 821, 985 years were obtained. For the period interval between 30 and 100 years, cycles of 38, 43, 45-47, 51, 53, 57, 63, 65-67, 70-80, 82, 85-86, 90, 93, 95, 98-99 years (see Fig.74) were obtained (above a spectral density of 20). For the smallest cycles, selected above a spectral density of 2, we extracted cycles of 12, 14, 16-20, 22-23, 25-26, 28-30 years (see Fig.75).

Comparing the results of the spectral analysis on the L-value, a-value and b-value, it can be concluded that some cycles occur in the analysis on the L, the a, as well as the b-value, whereas others only occur in two of the three color space coordinates. In all the datasets (L, a, and b), the following cycles occur: 17-18, 20, 21-23, 25-26, 28-29, 41, 43, 53, 57, 60-70, 70-80, 80-90, 90-100, 145-146, 162-163, 201-202, 211, 267-268, and 308-309 years. In the a-value and b-value dataset, cycles of 12-14, 301, 343-344, and 504 years occur. In the L-value and b-value dataset, cycles of 38, 239, and 468 years were extracted. Both in the L-value and the a-value dataset, a cycle of 994 years was obtained.

The Bartlett spectral method yielded less possible cycles than the Tukey-Hanning method, but there is some resemblance between the cycles found through the Bartlett method and the results from the Tukey-Hanning method. Between 3 and 6 cycles found with the Tukey-Hanning method were also found with the Bartlett method. The spectral density is always a unit of 100 higher for the Tukey-

Hanning method than for the Bartlett method; additionally, from a period of 500 years, the Bartlett method does not show as many, or as clear, peaks as the Tukey-Hanning method.

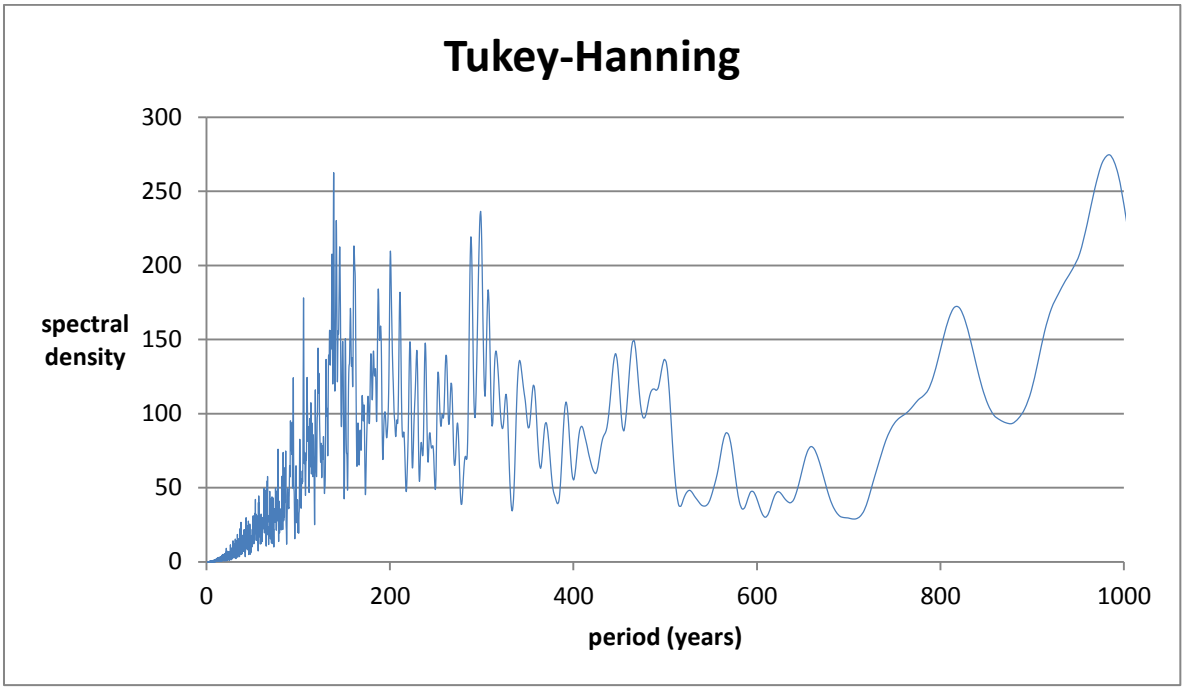

Fig. 73: Tukey-Hanning spectral analysis on the b-value, spectral density against period (interval 0-1000 years)

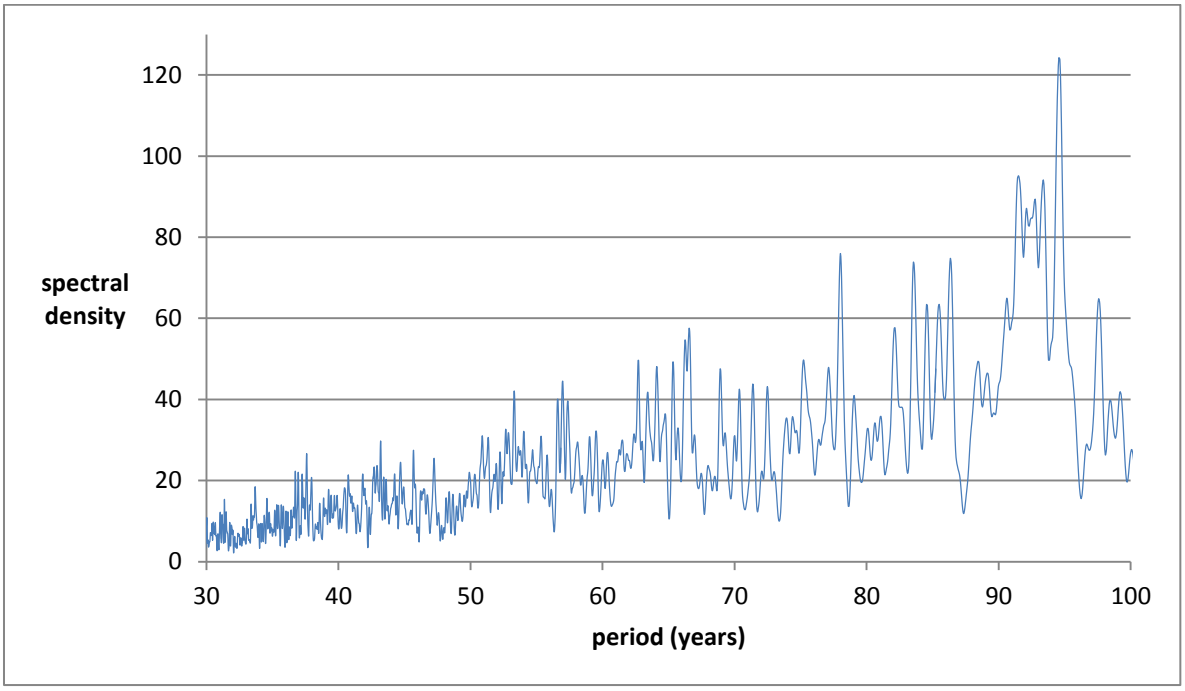

Fig. 74: Zoom of Fig.55, period interval between 30 and 100 years (Tukey-Hanning)

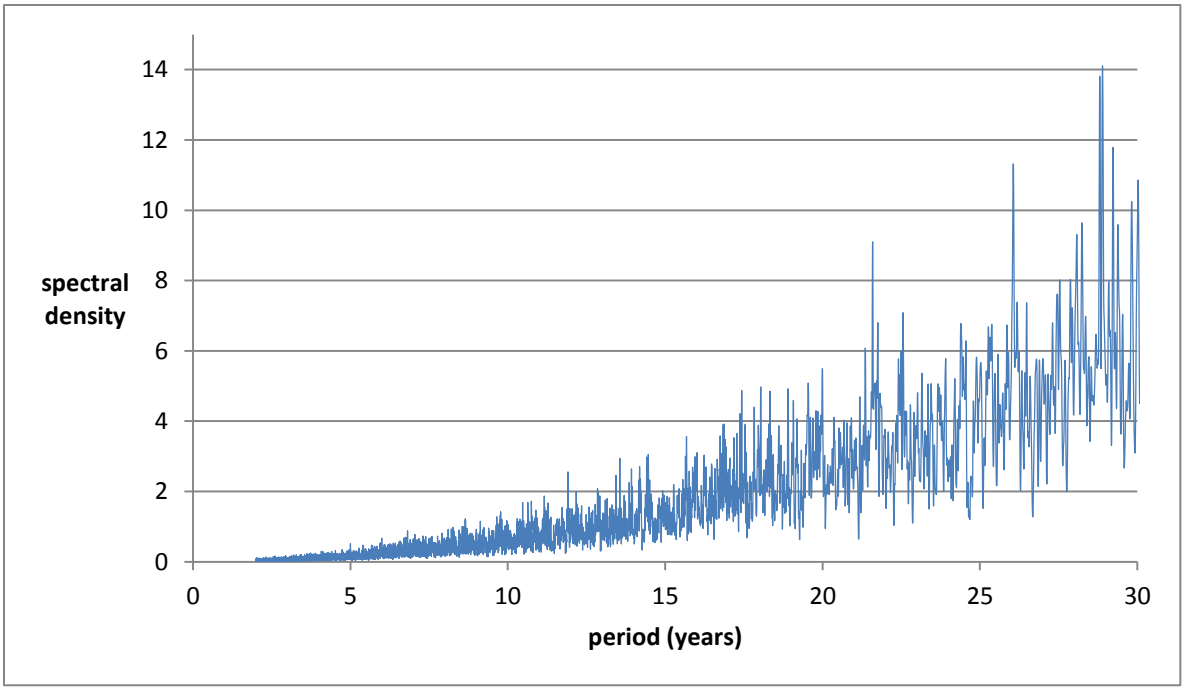

Fig. 75: Zoom of Fig.55, period interval between 0 and 30 years (Tukey-Hanning)

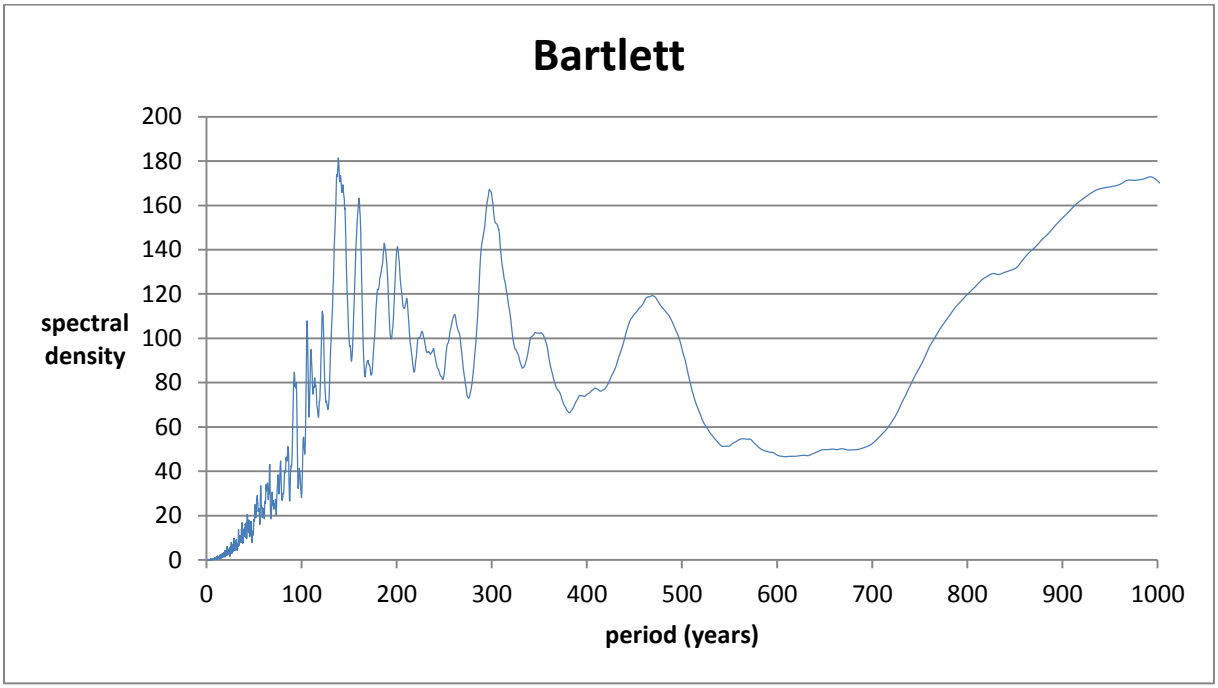

Fig. 76: Bartlett spectral analysis on the b-value: spectral density against period (interval 0-1000 years)

5.4 µ-XRF analysis

From the results of the µ-XRF analysis on sample PAR1A-III (50-60), some element ratios were calculated, which can be used to characterize the different laminae. According to the µ-XRF sum spectrum (see Fig.77), Mg, Cu, Zn, Sr, Rb, and Zr contain no useful information, as the amount of counts/s of each of these elements barely exceeds the detection limit. Because of this reason, these elements were not used for calculating the ratios.

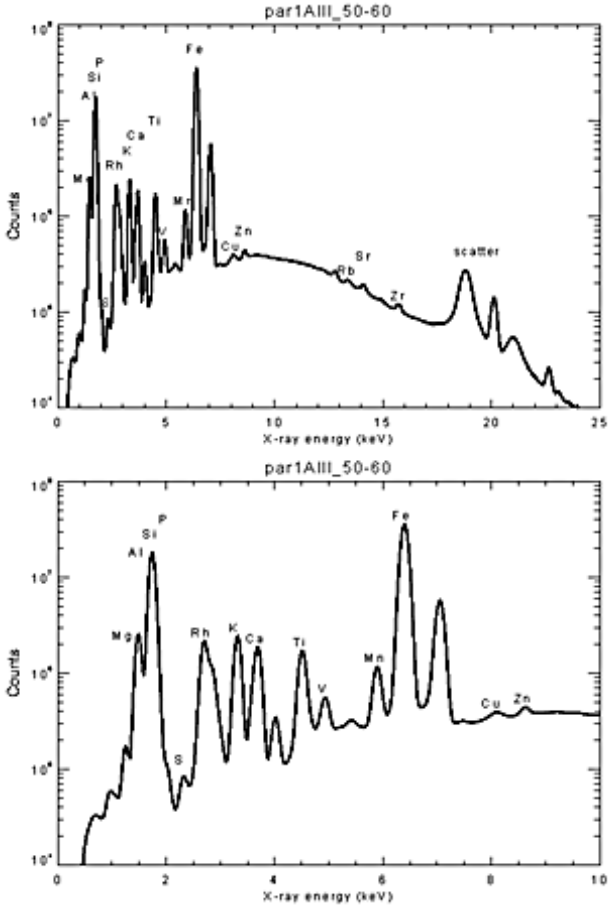

Fig. 77: µ-XRF sum spectrum, the lower panel is a zoom on the 0-10 keV region

Although there are sufficient Mn-counts, this element was not used either. The oil used in the microprobe instrument for the µ-XRF analysis contains Mn, and some oil remnants were still present in the pores of the sample after cleaning. Thus, contamination of the sample with Mn could have been possible. The assumption of contamination has been confirmed by looking at the 2D elemental maps (see Fig.78). The 2D µ-XRF map shows that the counts of Mn are restricted to very specific areas, whereas the other elements are all spread out over the area over which they were recorded. Therefore, Mn will not be used in our calculations.

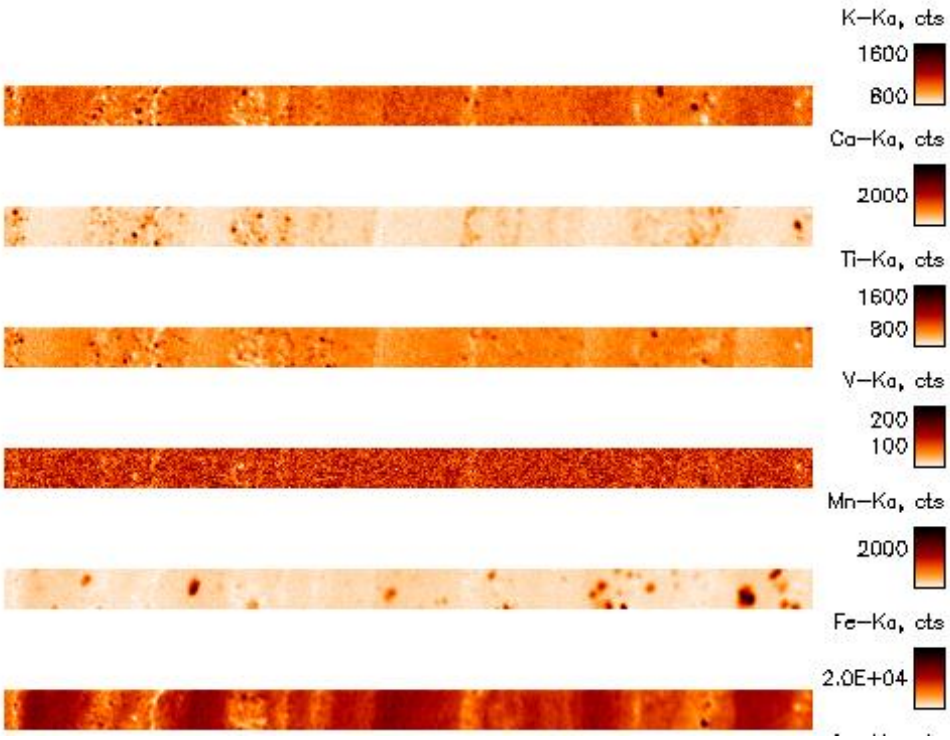

Fig. 78: 2D elemental µ-XRF maps

5.4.1 Correlations between elements

In order to decide which ratios could give us most information about the different laminae, the different elements (Al, Si, K, Ca, Ti, and Fe) were plotted against each other to examine how they correlate. Elements with the largest contrast between each other can characterize the laminae the best. Therefore, element correlations lower than $R^2 = 0.6$ and/or negative correlations were selected. A positive correlation means that both elements show the same changes, which is not interesting when one would like to express the differences between two elements. The level of $R^2 = 0.6$ was chosen, since a weak correlation is defined as having an r-value below 0.8, which corresponds with an $R^2 = 0.64$. From the 15 possible combinations between the elements, there were four which could not be used. The elements Si-Ca, K-Fe, and Al-Si correlated well and positively. The elements Ca-Al correlated positively and weak ($R^2 = 0.4724$), however, not weak enough to be useful as an elemental ratio. This since the R^2-value is still larger than $R^2 = 0.25$, below which a correlation is defined to be very weak. In Fig.79 an example is shown of two elements suitable to use as ratio (see appendix for all the other correlations).

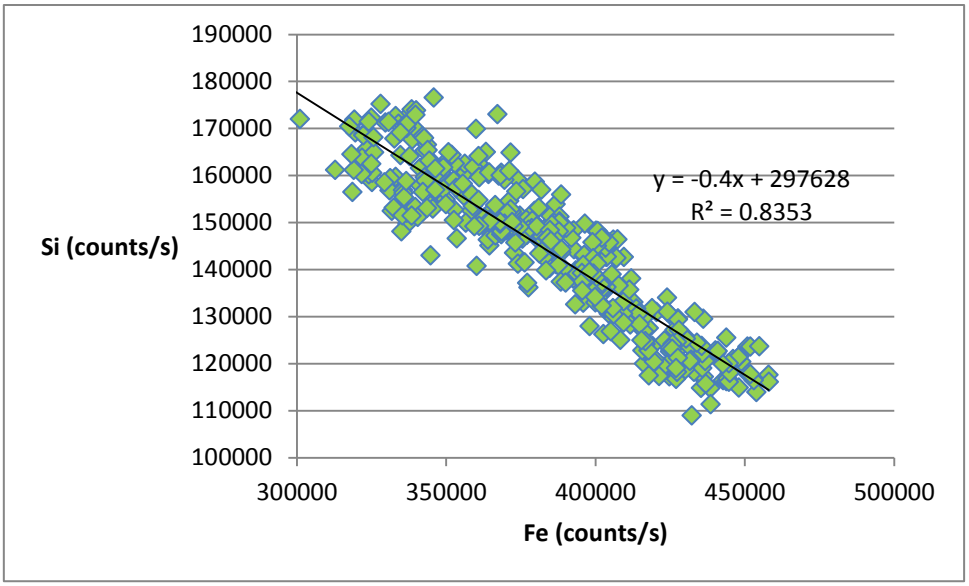

Fig. 79: Correlation of Si and Fe

We also plotted the elements Al, Si, K, Ca, Ti, and Fe against grain size to determine in which laminae they occur the most. The coarse grained laminae are characterized by more counts of Ca and Si, whereas the fine grained laminae show a preference for the Fe and K elements (see Fig.80). For the elements Ti and Al, there was no clear preference for the fine grained or coarse grained laminae.

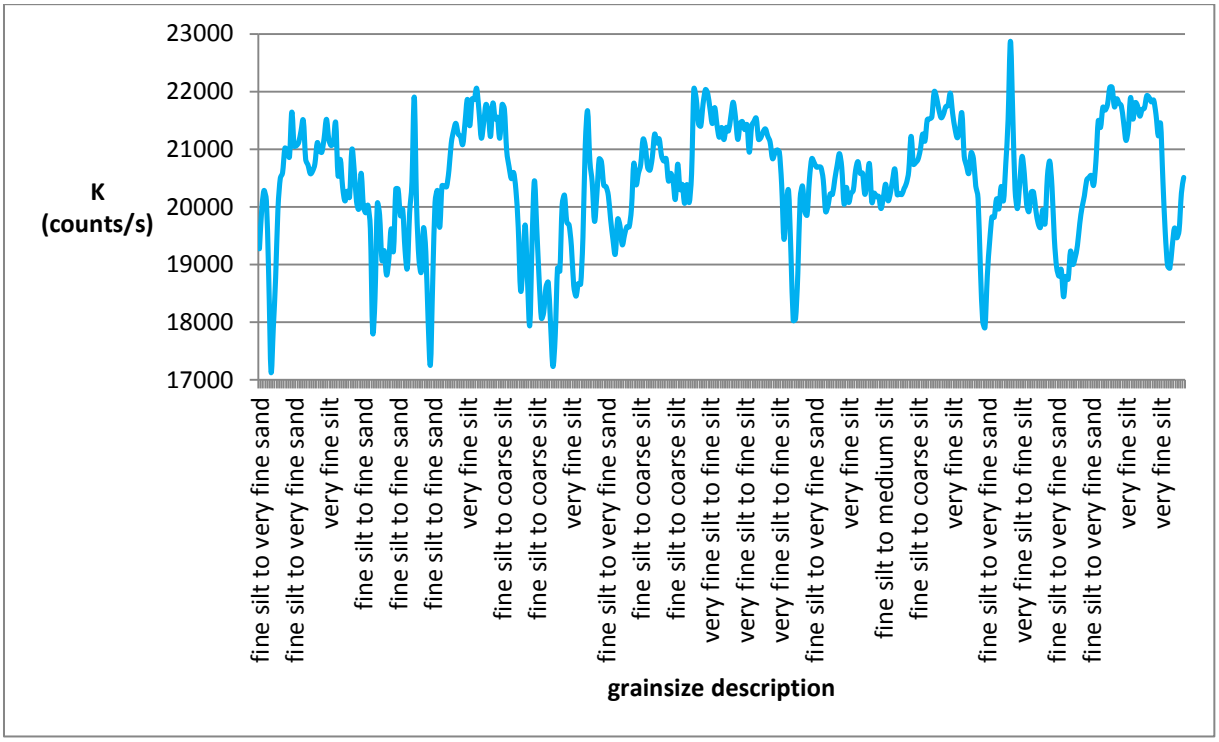

Fig. 80: K against grain size (the top of the sample PAR1A-III(50-60) is at the left side of the graph); grain size information is collected over a distance of 20 mm

5.4.2 Results of the elemental ratios

Different ratios were calculated and plotted against grain size (obtained with the petrographic microscope). Some of these ratios were better at characterizing laminae than others. The following elemental ratios were selected as being useful: log(Ca/K), log(Si/K), log(Fe/Al), log(Fe/Si), log(Al/K), log(Ca/Ti), log(Fe/Ca), log(Si/Ti). The ratios log(Fe/Ti) and log(K/Ti) show a particular trend, they will therefore be discussed later in this section. High values of log(Ca/K), log(Si/K), log(Al/K), log(Ca/Ti) and log(Si/Ti) correspond with coarser grained parts, whereas the finer grained parts are expressed by the lower values of these ratios. High values of log(Fe/Al), log(Fe/Si) and log(Fe/Ca) correspond with finer grained parts, whereas the low values of these ratios coincide with the coarser grained parts. In Fig.81 and Fig.82, two examples of elemental ratios are shown, that can be used to determine whether we have coarse grained or fine grained laminae, the others can be found in the appendix.

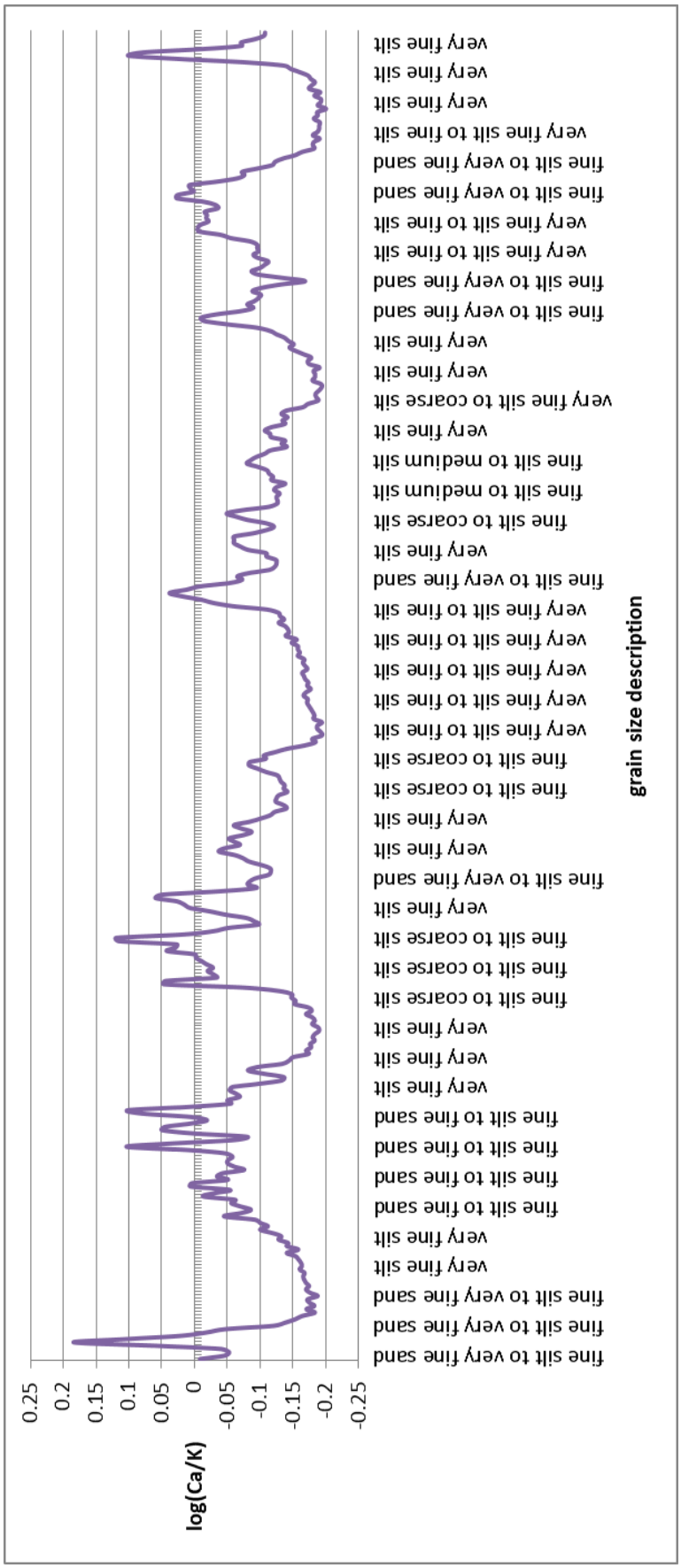

Fig. 81: log(Ca/K) against grain size (top sample PAR1A-III(50-60) is at the left side of the graph); grain size information is collected over a distance of 20 mm

Fig. 82: log(Fe/Si) against grain size (top sample PAR1A-III(50-60) is at the left side of the graph); grain size observations are collected over a distance of 20 mm

The log(Fe/Ti) and the log(K/Ti) ratios show a particular trend, which is more clear for the log(Fe/Ti) ratio, than for the log(K/Ti) ratio. The log(Fe/Ti) ratio climbs gradually towards higher values over the finer grained parts of the sample, then drops suddenly when it reaches the border with a coarser grained part. The ratio then stays lower as long as the laminae are coarser. When a more fine grained part is encountered, the ratio will again rise gradually and then drop suddenly at the next border with a coarser grained part. For the log(K/Ti) ratio, the same observations can be made. In Fig.83 and Fig.84 the log(Fe/Ti) and log(K/Ti) ratios are shown.

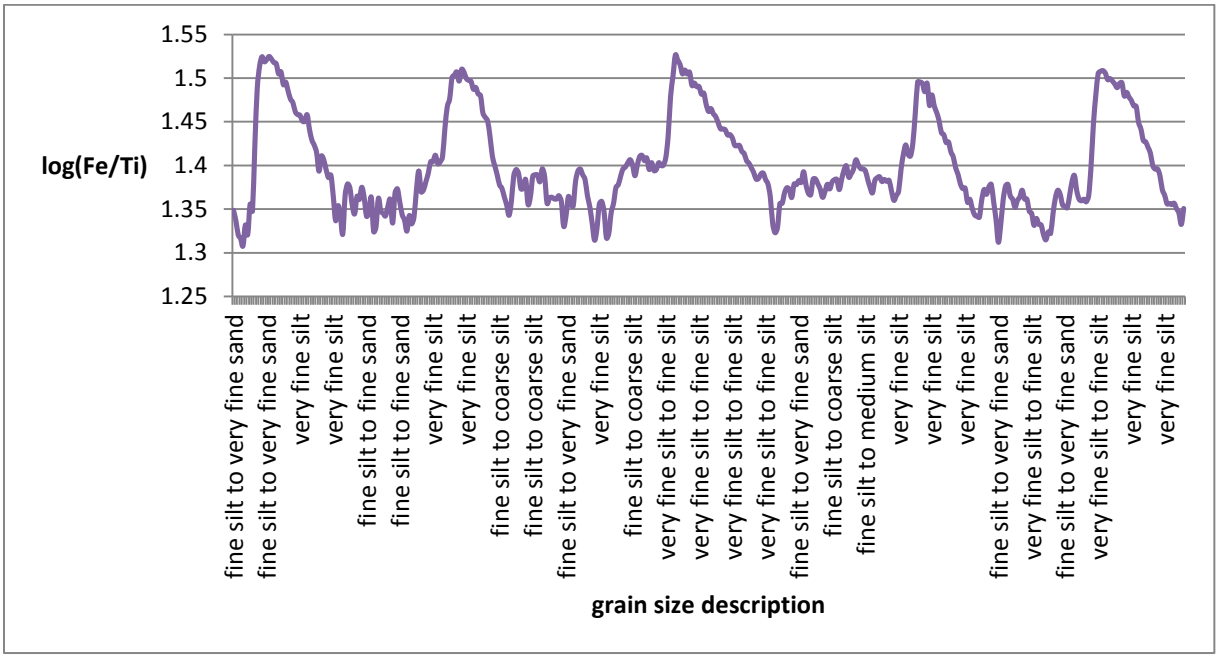

Fig. 83: log(Fe/Ti) against grain size (top of sample PAR1A-III(50-60) is at the left side of the graph); grain size observations are collected over a distance of 20 mm

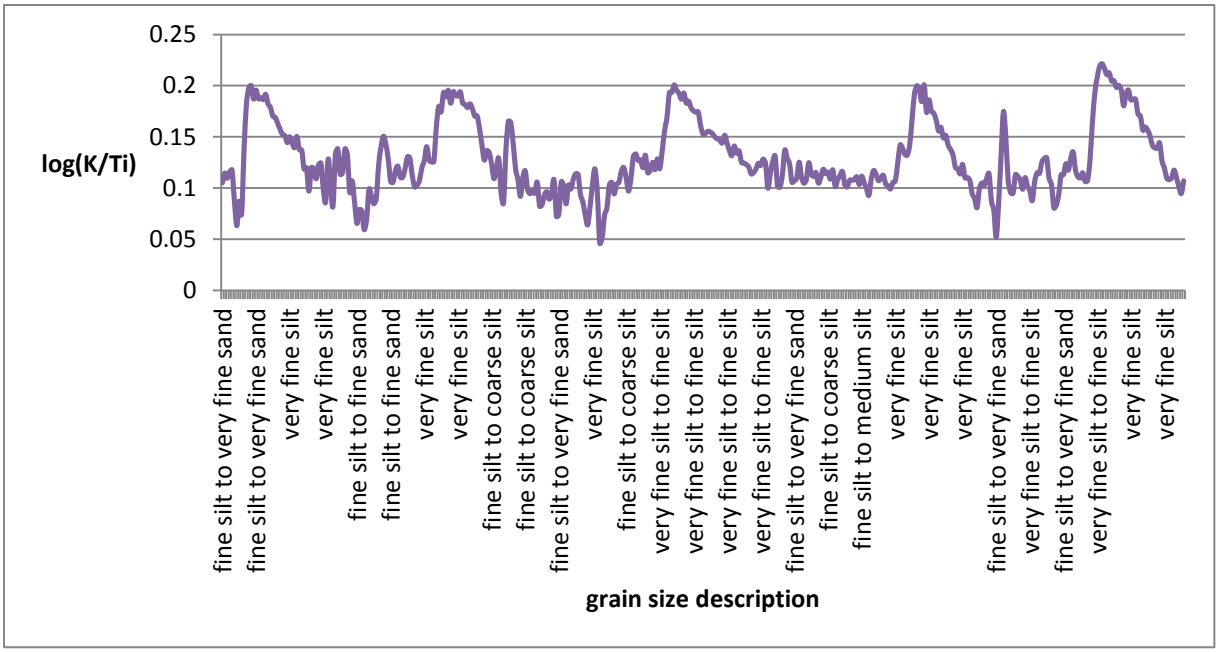

Fig. 84: log(K/Ti) against grain size (top of sample PAR1A-III(50-60) is at the left side of the graph); grain size observations are collected over a distance of 20 mm

5.4.3 The relationship between the µ-XRF and the color space coordinates

5.4.3.1 Grain size and the color space coordinates

On the part of sample PAR1A-III(50-60) for which a µ-XRF analysis was performed, a color analysis in the Lab color space mode with the program StratiSignal was done. It was easier to repeat the color analysis on the section on which the µ-XRF analysis was performed, than extracting this information from the color analysis dataset carried out on the complete core (PAR1A-III, PAR1A-IV and PAR1A-V). The results of this color analysis were then related with the petrographic microscope observations of the grain size. To the end that the L-values, the a-values and the b-values were plotted against grain size. Higher L-values (=lightness) for the coarser grained parts and lower L-values for the finer grained parts were observed. These results are shown in Fig.85.

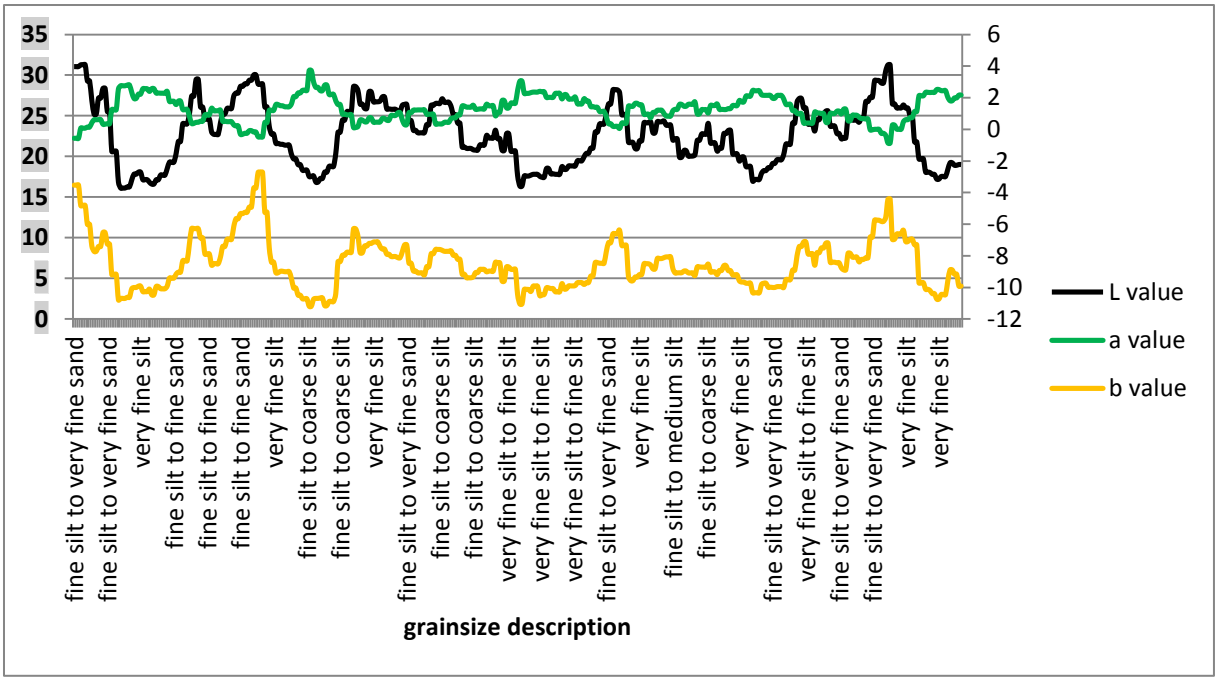

Fig. 85: Relationship between Lab-values and grain sizes (top sample PAR1A-III(50-60) is at the left side of the graph); grain size observations are collected over a distance of 20 mm

5.4.3.2 Elemental ratios and the L-value of the color space coordinates

The variations in the elemental ratios were related to grain size variations in sample PAR1A-III(50-60). Fig.86, Fig.87 Fig.88 display the log(Ca/K), log(Fe/Si) and log(Fe/Ti) ratio and the L-value. The L-value (=lightness) is a clear representation of grain size, as shown in section 5.4.3.1. A high lightness corresponds with coarser grain sizes, whereas a lower lightness is related to finer grain sizes. The ratios discussed in section 5.4.2 were also linked with grain size variations. Here Fig.86, Fig.87 and Fig.88 confirm that the ratios can be linked with the L-value and, therefore, are a representation of grain size variations. The high values of the log(Ca/K) ratio, which coincide with coarser grained parts, also correspond with higher L-values. High values of the log(Fe/Si) ratio are an expression of the finer grained parts and coincide with lower L-values. The trend expressed by the log(Fe/Ti) ratio is clearly visible in the L-values. The L-values gradually rise over the fine grained parts of the sample, together with rising log(Fe/Ti) values, up to a point where the ratio drops suddenly when a maximum in the L-value is reached (= border with a coarser grained part). Thereafter, the L-value is lower than that maximum that was reached, however, still high enough to correspond with coarser grained laminations. When the L-value reaches a minimum, it starts to gradually rise again, together with a gradually rising log(Fe/Ti) ratio (see Fig.83).

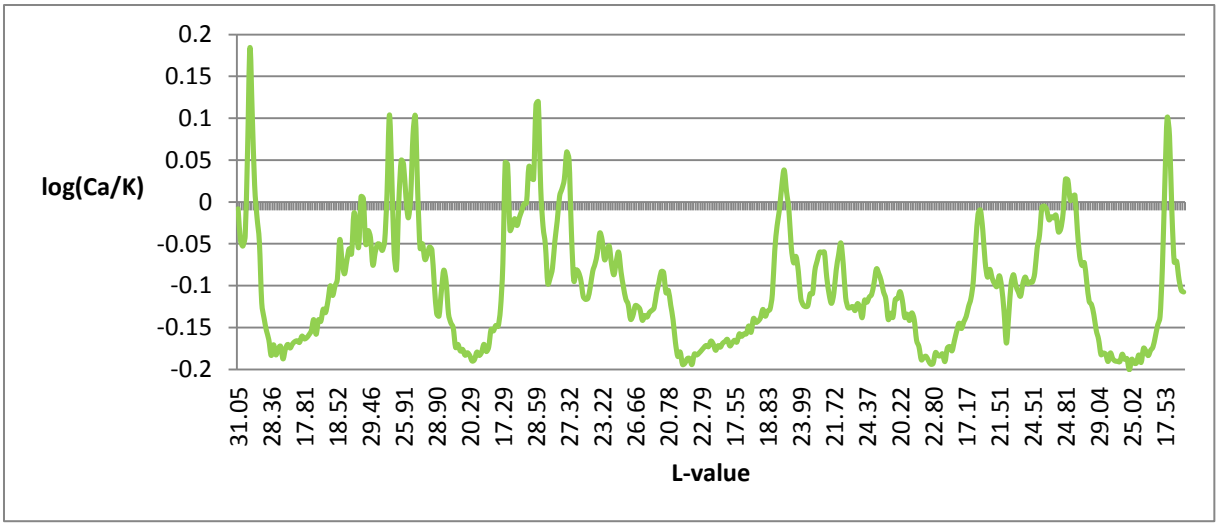

Fig. 86: log(Ca/K) against the L-value (top sample PAR1A-III(50-60) is at the left side of the graph)

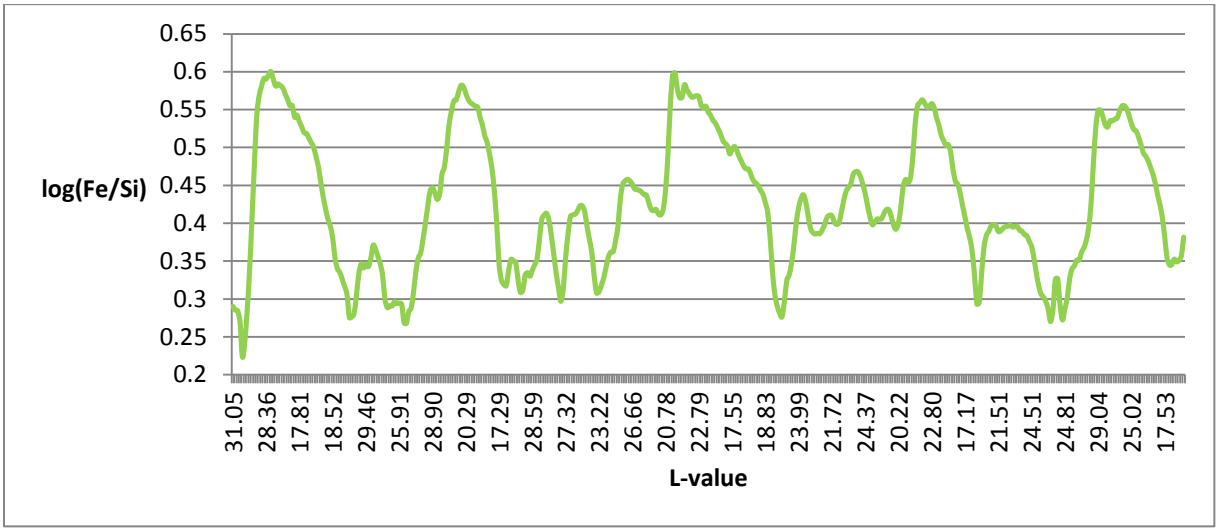

Fig. 87: log(Fe/Si) against the L-value (top sample PAR1A-III(50-60) is at the left side of the graph)

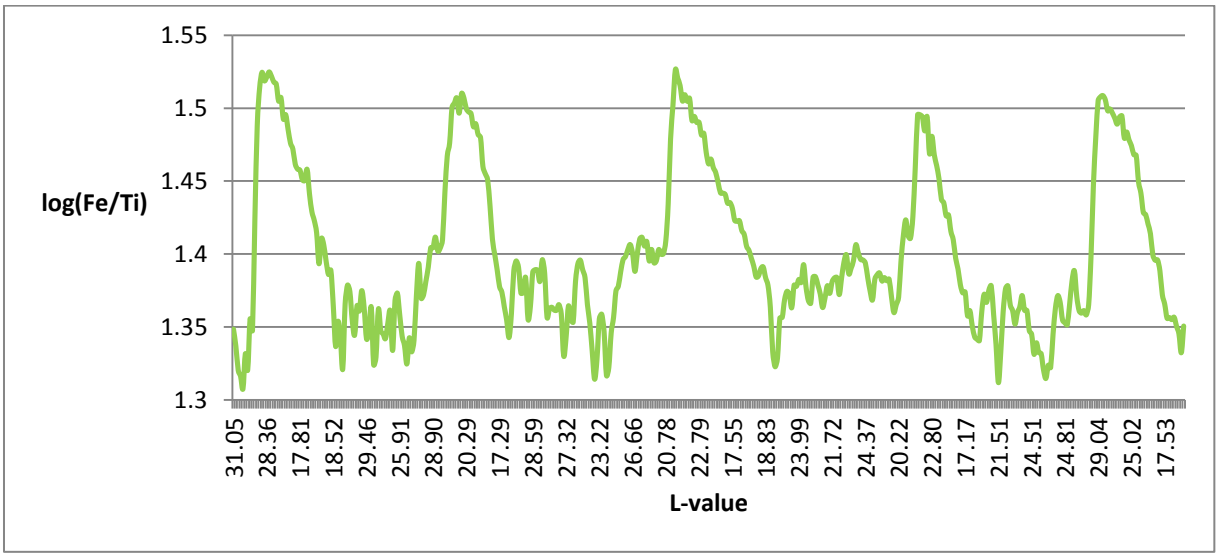

Fig. 88: log(Fe/Ti) against the L-value (top sample PAR1A-III(50-60) is at the left side of the graph)

5.4.4 Placing grain size changes in a time frame

The knowledge gleaned in the study of elemental ratios, obtained from the μ-XRF analysis on sample PAR1A-III(50-60), can be transposed on the whole record, by using the XRF data collected for the complete core by Heirman K. in her PhD research. In Fig.89, an example is shown with the log(Fe/Si) ratio. As discussed above (section 5.4.2), finer grained laminations are expressed by higher log(Fe/Si) values, whereas the coarser grained parts are expressed by lower log(Fe/Si) values. Consequently, plotting the ratio against a time axis makes it possible to place these changes in a time frame.

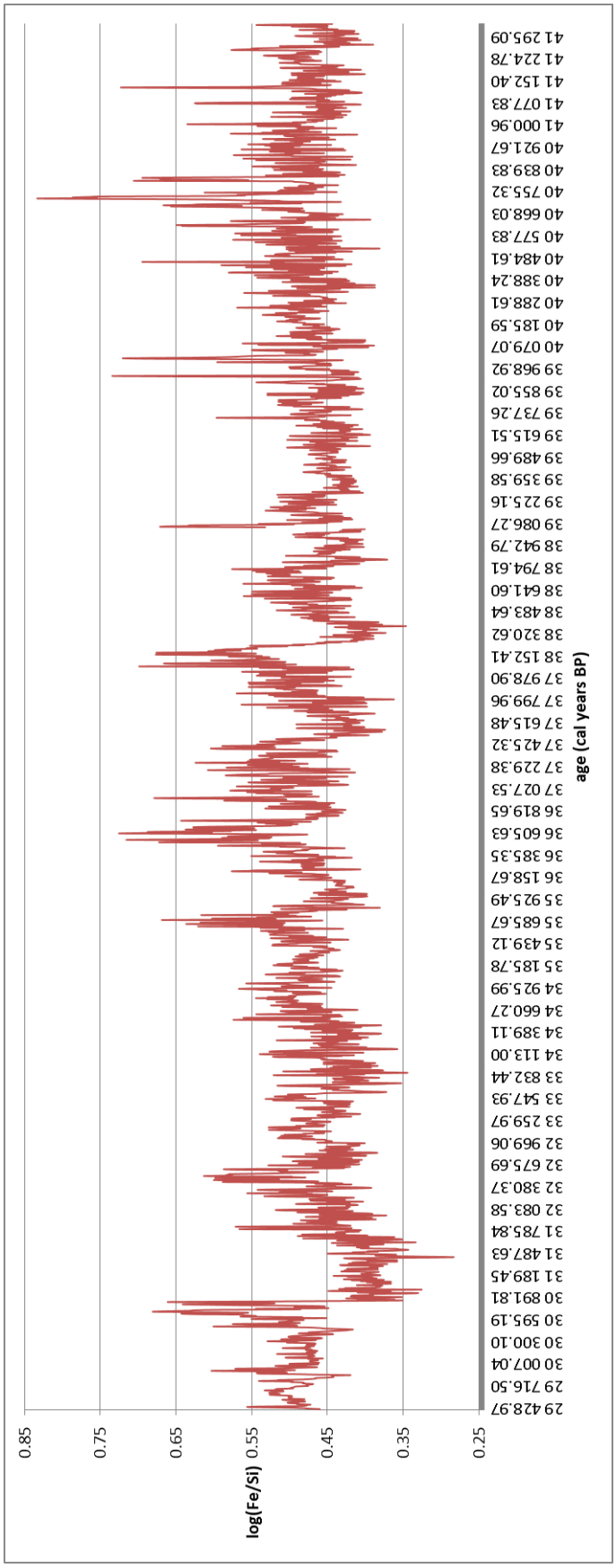

Fig. 89: the log(Fe/Si) ratio against a time axis;

for the whole record: PAR1A-III, PAR1A-IV and PAR1A-V

6. Discussion

6.1 Genesis of the laminations

There are three different types of laminations in the sedimentary record from Laguna Parrillar: 1) a fine grained component consisting of very well sorted, very fine silt ((<0.01)-0.01 mm) with low-lightness, 2) a coarser grained silt (0.01-0.05 mm) with an intermediate-lightness, and 3) the coarsest fraction consisting of laminations with a high-lightness, composed of a silt-sand mixture with a grain size between 0.01 and 0.15 mm (fine silt to fine sand). Turbidites are possibly occurring in between the laminations, but, univocal, coherent conclusions could not be made. However, it is important to recognize turbidites because these do not have a chronological meaning (Zolitschka, 2007).

Turbidites are the deposits of an underwater avalanche, responsible for distributing vast amounts of clastic sediments into a water body (ocean or lake). Turbidites were described for the first time by Bouma in 1964. A Bouma cycle begins with an erosional contact of a coarse layer of granule conglomerate in a sandy matrix. Then the cycle passes through the following states: a coarse and then medium grained, plane parallel sandstone, then a cross bedded sandstone, a rippled cross-bedded sand or silty sand, and finally through laminar siltstone and shale. One usually cannot observe a complete Bouma cycle at a single place.

The lowest magnification on the petrographic microscope is 10X4, which does not make it possible to give a good overall view on the sample and also makes it difficult to decide whether turbidites are observed or not. Some fining upwards trends were observed during the petrographic microscope observations, some had sharp bottom boundaries and some were irregular (i.e. an erosional feature). Additionally, these observed trends did not coincide with a particular grain size.

Another particular observation was that no diatoms, or other planktonic life forms, were found in the sedimentary record. Normally diatoms are found everywhere; however, the lake water in the central part of the lake basin, where the sediment cores were collected, is dark colored because of the presence of large amounts of organic matter. This organic matter, floating on the water's surface, blocks all sunlight on which the diatoms depend (personal comments, Dr. S. Bertrand).

Referring to Fig.90 and Fig.91 from McCulloch *et al* (2005a, 2005b) and Sugden *et al*. (2009), it can be inferred that Laguna Parrillar could possibly have been a proglacial lake in an early stage, but certainly for the last glacial period, it was just a lake surrounded by glaciers. The glacial limits during the Last Glacial Maximum drawn by McCulloch *et al*. (2005a) surround the Brunswick Peninsula, on which Laguna Parrillar is located. The late glacial moraine limits (McCulloch *et al*., 2005b) could have possibly formed a boundary in the area of the lake, but not close to the lake. Additionally, the

maps of the glacial stages in Sugden *et al*. (2009) show that the area of Laguna Parrillar was an ice-free zone surrounded by glaciers from the Last Glacial Maximum. To create these glacier reconstruction maps, they used SRTM-30plus (Shuttle Radar Topography Mission) topographic and eustatic sea level data. Nevertheless the scale of the map is too large, it is possible to infer that the lake area was probably not covered, or bordered, by an ice sheet from the point of the Last Glacial Maxiumum and on. Though, the ice sheet free area on the Brunswick peninsula becomes very small during the Glacial stage A that was prior to the Last Glacial Maximum. Glacial Stage A has been estimated to be around 90000 years BP (McCulloch *et al*., 2005a). Therefore, in the earlier history (before 90000 cal. years BP) of Laguna Parrillar, it could have been the case that the lake was a proglacial lake. However, the lake was not covered by ice sheets during the last glacial period.

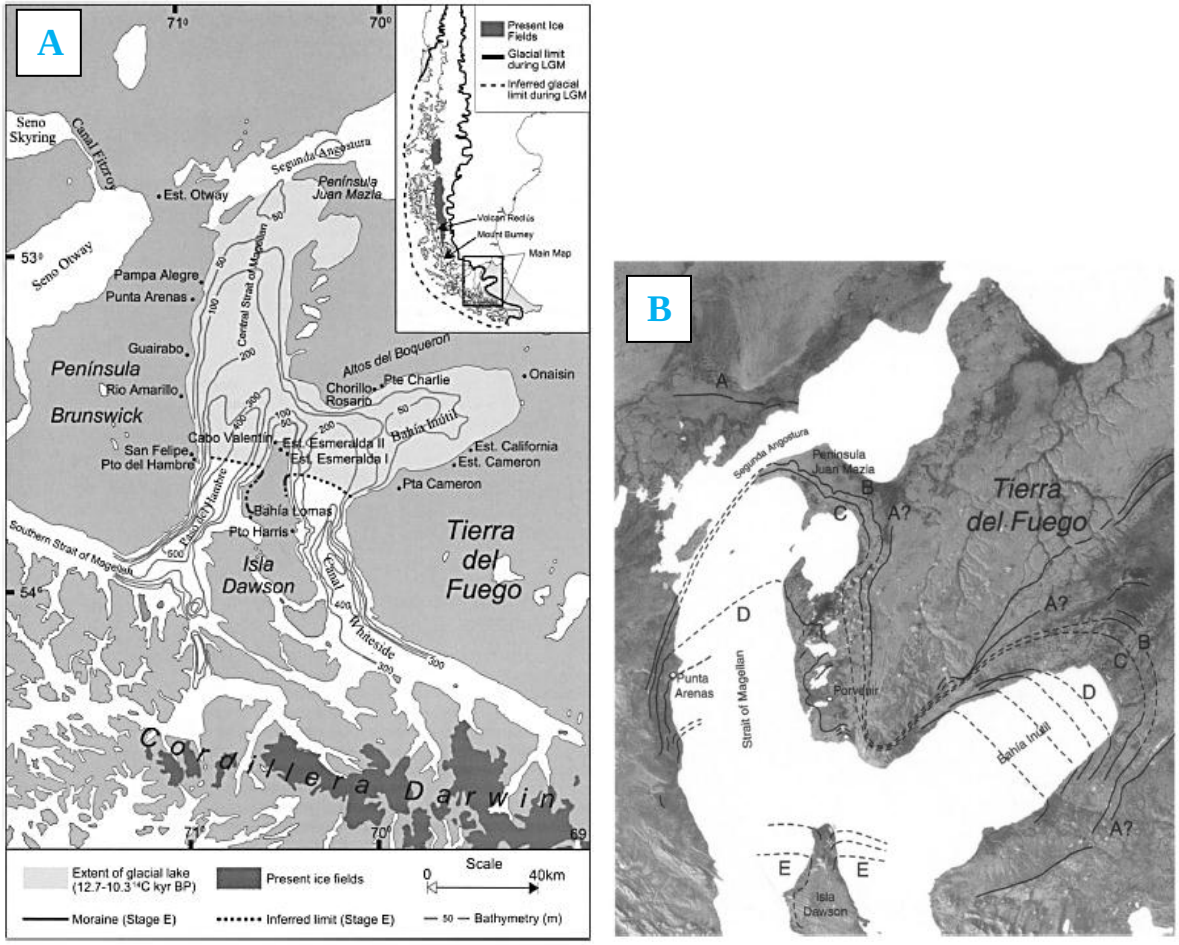

Fig. 90: A) This map shows the extent of the glacial lake during Stage E, the present ice fields, and the moraine limits of Stage E (source: McCulloch *et* al., 2005b); B) The moraine limits of the Last Glaciation in the Strait of Magellan and Bahía Inútil (source: McCulloch *et al.*, 2005a)

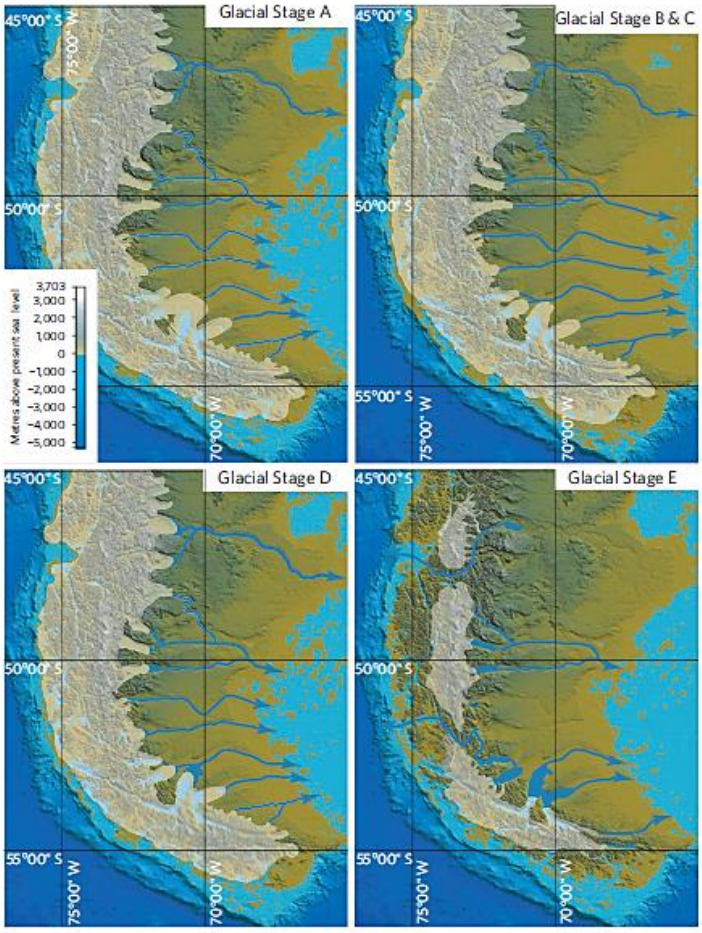

Fig. 91: Glaciers reconstructions during Stage A-E, the colors represent the meters above the present sea level, and also the reconstructed rivers are shown; source: Sugden *et al*., 2009

Kaiser and Lamy (2010) studied the Patagonian Ice Sheet fluctuations during MIS4 to MIS2 on a sedimentary record off the Chilean coast (ODP Site 1233). For the period that is comprised in this thesis research (between 29 and 41 ka, or late MIS3), they found ice advances around 30 ka, 32-33 ka, 36 ka, 38 ka (but minor), and 40 ka, inferred from the Fe and Ti maxima recorded in the sedimentary record. The ice advances coincided with maxima in dust supply to Antarctica. The alkenone based sea surface temperatures show several fluctuations, which are visible in Fig.92 (Kaiser and Lamy, 2010). From these findings we will try to form an image of the climate and climate changes existing around the lake.

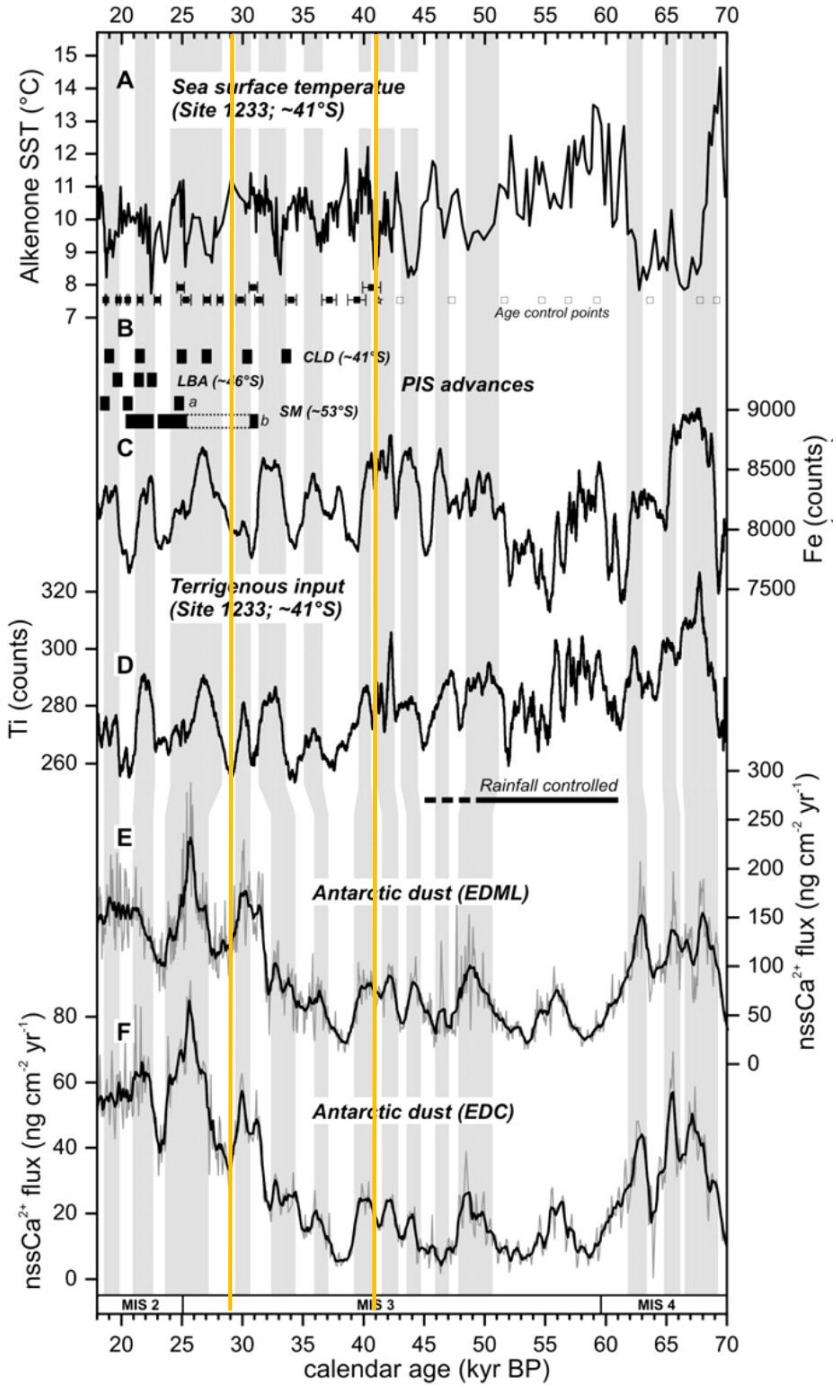

Fig. 92: The relationships between sea surface temperature changes (A; record from ODP Site 1233) in the southeast Pacific, Patagonian Ice Sheet activity (C,D) and Antarctic dust variability (E,F); the yellow lines comprise the time period studied for this thesis research; Source: Kaiser and Lamy, 2010.

During the investigated time period for this thesis research, Kaiser and Lamy (2010) observed at least 4 major ice advances of the Patagonian ice sheet. During the warmer periods, the size and height of the ice sheets were reduced, and there was a decrease in glacial activity and dust production. Additionally, the foehn winds east of the Andes were weakened during the warmer periods. During cold periods these winds were intensified, because of the increased height of the ice sheets, and enhanced aridity and dust mobilization. During the warmer periods, dust mobilization was inhibited by increased

vegetation and soil moisture, next to the absence of strong foehn winds. The Southern Hemisphere Westerlies also moved further south than during the colder periods (Kaiser and Lamy, 2010). This explains that Laguna Parrillar existed in a climate with fluctuations in ice sheet activity and dust production, as well as a climate with changes in vegetation cover.

In our model for lamination formation in Laguna Parrillar, we assume that during the periods that the lake water was not frozen rivers were able to transport sediments into the lake. The coarser sediment particles accumulated first on the lake bottom. According to Stokes' law, larger particles will reach the bottom earlier than smaller particles. The smaller grain size particles will stay longer in the water column before sinking towards the lake bottom. This happens when the lake water is frozen again and water turbulence decreases. This simple model can explain how laminations in the lake sediment can build up. We also concluded that the laminations are not seasonal and, therefore, not varves. Varves are couplets of seasonal laminae built up in one year. We found 1347 couplets through the microscope analysis over a time span of 11879 years, and 1272 couplets through the computer analysis over a time span of 11906 years. Therefore, if the laminations were seasonal, we had to find around 11900 couplets.

However, since the mass accumulation rate changes through time, it is possible that during some time periods the laminations were seasonal or almost seasonal, and couplets were formed every other year. This possibility will be further discussed in section 6.3.3.

6.2 The computer analysis versus the microscope analysis

6.2.1 Microscope analysis

The microscope analysis yielded 1347 couplets over a time span of about 11900 years. All the measured fine grained laminae and coarse grained laminae show no correlation with each other. However, there is a trend towards larger minimum thickness for the fine grained laminae with increasing thickness for the coarse grained laminae. The couplet thickness depends on the thickness of the coarse grained laminae (R^2=0.6519), not on the thickness of the fine grained laminae (R^2= 0.5104). Sander *et al*. (2002) studied the relationship between annual varve thickness and maximum annual discharge and found a very strong correlation between the two. They argue that six factors are of influence on the magnitude of a snowmelt flood: 1) amount of snow that accumulated during winter, 2) melt rate depending on air temperature and solar radiation, 3) how synchronously the melt in a river basin forms, 4) amount of water that can be stored in the soil, 5) soil frost that can influence the storage of water in the soil, and 6) water can be temporarily stored in lakes so that the flow is attenuated. Although we do not have varves in our record, and we do not have information on

precipitation for the time period studied in this thesis research, we can use the conclusions of Sander *et al*. (2002) for a hypothesis. If we can use the fact that the couplet thickness and the discharge magnitude are connected in our record, then we can make additional conclusions. We found that the couplet thickness depends on the thickness of the coarse grained laminae. Thus, possibly, the thickness of the coarse grained laminae depends on the discharge magnitude and, because of this, influences the couplet thickness.

The variations through time of the thickness of the fine grained and coarse grained laminae can explain why they did not correlate that well with each other. Intervals I (29548 to 34169 cal.years BP) and III (40095 to 41331 cal.years BP) showed both strong similarities in thickness between both the coarse and the fine grained laminae, whereas interval II consists of something completely different. Within interval II (34169 to 40095 cal.years BP), several different things happen.

The part of interval II from 40095 to 39000 cal. years BP shows that the peak heights of the coarse and fine grained laminae start to differ from each other and fluctuate between events in which the coarse grained laminae are either thicker or thinner than the fine grained laminae. This part can be considered a transition period.

From 39000 to 37000 cal. years BP, the coarse grained laminae become much thicker than the fine grained laminae, although the fine grained laminae become thicker as well. Consequently, this part of interval II is characterized by large differences in peak height.

Another transition zone can be recognized in the period between 37000 and 36000 cal. years BP. The thickness of the coarse grained and fine grained laminae decreases so that their peak heights come closer to each other. However, the fine grained laminae are first slightly thicker than the coarse grained laminae; yet, in the upper part of this interval the opposite is true. This appears similar to what we observed in the first transition zone (40095 to 39000 cal. years BP).

From 36000 up to 34169 cal. years BP, the thickness of the coarse grained laminae rises again, however, less than before. The thickness of the fine grained laminae stays more or less constant, allowing them to differ from the coarse grained laminae in peak height.

The shift into interval I coincides with a rise in thickness of the fine grained laminae, whereas the coarse grained laminae stay more or less constant. The end result of these changes is that both laminae no longer differ in peak height.

We seek for a phenomenon to explain why in some time periods the couplet thickness and the coarse grained lamina thickness are better connected than in other time periods. Additionally, why the thickness of the fine grained and the coarse grained laminae are sometimes better connected than in other time periods.

6.2.2 The possibility of Heinrich Events and Dansgaard-Oeschger cycles

In what follows, a possible explanation for the differences in thickness, between the coarse grained and fine grained laminae, is described. The peak around 38000 cal. years BP seems to correspond with the Heinrich Event 4 (see Fig.94), which has been dated on 38000 years BP by Hemming (2004). This coincides with the Dansgaard-Oeschger cycle 8 (see Fig.94). Both are an expression of ice rafting events (see also Fig.93, Fig.95, Fig.96).

Some researchers claim that Dansgaard-Oeschger cycles exhibit cyclicities of ~1500 years; however, the evidence is still questionable. They actually display more quasi-periodic cycles between 1000 and 2000 years, or they can be the expression of random, unpredictable cycles, in contrast to cyclic and predictable ones. In the Northern Hemisphere, Dansgaard-Oeschger cycles take the form of rapid warming episodes, after which a gradual cooling is observed (Ruddiman, 2008). There is also evidence to suggest that the Dansgaard-Oeschger cycles are globally synchronous (Voelker *et al*., 2002). Since these millennial-scale oscillations occur much faster than orbital-scale fluctuations, they are of big importance in understanding and predicting future climate changes on a human time scale (Ruddiman, 2008).

Heinrich Events are major ice rafting events, caused by destruction of ice sheets in the Northern Hemisphere. Heinrich Events occur during some, but certainly not all, cold spells preceding the rapid warming episodes known as Dansgaard-Oeschger cycles. Different possible hypotheses try to explain the cause of these major ice rafting events. One possibility is that these are caused by ice sheet instabilities. A growing ice sheet will reach a point where it will become unstable and will start to break down at its ice margins. One unstable ice sheet can start causing the sea level to rise, and, consequently, have an influence on the stability of other ice sheets (Ruddiman, 2008).

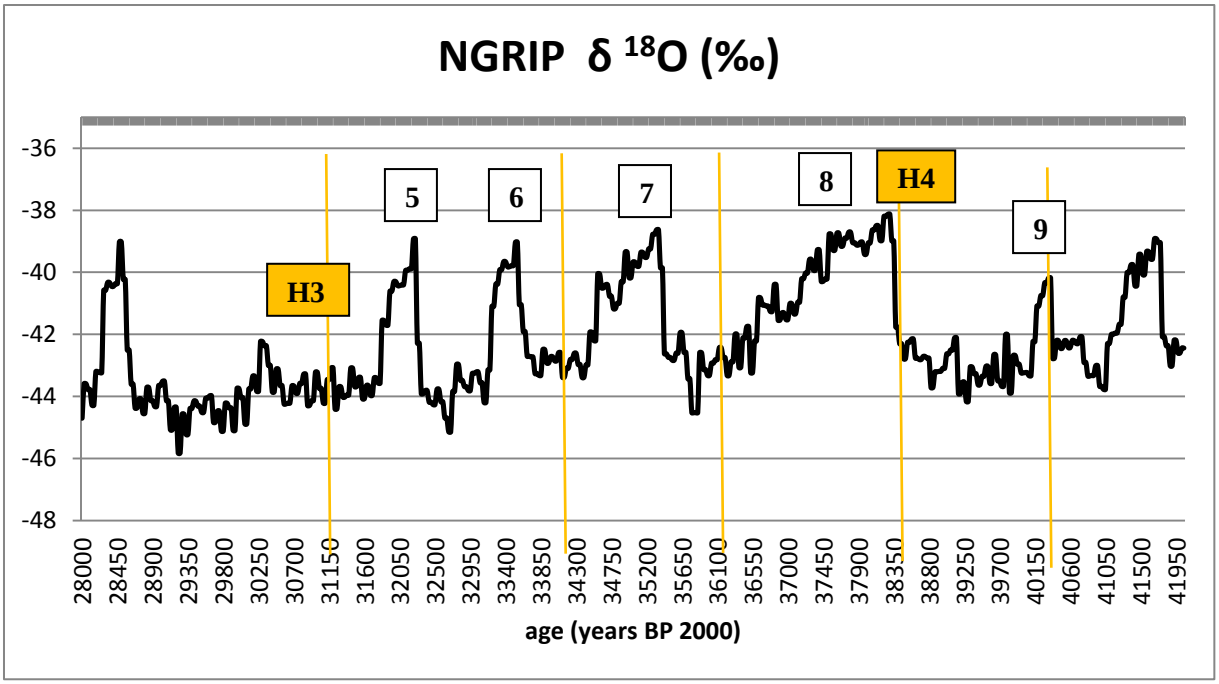

Fig. 93: NGRIP δ ^{18}O (‰) data against a time axis (years BP 2000); the numbers show the Dansgaard-Oeschger cycles, H4 = Heinrich Event 4, H3 = Heinrich Event 3, source: http://www.glaciology.gfy.ku.dk/data/NGRIP_d18O_50yrs.txt

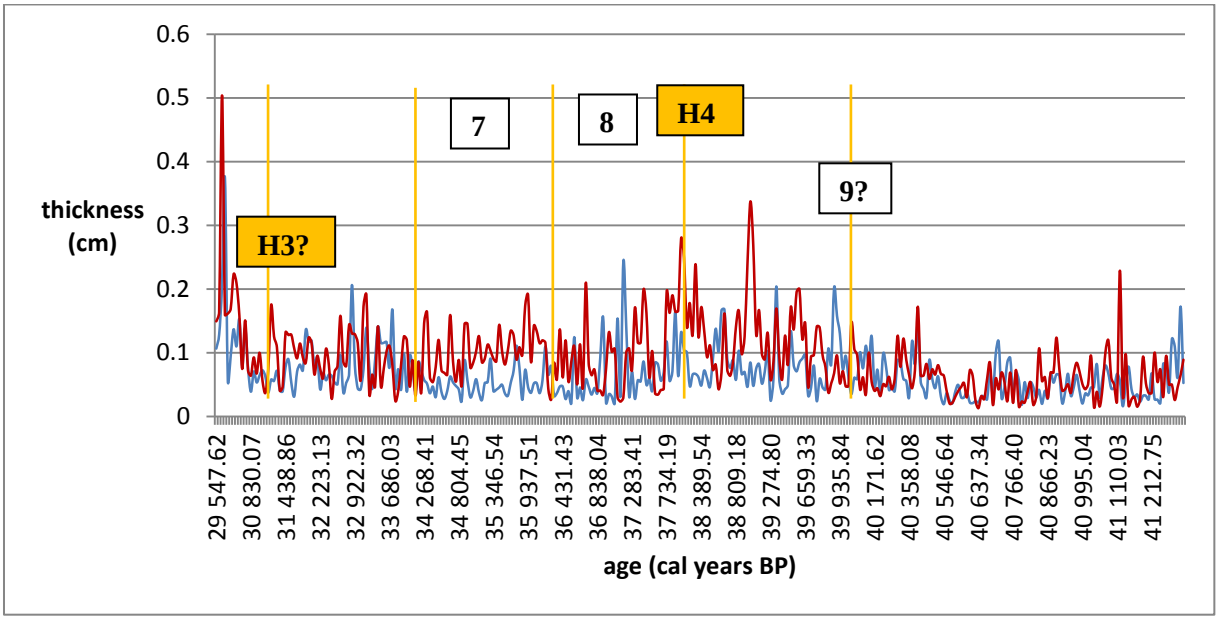

Fig. 94: The thickness of the coarse grained (red) and fine grained (blue) laminae against a time axis (moving average with subset size of 4); the numbers show the Dansgaard-Oeschger cycles, H4 = Heinrich Event 4, H3 = Heinrich Event 3, the yellow lines correspond with the yellow lines in Fig.4

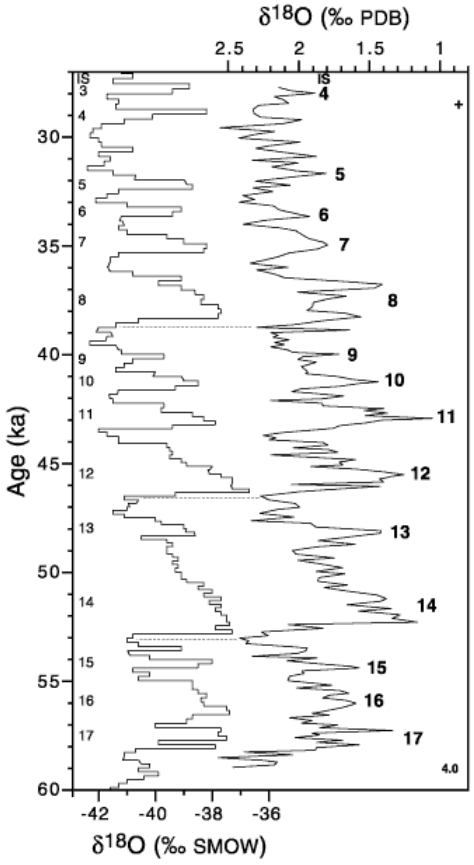

Fig. 95: Correlation of Dansgaard –Oeschger cycles between Hole 1017^{E} and GRIP for the interval between 60-27 ka, PDB = Peedee Belemnite, SMOW = Standard Mean Ocean Water; source: http://www-odp.tamu.edu/publications/167_SR/chap_21/c21_f6.htm

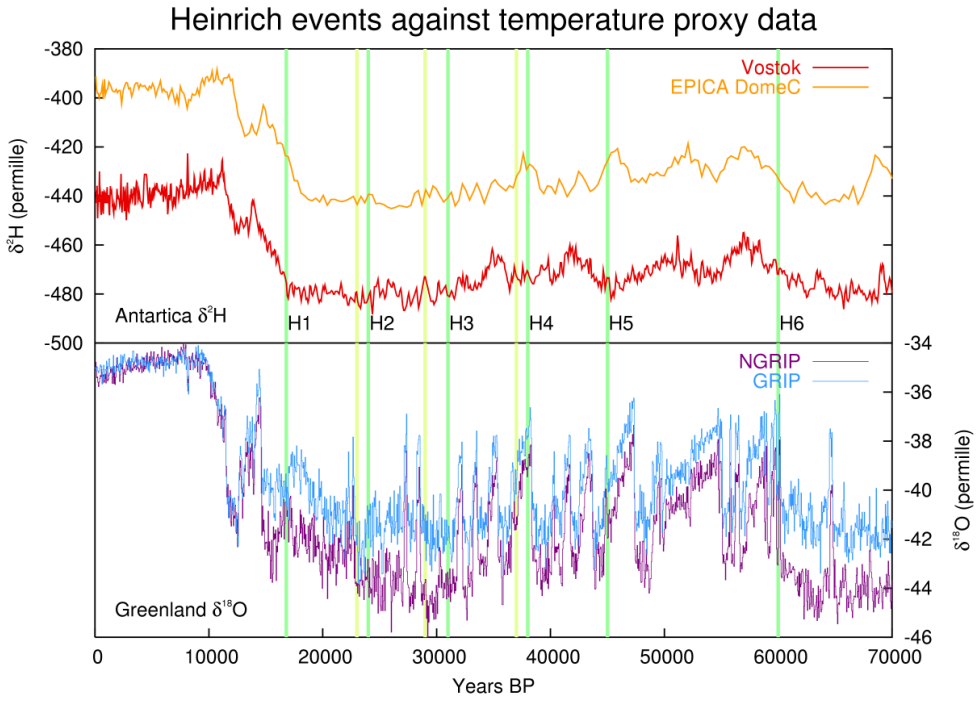

Fig. 96: Heinrich events against temperature proxy data from: Vostok, EPICA Dome C, NGRIP and GRIP; source: http://en.wikipedia.org/wiki/File:Heinrich-events.png

We will focus on the interval II (see Fig.39 from section 5.2.2), that displays clear differences with respect to intervals I and III. The Heinrich Event 4 (~38000 cal. years BP) coincides with a peak in the coarse grained lamina thickness; however, it is not the largest peak observed in the graph (see Fig.94). Consequently, it also coincides with the Dansgaard-Oeschger cycle 8, which also occurs around ~38000 cal. years BP. The gradual cooling of Dansgaard-Oeschger cycle 8 corresponds with the transition period from 37000 to 36000 cal. years BP described in section 6.2.1. Within this transition period, we described how the coarse grained laminae became thinner with respect to the period before it. In section 6.3.3, we will explain how thinner coarse grained laminae coincide with a colder climate. Therefore, this transition period can be the expression of the gradual cooling, making part of the Dansgaard-Oeschger cycle 8. This gradual cooling was preceded by a rapid warming, expressed by the thicker coarse grained laminae for the period between 37000-39000 cal. years BP. Additionally, the coarse grained and fine grained laminae differ in peak height within this period (37000-39000 cal. years BP). The Dansgaard-Oeschger cycle 7 coincides with the period from 36000 up to 34169 cal. years BP, within which the coarse grained laminae show a larger thickness and differ in peak height from the fine grained laminae. However, if we look closer, the coarse grained laminae are slightly thicker around 36000 cal. years BP and become thinner at the upper part of this period (around 34000 cal. years BP). This is similar to what was observed for Dansgaard-Oeschger cycle 8, only less pronounced. Possibly the Dansgaard-Oeschger cycle 8 was better pronounced because it coincides with the Heinrich Event 4. The Heinrich Event 3 and the Dansgaard-Oeschger cycle 9 are not expressed clearly in the laminae thickness data; therefore, no claims were made for these periods (see Fig.94).

6.2.3 Computer analysis

The computer analysis yielded 1272 couplets in total, over a time span of around 11900 years. As for the microscope analysis, a weak correlation exists between all the coarse grained laminae and all the fine grained laminae. Similarly with the microscope analysis, the minimum thickness of the fine grained laminae, move to larger values with rising thickness of the coarse grained laminae. However, for the computer analysis, the coarse grained laminae show a much more constant minimum thickness than for the microscope analysis. The couplet thickness is much better correlated with the coarse grained laminae (R^2= 0.7445) than with the fine grained laminae (R^2= 0.3175). The couplet thickness therefore depends on the thickness of the coarse grained laminae, as we also found with the microscope analysis.

Selecting the low-lightness laminae and intermediate-lightness laminae made clear that the low-lightness laminations have a larger minimum thickness than the intermediate-lightness laminations.

For building up the fine grained part, sediments with grain sizes of (<0.01) to 0.01 mm (low-lightness laminae) play a more important role than the sediments with grain sizes of 0.01 to 0.05 mm (intermediate-lightness laminae).

The results from the variations through time show a resemblance with the microscope measurements. The variations in couplet thickness and coarse grained lamina thickness show peaks of the same direction, as well as for the variations in fine grained lamina thickness compared with the couplet thickness. However, the peak height of the coarse grained lamina thickness is closer to the peak height of the couplet thickness than the peak height of the fine grained lamina thickness is (see Fig47., Fig.48 and Fig.49).

Furthermore, for the variations in time for the low-lightness laminae and intermediate-lightness laminae, it was noticed that the low-lightness laminae with a thickness of at least 0.15 cm coincide or follow Dansgaard-Oeschger cycles and/or Heinrich Events. For Dansgaard-Oeschger cycle 9 (~40000 cal. years BP), we found a low-lightness lamina peak of > 0.2 cm, followed by a peak of > 0.15 cm at 39000 cal. years BP. Dansgaard-Oeschger cycle 8 and Heinrich Event 4 correspond with a small peak of > 0.15 cm; however, over the gradual cooling period of Dansgaard-Oeschger cycle 8, a peak of > 0.25 cm (~37000 cal. years BP) and a peak of > 0.2 cm (~36000 cal. years BP) occur. Dansgaard-Oeschger cycle 7 (~35000 cal. years BP) coincides with a peak of > 0.2 cm, followed by a higher peak of > 0.25 cm (34000 cal. years BP). Finally, Dansgaard-Oeschger cycle 6 (~33000 cal. years BP) and Dansgaard-Oeschger cycle 5 (~32000 cal. years BP) concur with a peak of > 0.15 cm.

This possibly holds a promise in detecting Dansgaard-Oeschger cycles, and even Heinrich Events, in laminated sedimentary records from the Southern Hemisphere. The fact that we can find some kind of distinguishable characteristics in this laminated record, which furthermore seem to coincide with the Dansgaard-Oeschger cycles of the Northern Hemisphere, can give a hint towards the suggestion of globally synchronous Dansgaard-Oeschger cycles.

6.2.4 Comparison of the two analysis methods

There are some small differences between the results obtained through a microscope analysis and a computer analysis. The total amount of couplets found with the microscope analysis was more (1347 couplets) than with the computer analysis (1272 couplets). With the computer analysis, one depends on digital images with a limitation in resolution, which caused some problems as the images were not all sharp enough to see much detail. Additionally, it is not possible to zoom in on the laminations in order to better distinguish them; yet, with the microscope it is possible to zoom in. The minimum thickness measured with the microscope was also smaller (0.001 cm) than with the computer

measurements (0.008 cm). The microscope makes it possible to zoom in, with the computer there was a problem that for very small laminations the lines, those used in the analysis program to mark the boundaries between laminations, were sometimes as thick or thicker than the laminations themselves. Another problem with the characteristics of the laminations was that if they are curved it is very difficult to perform precise measurements. However, the computer measurements went five times faster than the microscope measurements. Furthermore, we did not have overlapping zones in the measurements with the computer analysis because one has a view of the current and following image at the same time. Image analysis also provides a better overview, and it is stratigraphically more logical to measure from bottom to top through the whole core. The preparation of the digital images for the computer analysis takes less time than the preparation of the thin sections for the microscope analysis. Though, we could only scan images of around 5 cm in length in turn.

Fig.97, Fig.98 and Fig.99 below compare the microscope analysis results with the computer analysis results for all the couplet thicknesses, all the fine grained, and all the coarse grained lamina thickness. There is a strong resemblance in the position of the peaks; however, the peak height for both the analysis methods are not everywhere the same because of the reasons mentioned above. For the couplet thickness, the measurement results differ the most for both the analysis methods between 41239 and 40488 cal. years BP and between 31907 and 29483 cal. years BP. The same is true when we compare the results for all the coarse grained lamina thickness. This is as well the case for all the fine grained lamina thickness, however, the results for both analysis methods are also different between 37406 and 34169 cal. years BP.

Besides the advantages and disadvantages of both the methods, it becomes clear that using different methods together will always give stronger results than focusing on only one method. Combining methods will make it possible to extract as much information from a record as one can.

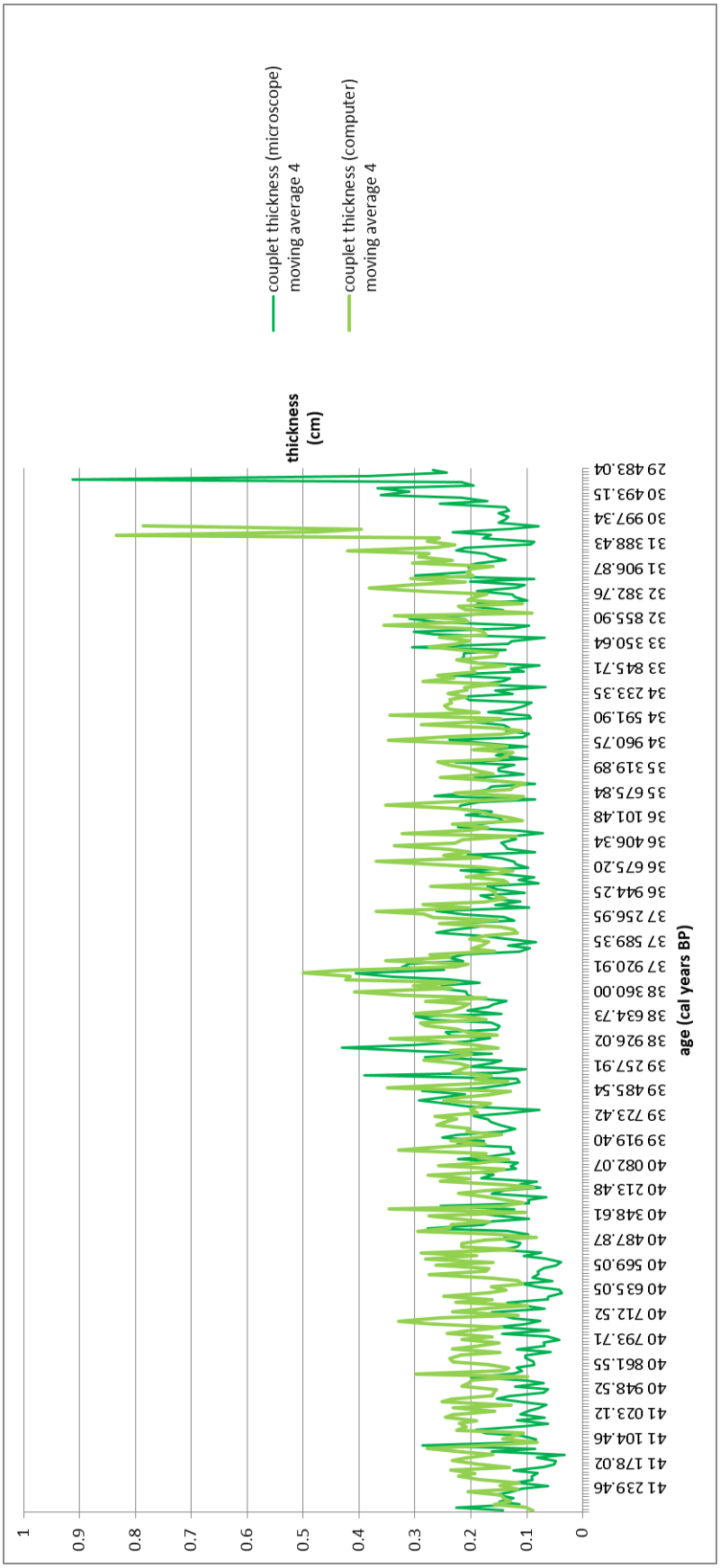

Fig. 97: comparing couplet thickness for computer analysis and microscope analysis techniques

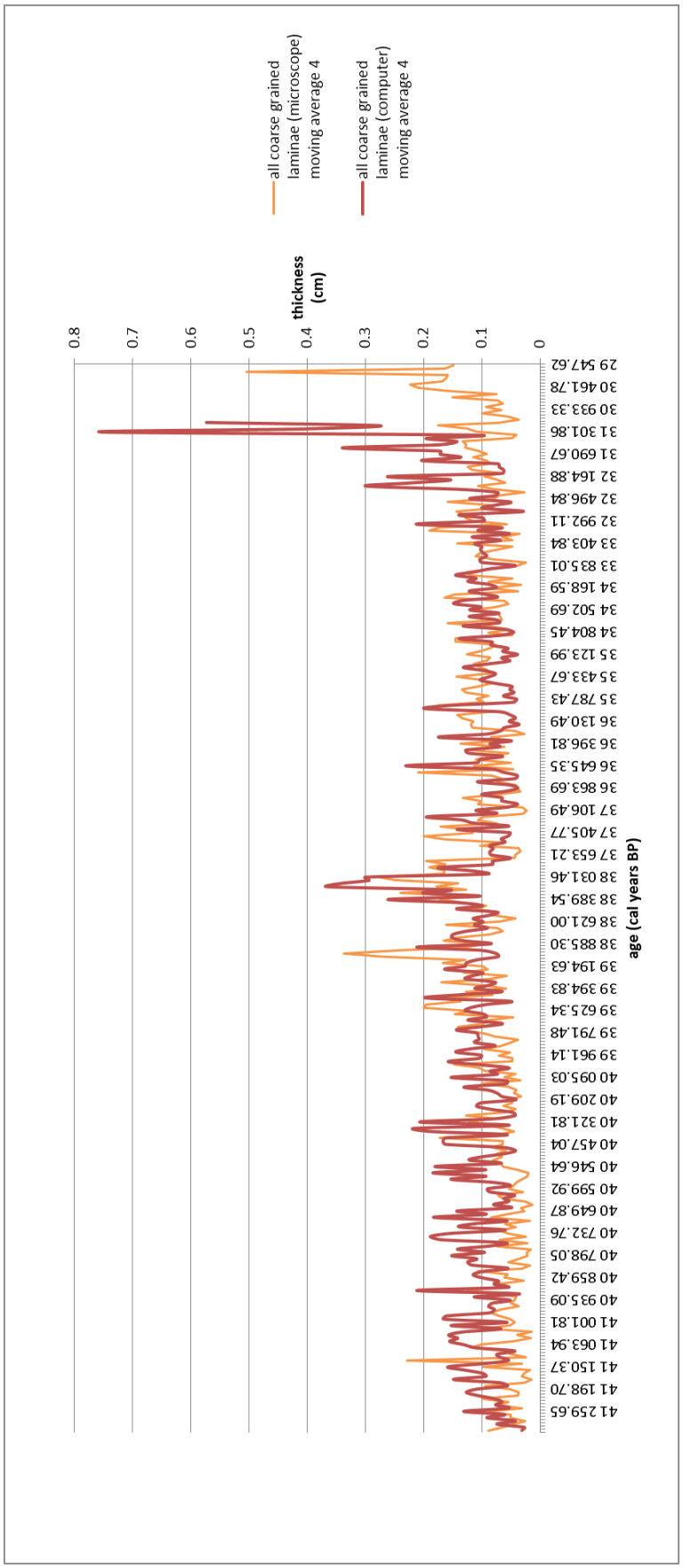

Fig. 98: comparing all coarse grained lamina thickness for computer analysis and microscope analysis techniques

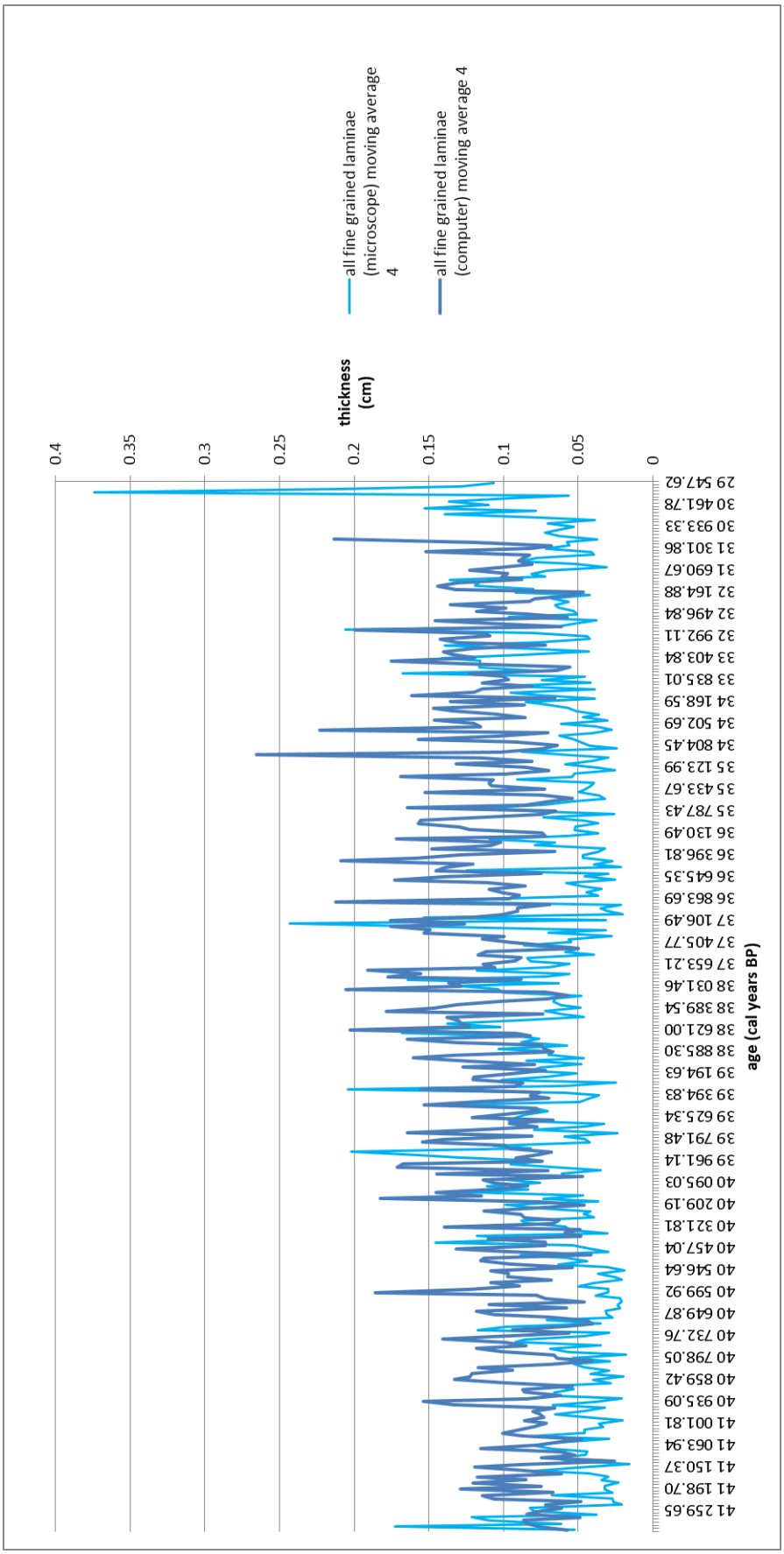

Fig. 99: comparing all fine grained lamina thickness for computer analysis and microscope analysis techniques

6.3 µ-XRF analysis

6.3.1 µ-XRF on sample PAR1A-III(50-60)

In what follows, we will compare the µ-XRF results with the grain size measurements, obtained from the petrographic microscope observations. The elements Ca and Si showed a clear preference for the coarser grained laminations, whereas Fe and K displayed a preference for the finer grained laminations. Although the elements Al and Ti showed no clear preferences, the element Ti will be considered as occurring in coarser grained sediments (see further). Some of the ratios calculated from these elements can be used to recognize grain size changes. The coarser grained laminations are expressed by high values of the log(Ca/K), log(Si/K), log(Al/K), log(Ca/Ti) and log(Si/Ti) ratios, whereas low values of these ratios coincide with the finer grained laminations. High values of the log(Fe/Al), log(Fe/Si), log(Fe/Ca) correspond with the finer grained laminations, whereas the coarser grained laminations show low values of these ratios. From the color analysis on the sample PAR1A-III(50-60), we could infer that high L-value coincide with coarser grained parts. Additionally, the elemental ratio variations correspond to the L-value. Therefore, these ratios are considered to be very useful in detecting grain size changes and show potential for use on the time scale of the whole record.

The log(Fe/Ti) and log(K/Ti) ratios can also be used for identifying grain size variations; however, they show a particular trend as well. For the log(Fe/Ti) ratio, for example, rising values over the finer grained parts were observed, followed by a sudden drop when a coarser grained part was reached. Over the coarser grained parts the log(Fe/Ti) ratio stays low. This explains that Ti is prominently present in the coarser grained parts, but that the Ti content gradually lowers through the fine grained lamina following the coarse grained parts, which can point to a fining upwards trend. The next drop in the log(Fe/Ti) ratio coincides with the boundary of the next coarse grained lamina.

6.3.2 Hypothesis of glacier fluctuations in the Laguna Parrillar area

As discussed above, the knowledge obtained on elemental ratios can be used on the time scale of the whole record. Furthermore, the log(Fe/Ti) ratio shows a particular trend in which the lowest ratio values coincide with the coarser grained parts, and the gradually rising ratio values explain changes through the finer grained parts.

These facts, together with the conclusions from the research of Kaiser and Lamy (2007, 2010), will be used to construct our hypothesis. Kaiser and Lamy (2007, 2010) did research on a core from ODP Site 1233 off the Chilean coast. They concluded that Fe and Ti are good proxies for terrigeneous input from the hinterland. Because they observed that Fe and Ti maxima coincided with glacier advances on

land, they inferred that Fe and Ti can be used to detect fluctuations in glacial activity. However, Kaiser and Lamy (2007, 2010) used Fe and Ti counts separately, and without log-ratios, whereas, we used the log(Fe/Ti) ratio. In what follows, our hypothesis will be explained (see Fig.100, Fig.101).

During periods with a colder climate and/or more precipitation, a glacier can grow and will therefore be more active. A glacier that is more active will erode more sediments than when it is less active. If more eroded sediment is formed, more sediment can be transported towards the lake. If there is more sediment, than thicker layers can also be formed. Thicker coarse grained layers will proportionally contain more Ti than thinner coarse grained layers. Consequently, these Ti maxima coincide with time periods in which the glaciers in the surrounding area are more active and growing.

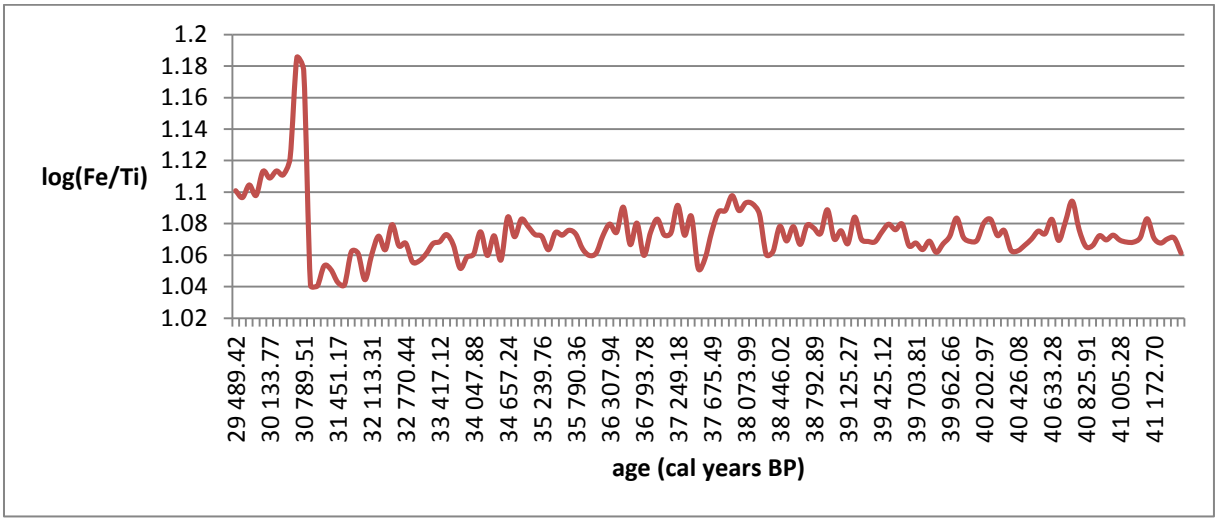

Fig. 100: **The log(Fe/Ti) ratio on the time-scale of the whole record (moving average with subset size of 20)**

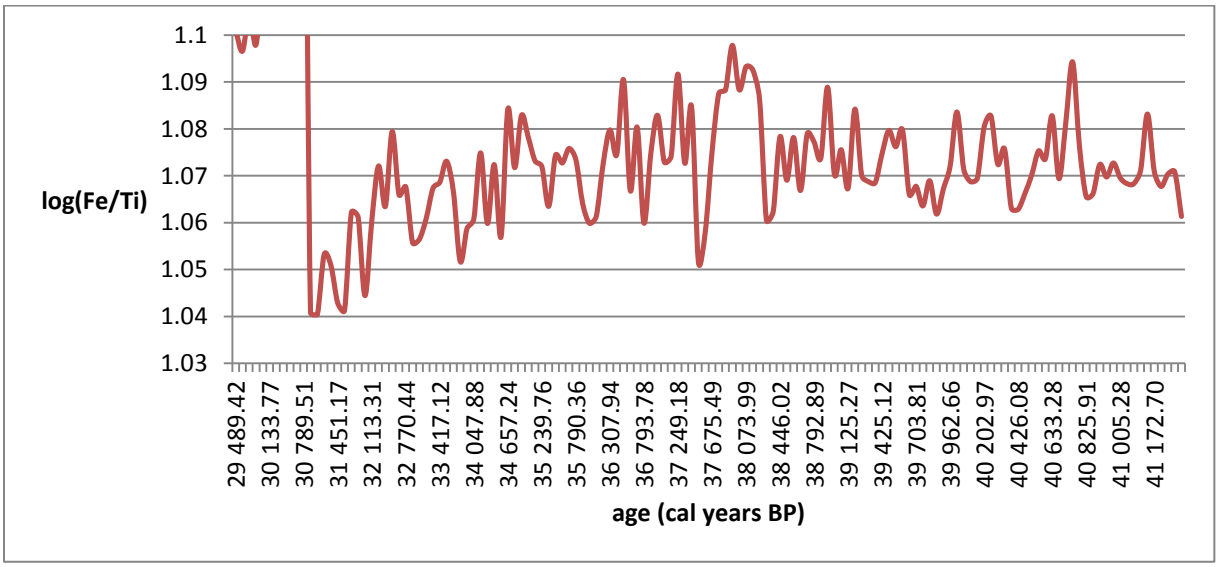

Fig. 101: Zoom of Fig.11; the log(Fe/Ti) values between 1.03 and 1.1 (moving average with subset size of 20)

This hypothesis was further investigated, and to do so, the amount of ice-free layers (=coarse grained layers) within intervals of 100 years were selected from the microscope analysis data (see Fig.103). We found a general trend towards less ice-free layers per 100 years. Additionally, the sum of the thickness of the ice-free layers per 100 year interval was calculated (see Fig.104). The general trend is one moving towards smaller total thickness of the ice-free layers. Looking closer to the log(Fe/Ti) graph, a trend towards lower values can be observed as well.

Between 41000 and 38000 cal. years BP, there is a quick drop in the amount of ice-free layers, after which this amount continues to drop at a slower rate. If there are less ice-free layers, climate in the area became colder. We assume that an ice-free layer lasts for one summer season, and at least every winter, the lake is completely covered by an ice-layer. Consequently, if there are less ice-free layers per 100 year interval, climate is colder, since the total amount of time that the lake is completely covered with an ice-layer is longer. What we actually see is that in a 100 year interval there are less cycles in which the lake is alternating between: covered by ice or not covered by ice. We will give a hypothetical example: when we count 10 ice-free layers in a 100 year interval, it means that the lake will be open for 10 summer periods, however, the lake will be continuously closed for the rest of the time within that interval, thus for 90 years. Whereas, if we count 50 ice-free layers within a 100 year interval, the lake will be open for 50 summer periods, and continuously closed for the rest of this interval, which is in this case for 50 years. This can mean that the laminations accumulating in the lake come very close to being yearly, at least during restricted time periods.

Within this line of thought, we can understand why the total thickness of the ice-free layers is smaller within the colder period between 38000 and 29000 cal. years BP. If the lake opens and closes many times (e.g. 50 times) within a 100 year interval, there is a greater chance for the sediment to accumulate in the lake. If, on the other hand, the lake does not open and closes many times within a 100 year interval (e.g. 10 times), then less sediment will have accumulated in the end. We further want to emphasize that there are similarities between the trend for the amount and total thickness of the ice-free layers, and the accumulation rate changes over the record. However, the graph with the accumulation rate (see Fig.105) does not show the changes per 100 year interval, consequently, we can only observe that there is a trend towards lower accumulation rates.

The log(Fe/Ti) ratio shows a trend that starts with fluctuations around a more or less constant value 1.07. This occurs between 41000 and 38000 cal. years BP. From 38000 cal. years BP on, there is a decrease in the log(Fe/Ti) ratio, with a steep rise around 30900 cal. years BP, after which the ratio continues decreasing. This decrease in the log(Fe/Ti) ratio from 38000 cal. years BP on, which is linked to a rise in Ti content, corresponds with the Ti counts from Kaiser and Lamy (2010), which also

rise from 38000 cal. years BP on. The period within which our log(Fe/Ti) ratio decreases coincides with the period for which a slow decrease in the amount of ice-free layers and total thickness of the ice-free layers were observed. Consequently, we have to conclude that the decrease in the log(Fe/Ti) ratio coincides with a colder climate in which the lake alternates less often between being open and closed. Although the log(Fe/Ti) ratio within this period also coincides with a decrease in total thickness of the coarse grained layers (=ice-free layers), this does not means that less eroded sediment was formed by the more active glaciers during this cold period. The Fig.102 displays how thick the ice-free layers were per 100 year interval. From 38000 cal. years (except for the period between 29000 and 30000 cal. years BP), we see that the ice-free layers are less thick than during the warmer period (38000-41000 cal. years BP). A Possible explanation could be that climate was too cold, and therefore less melt-water was able to form during the early summer season. Thus, less sediment was also transported into the lake. Consequently, the ice-free layers during a cold climate are thinner than the ones formed under a warmer climate.

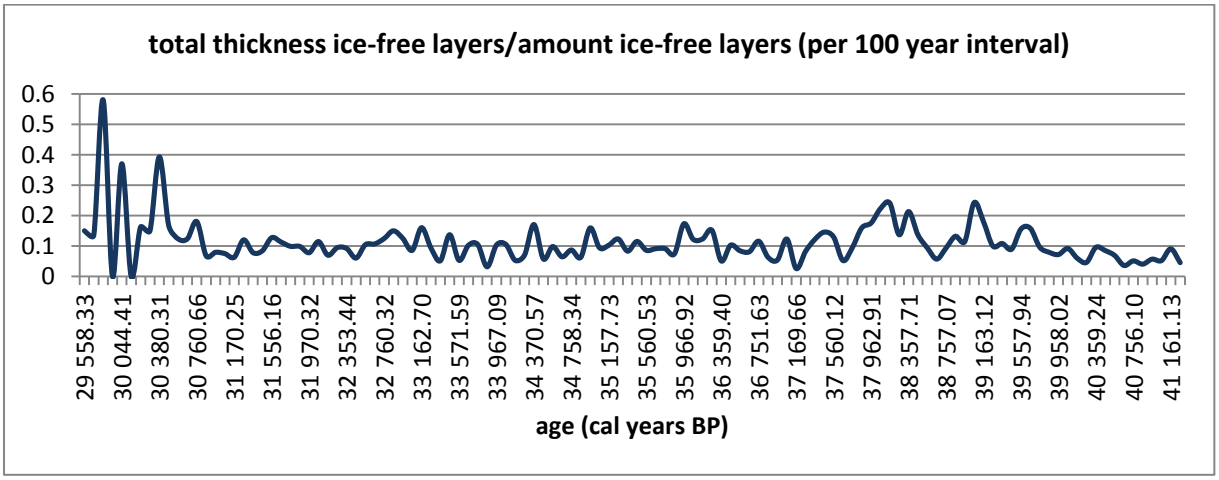

Fig. 102: The thickness of the ice-free layers per 100 year interval; Total thickness ice-free layers/amount ice-free layers against a time axis

Finally, we can conclude that a decreasing log(Fe/Ti) ratio describes a climate that becomes colder (possibly combined with more precipitation), with growing and more active glaciers that will produce more sediment through erosion, and with proportionally more Ti. However, within a 100 year interval (for this colder climate), the lake will stay closed longer, alternating with periods in which the lake is open during summer. Therefore, the total amount of coarse grained layers that are able to accumulate will be lower, consequently, the total thickness of these layers will be lower. Additionally, these ice-free layers are thinner, since less melt-water is formed because the climate is too cold, and therefore less sediment is transported into the lake. Nevertheless, the ice-free layers formed during the colder period (between 29000 and 38000 cal. years BP), will contain more Ti than the layers formed in a warmer climate, as the glaciers in the area are more active. All the extra sediment produced by the

more active glacier will proportionally have more Ti, but the sediment has less opportunities to reach the lake, because the lake stays closed longer, and there is less melt-water to transport the sediment. However, the sediment that does reach the lake will contain more Ti.

We also want to make the remark that we used the log(Fe/Ti) ratio because of the particular trend they revealed; furthermore, we were able to compare our results with the research by Kaiser and Lamy (2007, 2010). However, possibly other elemental ratios can be used as well, since we discovered other useful ratios which can express variations in grain size.

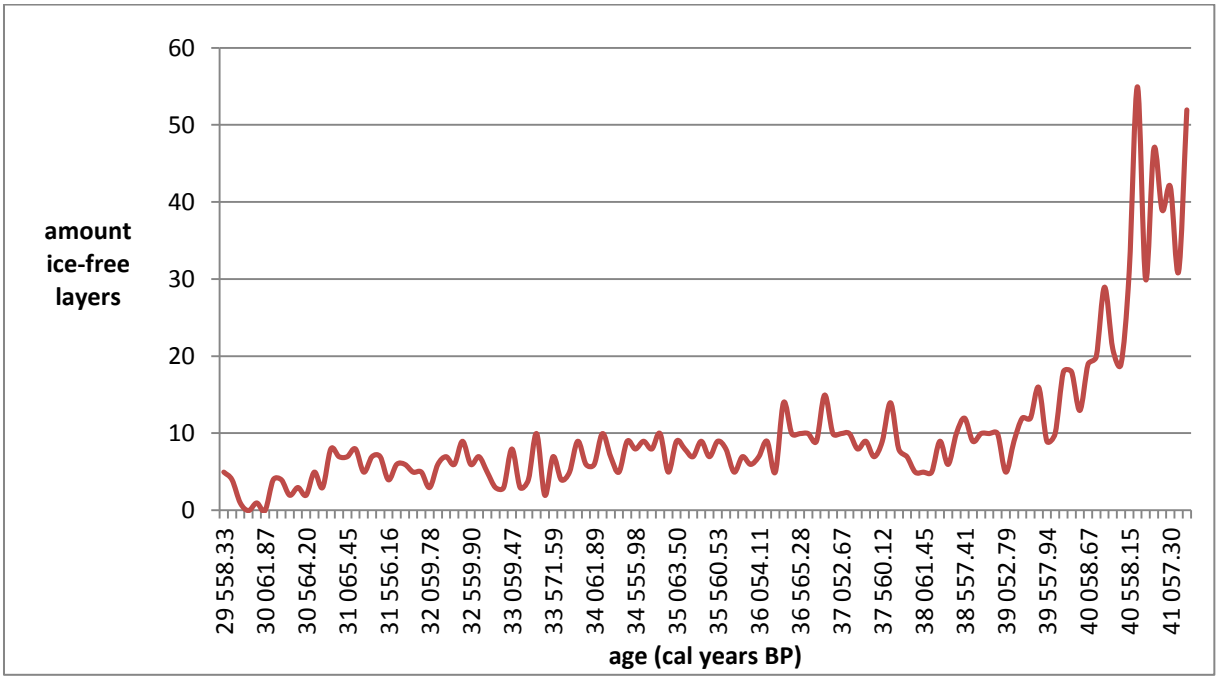

Fig. 103: Amount of ice-free layers per 100 year interval

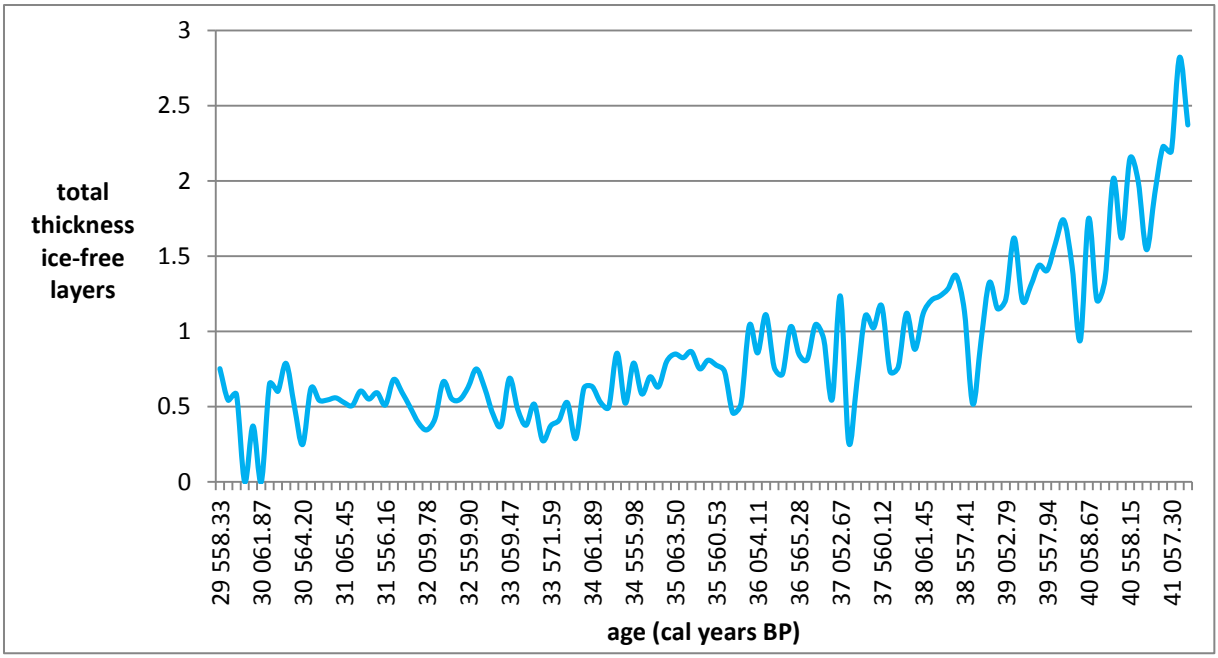

Fig. 104: Total thickness of all the ice-free layers per 100 year interval

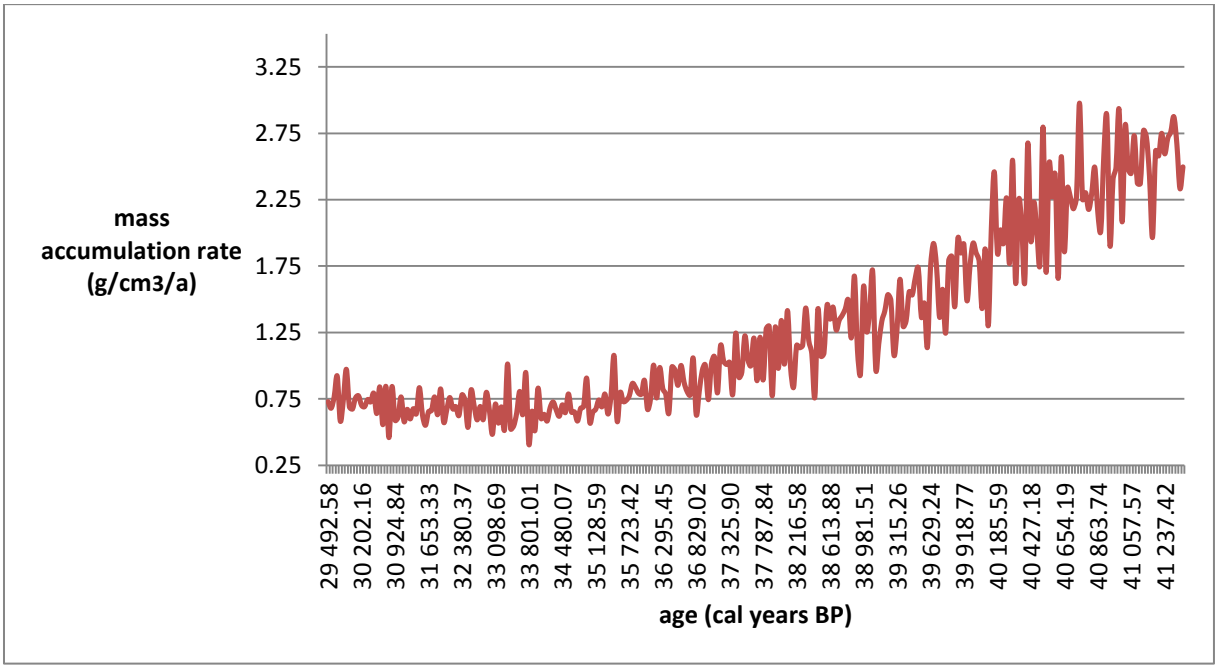

Fig. 105: The mass accumulation rate changes against a time axis

6.3.3 Comparison of the hypothesis with recent research on Patagonian Ice Sheet fluctuations

Similarities can be found between the results from the research of Caniupán *et al*. (in press) with the hypothesis discussed for this study (see section 6.3.3). Nevertheless, Caniupán *et al*. (in press) concluded that they observed a long-term warming trend between 50000 and 25000 years BP. We can clearly see on Fig.106 that our time period (41000-29000 cal. years BP) is a period within which a cooling can be observed as part of the larger warming trend discovered by Caniupán *et al*., (in press). Consequently, this can confirm our claim that the general trend (between 41000 and 29000 cal. years BP) towards less ice free layers (see Fig.103) corresponds to a climate that becomes colder.

During late MIS 3, Caniupán *et al*. (in press) detected high values of ice rafted debris and concluded that these coincide with ice sheet advances. This is also a conclusion that fits in our hypothesis, within which we claimed that the glaciers in the area of Laguna Parrillar became more active from 41000 to 29000 cal. years BP.

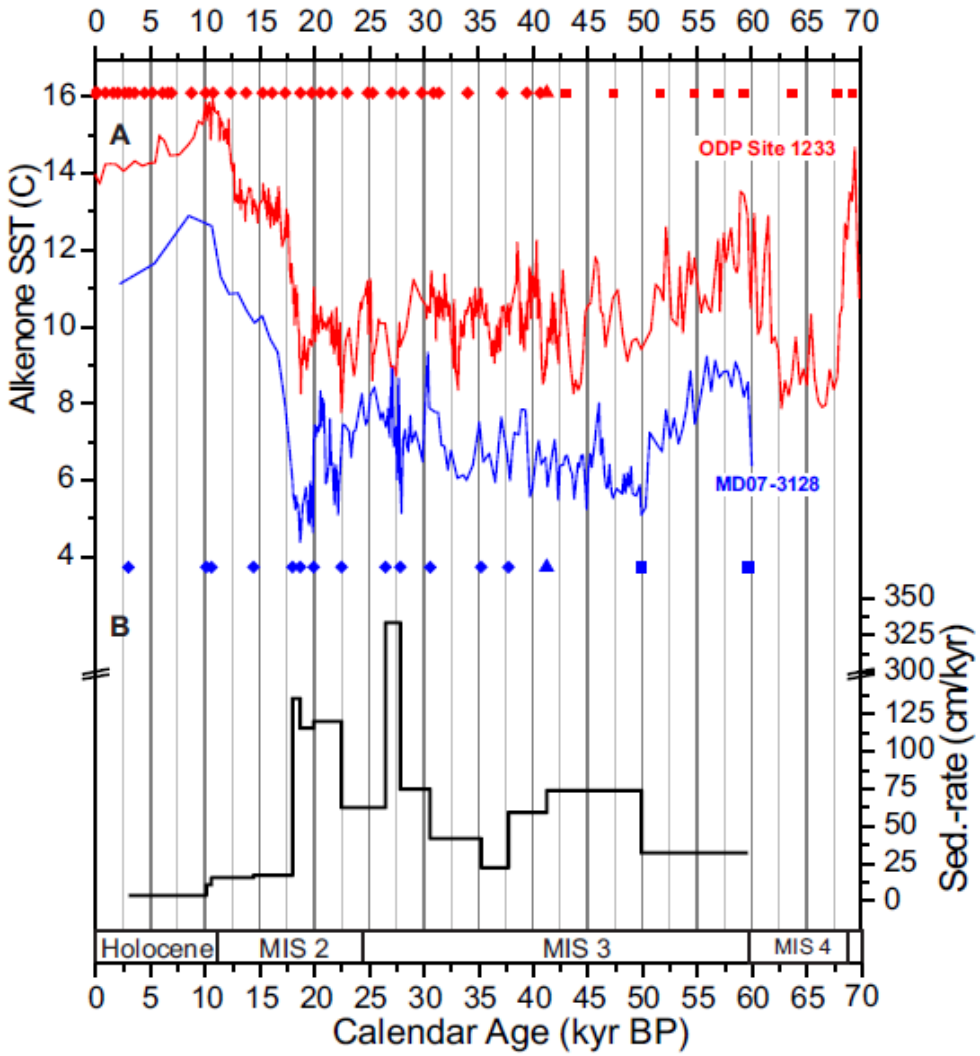

Fig. 106: **Alkenone-based sea surface temperatures for ODP Site 1233 (Kaiser and Lamy, 2010) and for core MD07-3128 (Caniupán *et al.* ; in press) Source: Caniupán *et al.* (in press)**

6.4 Detecting cyclicities through spectral analysis on the color analysis

6.4.1 Color analysis

In what follows, we will discuss the potential of the color analysis performed on the whole record in detecting cyclicities. The cyclicities will be discussed in the following sections. The L-value peaks correspond with the b-value peaks, which are of the same direction. The a-value peaks have an opposite direction. Only a few time periods have laminations with a combination of green, yellow, and a high-lightness (see Fig.107). The rest of the core has a dominant combination of magenta, blue, and a low- or intermediate-lightness. Furthermore, combining color analysis results on sample PAR1A-III(50-60) with grain size data obtained on this sample revealed the fact that higher L-values indeed occur at the coarser grained parts of the sample. Additionally, we also combined µ-XRF analysis results with color analysis results on sample PAR1A-III(50-60). The ratio values, for which we concluded that they correspond with coarser grained laminations, also correspond with higher L-values (see Fig.108). Consequently, we can demonstrate that the color analysis results performed on the whole record can illustrate different types of changes through the core; for example one can detect changes in grain size or even changes in chemistry. Therefore, we consider the color analysis useful in detecting cyclicities.

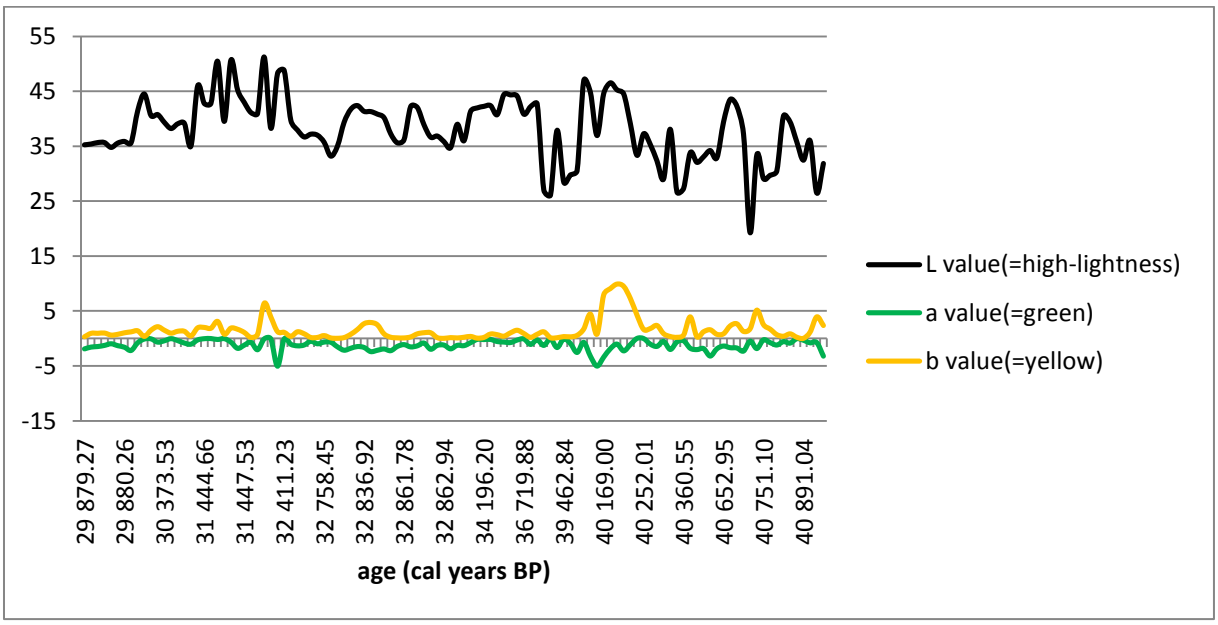

Fig. 107: The a-value < 0 and the b-value > 0 and their corresponding L-value (i.e. high-lightness) selected from the record

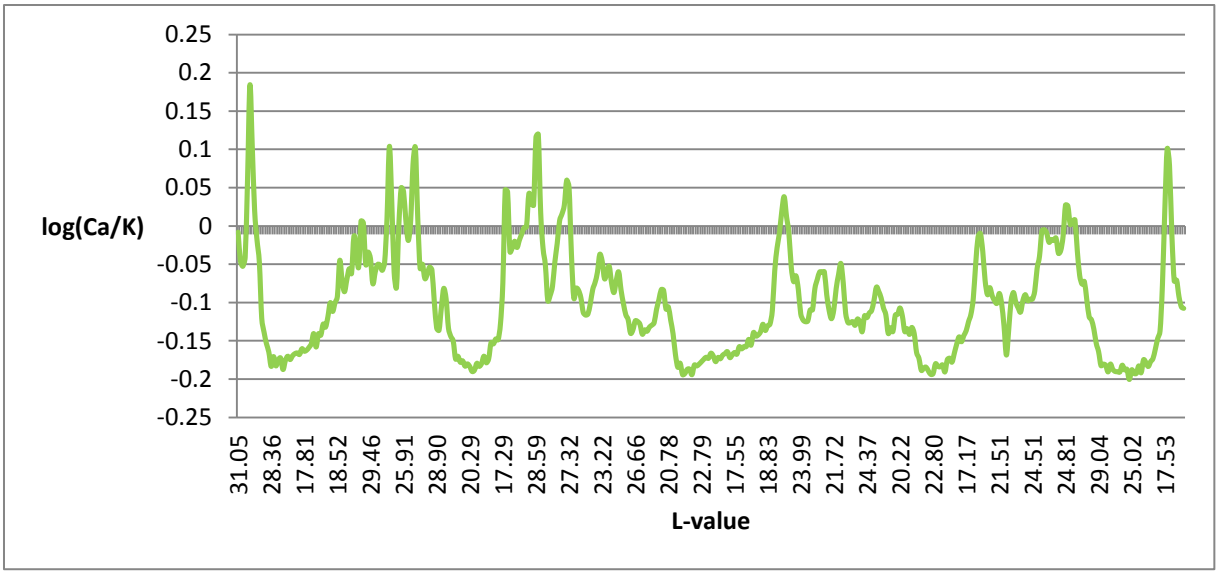

Fig. 108: The log(Ca/K) ratio against the L-value; high log(Ca/K) values correspond with coarser grained laminae, here the graph makes clear that the high values for this ratio also correspond with higher L-values

6.4.2 The cycles unraveled by spectral analysis

Comparing the Tukey-Hanning spectral method with the Bartlett method, we can conclude that many more cycles can be found with the Tukey-Hanning method (see Fig.109 for an example from the Tukey-Hanning method). However, we have to point to some problems. The Tukey-Hanning method yielded so many cycles that it was difficult to separate the important cycles from all the rest. It especially became very difficult for the high frequency (smaller periods) part. Using a logarithmic scale did not give better results. However, studies on climate cyclicities which use spectral analysis (e.g. Fagel *et al*., 2008 and Zhang *et al*., 2010) also calculate confidence intervals, so that they can select the peaks that are lying in between 90 or 95 percent confidence intervals.

From the many peaks, we selected those that appeared as very distinct, however, at lower than a period of 10 years, it was difficult to distinguish between the cycles or to decide which cycles could be more important. The L-value, a-value and b-value had the following cycles in common: 10-20 (clear peaks: between 15-20 years and around 11-13 years), 20-30, 38, 40-50, 50-60, 60-70, 70-80, 80-90 (most clear: 82, 84, 85/86), 90-100 (most clear: 92/93, 95) years. Also more isolated cycles of 201/202 years and 289 years could be extracted.

Some of the cycles that were clearly distinguishable were only found for the L-value, a-value or b-value datasets. We will further focus on the cycles between 10 and 80 years found for all the three datasets, since these will contain the most important climate information. In the following section, we will try to explain what the forcing factors could be behind these cyclicities.

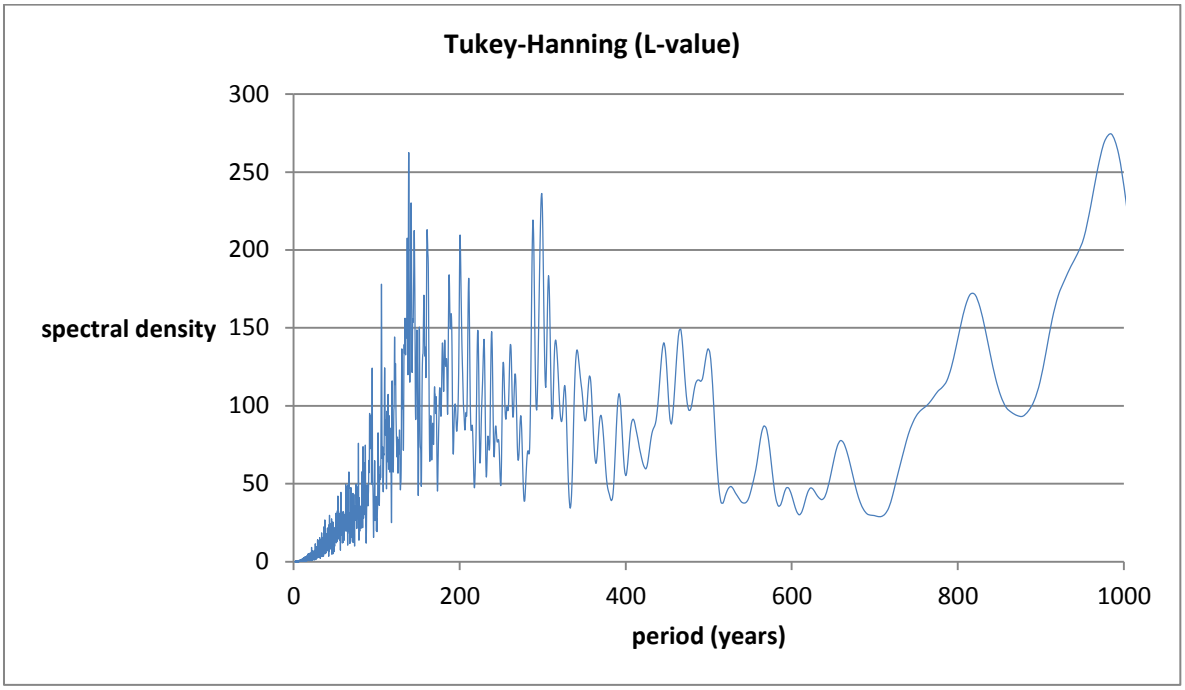

Fig. 109: An example showing the results from the spectral analysis on the L-value dataset using the Tukey-Hanning spectral method; spectral density against period

6.5 Explaining cyclicities

We will involve two possible forcing factors as an explanation for the observed cyclicities: the Antarctic Oscillation and El Niño Southern Oscillation. Zhang *et al*. (2010) did a statistical reconstruction of the Antarctic Oscillation Index for austral summer (December-January-February) based on multiple proxies from the Southern Hemisphere. They performed a power spectral analysis and found the following distinct leading periods during the last 500 years: ~37.6, ~24.1, ~12.6, ~6.8, ~6.3, ~5.1, ~3.5, ~2.6, ~2.4 and ~2.1 years. They also concluded that their reconstruction can be considered reliable for the last 460 years.

Allen (2000) explains that spectral analyses of global historical sea surface temperature and mean sea level pressure anomalies revealed the following significant climate signals: at 2-2.5, 2.5-7, 11-13, 15-20, 20-30, and 60-80 years and a long-term secular trend. The El Niño Southern Oscillation (ENSO) signal consists of quasi-biennial (2 to 2.5 years) and lower frequency (2.5 to 7 years) components. These components interact to produce important modulations of the ENSO phenomenon, whereas the longer duration characteristics and climate fluctuations are the result of decadal- to secular-scale influences. Long lasting El Niño and La Niña phases are explained by the phasing of quasi-decadal (11-13 year) and interdecadal (15-20 year) ENSO-like signals with higher frequency (2-2.5 year) and lower frequency (2.5-7 year) components (Allen, 2000).

In our record, we found cyclicities between 15 and 20 years and between 11 and 13 years, which can be explained by ENSO-like cycles. Furthermore, we found cyclicities around 38 and 24 years, which seem to be connected with Antarctic Oscillation cycles.

Because the cyclicities for ENSO and the Antarctic Oscillation are the results from studies of more recent time periods, we do not know if these oscillations would have had the same expression within the time period of 29000 and 41000 years BP. We can only suggest that these climate oscillations could have had an influence on our record, because of the similarities in the cycles that we found.
However, calculating the cyclicities for the ice-free layers (discussed in the section 6.3.2), for example, yielded the following cycles (displayed in Fig.110): 10, 11.1, 14.3, 16.7, 20, 33.3, 50, and 100 years. The cycles of 11.1, 16.7 and 20 years appear to be close to ENSO-like cyclicities, thus the coarse grained laminae could possess the expression of an ENSO-like phenomenon.

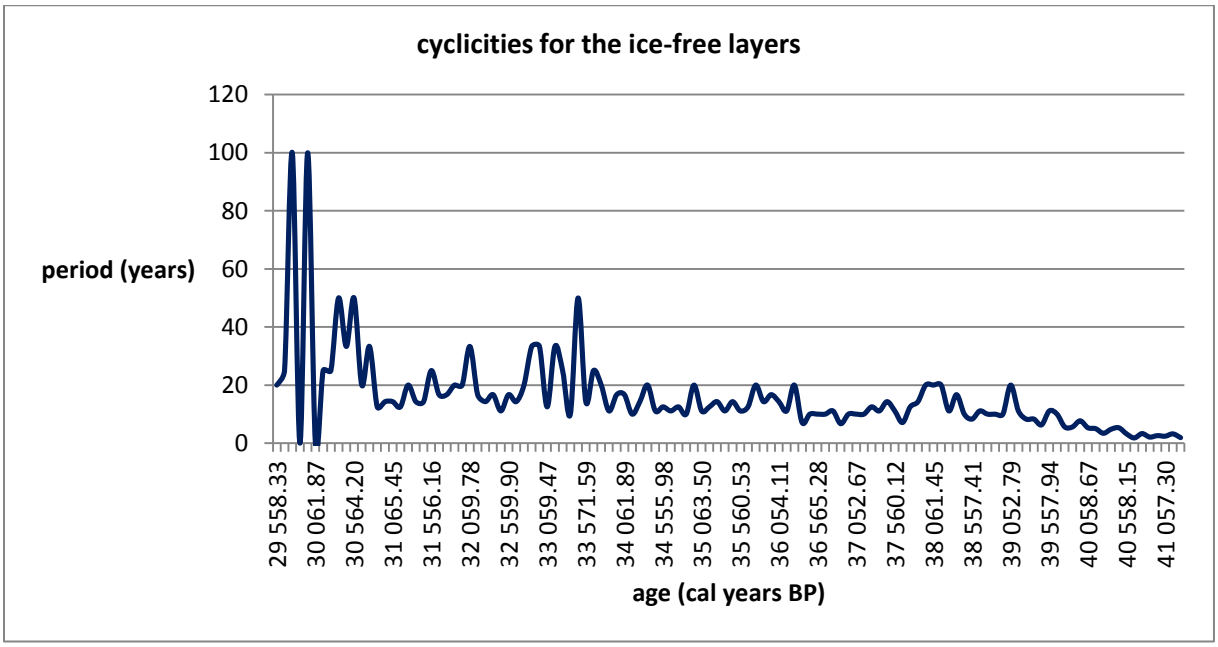

Fig. 110: the cycles per 100 year interval for the ice-free layers (calculated from the microscope measurements); period against a time axis.

7. Conclusions

The petrographic microscope observations, together with information from previous research, allowed us to build up a lamina formation model. There are three different types of laminae: 1) silt-sand laminae with a high-lightness and grain size between 0.01 and 0.15 mm, 2) coarse grained silt with an intermediate-lightness and grain size between 0.01 and 0.05 mm, 3) very fine silt with a low-lightness and a grain size between (<0.01) and 0.01 mm. In our lamina formation model, the sediment is brought into the lake through rivers and/or melt-water floods. The coarser grained sediments settle down first, according to Stokes' law, and the finer grained sediments settle down much later, when the lake is covered by an ice-layer and water turbulences decrease. The laminations are not seasonal and therefore not varves. We found 1347 couplets through microscope analysis and 1272 couplets through the computer analysis. Over a time span of around 11900 years, we had to find around 11900 couplets to make the laminations seasonal. However, some of the laminations are possibly seasonal or almost seasonal during very restricted time periods, since the accumulation rate changes through time. Furthermore, no diatoms were found in the record, since organic matter is floating on the water surface at the central part of the lake (nowadays, but possibly also 29000 to 41000 years ago), and therefore blocking all sunlight on which the diatoms depend.

Laguna Parrillar was likely a pro-glacial lake in the early history of the lake; however, since the last glacial period, it was a lake surrounded by glaciers. The lake existed in an environment with fluctuations in the Patagonian Ice Sheet activity, dust production, wind activity, and changes in moisture and vegetation cover.

For the microscope analysis, as well as for the computer analysis, we found that the coarse grained laminae have a constant minimum thickness, whereas the fine grained laminae move to a larger minimum thickness when the thickness of the coarse grained laminae rises. Both of the analysis methods yielded a good correlation between the couplet thickness and the thickness of the coarse grained laminae. We therefore inferred that the couplet thickness depends on the thickness of the coarse grained laminae, which depend on the discharge magnitude of a melt-water flood.

An explanation for the observed differences (or similarities) between the variation in thickness of the fine grained and coarse grained laminae through time were found in Dansgaard-Oeschger cycles and Heinrich Events. Dansgaard-Oeschger cycle 7, Dansgaard-Oeschger cycle 8 and Heinrich Event 4 were clearly visible in the thickness variations of the coarse grained laminae. The start of a Dansgaard-Oeschger cycle, which is accompanied by a rapid warming, was observed as a rising thickness for the coarse grained laminae. Therefore, the coarse grained lamina thickness differs from the fine grained lamina thickness within these periods. The gradual cooling at the end of the Dansgaard-Oeschger

cycles, was observed as a decrease in thickness of the coarse grained laminae, whereby they came closer to the fine grained lamina thickness.

For the computer analysis, we also selected the low-lightness and intermediate-lightness laminae from the dataset. The low-lightness laminae appeared to have a larger minimum thickness than the intermediate-lightness laminae. Furthermore, the thickness of the intermediate-lightness laminae fluctuates between constant values, whereas the low-lightness laminae show some distinct peaks in time. These low-lightness peaks seem to coincide, or follow, Dansgaard-Oeschger cycles and/or Heinrich Events. We suggested that this can hold a promise in detecting Dansgaard-Oeschger cycles, and even Heinrich Events, in the laminated sediments of the Southern Hemisphere.

The computer analysis and microscope analysis yielded results with a strong resemblance. The position of the peaks are the same; however, the peak heights differ slightly. The microscope analysis could solve some problems inherent to the characteristics of the laminae. This was the case when the laminations were too thin are too curved to make precise measurements through the computer analysis. However, the computer measurements went five times faster than the microscope measurements. Additionally, there were no overlapping zones when using the computer analysis. Though, besides the advantages and disadvantages of both methods, we concluded that using different methods together will give stronger results than focusing on only one method.

The µ-XRF analysis yielded some useful elemental ratios to detect grain size changes. Coarser grained laminations are expressed by high values of log(Ca/K), log(Si/K), log(Al/K), log(Ca/Ti) and log(Si/Ti) ratios, the low values of these ratios coincide with finer grained laminations. High values of log(Fe/Al), log(Fe/Si) and log(Fe/Ca) ratios correspond with the finer grained laminations, whereas the low values concur with coarser grained laminations.

We used the particular trend in the log(Fe/Ti) ratio for our hypothesis of glacier fluctuations. Low values of this ratio correspond with coarser grained parts, and gradually rising values correspond with changes in the finer grained parts (fining upwards). We observed that from 38000 to 29000 cal. years BP, the log(Fe/Ti) ratio decreases (i.e. a rise in Ti), coinciding with a period in which there are less ice-free layers per 100 year interval. Therefore, we concluded that climate became colder between 38000 and 29000 cal. years BP. When climate is colder (possibly combined with more precipitation) glaciers grow and become more active and, therefore, produce more eroded sediment with proportionally more Ti (with respect to a warmer period). However, the total thickness of the ice-free layers (=coarse grained laminae) within a 100 year interval, as well as the thickness of every distinct ice-free layer, are smaller during this cold period. We argue that the total thickness is less because sediment has fewer chances to reach the lake when it is more often closed than open within a 100 year

interval. Additionally, the thickness of the coarse grained laminae is smaller, since less melt-water was able to form in this colder climate; therefore, less sediment was transported.

The color analysis over the entire record was considered very useful in detecting cyclicities, since it can illustrate different types of changes throughout the core, like grain size changes or changes in chemistry. The spectral analysis performed on the color analysis results yielded many different cycles, from which we were able to extract some important ones regarding climate change. We involved two possible forcing factors to explain the observed cyclicities: the Antarctic Oscillation and El Niño Southern Oscillation (ENSO). We found cycles of 11-13 years and 15-20 years, which can be explained by ENSO-like cyclicities. Furthermore, cyclicities around 38 and 24 year were extracted, which can be linked with Antarctic Oscillation cycles. Calculating the cyclicities for the ice-free layers (from the microscope analysis) yielded cycles of 11.1, 16.7 and 20 years, which could be the expression of an ENSO-like phenomenon.

8. Dutch Summary

Natuurlijke archieven van klimaat en milieu in verleden tijdperken, zoals gelamineerde meersedimenten, zijn noodzakelijk om ons begrip van het klimaat in het Holoceen, maar ook verder terug in de tijd, te vergroten. Zij kunnen ook nuttig zijn in het schatten van de menselijke impact op het milieu in het verleden. Indien we willen focussen op de menselijke impact op het klimaat dan hebben we informatie nodig op een temporale resolutie van minder dan 30 jaar. Gelamineerde meersedimenten zijn één van de weinige geologische archieven die deze hoge resoluties kunnen leveren.

Fig. 111: Kaart van het zuidelijke deel van Chili, met locaties van de Noord Patagonische en Zuid Patagonische ijskappen, alsook de ijskap van Cordillera Darwin, de locatie van het meer Laguna Parrillar wordt aangegeven door de pijl; bron:http://maps.grida.no/go/graphic/south_america_southern_ice_fields

Dit thesis onderzoek werd uitgevoerd op een gelamineerde sedimentkern van het meer Laguna Parrillar in zuid Patagonië, Chili (zie Fig.1). De sedimentkern werd genomen op een latitude van -53,41182°S en een longitude van -71,28645°W met het UWITEC piston core systeem en platform. Zuid Patagonië is van een exclusief belang in het klimaatonderzoek, wegens het feit dat het terrestrische klimaat archieven kan leveren in een overwegend oceanisch domein (Sugden *et al*., 2005). De meersedimenten van Laguna Parrillar kunnen gebruikt worden om de relatieve positie, sterkte en cycliciteiten te bepalen van globale atmosferische circulatie systemen. Voorts zijn meersedimenten heel interessant omdat meren kleine ingesloten waterlichamen zijn die daardoor snel op externe klimaat aandrijfkrachten kunnen reageren (Heirman K., persoonlijke commentaar). Omdat

het gebied van zuid Patagonië samenvalt met de zone waarover de zuidelijke Westerlies actief zijn, is dit gebied veelbelovend in het linken van de klimaatprocessen in de mid-latitudes met het Antarctisch domein, alsook om de verschillende, in competitie zijnde, hypotheses van mechanismen van klimaatverandering te testen (Sugden *et al*., 2005).

Voor dit thesisonderzoek werd eerst een lamina formatiemodel opgesteld door het bestuderen van één van de slijpplaatjes (PAR1A-III(50-60)) onder een petrografische microscoop. Op dit slijpplaatje werd ook een µ-XRF analyse uitgevoerd door de "X-ray Microspectroscopy and Imaging Group" met een EDAX EAGLE-III microprobe. Verder hebben we volgende onderzoeksmethodes en technieken gebruikt: Een microscoop analyse, een computer analyse, een kleuranalyse en een spectraalanalyse. Voor de microscoop analyse moesten slijpplaatjes vervaardigd worden. Daarvoor werd de sedimentkern bestaande uit drie delen (PAR1A-III, PAR1A-IV en, PAR1A-V), onderverdeeld in kleinere monsters. Dit waren sedimentblokjes van 4 cm breed en ongeveer 11 cm lang. Deze werden vervolgens bevroren in vloeibare stikstof, waarna ze in een vriesdroger werden geplaatst voor twee dagen. Na dit proces is al het interstitieel water gesublimeerd en konden de poriën opgevuld worden met een hars-mengsel via een impregnatie techniek, onder vacuüm uitgevoerd. Dit mengsel bestond uit 130 ml TRA hars, 50 ml aceton, 8 druppels MEKP (methylethyketon peroxide), 0.4 druppels cobalt(II)2-ethylhexanoate 65 wt% (katalysator) (naar een recept van Boës *et al*., 2005). Vervolgens werden de blokjes van geïmpregneerd sediment in een oven geplaatst bij 40-50 °C zodat ze verder konden uitdrogen maar ook ter compensatie van energieverliezen (tijdens de impregnatie) en om de polymerisatiesnelheid te verhogen. De blokjes werden dan middendoor gesneden. De ene helft diende voor het vervaardigen van de slijpplaatjes de andere helft werd egaal gepolijst en gebruikt voor het inscannen van de digitale beelden, nodig voor de computer analyse.

De microscoop metingen werden uitgevoerd op een microscoop gebruikt om boomringen op te meten, en dat gebruik maakt van het programma TSAPWIN. Dit gebeurde in het Laboratorium voor Houttechnologie (Faculteit Bio-Ingenieurswetenschappen). De computer analyse werd uitgevoerd gebruik makend van een script-file voor varven analyse, ontwikkelt aan Tufts University (USA, Massachusetts, Medford) (zie Fig.2). Op de volledige kern werd een kleuranalyse uitgevoerd via het programma StratiSignal in het 3D L*a*b* kleurmodel en nadien werd daar een spectraalanalyse op uitgevoerd via het programma XLSTAT.

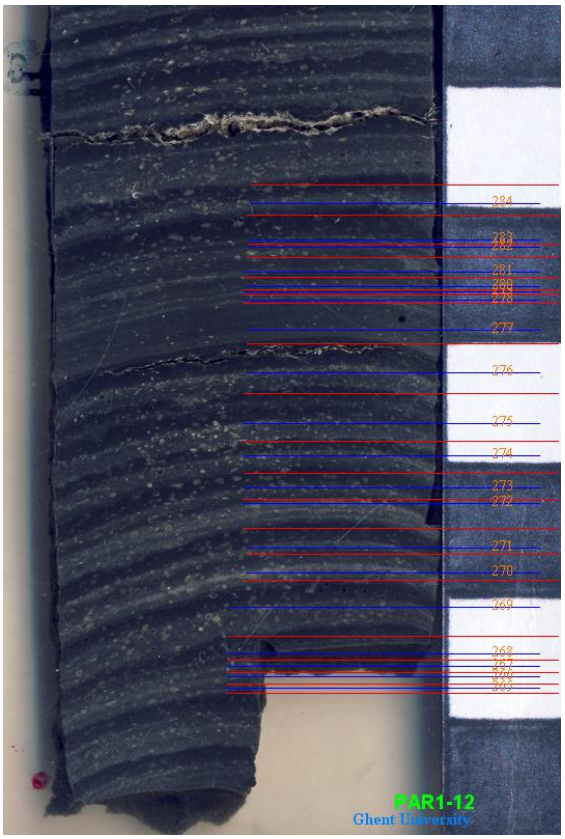

Fig. 112: Bovenste deel van het monster PAR1A-III(50-60) met de resultaten van de computer metingen, de nummers geven het coupletnummer weer, rode lijnen geven de basis van een grofkorrelige laag weer, blauwe lijnen de basis van een fijnkorrelige laag. Op een deel van dit sample werden ook de µ-XRF metingen uitgevoerd. De schaal naast het sample is een cm-schaal (1 vakje = 1 cm) en was nodig voor calibratie.

Het doel van deze studie was om hoge resolutie palaeo-klimatologische en palaeo-milieu informatie te bekomen op het Laat-Pleistocene sedimentaire record van Laguna Parrillar. We bestudeerden een tijdsperiode van ongeveer 12000 jaar (tussen 29000 en 41000 cal. years BP), overeenstemmend met laat MIS (Marine Isotope Stage) 3. Uiteindelijk wilden we kunnen besluiten of de laminaties seizoenaal zijn, en dus varven, of niet. We wilden ook bepalen welke cycliciteiten er in de kern voorkomen en besluiten trekken over de aandrijvende krachten achter deze cycliciteiten. We zullen de voordelen en nadelen van het gebruik van een computer analyse en een microscoop analyse uiteenzetten, we zullen de relaties aantonen tussen de sediment parameters en eigenschappen en zullen enkele hypotheses voorstellen.

De observaties aan de petrografische microscoop, samen met informatie uit voorgaand onderzoek, maakten het mogelijk om een lamina formatiemodel op te stellen. We stelden vast dat er drie types laminaties voorkomen in de kern: 1) silt-za nd laminaties met een hoge helderheid en korrelgrootte tussen 0.01 en 0.15 mm, 2) grofkorrelige silt laminaties met een intermediaire helderheid en korrelgrootte tussen 0.01 en 0.05 mm, 3) zeer fijne silt laminaties met een lage helderheid en

korrelgrootte tussen (<0.01) en 0.01 mm. In ons lamina formatiemodel wordt het sediment via rivieren en/of een smeltwater stroom naar het meer gebracht. De grofkorrelige sedimenten zullen, volgens de wet van Stokes, het eerst bezinken. De fijnkorrelige sedimenten bezinken later, wanneer het meer is dichtgevroren en de water turbulentie is afgenomen. De laminaties in de kern zijn niet seizoenaal, en dus geen varven. We vonden 1347 couplets via de microscoop analyse en 1272 couplets via de computer analyse. Over een tijdspanne van ongeveer 11900 jaar hadden we dus ongeveer 11900 couplets moeten vinden. Echter, sommige van de laminaties zijn mogelijks wel seizoenaal of bijna seizoenaal, aangezien de accumulatiesnelheid doorheen de tijd veranderd is. Verder vonden we geen diatomeeën in de kern, terwijl diatomeeën gewoonlijk abundant voorkomen. Dat komt doordat er aan het wateroppervlak grote hoeveelheden organisch materiaal voorkomen die het zonlicht blokkeren (tegenwoordig, maar ook evengoed mogelijk 29000 tot 41000 jaar geleden), waarvan de diatomeeën afhankelijk zijn.

Laguna Parrillar was mogelijks een pro-glaciaal meer in de vroege geschiedenis van het meer, maar sinds de laatste glaciale periode was het meer gewoon omringd door ijskappen. In de tijdsperiode tussen 29000 en 41000 jaar geleden bestond het meer in een milieu gekenmerkt door fluctuaties in de activiteit van de Patagonische ijskappen, stof productie, wind activiteit en veranderingen in vochtigheidsgraad en vegetatie bedekking.

Voor de microscoop analyse en de computer analyse vonden we dat de grofkorrelige lagen een constante minimale dikte hebben, terwijl de fijnkorrelige lagen naar hogere minimale diktes bewegen als de grofkorrelige lagen dikker worden. Voor beide analyse methodes vonden we ook een goede correlatie tussen de couplet dikte en de dikte van de grofkorrelige lagen. We leiden daaruit af dat de couplet dikte afhankelijk is van de dikte van de grofkorrelige lagen, en dat die op hun beurt afhangen van de magnitude van de smeltwater stroom.

Voor de variaties in de tijd van de dikte van de fijnkorrelige en grofkorrelige lagen, werden periodes gevonden waarin de diktes gelijkaardig zijn, en andere periodes waarin ze sterk verschillen. Een verklaring hiervoor werd gezocht in Dansgaard-Oeschger cycli en Heinrich Events. De Dansgaard-Oeschger cyclus 7, Dansgaard-Oeschger cyclus 8 en Heinrich Event 4 waren duidelijk zichtbaar in de variaties in dikte van de grofkorrelige lagen. Een Dansgaard-Oeschger cyclus wordt ingeleid door een snelle opwarming. Dit werd waargenomen als een stijgende dikte voor de grofkorrelige lagen. We konden immers ook aantonen dat de grofkorrelige lagen dunner zijn tijdens een koudere periode, ten opzichte van een warmere periode (zie verder). Door die toename in dikte, verschillen de grofkorrelige lagen sterk van de fijnkorrelige in die periode. De graduele afkoeling aan het eind van de Dansgaard-Oeschger cyclus, werd waargenomen als een afnemende dikte voor de grofkorrelige lagen, waardoor ze dus weinig in dikte verschillen met de fijnkorrelige lagen in die periode.

Voor de computer analyse werden ook laminaties met lage helderheid en laminaties met intermediaire helderheid geselecteerd uit de dataset. De laminaties met lage helderheid bleken een grotere minimale dikte te hebben dan de laminaties met intermediaire helderheid. Doorheen de tijd fluctueert de dikte van de laminaties met intermediaire helderheid tussen vaste waarden, terwijl de laminaties met lage helderheid juist geïsoleerde hoge pieken in dikte vertonen. Deze pieken blijken samen te vallen of te volgen op Dansgaard-Oeschger cycli en/of Heinrich Events. We suggereren dat dit veelbelovend kan zijn in het detecteren van Dansgaard-Oeschger cycli, en zelf Heinrich events, in de gelamineerde sedimenten van de zuidelijke hemisfeer.

De resultaten van de microscoop analyse en de computeranalyse vertonen een sterke gelijkenis. De posities van de pieken zijn dezelfde, echter de hoogtes verschillen lichtjes. De minimum dikte die met de microscoop gemeten kon worden was 0.001 cm, terwijl dat voor de computer metingen 0.008 cm was. De microscoop analyse was in staat om enkele problemen op te lossen die optraden bij de computer analyse en inherent zijn aan de karakteristieken van de laminaties. Zo waren er problemen wanneer de laminaties te dun waren of wanneer ze te veel gekromd waren. Echter, de computer analyse ging wel vijf keer sneller dan de microscoop analyse, bovendien hadden we geen overlappende zones die nadien moesten weggewerkt worden. Alhoewel beide methodes hun voordelen en nadelen hebben, besloten we dat het gebruiken van verschillende methodes samen veel sterkere resultaten geeft dan wanneer men slechts één methode zou gebruiken.

Via de resultaten van de µ-XRF analyse konden we een aantal elementratio's berekenen die heel nuttig bleken te zijn in het detecteren van korrelgrootte veranderingen. Grofkorrelige lagen worden uitgedrukt door hoge waarden van de log(Ca/K), log(Si/K), log(Al/K), log(Ca/Ti) en log(Si/Ti), terwijl de fijnkorrelige lagen overeenkomen met de lage waarden van deze ratio's. Hoge waarden van de log(Fe/Al), log(Fe/Si) en log(Fe/Ca) ratio's zijn een reflectie van de fijnkorrelige lagen, de grofkorrelige lagen komen dan overeen met de lage waarden van deze ratio's.

Er werd een bijzondere trend waargenomen voor de log(Fe/Ti) ratio. Deze bleek laag (=hoge hoeveelheid Ti) te zijn voor de grofkorrelige waarden, terwijl voor de fijnkorrelige lagen de log(Fe/Ti) ratio gradueel stijgt (mogelijks wegens een fining upwards trend). We observeerden dat van 38000 tot 29000 jaar geleden de log(Fe/Ti) ratio daalt (i.e. een stijgende hoeveelheid Ti), samenvallend met de observatie van een trend naar steeds minder ijsvrije lagen per 100 jaar interval. We besloten hierbij dat het klimaat kouder werd tussen 38000 en 29000 jaar geleden. Wanneer het klimaat kouder wordt (mogelijks gecombineerd met meer precipitatie), zullen de gletsjers in de omgeving groeien en meer actief worden. Daardoor produceren ze meer geërodeerd sediment waarin proportioneel ook meer Ti zit dan tijdens een warmere periode waarin ze minder actief zijn. Echter, we namen ook waar (voor de

periode tussen 29000 en 38000 jaar geleden) dat de totale dikte van de ijsvrije lagen (= grofkorrelige lagen) per 100 jaar interval kleiner is, alsook de dikte van elk ijsvrij laagje apart. We suggereren dat de totale dikte van de ijsvrije lagen lager is doordat het sediment minder kansen krijgt om in het meer terecht te komen doordat het meer langer gesloten is dan open binnen een 100 jaar interval, ten opzichte van een warmere periode. De dikte van de ijsvrije lagen apart is dunner omdat er minder smeltwater kan gevormd worden wanneer het kouder is, waardoor minder sediment getransporteerd wordt.

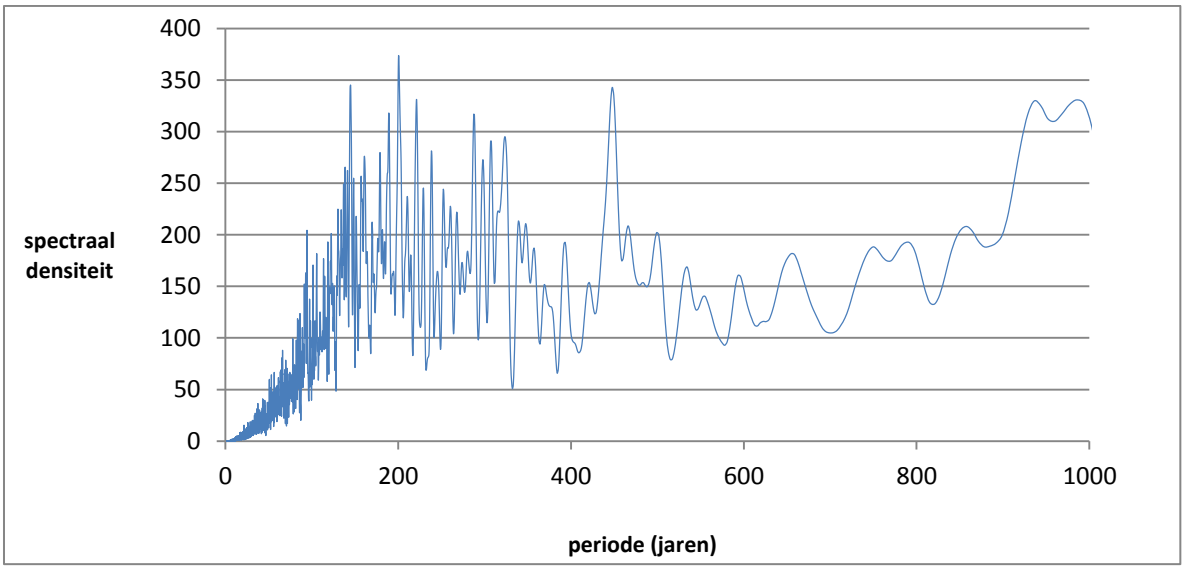

Fig. 113: Een voorbeeld van hoe de resultaten van een spectraalanalyse worden weergegeven. Hier wordt de spectraal densiteit ten opzichte van de periode voor een interval tussen 0 en 1000 jaar weergegeven voor een Tukey-Hanning spectraalanalyse op de L-waarde van de kleuranalyse resultaten.

De kleuranalyse die op de volledige kern werd uitgevoerd, werd als zeer nuttig beschouwd om cycliciteiten te detecteren. De resultaten bleken een goede illustratie te zijn van de verschillende veranderingen doorheen de kern, zoals korrelgrootte veranderingen of veranderingen in chemie. De spectraalanalyse uitgevoerd op de resultaten van de kleuranalyse produceerden dan ook veel verschillende cycliciteiten (zie Fig.3 voor een voorbeeld). Daaruit konden we de cycli selecteren die te maken hebben met klimaatsveranderingen. We hebben twee aandrijffactoren betrokken bij het zoeken naar mogelijke oorzaken voor deze cycli: de Antarctic Oscillation en de El Niño Southern Oscillation (ENSO). We vonden cycli van 11-13 jaar en 15-20 jaar, die kunnen verklaard worden als ENSO-achtige cycliciteiten. Verder vonden we cycli van ongeveer 38 en 24 jaar die kunnen gelinkt worden met de Antarctic Oscillation cycli. Als we de cycliciteiten berekenen voor de ijsvrije lagen (= grofkorrelige lagen) van de microscoop analyse, dan vinden we cycliciteiten van 11.1, 16.7 en 20 jaar. Deze kunnen de expressie zijn van een ENSO-achtig fenomeen.

9. References

Allan R.J. *ENSO and climatic variability in the past 150 years*. In: Diaz H.F. and Markgraf V. (eds.), 2000. El Niño and the Southern Oscillation: multiscale variability and global and regional impacts. Cambridge University Press, Cambridge, 496.

Bartole R., De Muro S., Morelli D. and Tosoratti F., 2008. *Glacigenic features and Tertiary stratigraphy of the Magellan Strait (southern Chile)*. Geologica Acta Vol.6 n°1, 85-100.

Basile I., Grousset F.E., Revel M., Petit J.R., Biscaye P.E. and Barkov N.I., 1997. *Patagonian origin of glacial dust deposited in East Antarctica (Vostok and Dome C) during glacial stages 2, 4 and 6*. Earth and Planetary Science Letters 146, 573-589.

Bentley M.J., Sugden D.E., Hulton N.R.J. and McCulloch R.D., 2005. *The landforms and pattern of deglaciation in the Strait of Magellan and Bahía Inútil, southernmost South America*. Geografiska annaler 87 A (2), 313 -333.

Bianchi C. and Gersonde R., 2004. *Climate evolution at the last deglaciation: the role of the Southern Ocean*. Earth and Planetary Science Letters 228, 407 – 424.

Boës X. and Fagel N., 2005. *Impregnation method for detecting annual laminations in sediment cores: an overview.* Sedimentary Geology 179, 185-194.

Bouma A.G., 1969. *Methods for the study of sedimentary structures*. Wiley, N.Y., 458.

Caniupán M., Lamy F., Lange C.B., Ninnemann U., Kaiser J., Arz H., Kilian R., Baeza Urrea O., Aracena C., Hebbeln D., Kissel C., Laj C., Mollenhauer G. and Tiedemann R., (In press). *Millennial-scale sea surface temperature and Patagonian Ice Sheet changes off southernmost Chile (53°S) over the past ~60 kyr*.

Carvalho L.M.V., Jones C. and Ambrizzi T., 2005. *Opposite phases of the Antarctic Oscillation and relationships with intraseasonal to interannual activity in the tropics during the austral summer*. Journal of climate 18, 702-718.

Clapperton C., 1993. *Quaternary Geology and Geomorphology of South America*. Elsevier, Amsterdam, 779.

Crevello P.D., Rine J.M. and Lanesky D.E., 1981. *A method for impregnating unconsolidated and slabs of calcareous and terrigenous muds*. J. Sed. Petrol.51, 658-660.

Diraison M., Cobbold P.R., Gapais D. and Rossello E.A., 1996. *Tertiary kinematics of the southern Andes and the development of the Magellan Foreland Basin (Patagonia)*. Third ISAG, St Malo (France), 347-350.

England M.H., Godfrey J.S., Hirst A.C. and Tomczak M., 1993. *The mechanism for Antarctic Intermediate Water renewal in a world ocean model*. Journal of Physical Oceanography 23, 1553-1560.

Fagel N., Boës X. and Loutre M.F., 2008. *Climate oscillations evidenced by spectral analysis of southern Chilean lacustrine sediments: the assessment of ENSO over the last 600 years*. Journal of Paleolimnology 39, 253-266.

Francus P., 1998. *An image-analysis technique to measure grain size variation in thin sections of soft clastic sediments*. Sediment.Geol. 121, 289-298.

Haberzettl T., Corbella H., Fey M., Janssen S., Lücke A., Mayr C., Ohlendorf C., Schäbitz F., Schleser G.H., Wille M., Wulf S. and Zolitschka B., 2007. *Lateglacial and Holocene wet-dry cycles in southern Patagonia: chronology, sedimentology and geochemistry of a lacustrine record from Laguna Potrok Aike, Argentina*. The Holocene 17(3), 297-310.

Harrison S.P., Kohfeld K.E., Roelandt C. and Claquin T., 2001. *The role of dust in climate changes today, at the Last Glacial Maximum and in the future*. Earth-Science Reviews 54, 43-80.

Heirman K., Van Daele M., Moernaut J., 2009. *Expedition report, region de la Araucania, region de los Rios, region de los Lagos, region Magallanes y la Antarctica chilena, Chile*. (not published).

Heusser C.J., 1989. *Southern Westerlies during the Last Glacial Maximum*. Quaternary Research 31, 423-425.

Kaiser J. and Lamy F., 2010. *Links between Patagonian Ice Sheet fluctuations and Antarctic dust variability during the last glacial period (MIS 4-2)*. Quaternary Science Reviews 29, 1464-1471.

Kaplan M.R., Moreno P.I. and Rojas M., 2008. *Glacial dynamics in southernmost South America during Marine Isotope Stage 5e to the Younger Dryas chron: a brief review with a focus on cosmogenic nuclide measurements*. Journal of Quaternary Science 23 (6-7), 649-658.

Lamoureux S.F., 1994. *Embedding unfrozen lake sediments for thin section preparation*. J. Paleolimnol. 10, 141-146.

Liao H. and Seinfeld J.H., 1998. *Radiative forcing by mineral dust aerosols: sensitivity to key variables*. Journal of Geophysical Research 103 (D24), 31637-31645.

Lohmann U. and Feichter J., 1997. *Impact of sulfate aerosols on albedo and lifetime of clouds: A sensitivity study with the ECHAM4 GCM*. Journal of Geophysical Research 102 (D12), 13685-13700.

Mann M.E., Bradley R.S. and Hughes M.K. In: Diaz H.F. and Markgraf V. (eds.), 2000. El Niño and the Southern Oscillation: multiscale variability and global and regional impacts. Cambridge University Press, Cambridge, 496.

Markgraf V., 1987. *Paleoenvironmental changes at the northern limit of the subantarctic Nothofagus forest, Lat 37°S*. Quaternary Research 28, 119-129.

Markgraf V. and Diaz H.F. *The past ENSO record: A synthesis*. In: Diaz H.F. and Markgraf V. (eds.), 2000. El Niño and the Southern Oscillation: multiscale variability and global and regional impacts. Cambridge University Press, Cambridge, 496.

Mazzarini F. and D'Orazio M., 2003. *Spatial distribution of cones and satellite-detected lineaments in the Pali Aike Volcanic Field (southernmost Patagonia): insights into the tectonic setting of a Neogenic rift system*. Journal of Volcanology and Geothermal Research 125, 291-305.

McCulloch R.D. and Davies S.J., 2001. *Late-glacial and Holocene palaeoenvironmental change in the central Strait of Magellan, southern Patagonia*. Palaeogeography, Palaeoclimatology, Palaeoecology 173, 143 – 173.

McCulloch R.D., Bentley M.J., Purves R.S., Hulton N.R.J., Sugden D.E. and Clapperton C.M., 2000. *Climatic inferences from glacial and palaeoecological evidence at the last glacial termination, southern South America*. Journal of Quaternary Sciences 15, 409-417.

McCulloch R.D., Fogwill C.J., Sugden D.E., Bentley M.J. and Kubik P.W., 2005a. *Chronology of the last glaciation in Central Strait of Magellan and Bahía Inútil, southernmost South America*. Geografiska Annaler 87 A (2), 289 - 312.

McCulloch R.D., Bentley M.J., Tipping R.M. and Clapperton C.M., 2005b. *Evidence for late-glacial ice dammed lakes in the central Strait of Magellan and Bahía Inútil, southernmost South America*. Geografiska Annaler 87 A (2), 335 - 362.

Pike J. and Kemp A.E.S., 1996. *Preparation and analysis techniques for studies of laminated sediments*. In: Kemp A.E.S.(Ed.), Palaeoclimatology and Palaeooceanography from laminated sediments. Geol. Soc. Spec. Publ. 116, 37-48.

Rabassa J., Coronato A., Bujalesky G., Salemme M., Roig C., Meglioli A., Heusser C., Gordillo S., Roig F., Borromei A. and Quattrocchio M., 2000. *Quaternary of Tierra del Fuego, southernmost South America: an updated review*. Quaternary International 68-71, 217-240.

Rea D.K., 1994. *The paleoclimatic record provided by eolian deposition in the deep sea: the geologic history of wind*. Reviews of Geophysics 32 (2), 159-195.

Ruddiman W.F., 2008. *Earth's climate: Past and Future (2nd edition)*. W.H. Freeman and Company, New York, 388.

Sander M., Bengtsson L., Holmquist B., Wohlfarth B. and Cato I., 2002. *The relationship between annual varve thickness and maximum annual discharge (1909-1971)*. Journal of Hydrology 263, 23-35.

Shulmeister J., Goodwin I., Renwick J., Harle K., Armand L., McGlone M.S., Cook E., Dodson J., Hesse P.P., Mayewski P. and Curran M., 2004. *The Southern Hemisphere westerlies in the Australasian sector over the last glacial cycle: a synthesis*. Quaterna ry International 118-119, 23-53.

Sijp W.P. and England M.H., 2008. *The effect of a northward shift in the southern hemisphere westerlies on the global ocean*. Progress in Oceanography 79, 1-19.

Silvestri G.E. and Vera C.S., 2003. *Antarctic Oscillation signal on precipitation anomalies over southeastern South America*. Geophysical Research Letters 30 (21), 2115.

Sugden D.E., Bentley M.J., Fogwill C.J., Hulton N.R.J., McCulloch R.D. and Purves R.S., 2005. *Late-Glacial glacier events in southernmost South America: a blend of 'northern' and 'southern' hemispheric climatic signals?* Geografiska Annaler 87 A (2), 273 – 288.

Sugden D.E., McCulloch R.D., Bory A. J.-M. and Hein A.S., 2009. *Influence of Patagonian glaciers on Antarctic dust deposition during the last glacial period*. Nature Geoscience 2, 281-285.

Tadros M.T.Y. and Shaltout M.A.M., 2003. *Effect of Hanning and Parzen windows and Kalman filter on the spectral analysis of constant and solar activities*. Solar Energy 43 (6), 331-338.

Tegen I., 2003. *Modeling the mineral dust aerosol cycle in the climate system*. Quaternary Science Reviews 22, 1821-1834.

Thompson D.W.J. and Wallace J.M., 2000. *Annular modes in the Extratropical Circulation. Part I: Month-to-Month variability*. Journal of Climate 13, 1000-1016.

Voelker A.H.L. and workshop participants, 2002. *Global distribution of centennial-scale records for Marine Isotope Stage (MIS) 3: a database*. Quaternary Science Reviews 21, 1185-1212.

Wilcox D., Dove B., Mc David D. And Greer D., 1996. UTHSCSA Image Tool for Windows, version 2.00: University of Texas Health Science Center in San Antonio. Updated version Image Tool 3.0 program retrieved from http://geology.tufts.edu/varves (May 27, 2011).

Wyrwoll K.-H., Dong B. and Valdes P., 2000. *On the position of Southern Hemisphere Westerlies at the Last Glacial Maximum: an outline of AGCM simulation results and evaluation of their implications*. Quaternary Science Reviews 19, 881-898.

Zhang Z.-Y., Gong D.-Y., He X.-Z., Lei Y.-N. and Feng S.-H., 2010. *Statistical reconstruction of the Antarctic Oscillation Index based on multiple proxies*. Atmospheric and Oceanic Science Letters 3 (5), 283-287.

Zolitschka B., 2007. *Varved lake sediments*. Encyclopedia of Quaternary Science, 3105 – 3114.

Internet sources

UNEP/GRID-Arendal, El Niño-Southern Oscillation (ENSO) Phenomenon, *UNEP/GRIDArendal Maps and Graphics Library*, http://maps.grida.no/go/graphic/el-ni-o-southern-oscillation-enso-phenomenon (Accessed 2 June 2011)

UNEP/GRID-Arendal, South America, southern ice fields, *UNEP/GRID-Arendal Maps and Graphics Library*, http://maps.grida.no/go/graphic/south_america_southern_ice_fields (Accessed 2 June 2011)

http://en.wikipedia.org/wiki/ (Accessed June 2, 2011; June 4, 2011)

http://en.wikipedia.org/wiki/Lab_color_space (accessed June 17, 2011)

http://en.wikipedia.org/wiki/Planetary_boundary_layer (accessed July 23, 2011)

http://en.wikipedia.org/wiki/Heinrich_event (accessed August 11, 2011)

http://en.wikipedia.org/wiki/Dansgaard%E2%80%93Oeschger_event (accessed August 11, 2011)

http://www.glaciology.gfy.ku.dk/data/NGRIP_d18O_50yrs.txt (accessed August 11, 2011)

ftp://ftp.ncdc.noaa.gov/pub/data/paleo/icecore/antarctica/epica_domec/edc_dd.txt (accessed August 11, 2011)

10. Appendix

CORRELATIONS BETWEEN ELEMENTS

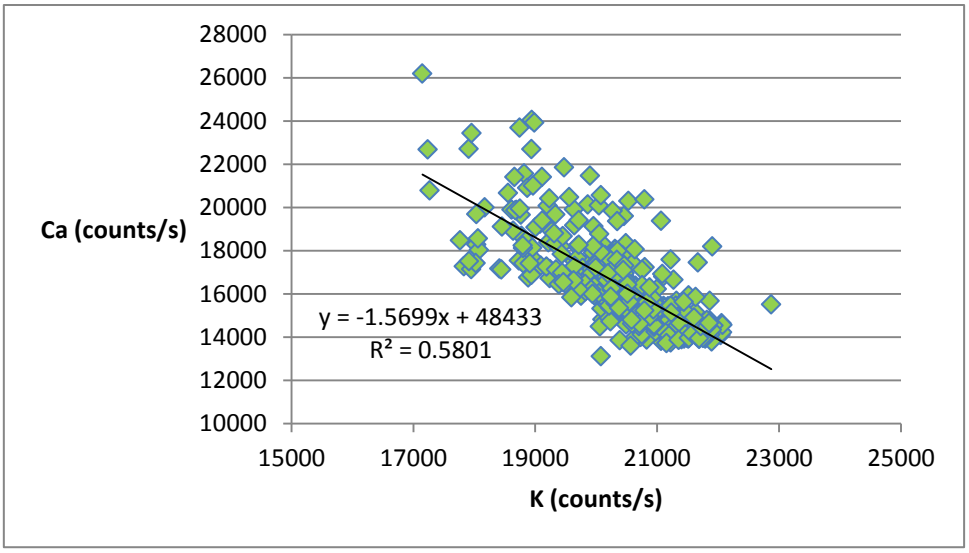

Fig.1

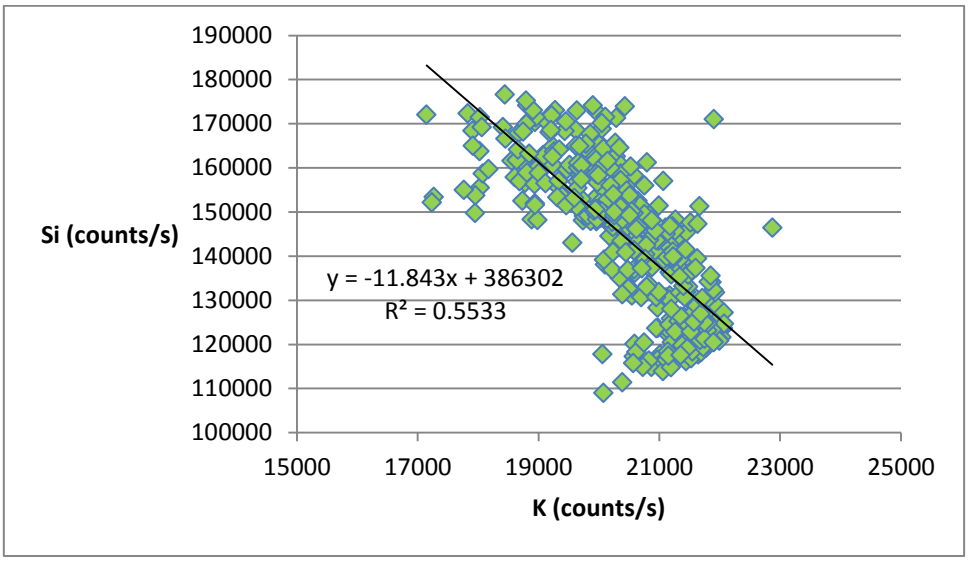

Fig.2

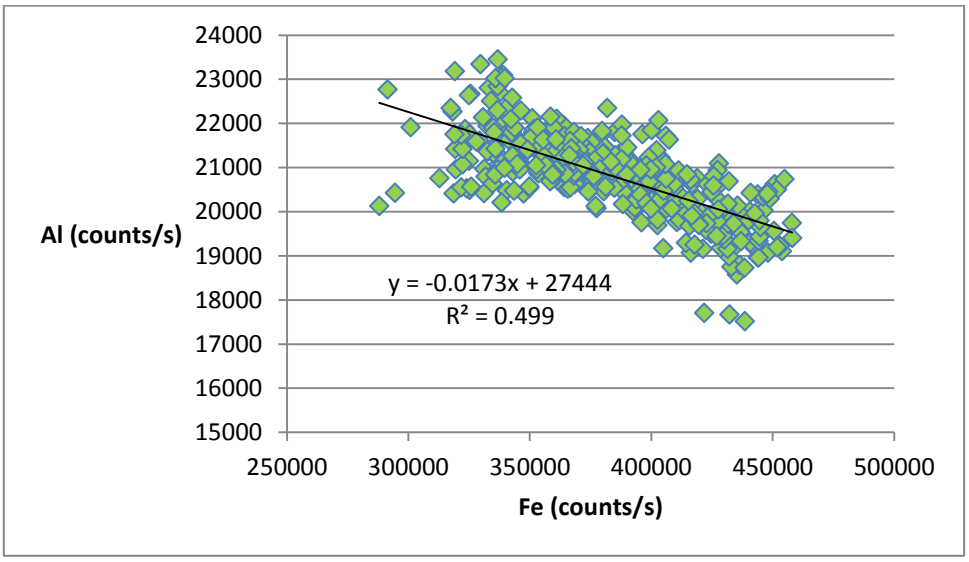

Fig.3

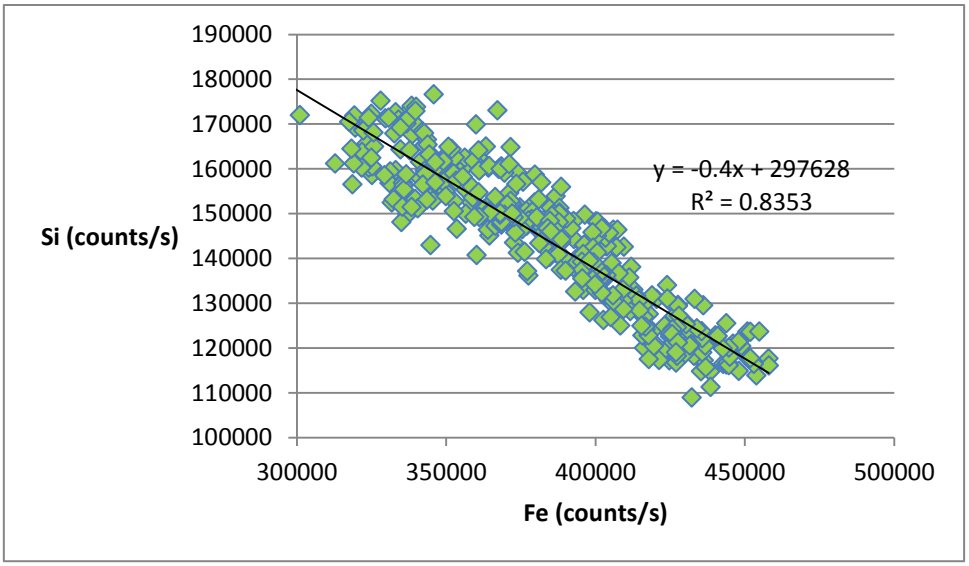

Fig.4

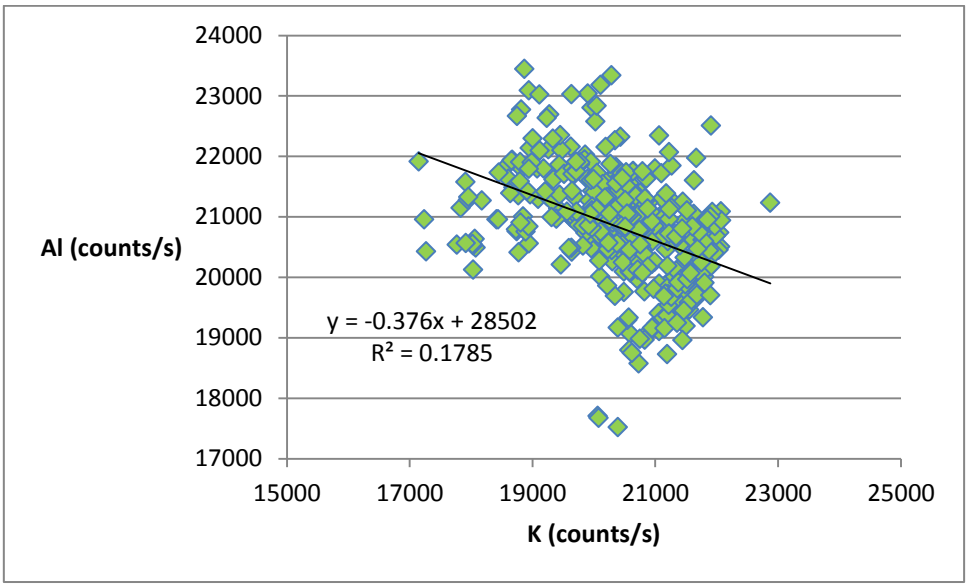

Fig.5

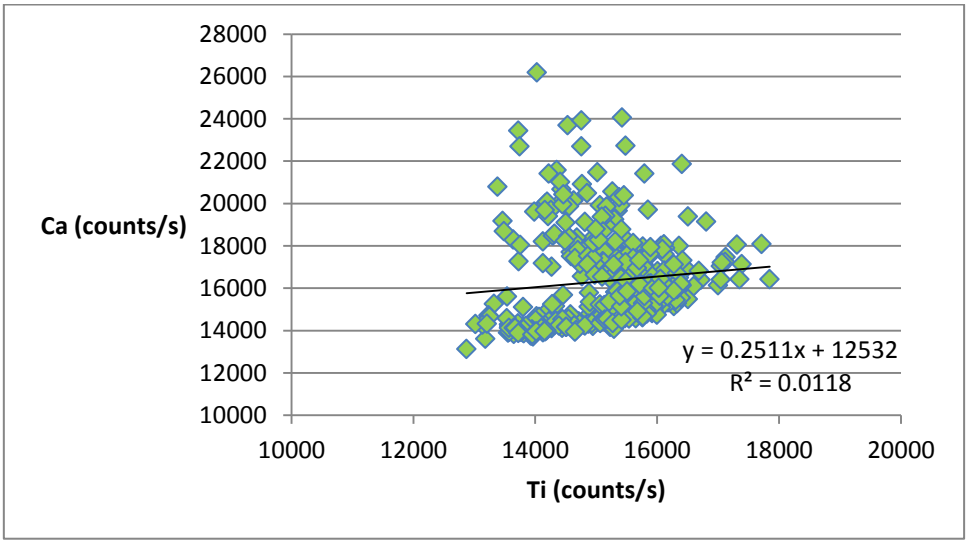

Fig.6

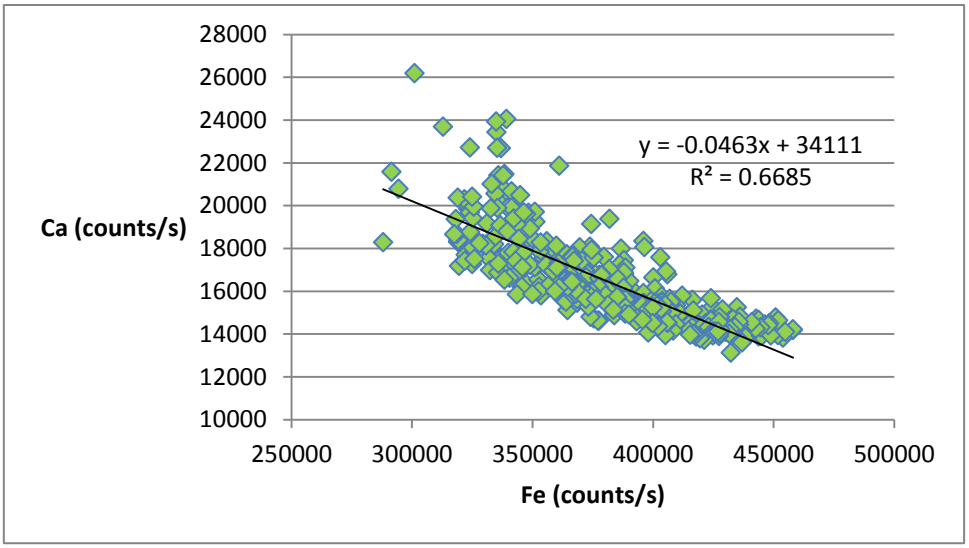

Fig.7

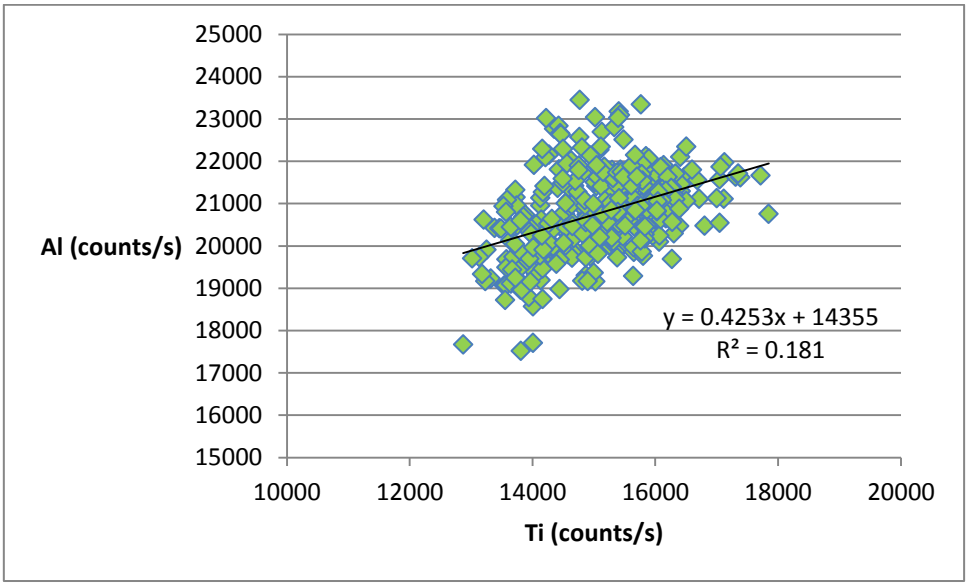

Fig.8

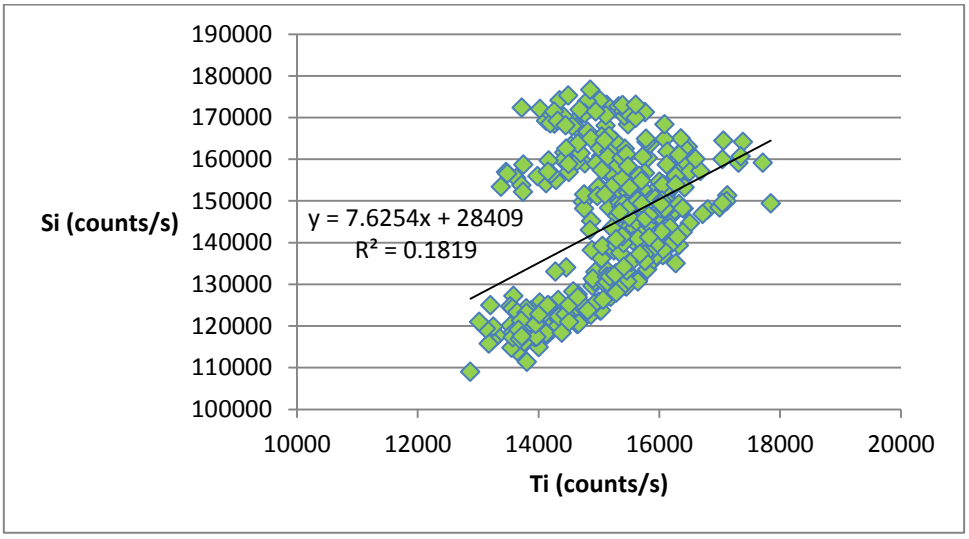

Fig.9

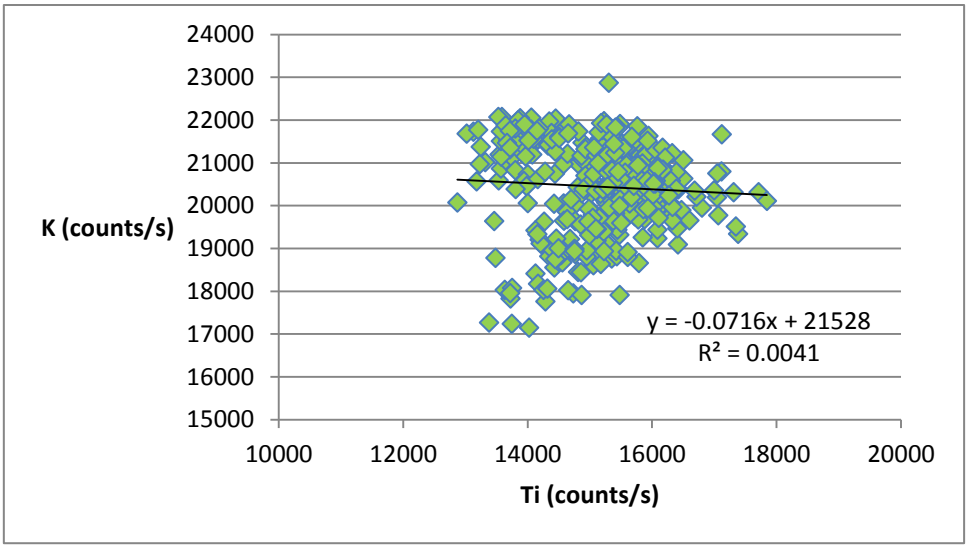
24000
23000
22000
21000
20000
19000
18000
17000
16000
15000
K (counts/s)
y = -0.0716x + 21528
R² = 0.0041
10000
12000
14000
16000
18000
20000
Ti (counts/s)

Fig.10

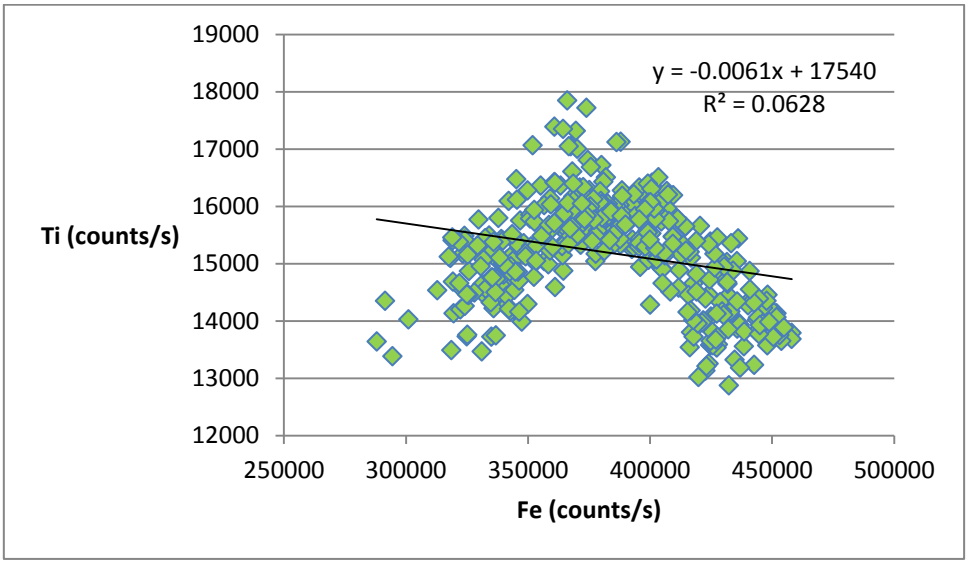
19000
18000
17000
16000
15000
14000
13000
12000
Ti (counts/s)
y = -0.0061x + 17540
R² = 0.0628
250000
300000
350000
400000
450000
500000
Fe (counts/s)

Fig.11

Fig.1: The element Fe against grain size. The grain size description was obtained from the petrographic microscope observations on the section of sample PAR1A-III(50-60), on which also a µ-XRF analysis was performed. The grain size is described over a distance of 20 mm on sample PAR1A-III(50-60). The top of the sample is at the left side of the graph.

Fig.2: The element Ca against grain size. The grain size description was obtained from the petrographic microscope observations on the section of sample PAR1A-III(50-60), on which also a µ-XRF analysis was performed. The grain size is described over a distance of 20 mm on sample PAR1A-III(50-60). The top of the sample is at the left side of the graph.

Fig.3: The element K against grain size. The grain size description was obtained from the petrographic microscope observations on the section of sample PAR1A-III(50-60), on which also a µ-XRF analysis was performed. The grain size is described over a distance of 20 mm on sample PAR1A-III(50-60). The top of the sample is at the left side of the graph.

Fig.4: The element Si against grain size. The grain size description was obtained from the petrographic microscope observations on the section of sample PAR1A-III(50-60), on which also a µ-XRF analysis was performed. The grain size is described over a distance of 20 mm on sample PAR1A-III(50-60). The top of the sample is at the left side of the graph.

Fig.5: The element Al against grain size. The grain size description was obtained from the petrographic microscope observations on the section of sample PAR1A-III(50-60), on which also a µ-XRF analysis was performed. The grain size is described over a distance of 20 mm on sample PAR1A-III(50-60). The top of the sample is at the left side of the graph.

Fig.6: The element Ti against grain size. The grain size description was obtained from the petrographic microscope observations on the section of sample PAR1A-III(50-60), on which also a µ-XRF analysis was performed. The grain size is described over a distance of 20 mm on sample PAR1A-III(50-60). The top of the sample is at the left side of the graph.

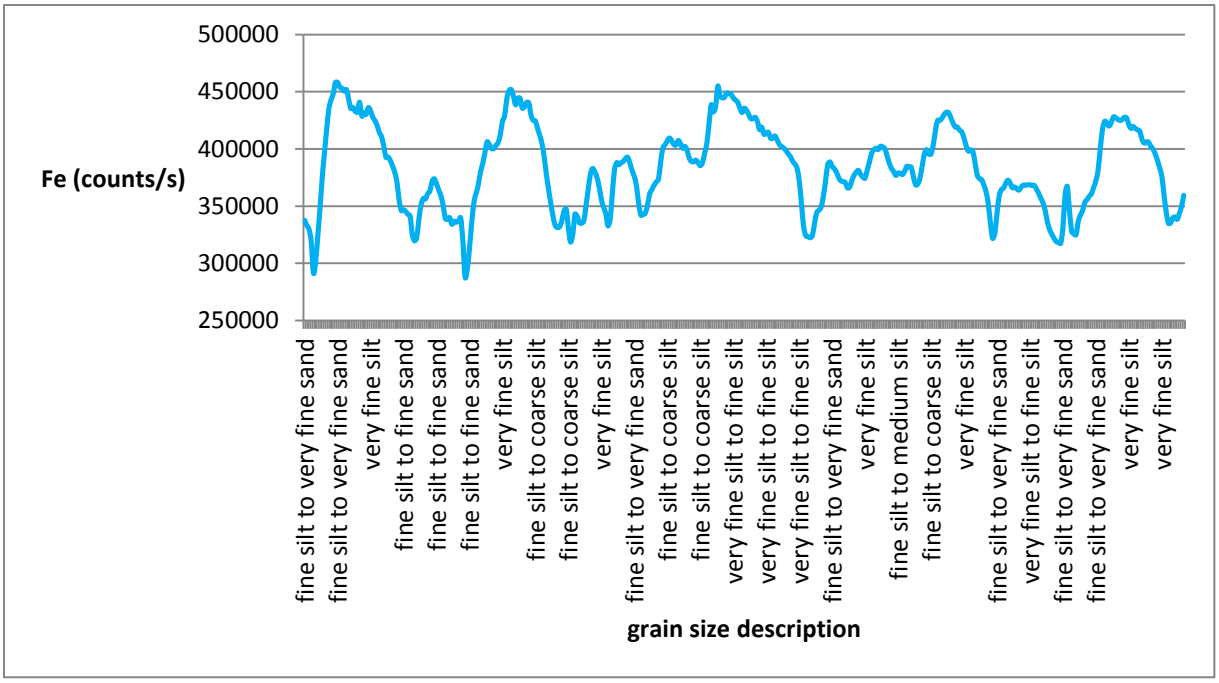
Fe (counts/s)
500000
450000
400000
350000
300000
250000
fine silt to very fine sand
fine silt to very fine sand
very fine silt
fine silt to fine sand
fine silt to fine sand
fine silt to fine sand
very fine silt
fine silt to coarse silt
fine silt to coarse silt
very fine silt
fine silt to very fine sand
fine silt to coarse silt
fine silt to coarse silt
very fine silt to fine silt
very fine silt to fine silt
very fine silt to fine silt
fine silt to very fine sand
very fine silt
fine silt to medium silt
fine silt to coarse silt
very fine silt
fine silt to very fine sand
very fine silt to fine silt
fine silt to very fine sand
fine silt to very fine sand
very fine silt
very fine silt
grain size description

Fig.1

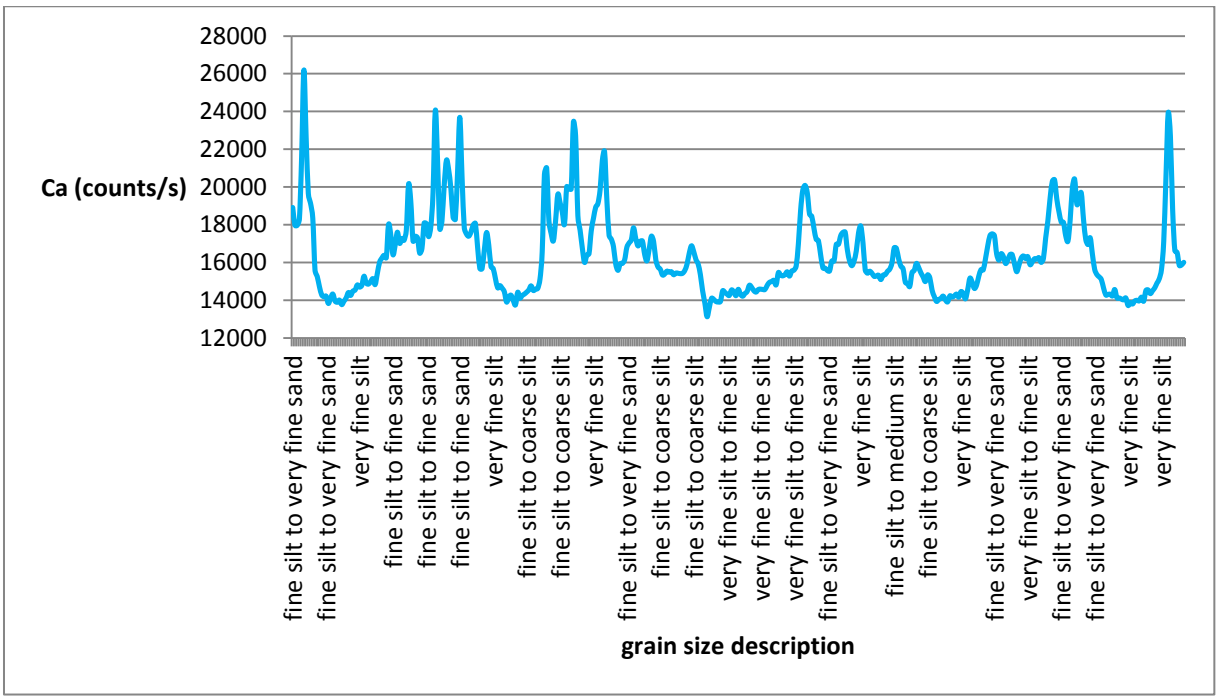
Ca (counts/s)
28000
26000
24000
22000
20000
18000
16000
14000
12000
fine silt to very fine sand
fine silt to very fine sand
very fine silt
fine silt to fine sand
fine silt to fine sand
fine silt to fine sand
very fine silt
fine silt to coarse silt
fine silt to coarse silt
very fine silt
fine silt to very fine sand
fine silt to coarse silt
fine silt to coarse silt
very fine silt to fine silt
very fine silt to fine silt
very fine silt to fine silt
fine silt to very fine sand
very fine silt
fine silt to medium silt
fine silt to coarse silt
very fine silt
fine silt to very fine sand
very fine silt to fine silt
fine silt to very fine sand
fine silt to very fine sand
very fine silt
very fine silt
grain size description

Fig.2

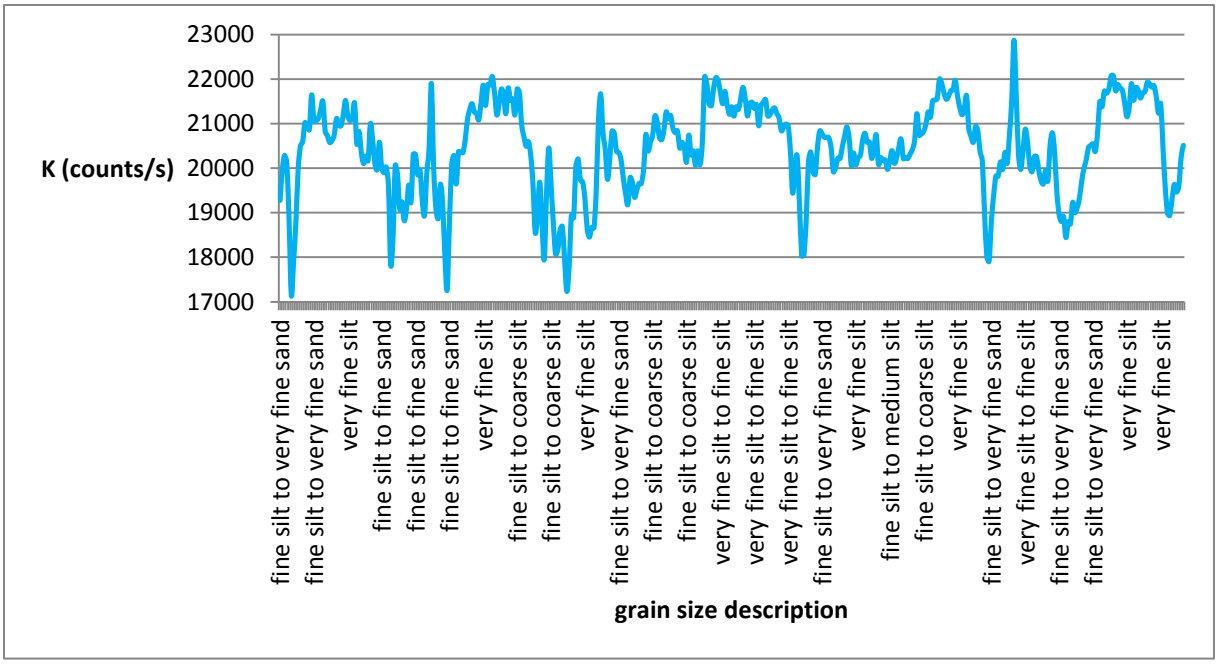
K (counts/s)
23000
22000
21000
20000
19000
18000
17000
fine silt to very fine sand
fine silt to very fine sand
very fine silt
fine silt to fine sand
fine silt to fine sand
fine silt to fine sand
very fine silt
fine silt to coarse silt
fine silt to coarse silt
very fine silt
fine silt to very fine sand
fine silt to coarse silt
fine silt to coarse silt
very fine silt to fine silt
very fine silt to fine silt
very fine silt to fine silt
fine silt to very fine sand
very fine silt
fine silt to medium silt
fine silt to coarse silt
very fine silt
fine silt to very fine sand
very fine silt to fine silt
fine silt to very fine sand
fine silt to very fine sand
very fine silt
very fine silt
grain size description

Fig.3

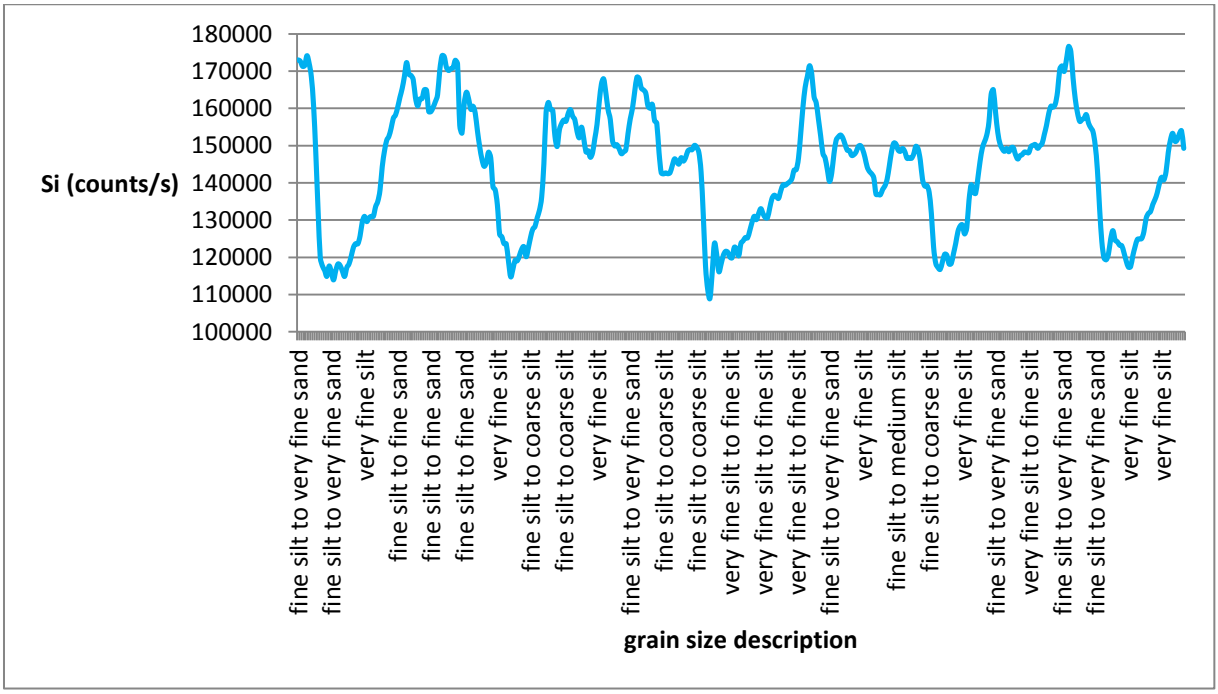
Si (counts/s)
180000
170000
160000
150000
140000
130000
120000
110000
100000
fine silt to very fine sand
fine silt to very fine sand
very fine silt
fine silt to fine sand
fine silt to fine sand
fine silt to fine sand
very fine silt
fine silt to coarse silt
fine silt to coarse silt
very fine silt
fine silt to very fine sand
fine silt to coarse silt
fine silt to coarse silt
very fine silt to fine silt
very fine silt to fine silt
very fine silt to fine silt
fine silt to very fine sand
very fine silt
fine silt to medium silt
fine silt to coarse silt
very fine silt
fine silt to very fine sand
very fine silt to fine silt
fine silt to very fine sand
fine silt to very fine sand
very fine silt
very fine silt
grain size description

Fig.4

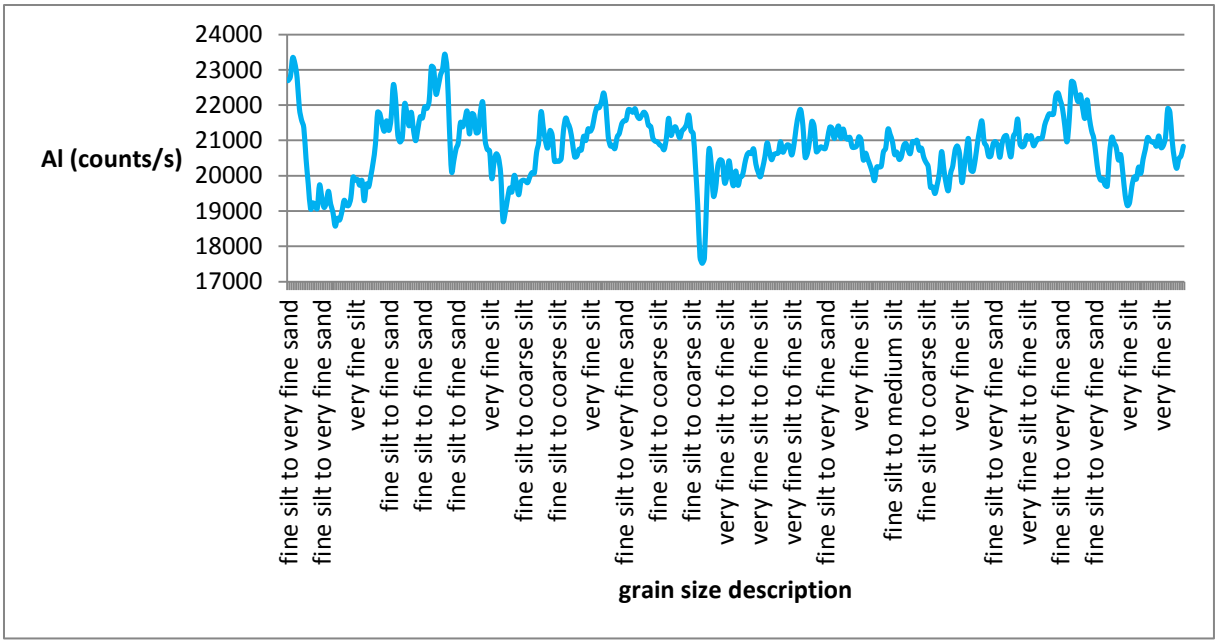
Al (counts/s)
24000
23000
22000
21000
20000
19000
18000
17000
fine silt to very fine sand
fine silt to very fine sand
very fine silt
fine silt to fine sand
fine silt to fine sand
fine silt to fine sand
very fine silt
fine silt to coarse silt
fine silt to coarse silt
very fine silt
fine silt to very fine sand
fine silt to coarse silt
fine silt to coarse silt
very fine silt to fine silt
very fine silt to fine silt
very fine silt to fine silt
fine silt to very fine sand
very fine silt
fine silt to medium silt
fine silt to coarse silt
very fine silt
fine silt to very fine sand
very fine silt to fine silt
fine silt to very fine sand
fine silt to very fine sand
very fine silt
very fine silt
grain size description

Fig.5

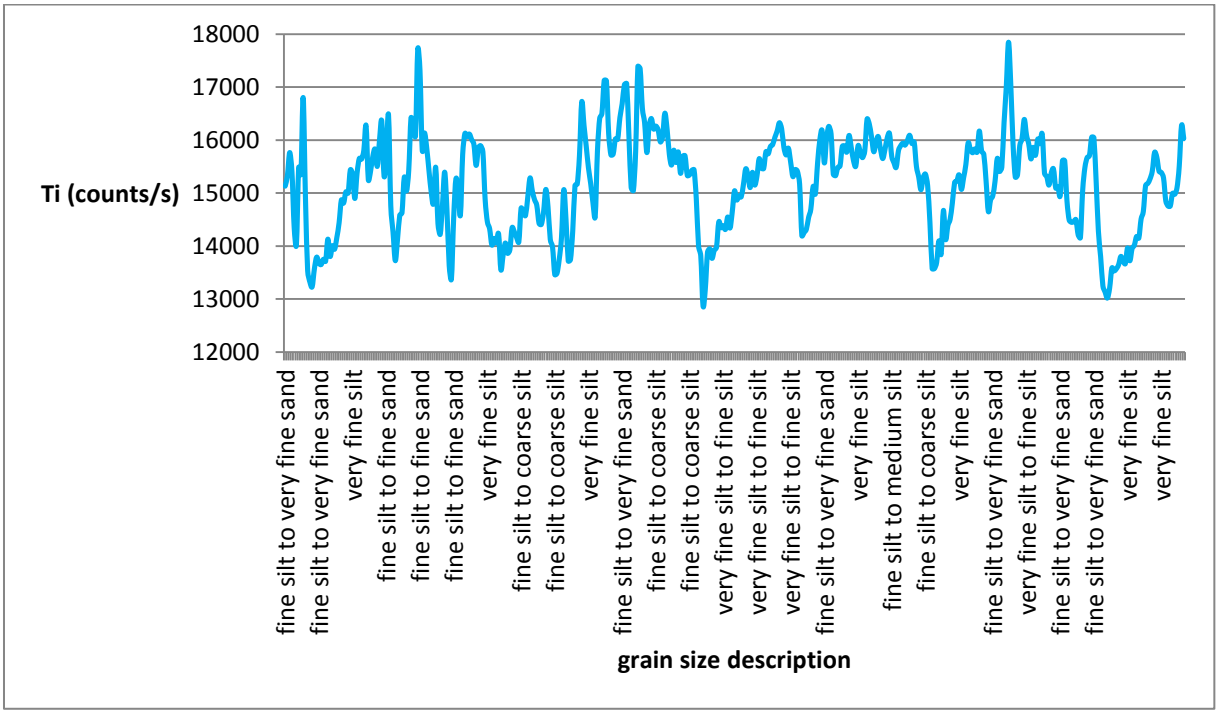
Ti (counts/s)
18000
17000
16000
15000
14000
13000
12000
fine silt to very fine sand
fine silt to very fine sand
very fine silt
fine silt to fine sand
fine silt to fine sand
fine silt to fine sand
very fine silt
fine silt to coarse silt
fine silt to coarse silt
very fine silt
fine silt to very fine sand
fine silt to coarse silt
fine silt to coarse silt
very fine silt to fine silt
very fine silt to fine silt
very fine silt to fine silt
fine silt to very fine sand
very fine silt
fine silt to medium silt
fine silt to coarse silt
very fine silt
fine silt to very fine sand
very fine silt to fine silt
fine silt to very fine sand
fine silt to very fine sand
very fine silt
very fine silt
grain size description

Fig.6

Fig.1: The ratio log(Ca/K) against grain size. The grain size description was obtained from the petrographic microscope observations on the section of sample PAR1A-III(50-60), on which also a µ-XRF analysis was performed. The grain size is described over a distance of 20 mm on sample PAR1A-III(50-60). The top of the sample is at the left side of the graph.

Fig.2: The ratio log(Si/K) against grain size. The grain size description was obtained from the petrographic microscope observations on the section of sample PAR1A-III(50-60), on which also a µ-XRF analysis was performed. The grain size is described over a distance of 20 mm on sample PAR1A-III(50-60). The top of the sample is at the left side of the graph.

Fig.3: The ratio log(Fe/Al) against grain size. The grain size description was obtained from the petrographic microscope observations on the section of sample PAR1A-III(50-60), on which also a µ-XRF analysis was performed. The grain size is described over a distance of 20 mm on sample PAR1A-III(50-60). The top of the sample is at the left side of the graph.

Fig.4: The ratio log(Fe/Si) against grain size. The grain size description was obtained from the petrographic microscope observations on the section of sample PAR1A-III(50-60), on which also a µ-XRF analysis was performed. The grain size is described over a distance of 20 mm on sample PAR1A-III(50-60). The top of the sample is at the left side of the graph.

Fig.5: The ratio log(Al/K) against grain size. The grain size description was obtained from the petrographic microscope observations on the section of sample PAR1A-III(50-60), on which also a µ-XRF analysis was performed. The grain size is described over a distance of 20 mm on sample PAR1A-III(50-60). The top of the sample is at the left side of the graph.

Fig.6: The ratio log(Ca/Ti) against grain size. The grain size description was obtained from the petrographic microscope observations on the section of sample PAR1A-III(50-60), on which also a µ-XRF analysis was performed. The grain size is described over a distance of 20 mm on sample PAR1A-III(50-60). The top of the sample is at the left side of the graph.

Fig.7: The ratio log(Fe/Ca) against grain size. The grain size description was obtained from the petrographic microscope observations on the section of sample PAR1A-III(50-60), on which also a µ-XRF analysis was performed. The grain size is described over a distance of 20 mm on sample PAR1A-III(50-60). The top of the sample is at the left side of the graph.

Fig.8: The ratio log(K/Ti) against grain size. The grain size description was obtained from the petrographic microscope observations on the section of sample PAR1A-III(50-60), on which also a µ-XRF analysis was performed. The grain size is described over a distance of 20 mm on sample PAR1A-III(50-60). The top of the sample is at the left side of the graph.

Fig.9: The ratio log(Si/Ti) against grain size. The grain size description was obtained from the petrographic microscope observations on the section of sample PAR1A-III(50-60), on which also a µ-XRF analysis was performed. The grain size is described over a distance of 20 mm on sample PAR1A-III(50-60). The top of the sample is at the left side of the graph.

Fig.10: The ratio log(Fe/Ti) against grain size. The grain size description was obtained from the petrographic microscope observations on the section of sample PAR1A-III(50-60), on which also a µ-XRF analysis was performed. The grain size is described over a distance of 20 mm on sample PAR1A-III(50-60). The top of the sample is at the left side of the graph.

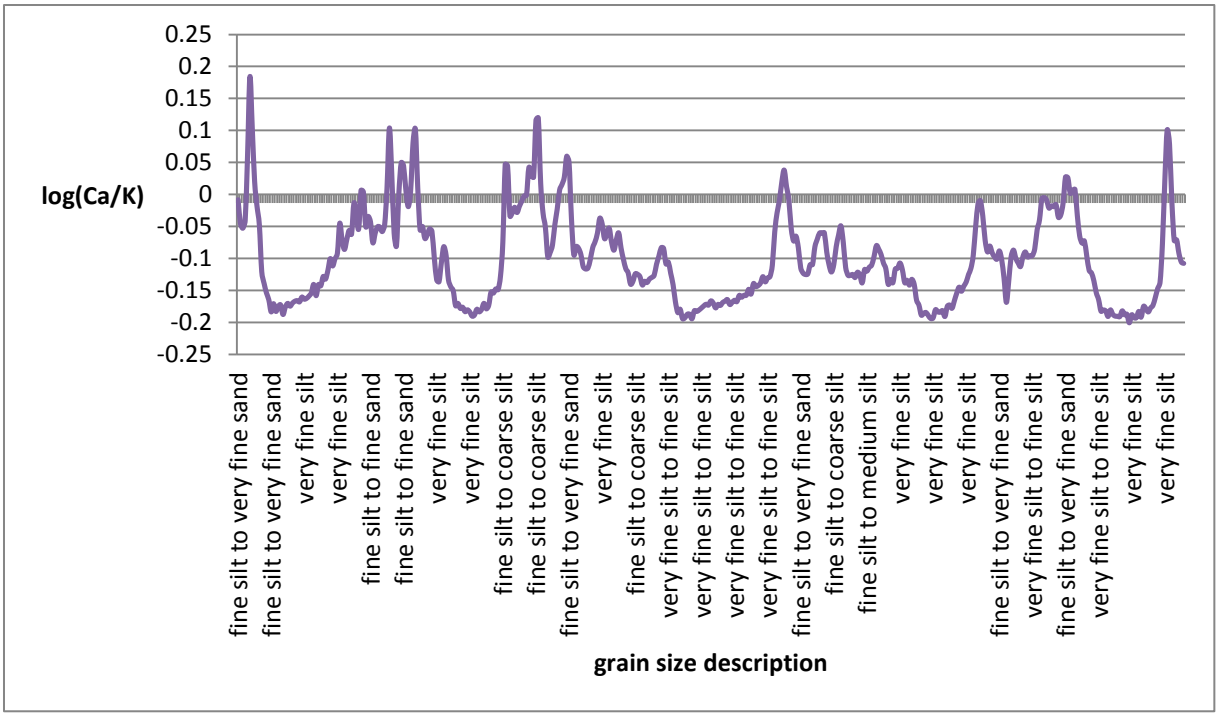
log(Ca/K)
0.25
0.2
0.15
0.1
0.05
0
-0.05
-0.1
-0.15
-0.2
-0.25
fine silt to very fine sand
fine silt to very fine sand
very fine silt
very fine silt
fine silt to fine sand
fine silt to fine sand
very fine silt
very fine silt
fine silt to coarse silt
fine silt to coarse silt
fine silt to very fine sand
very fine silt
fine silt to coarse silt
very fine silt to fine silt
very fine silt to fine silt
very fine silt to fine silt
very fine silt to fine silt
fine silt to very fine sand
fine silt to coarse silt
fine silt to medium silt
very fine silt
very fine silt
very fine silt
fine silt to very fine sand
very fine silt to fine silt
fine silt to very fine sand
very fine silt to fine silt
very fine silt
very fine silt
grain size description

Fig.1

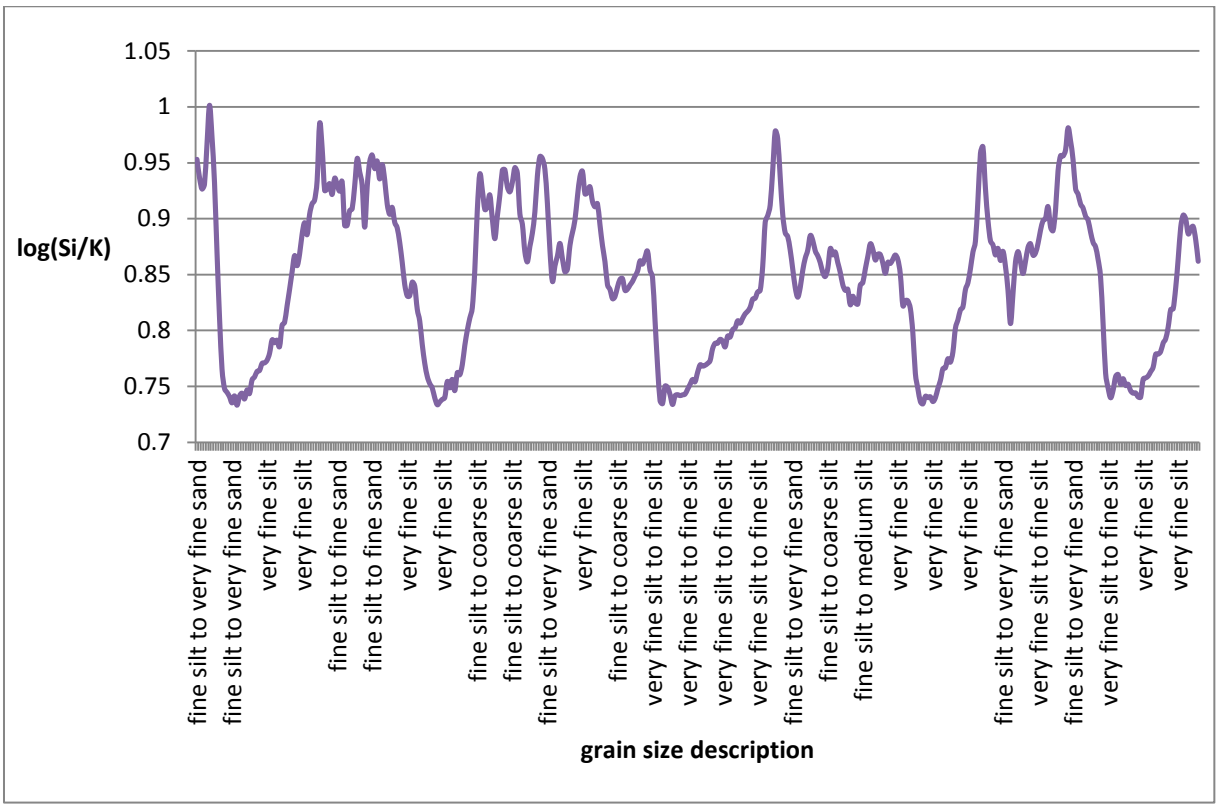
log(Si/K)
1.05
1
0.95
0.9
0.85
0.8
0.75
0.7
fine silt to very fine sand
fine silt to very fine sand
very fine silt
very fine silt
fine silt to fine sand
fine silt to fine sand
very fine silt
very fine silt
fine silt to coarse silt
fine silt to coarse silt
fine silt to very fine sand
very fine silt
fine silt to coarse silt
very fine silt to fine silt
very fine silt to fine silt
very fine silt to fine silt
very fine silt to fine silt
fine silt to very fine sand
fine silt to coarse silt
fine silt to medium silt
very fine silt
very fine silt
very fine silt
fine silt to very fine sand
very fine silt to fine silt
fine silt to very fine sand
very fine silt to fine silt
very fine silt
very fine silt
grain size description

Fig.2

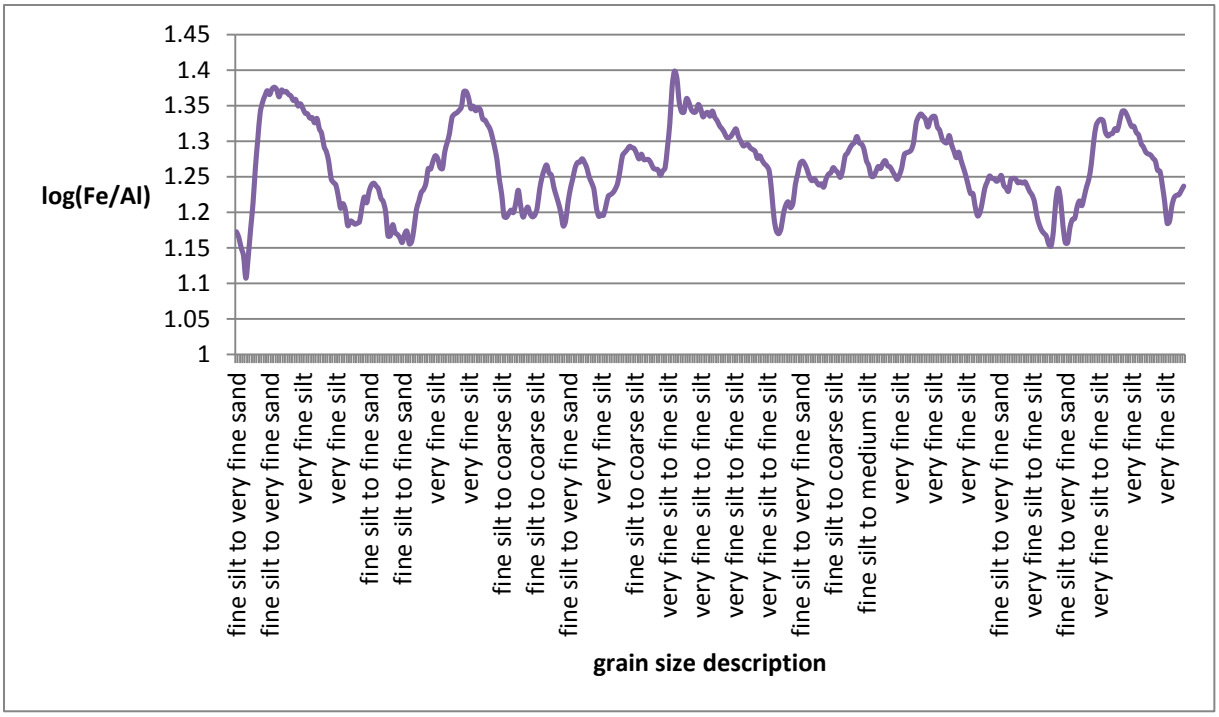
log(Fe/Al)
1.45
1.4
1.35
1.3
1.25
1.2
1.15
1.1
1.05
1
fine silt to very fine sand
fine silt to very fine sand
very fine silt
very fine silt
fine silt to fine sand
fine silt to fine sand
very fine silt
very fine silt
fine silt to coarse silt
fine silt to coarse silt
fine silt to very fine sand
very fine silt
fine silt to coarse silt
very fine silt to fine silt
very fine silt to fine silt
very fine silt to fine silt
very fine silt to fine silt
fine silt to very fine sand
fine silt to coarse silt
fine silt to medium silt
very fine silt
very fine silt
very fine silt
fine silt to very fine sand
very fine silt to fine silt
fine silt to very fine sand
very fine silt to fine silt
very fine silt
very fine silt
grain size description

Fig.3

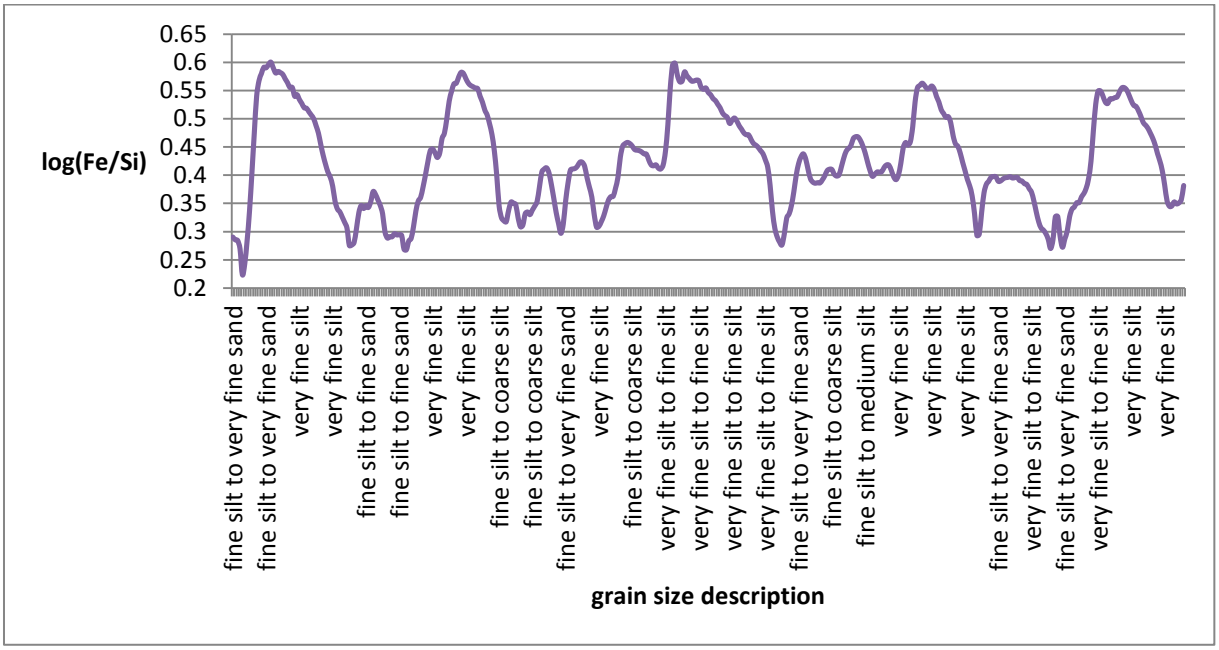
log(Fe/Si)
0.65
0.6
0.55
0.5
0.45
0.4
0.35
0.3
0.25
0.2
fine silt to very fine sand
fine silt to very fine sand
very fine silt
very fine silt
fine silt to fine sand
fine silt to fine sand
very fine silt
very fine silt
fine silt to coarse silt
fine silt to coarse silt
fine silt to very fine sand
very fine silt
fine silt to coarse silt
very fine silt to fine silt
very fine silt to fine silt
very fine silt to fine silt
very fine silt to fine silt
fine silt to very fine sand
fine silt to coarse silt
fine silt to medium silt
very fine silt
very fine silt
very fine silt
fine silt to very fine sand
very fine silt to fine silt
fine silt to very fine sand
very fine silt to fine silt
very fine silt
very fine silt
grain size description

Fig.4

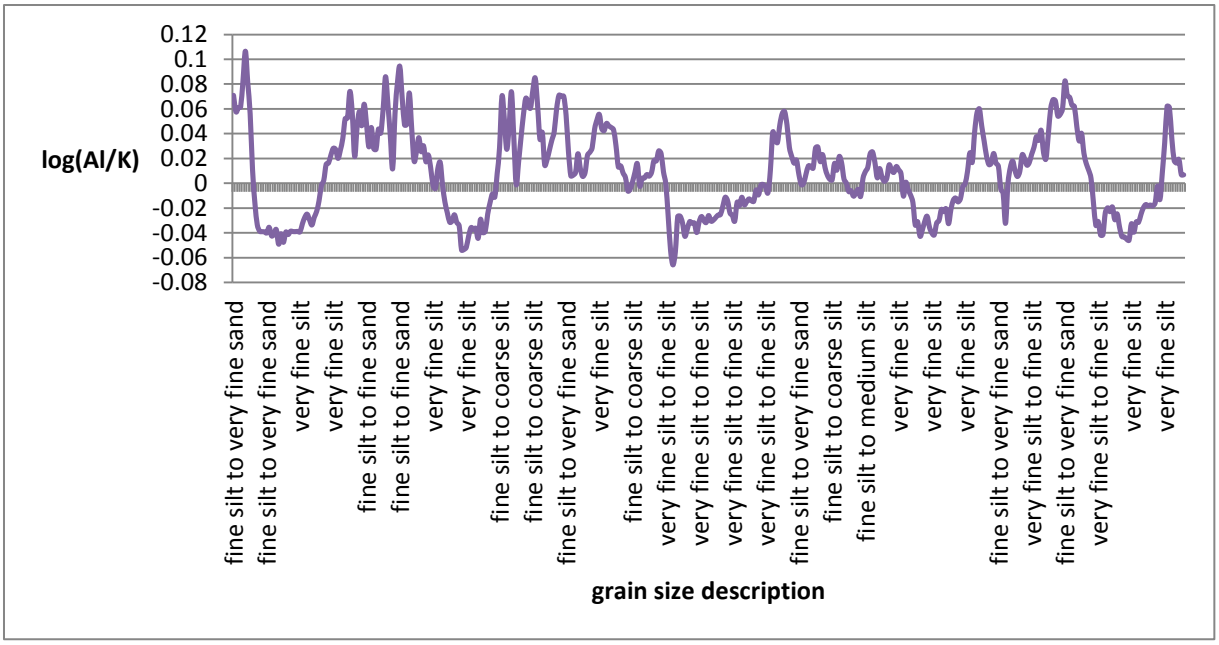
log(Al/K)
0.12
0.1
0.08
0.06
0.04
0.02
0
-0.02
-0.04
-0.06
-0.08
fine silt to very fine sand
fine silt to very fine sand
very fine silt
very fine silt
fine silt to fine sand
fine silt to fine sand
very fine silt
very fine silt
fine silt to coarse silt
fine silt to coarse silt
fine silt to very fine sand
very fine silt
fine silt to coarse silt
very fine silt to fine silt
very fine silt to fine silt
very fine silt to fine silt
very fine silt to fine silt
fine silt to very fine sand
fine silt to coarse silt
fine silt to medium silt
very fine silt
very fine silt
very fine silt
fine silt to very fine sand
very fine silt to fine silt
fine silt to very fine sand
very fine silt to fine silt
very fine silt
very fine silt
grain size description

Fig.5

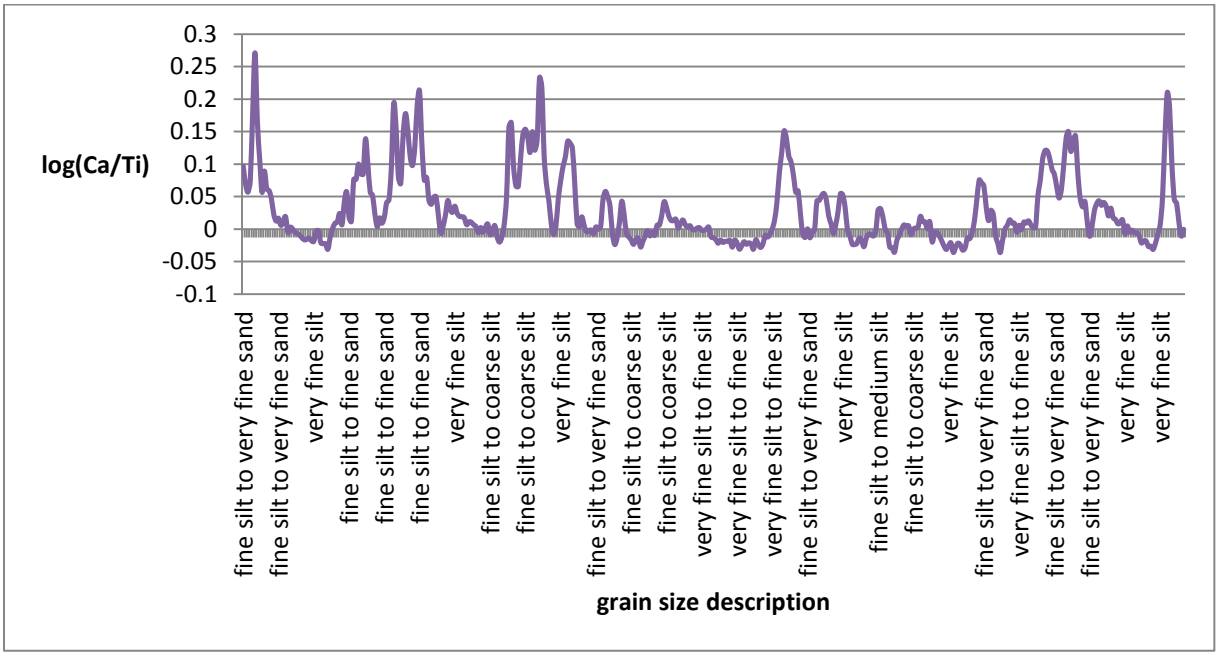
log(Ca/Ti)
0.3
0.25
0.2
0.15
0.1
0.05
0
-0.05
-0.1
fine silt to very fine sand
fine silt to very fine sand
very fine silt
fine silt to fine sand
fine silt to fine sand
fine silt to fine sand
very fine silt
fine silt to coarse silt
fine silt to coarse silt
very fine silt
fine silt to very fine sand
fine silt to coarse silt
fine silt to coarse silt
very fine silt to fine silt
very fine silt to fine silt
very fine silt to fine silt
fine silt to very fine sand
very fine silt
fine silt to medium silt
fine silt to coarse silt
very fine silt
very fine silt
fine silt to very fine sand
very fine silt to fine silt
fine silt to very fine sand
fine silt to very fine sand
very fine silt
very fine silt
grain size description

Fig.6

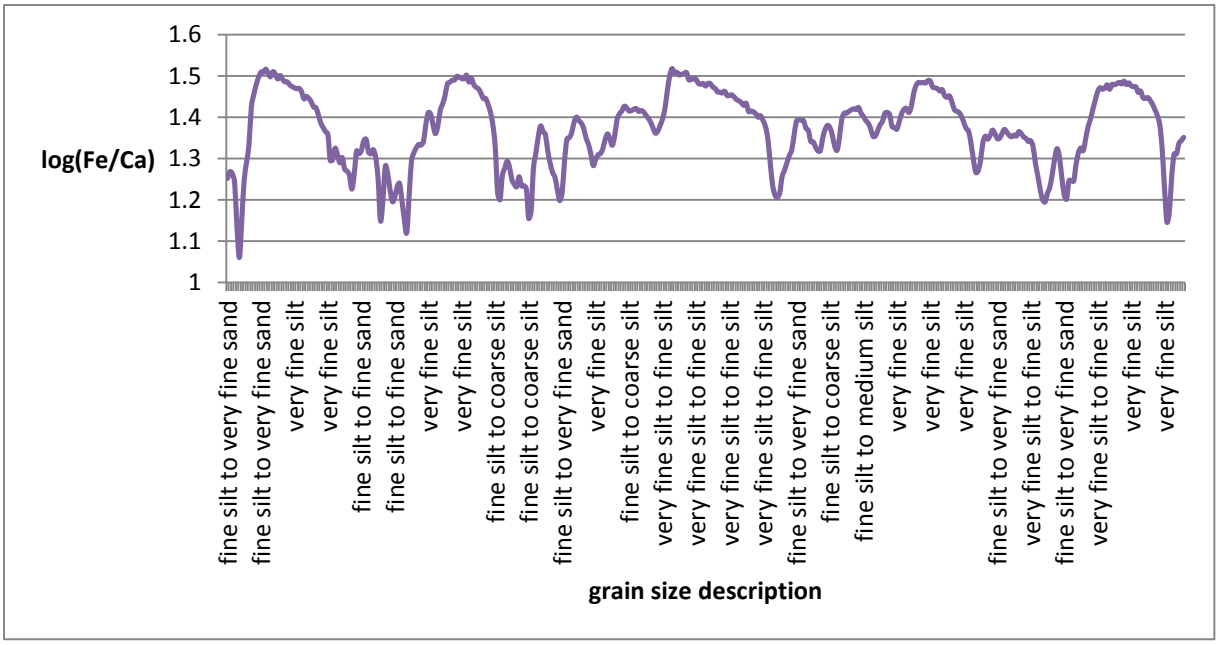
log(Fe/Ca)
1.6
1.5
1.4
1.3
1.2
1.1
1
fine silt to very fine sand
fine silt to very fine sand
very fine silt
very fine silt
fine silt to fine sand
fine silt to fine sand
very fine silt
very fine silt
fine silt to coarse silt
fine silt to coarse silt
fine silt to very fine sand
very fine silt
fine silt to coarse silt
very fine silt to fine silt
very fine silt to fine silt
very fine silt to fine silt
very fine silt to fine silt
fine silt to very fine sand
fine silt to coarse silt
fine silt to medium silt
very fine silt
very fine silt
very fine silt
fine silt to very fine sand
very fine silt to fine silt
fine silt to very fine sand
very fine silt to fine silt
very fine silt
very fine silt
grain size description

Fig.7

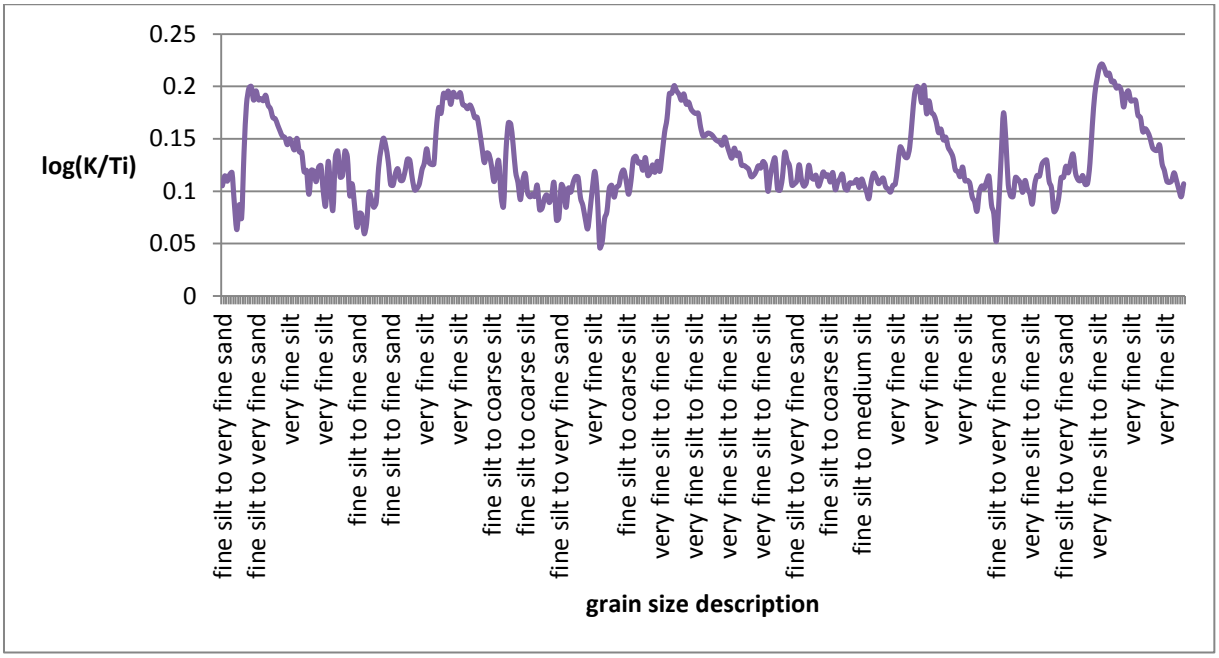
log(K/Ti)
0.25
0.2
0.15
0.1
0.05
0
fine silt to very fine sand
fine silt to very fine sand
very fine silt
very fine silt
fine silt to fine sand
fine silt to fine sand
very fine silt
very fine silt
fine silt to coarse silt
fine silt to coarse silt
fine silt to very fine sand
very fine silt
fine silt to coarse silt
very fine silt to fine silt
very fine silt to fine silt
very fine silt to fine silt
very fine silt to fine silt
fine silt to very fine sand
fine silt to coarse silt
fine silt to medium silt
very fine silt
very fine silt
very fine silt
fine silt to very fine sand
very fine silt to fine silt
fine silt to very fine sand
very fine silt to fine silt
very fine silt
very fine silt
grain size description

Fig.8

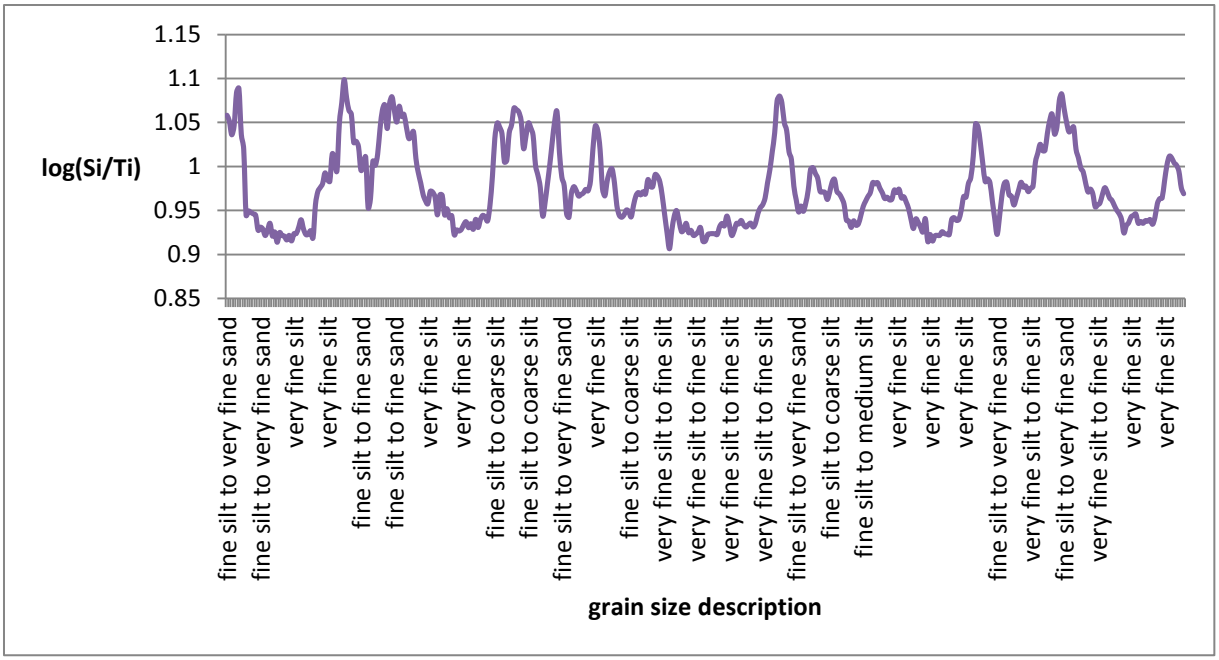
log(Si/Ti)
1.15
1.1
1.05
1
0.95
0.9
0.85
fine silt to very fine sand
fine silt to very fine sand
very fine silt
very fine silt
fine silt to fine sand
fine silt to fine sand
very fine silt
very fine silt
fine silt to coarse silt
fine silt to coarse silt
fine silt to very fine sand
very fine silt
fine silt to coarse silt
very fine silt to fine silt
very fine silt to fine silt
very fine silt to fine silt
very fine silt to fine silt
fine silt to very fine sand
fine silt to coarse silt
fine silt to medium silt
very fine silt
very fine silt
very fine silt
fine silt to very fine sand
very fine silt to fine silt
fine silt to very fine sand
very fine silt to fine silt
very fine silt
very fine silt
grain size description

Fig.9

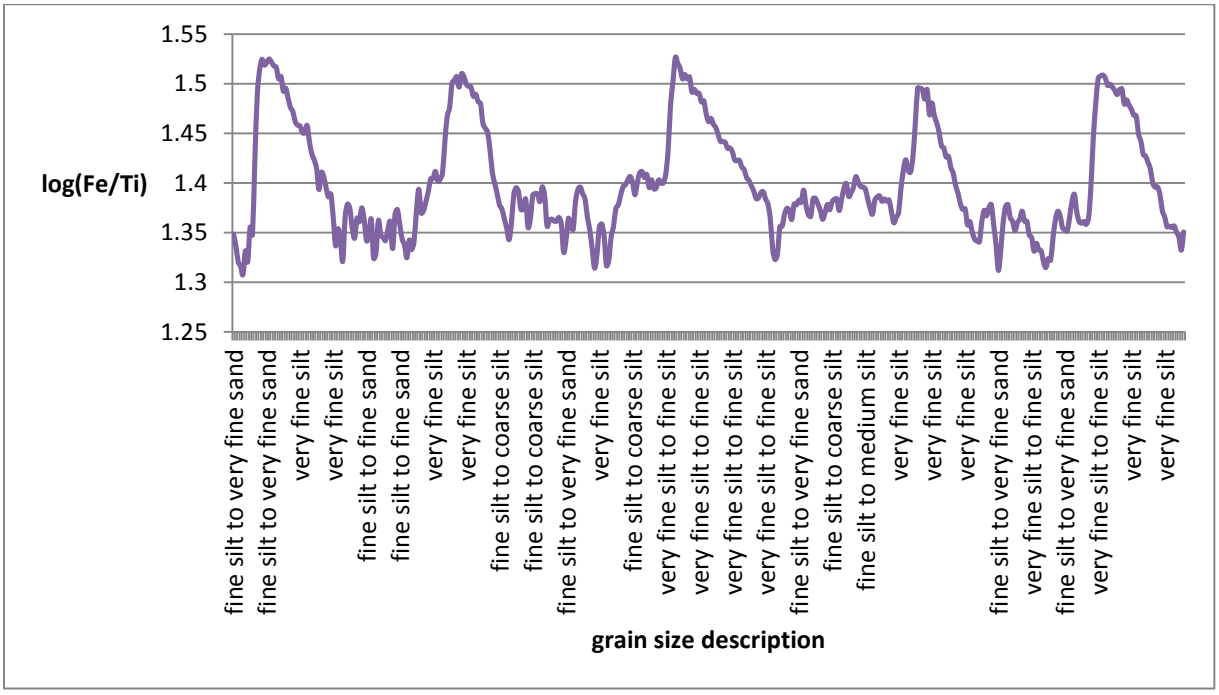
log(Fe/Ti)
1.55
1.5
1.45
1.4
1.35
1.3
1.25
fine silt to very fine sand
fine silt to very fine sand
very fine silt
very fine silt
fine silt to fine sand
fine silt to fine sand
very fine silt
very fine silt
fine silt to coarse silt
fine silt to coarse silt
fine silt to very fine sand
very fine silt
fine silt to coarse silt
very fine silt to fine silt
very fine silt to fine silt
very fine silt to fine silt
very fine silt to fine silt
fine silt to very fine sand
fine silt to coarse silt
fine silt to medium silt
very fine silt
very fine silt
very fine silt
fine silt to very fine sand
very fine silt to fine silt
fine silt to very fine sand
very fine silt to fine silt
very fine silt
very fine silt
grain size description

Fig.10